THEORIES OF SLOW DYNAMICS: FROM GLASSY COLLOIDAL SUSPENSIONS TO ENTANGLED MACROMOLECULAR LIQUIDS

BY

DANIEL SUSSMAN

DISSERTATION

Submitted in partial fulfillment of the requirements
for the degree of Doctor of Philosophy in Physics
in the Graduate College of the
University of Illinois at Urbana-Champaign, 2012

Urbana, Illinois

Doctoral Committee:

Research Associate Professor Timothy Stelzer, Chair
Professor Kenneth Schweizer, Director of Research
Associate Professor Karin Dahmen
Professor Steve Granick

Abstract

Motivated by the intriguing slowing down of dynamics in glassy and polymeric fluids, microscopic theories for the dynamical behavior of these systems are explored. Of particular interest is the relative importance of equilibrium structure and topological constraints on system dynamics, and theories studying each effect are constructed and applied in this dissertation.

The first part of this thesis treats suspensions of hard-sphere colloids — the theorist's idealization of a dense liquid — by connecting two-point equilibrium structure with the emergence of glassy dynamics. An earlier single-particle theory is qualitatively extended to study the dynamically correlated motion of two tagged particles in the fluid. A theory for Gaussian density fluctuations is constructed at the level of two tagged particles in a fluid of identical particles, and this theory is then extended to study highly non-Gaussian activated "hopping" events by modeling motion on a dynamic free energy surface. By coarse graining over the initial separation between the tagged particles many aspects of "dynamic heterogeneity," a set of phenomena accompanying the glass transition, can be understood. Connections with diverse alternative theories for describing the glass transition are also made.

The second part of this thesis studies polymeric fluids from a quite different perspective. By modeling macromolecules of various geometries as infinitely thin, zero-excluded-volume objects (rods, crosses, random walks) all equilibrium structural information is removed from the problem. Instead, system dynamics are determined by exactly including *topological* constraints, i.e., by rigorously enforcing macromolecular uncrossability at the two-body level.

This advance permits a wide variety of phenomena to be studied. The initial focus is on the equilibrium dynamics of cross- and rod-shaped macromolecules, and the theory is compared with both simulation and experimental results on synthetic and biological polymers. The theory is generalized to treat flexible polymers as random walks of coarse-grained primitive path steps.

The non-equilibrium behavior of rods under nonlinear rheological conditions is then studied in depth. We first posit a generalized Maxwell model for the constitutive equations controlling relaxation after an instantaneous step strain, the so-called "fundamental deformation." This model is then generalized to a generic, time-dependent shear deformation, and the consequences for continuous, constant-rate shear flows are studied. Finally, we exploit our ability to describe polymer interactions microscopically to compute the entanglement shear modulus directly from intermolecular contributions; this represents a potentially radical departure from the standard theoretical model of how stresses are stored in dense polymeric media.

Acknowledgments

It is my great pleasure to acknowledge some of the many people who have helped me during my time at the University of Illinois. While the infinite expanse of surrounding cornfields can occasionally be a bit dispiriting, the intellectual atmosphere has been nothing short of remarkable. The courses I had the good fortune to take with Profs. Baym, Goldenfeld, Stone, and Phillips profoundly changed the way I think about physics, and the breadth of research carried out by the faculty helped me find a project that more closely matched both my interests and my strengths than I would have thought possible. In short, I am lucky to have found a graduate program as well suited for me as the U of I Physics department.

I am extremely fortunate to have had Ken Schweizer as my advisor. His physical insight across a formidably broad range of soft condensed matter systems was an inspiration from day one, and I can only hope that in my time working with him I have acquired some small portion of that ability to intuit the zeroth-order physics of a problem. I will also not forget his general kindness and support of my work even when progress was slow. I recall the many consecutive meetings when I was first starting to work on topologically influenced dynamics but was so beset by difficulties that I was on the verge of switching topics. Yet my lab notebook recording those meetings bears witness to his encouragement with countless notes of "Ken: Give it one more week" as, with weeks turning into months, I struggled towards a working theory. Some of the most intellectually stimulating work I have done can be traced back directly to that patience and that enthusiasm for tackling difficult but rewarding problems.

My work could not have been done without the friendly research environment fostered

by the Schweizer research group, but I would like to particularly mention a few individuals. From my early years in the group I would like to thank Lisa Hall and Mukta Tripathy for welcoming me to the group, helping me learn most of what I now know about liquid state theory, answering my many questions, and generally being good friends. From my later years I must thank Umi Yamamoto for always being willing to listen and serve as a sounding board for some of my ideas, despite how poorly thought out they at times were.

I would also like to thank Steve Granick, who has been generous with advice about grad school and carrying out research, and who helped greatly during my time on the job hunt. Sitting in on many of his group's weekly meetings taught me a tremendous amount, giving me a much better appreciation for and understanding of how the experimental results I so love to compare with are actually arrived at. The students and postdocs in his research group also deserve my thanks for putting up with my questions during those meetings, no matter how uninformed or naive. In particular I extend my thanks to Bo Wang and Juan Guan for their endless patience in explaining the fascinating experiments on biopolymers they were in the midst of.

Many thanks also go to Grzegorz Szamel; not many people would so willing dig through work they carried out twenty years earlier to help a young graduate student from a different institution find a measly factor of two in an unpleasantly technical calculation. I also owe him a great deal for his help as I applied for postdoctoral positions, as well as the excellent scientific and career-oriented advice he has offered.

Most importantly, where would I be without my family and my friends? Certainly not on the verge of finishing graduate school career. Your love and support humbles me.

Finally, I would like to acknowledge funding sources. During my first year the department generously supported me as a teaching assistant to 150 of the best PHYS 101 students ever to grace the campus. My four years as a research assistant were supported by the National Science Foundation under Grant No. NSF-DMR-0642573.

Table of Contents

Chapter 1

INTRODUCTION

Broadly speaking, this dissertation looks at two mechanisms that can radically slow down system dynamics in the fluid state. The first, presented in the context of glassy colloidal suspensions, is an investigation into the connection between equilibrium fluid structure and correlated dynamical motion. The second, in attempting a microscopic account of entangled polymer dynamics under a variety of equilibrium and nonlinear rheological conditions, ignores structural considerations and explores the effect of topological constraints on the dynamics. Leaving aside for the moment the intrinsic theoretical interest of these problems and the practical importance of glassy and polymeric materials, at first blush the chosen systems seem to arise out of fairly unrelated questions from the edges of fluid mechanics: "What happens to a fluid when it is supercooled rapidly enough to avoid crystallization?" or "What occurs when the constituent parts of the fluid become long and complicated enough to form entanglements?"

As we will see, though, some of the fundamental obstacles to a microscopic understanding of these systems are much the same. This is not the textbook view. In particular, neither set of systems has yet yielded to a critical phenomena or renormalization-group approach, and in the phase-space regimes of interest primary fluctuations have a distinctly non-Gaussian character (e.g. in glassy systems the dominant relaxation mechanism appears to be thermally activated "barrier-hopping" events). Describing such fluctuations is a daunting challenge within any statistical-mechanical framework. Our approach to both problems will involve first formulating a microscopic model that operates at the Gaussian-fluctuation level, and then invoking a particular framework to treat the non-Gaussian fluctuations. The first step

separates the two problems but, once done, the second step provides a unifying perspective. Below we briefly introduce the basic phenomenology of the two systems we wish to study, describing for each why a mean-field theory with Gaussian fluctuations is insufficient, and then work through a simple example of moving to the level of non-Gaussian fluctuations.

1.1 The Colloidal Glass Transition

[1]Understanding the glassy dynamics of molecular liquids is an outstanding challenge in condensed matter physics, chemistry, and materials science. Although theorists have searched for a (possibly avoided) transition to an underlying ideal glass phase, the "glass transition" is in fact a *dynamic* crossover to a regime of activated behavior in the liquid state associated with a crossover temperature or density, T_c or ρ_c. Experimentally, the glass transition point T_g or ρ_g is a working definition that answers a very practical question: when does the characteristic relaxation time of the system exceed the experimental time scale (e.g. $\tau_\alpha \sim 10^2 - 10^4$s, where τ_α is a time scale associated with particle motions larger than the short-time vibrational modes of a particle rattling in its cage of local neighbors)? This is often framed as the dynamic viscosity of the smaple growing to $\sim 10^{12}$ Pa s — the two quantities are proportionally related by the high-frequency shear modulus [1].

The dynamical changes in the fluid occur over a region of the control parameter (temperature or volume fraction, $\phi = \rho\pi\sigma^3/6$, with σ the particle diameter) where the static structure changes very little. For instance, the radial distribution function $g(r)$ describes the probability of finding a fluid particle at position r given a tagged particle at the origin; the normal liquid and supercooled liquid or glassy $g(r)$'s have only minor quantitative differences. This is shown in Fig. 1.1A, which plots both the radial distribution function and the static structure factor, $S(k) = 1 + \rho \int \exp\left(-\vec{k}\cdot\vec{r}\right)(g(\vec{r}) - 1)d\vec{r}$ for a hard-sphere suspension. Over the range of volume fractions shown ($\phi = 0.5, 0.53, 0.56$) the characteristic

[1]This section contains text from *D. M. Sussman and K. S. Schweizer, Phys. Rev. E* **85**, 061504 (2012), Copyright APS 2012

relaxation time changes by over two orders of magnitude, but the two-point correlation functions change very little. Recently there has been theoretical and simulation-based efforts to study whether there is a larger structural signature of the glass transition in higher-order correlation functions, but at the moment such studies are inconclusive [2].

The most basic experimental fact in describing glasses is that when a fluid is cooled below its freezing point rapidly enough to avoid crystallization its viscosity grows enormously over a relatively narrow range of the control parameter (typically temperature, T, or density, ρ, for molecular liquids and colloidal suspensions, respectively). For instance, the viscosity of the molecular liquid *ortho*-terphenyl (OTP) increases by 11 orders of magnitude as the temperature is rapidly dropped from 293 K to 243 K [3]. The theorist's idealization of a dense liquid - diffusing spherical particles interacting only via hard-core interactions - can be approximately realized in the laboratory in the form of colloidal suspensions, for instance $\sim$ 1 micron poly(methyl methacrylate) beads stabilized with a thin surface layer of poly-hydroxysteric acid to minimize van der Waals-induced aggregation [4]. For these colloidal particles, though, the bare relaxation times is not the picosecond motion of molecular liquids but is rather on the order of $\sim 0.001 - 1$s. The consequence is that these experiments, while much easier to perform (e.g. with light microscopy), can only probe $4 - 5$ orders of magnitude of glassy slowing down. Coincident with this dramatic increase in the typical time scale of system relaxation, simulations and experiments have found many other signature dynamical behaviors as a fluid enters the glassy regime (even in the limited regime that colloidal experiments and simulations can probe). Notably, as particle volume fraction increases, typical particle trajectories change from smooth and diffusive-like to being characterized by intermittent "hopping" events separated by long periods of highly localized vibrational motion [5]; this is schematically illustrated in Fig. 1.1B. This effect shows up as a plateau in the mean square displacement of ensemble-averaged particle displacements, and can also be directly visualized in confocal microscopy experiments on hard-sphere colloidal suspensions and computer simulations.

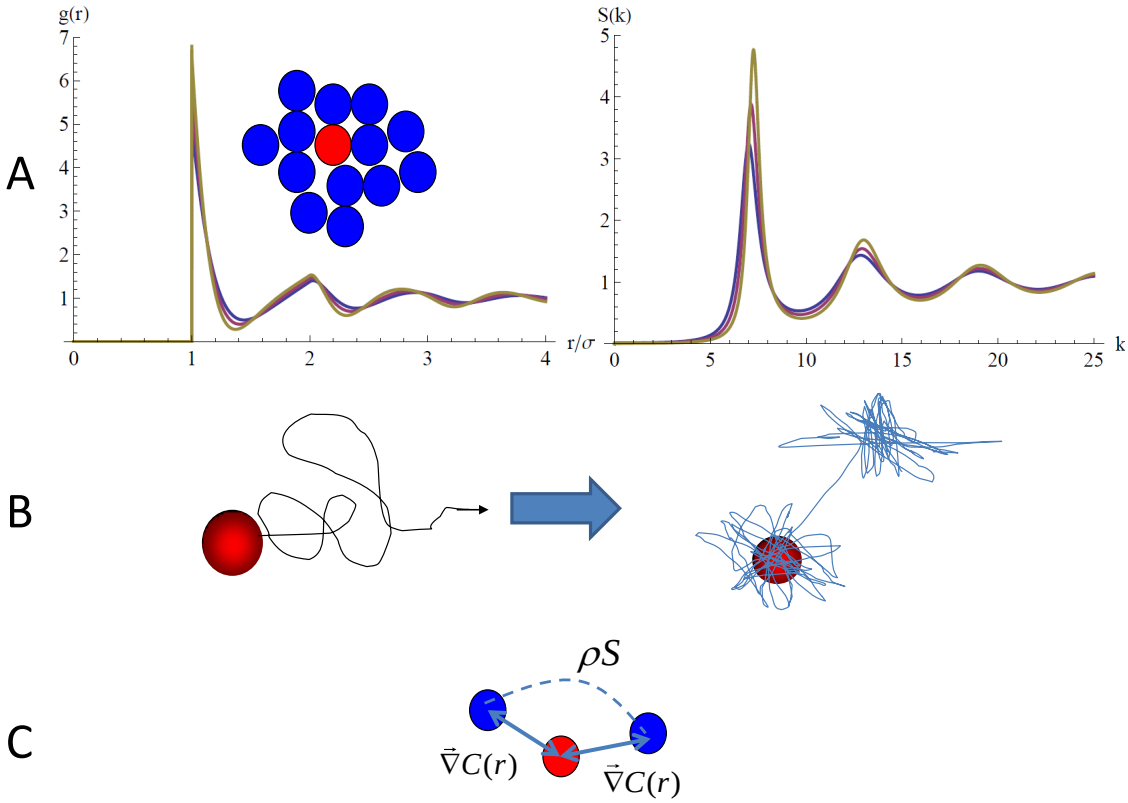

Figure 1.1: (A) Approximate two-point equilibrium correlation functions, $g(r)$ and $S(k)$, using the Percus-Yevick closure [6] over a range of hard-sphere volume fractions ($\phi = 0.5,\ 0.53,\ 0.56$) in which the relaxation time increases by over two orders of magnitude. (B) Cartoon change of typical particle trajectories from diffusive to caged. (C) Schematic real-space picture of the terms contributing to the vertex in the self-consistent localization-length equation.

Complicating the picture even more, the dynamics of the fluid become heterogeneous in time and space, with clusters of more mobile particles forming against a background of largely immobile particles. This feature is evident in direct microscopy observations and also manifests itself through more subtle experimental signatures. One example is the breakdown of the Stoke-Einstein (SE) relation between the viscosity and diffusion; in the normal fluid state SE relates the translation diffusion constant D to the viscosity η by $D \sim \eta^{-1}$. In the supercooled regime, though, diffusion has a *weaker* dependence on viscosity than that suggested by SE. Additionally, correlation functions that are normally expected to decay exponentially with characteristic time τ, such as observations from dielectric relaxation or NMR spectroscopy, are found to have a so-called "stretched-exponential" decay, $C(t) \approx exp\left(-(t/\tau)^{\beta}\right)$, with $\beta < 1$ [3]. A common interpretation given to these observations is that beyond the glass transition the fluid is transiently divided into heterogeneous regions with different characteristic relaxation times. The lifetime of these regions is typically of order τ_{α}. Averaging exponentially decaying correlation functions over these regions results in stretched exponential correlation functions. Furthermore, if one imagines that diffusion/mass transport is dominated by contributions from fast regions but that viscosity/rotational relaxation requires the slow tails of the distribution to be sampled, then the decoupling of relaxation and diffusion also follows [7]. These "dynamic heterogeneities," along with the dynamical crossover to activated barrier crossing behavior, are among the prime reasons why the well-developed theories of simple liquid behavior break down in the glassy regime [2].

In some ways the field suffers from an embarrassment of riches in the sense that a wide variety of seemingly very different ideas and theoretical methods are able to capture some features of glassy dynamics with varying levels of predictive or descriptive power. An incomplete list includes: the random first order transition entropy crisis approach (RFOT) built on spin-glass-like ideas; microscopic force-level theories based on collective density fluctuations (mode coupling theory) and activated particle hopping (nonlinear Langevin equation

theory); coarse-grained dynamic facilitation models based on diffusing mobility fields and phenomenological kinetic constraints; potential-energy-landscape approaches; and the concept of frustration-limited domains [2]. At the same time, issues as fundamental as whether the controlling mechanisms of the transition are dynamic, structural, and/or thermodynamic, and whether dynamic heterogeneity is important to first order for the massive slowing down of structural relaxation, remain highly contested [8].

In terms of approaches that attempt to operate at a truly predictive, microscopic, force-level description, the most advanced program is mode-coupling theory (MCT) [9–11], which nonlinearly couples liquid relaxation to collective pair-density fluctuations to try to explain glassy dynamics. After invoking uncontrolled projection and dynamic Gaussian (factorization) approximations (described in more detail in Sec. 1.3), the collective and self dynamic structure factors can be computed using only the equilibrium pair structure as input. Despite the very modest changes in equilibrium pair structure as the glass transition is crossed, MCT has a highly nonlinear feedback mechanism that greatly amplifies these small changes in structure, resulting in a divergent dynamical slowing down of the system. Ideal MCT has had considerable success in the dynamic "precursor" or "crossover" regime in which the relaxation slows down by only a few orders of magnitude. However, the use of a particular uncontrolled approximation, essentially the factorization of a four-point correlator into a product of two-point correlators (a dynamic Gaussian approximation), results in a spurious non-ergodicity transition at a relatively high temperature in viscous liquids (or low volume fraction in particle suspensions). In reality, ergodicity is restored via highly non-Gaussian activated barrier hopping events. As alluded to above, it is the fundamental importance of these non-Gaussian ergodicity-restoring fluctuations and their dynamic correlations that limits MCT and which this work seeks to address.

1.2 Entangled Polymer Liquids

Solutions and melts of polymers, long macromolecules of diverse topology formed by repeating molecular units, are prime ingredients in modern materials. Schematically depicted in Fig. 1.2A, polymers can be manufactured in a variety of geometrical shapes, from rigid rods to flexible chains to branched "star" polymers (and, indeed, even more exotic shapes, such as H's and combs). The topology of the polymers composing a melt is extremely important in determining the material properties of the bulk, often more important than the particular chemistry of the chain. As such, it is easiest to initially adopt a coarse-grained model of polymers as being N linked statistical segments of size σ, each of which is a coarse-graining over some chemistry-dependent number of molecular repeat units, that are connected into the geometry we wish to study (rods, random walks, etc.). By also introducing a material parameter that quantifies how chemically different polymer species fill space — the "invariant packing length" $p = (\rho_s \sigma^2)^{-1}$ with ρ_s the segmental density — polymers fluids can be described at a fairly universal level. Typical numbers for these material parameters in, e.g., polyethylene melts are of order $\sigma \sim 1\text{nm}$, $\rho_s \sim 0.8\text{g/cm}^{-3}$, and $p \sim 0.17\text{nm}$. In a melt, at this level of coarse graining synthetic chains become essentially random walks, whose spatial extent can be characterized by the mean end-to-end vector, $R_{ee} = \sigma\sqrt{N}$, or the radius of gyration, $R_g = \sigma\sqrt{N/6}$. For synthetic chains these length scales are typically on the order of $10 - 100\text{nm}$.

The viscoelastic properties of polymeric systems are both spectacular and spectacularly sensitive to polymer architecture. For instance, in a melt of relatively short chains the self-diffusion is inversely proportional to chain length, $D \sim N^{-1}$, and the viscosity is proportional to chain length, $\eta \sim N$. However, when the chains grow sufficiently long, $N > N_e$, the power laws become much more strongly dependent on chain length, with $D \sim N^{-2.3}$ and $\eta \sim N^{3.4}$. In this crossover from "unentangled" to "entangled" behavior the response of the system to external deformation also changes, with entangled chains exhibiting a soft rubbery response

over some (potentially long) intermediate time scale. This is schematically shown in the shear modulus depicted in Fig. 1.2B, which develops a plateau between the characteristic times τ_e, the time at which a chain first feels an entanglement, and τ_{rot}, the terminal relaxation time. The value of the plateau determines how strong the elastic response is in that time window (typically the plateau is of order $0.1 - 1$MPa — much less than the GPa scale associated with a glassy short-time modulus) and is sensitive to the material parameter p; the duration of the plateau depends on the properties of the melt in that it scales as N^3¿ Nevertheless, the generic viscoelastic response of polymer melts is common across all entangled chains. All of these results can change drastically when considering other polymer architectures. For instance, melts of star polymers have an *exponential* suppression of diffusion with arm length and an exponential growth of the viscosity.

Achieving a first-principles theoretical understanding of the spectacular viscoelasticity of strongly entangled synthetic and biological polymer liquids is an extremely challenging problem in time-dependent statistical mechanics, but one that has potentially broad implications: for the processing of synthetic macromolecules [12]; understanding the motion of biopolymers in the cellular matrix [13]; and even in more exotic systems, such as the behavior of entangled flux lines in high-T_c superconductors [14]. The unifying feature across these different systems and physical phenomena is the concept of "topological constraints," an interplay between the long-range connectivity of the constituent parts and their inability to pass through each other, i.e. their "uncrossability." For highly extended objects this singular contribution to the intermolecular potential dominates viscoelasticity and relaxation, but capturing these topological interactions within a microscopic framework has generally been impossible. In polymer physics the most popular and well-developed approaches for linear macromolecules (rigid rods and flexible chains) are built on the phenomenological ideas of deGennes, Doi, and Edwards [12, 15]. There a single-polymer dynamic mean-field theory is constructed in which inter-chain interactions are replaced by ansatz with an infinitely strong confining "tube" that strictly forbids large-scale displacement transverse to

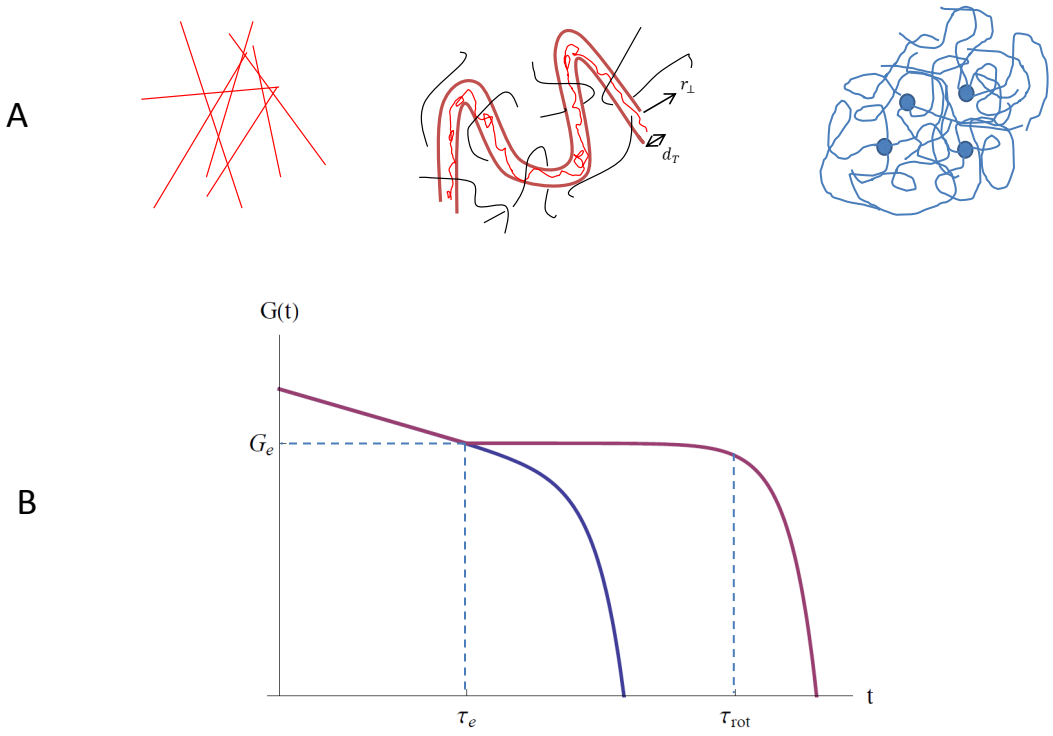

Figure 1.2: (A) Cartoon of entangled rods (left), a flexible chain in a tube of diameter d_T perpendicular to the polymer backbone formed by other chains (center) and four-armed star polymers (right). (B) Schematic log-log plot of the shear modulus for an unentangled (blue) and entangled (red) melt of flexible polymers.

the polymer backbone. Multiple corrections to the quiescent tube model which enhance polymer mobility and reduce motional anisotropy are experimentally important [16], but are not derived in a rigorous way. Both the corrections and even the tube itself simply rely on inspired guesswork to encode the consequences of topological constraints on the physical motion of a single tagged polymer.

To make some of these ideas clearer, it is worthwhile to quickly review the simplest tube-model derivation of scaling laws. The model is meant to apply to a Brownian suspension of infinitely thin rigid rods of length L and number density ρ, where the bare diffusion tensor has components $D_{\parallel,0}$, $D_{\perp,0}$, and $D_{rot,0}$ for longitudinal, transverse, and rotational motions (here we closely follow the development in [12] and [17]). This system is schematically illustrated in Fig. 1.3. Since the rods are infinitely thin their equilibrium structure is that of an ideal gas (and is thus unimportant), but the topological constraint of rod-rod uncrossability can have a profound effect on the system's dynamics. The tube model is meant to apply for large dimensionless densities, $\rho L^3 \gg 1$, and the key idea is to replace the complicated many-rod system by a dynamic mean field theory for the effective motion of a single rod. In this picture the longitudinal motion of the tagged rod is unconstrained (infinitely thin rods will never run into another needle end-on), but its transverse and rotational diffusion is hindered by an effective confining tube of diameter d_T. In general, this length scale and the mean-field confining potential generating it are *not* constructed in a self-consistent, first-principles manner; they are simply postulated with adjustable parameters to fit experimental data.

The calculation of this most crucial parameter of the theory for entangled rods comes from solving the following geometry problem: draw a cylinder of radius r around the tagged rod, and calculate the number of other rods that intersect this cylinder, $N(r)$. The tube diameter is then estimated as $N(d_T/2) \approx 1 \rightarrow d_T \approx (\rho L^2)^{-1}$. From here the tube-model predictions for the reduction of the long-time diffusion in the hindered directions follows immediately. Within the tube the rod can neither translate laterally nor rotate (i.e. the constraints are infinitely strong), and the characteristic time for a rod to exit its local tube

longitudinally follows from Fick's law as $\tau_r \sim L^2/D_{\parallel,0}$. Each time it exits the tube the rod enters a new tube, and on average this new tube is displaced $\Delta r_\perp \sim d_{tube}$ laterally and rotated $\Delta\theta \sim d_{tube}/L$ relative to the axis of the original tube. Long-time diffusion proceeds via these small steps each time the rod "reptates" out of tube, leading to

$$D_{rot} \sim \frac{\Delta\theta^2}{\tau_r} \sim \frac{D_{\parallel,0}L^{-2}}{(\rho L^3)^2}, \quad D_\perp \sim \frac{d_T^2}{\tau_r} \sim \frac{D_{\parallel,0}}{(\rho L^3)^2}. \tag{1.1}$$

The proportionality of transverse and rotational motion at high densities is a welcome simplifying fact. For reasons of tractability we will be studying a microscopic theory of rods with frozen rotational motion; dealing with rod rotations even under simplified conditions or reduced dimensionality adds a great deal of complexity to the calculation [18, 19], and so we will exploit the slaving of transverse and rotational motion in our approach.

The scaling relations above are compared with simulation data in Fig. 1.3 — at high densities they are fairly accurate, but they of course give no hint about their regime of validity or the crossover behavior from unentangled to entangled dynamics. Nor do they have anything to say about the prefactors, for instance β relates the rotational diffusion constant to the reduced density, $D_{rot}/D_{rot,0} = \beta(\rho L^3)^{-2}$, and turns out to be surprisingly large: fitting the data requires $\beta \sim 10^3 - 10^4$ [12]. In flexible chain systems the scaling relations are slightly less accurate even for high degrees of entanglement. To take one example, the terminal relaxation time is predicted to grow with chain length as $\tau \sim N^3$, but experiments find a power law closer to the aforementioned $\tau \sim N^{3.4}$ [12].

The Doi-Edwards (DE) reptation-tube approach is a powerful one that can be extended to polymers of diverse architecture. However, the confining tube has not been deduced from the statistical mechanics of the fundamental inter-polymer interactions in a first-principles, self-consistent manner. Recent perspective and opinion articles [22, 23] emphasize that the tube model lacks a microscopic foundation, and a "bottom up" conceptual breakthrough on the crucial tube diameter length scale is needed to address open questions, such as: What

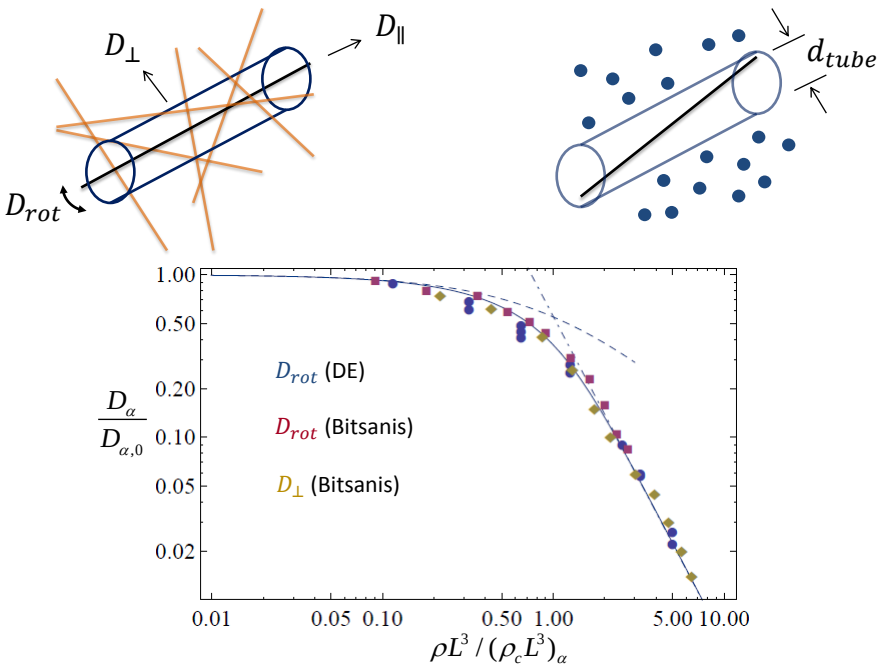

Figure 1.3: Cartoon defining the tube diameter and the direction of the diffusion constants relative to a tagged rod. The plot shows simulation data from [20,21] for decreasing normalized diffusion constants versus normalized density, and compares it with scaling functions representing independent binary collisions (dashed) and reptative motion (dot-dashed), as well as the theoretical expectation from a model which avoids tube-model approximations [17] (solid).

is the nature of an entanglement and of the tube confinement field? Can it be derived theoretically? Can the connection between polymer chemistry, concentration, and the tube diameter be understood from first principles? In later chapters we hope to show that these questions, and many more, can be answered in the affirmative.

To a certain extent some of these questions can be addressed reasonably accurately via a microscopic but purely Gaussian theory. Indeed, for rigid rods a relatively overlooked microscopic theory exists that reproduces many of the scaling features of the phenomenological harmonic tube theory [17,24]. However, the assumptions of an infinitely strong confinement potential is both physically unrealistic and potentially problematic in driven non-equilibrium situations. Several recent experimental and simulation studies have challenged the commonly postulated one-parameter harmonic approximation for the tube confinement field. Particularly relevant for this thesis are experiments and complementary theoretical work on entangled solutions of the semiflexible biopolymer F-actin [25,26], and simulations of F-actin and rigid-rod model polymers [27]. By studying displacement distributions at intermediate times, or averaging mean-square displacements over many trajectories, these studies have revealed an effective transverse confining potential that is significantly softer than harmonic. Evidence of strong anharmonic softening has also been observed in DNA solutions [28] and in simulations of entangled flexible chain melts [29, 30]. Anharmonicities in the confining field qualitatively modify the equilibrium distribution, of course, but they are of utterly crucial importance when it comes to polymer rheology. Flowing or otherwise deforming a polymer sample can introduce very large stresses, and in the presence of stress a harmonic confining potential (which can provide a restoring force of effectively infinite strength) and an anharmonically softened one (which can support only a finite restoring force) lead to completely different predictions for the response of the system to deformation.

1.3 The Nonlinear Langevin Equation

[2]Since the abstracted strategy of (i) solving a Gaussian microscopic theory and (ii) extending it to treat non-Gaussian fluctuations motivates much of our work, here we outline a relatively simple example that appears in the literature, the "single-particle non-linear Langevin equation (NLE) theory" for glassy hard-sphere colloidal suspensions [31]. Ultimately, for these systems the NLE was derived using dynamic density-functional methods under a type of "local-equilibrium" approximation [32]; here we present a still-technical but more heuristic "derivation" but one that contains all of the essential physics.

The initial goal is a single-particle localization length based on Gaussian fluctuations or an amorphous Einstein-solid model of a glass. We start with a simplified ("naive") version of a mode-coupling theory (NMCT [33]) that self-consistently renormalizes the effective friction acting on a tagged particle. The generalized Langevin equation for a tagged particle of mass m and diameter σ in an overdamped Brownian hard-sphere suspension follows from choosing the variables of interest to be the tagged particle position $\vec{R}(t)$ and velocity $\vec{V}(t)$. Using standard projection-operator methods one has [34]

$$m\frac{d\vec{V}(t)}{dt} = -\int_0^t dt' M(t-t')\vec{V}(t') + \vec{f}^Q(t). \tag{1.2}$$

The superscript Q indicates time-evolution according to projected dynamics, and the projected random force $\vec{f}^Q$ satistfies the fluctuation-dissipation relation and is orthogonal to both $\vec{R}$ and $\vec{V}$. Decomposing the random force into a rapidly fluctuating part due to short-time friction (ζ_s) and a slowly-changing part associated with structural relaxation [34], the memory function is given by [6, 9, 10, 31]

$$M(t) = \frac{\beta}{3}\langle \vec{f}(0)\cdot\vec{f}^Q(t)\rangle \approx \zeta_s\delta(t) + K(t), \tag{1.3}$$

[2]This section contains text and a figure reprinted with permission from *D. M. Sussman and K. S. Schweizer, J. Chem. Phys.* **134** *064516 (2011)* Copyright 2011, American Institute of Physics.

where $\beta = 1/k_B T$. The heart of NMCT is an approximate computation of the slowly decaying part, $K(t)$. To do this, forces are projected onto a bilinear product of tagged particle density and the fluid collective density, conveniently written in fourier space as $\rho_s(\vec{k},t) = \exp\left(i\vec{k}\cdot\vec{r}_1\right)$ and $\rho_c(k,t) = \sum_{i=1}^{N}\exp\left(i\vec{k}\cdot\vec{r}_i\right)$. The projected dynamics are replaced by the true dynamics, and four-point correlation functions are factorized into products of two-point correlation functions (i.e. a "dynamic Gaussian" approximation). Schematically,

$$\langle \vec{f}(0)\cdot\vec{f}^{Q}(t)\rangle \sim \left\langle \rho_s(\vec{k}_1,0)\rho_c(\vec{k}_2,0)\rho_s(\vec{k}_3,t)\rho_c(\vec{k}_4,t)\right\rangle \sim \left\langle \rho_s(\vec{k}_1,0)\rho_s(\vec{k}_3,t)\right\rangle \left\langle \rho_c(\vec{k}_2,0)\rho_c(\vec{k}_4,t)\right\rangle . \tag{1.4}$$

Intuitively, this vertex can be thought of as a real-space accounting of forces between particles as mediated by the fluid (shown in Fig. 1.1C). An effective interparticle potential can be understood as $U_{eff}(r) \sim -k_B T\vec{\nabla}C(r)$ (where $C(r)$ is the real-space direct correlation function, related to the structure factor by $S(k) = (1-\rho C(k))^{-1}$) and ρS quantifies interparticle correlations of the forces beyond the binary-interaction level. Working through a detailed calculation results in [31, 33]

$$K(t) = \frac{1}{3\beta}\int \frac{d\vec{k}}{(2\pi)^3} k^2 \rho C^2(k) S(k) \Gamma_s(k,t)\Gamma_c(k,t). \tag{1.5}$$

Here ρ is the fluid number density, and Γ_s and Γ_c are the single-particle and collective propagators (i.e. dynamic structure factors normalized by their $t=0$ value):

$$\Gamma_s(\vec{k},t) = \langle e^{i\vec{k}\cdot(\vec{R}(0)-\vec{R}(t))}\rangle \approx \exp\left(-k^2\langle r^2(t)\rangle/6\right) \tag{1.6}$$

$$\Gamma_c(\vec{k},t) = S^{-1}(k)\sum_{i,j=1}^{N} N^{-1}\langle e^{i\vec{k}\cdot(\vec{R}_i(0)-\vec{R}_j(t))}\rangle \approx \Gamma_s(k/\sqrt{S(k)},t). \tag{1.7}$$

The second approximate equalities above reflect yet another Gaussian approximation made for the single-particle propagator, followed by a modified Vineyard approximation to relate the collective propagator to the single-particle propagator in a way which properly captures

the effect of equilibrium cage-scale structure on local-scale collective density fluctuations (the de Gennes narrowing effect) [6, 31]. The variable $r(t)$ now refers to the scalar displacement of the tagged particle from its position at $t = 0$, and the theory has been closed at the mean-square-displacement (MSD) level.

An ideal glass transition occurs when a long-time localized solution for the ensemble-averaged MSD, $r_{loc} \equiv \langle r^2(t \to \infty)\rangle < \infty$, first emerges. NMCT adopts an amorphous Einstein solid model for the frozen glass structure, corresponding to each particle experiencing localization via a harmonic spring about an amorphous, liquid-like set of positions:

$$\Gamma_s(k, t \to \infty) = \exp\left(-k^2 r_{loc}^2/6\right), \tag{1.8}$$

$$\Gamma_c(k, t \to \infty) = \exp\left(-k^2 r_{loc}^2/6S(q)\right). \tag{1.9}$$

A self-consistent equation governing the localization length can be derived, either by using the generalized Langevin equation with the NMCT simplifications [32], or, more simply, by writing down the intuitive equipartition relation $K(t \to \infty)r_{loc}^2/2 = 3k_BT/2$, thinking of the long-time limit of the memory function as a localizing "spring." In either case one obtains [31]

$$\frac{1}{r_{loc}^2} = \frac{1}{9}\int \frac{d\vec{k}}{(2\pi)^3} k^2 \rho C^2(k) S(k) \exp\left(\frac{-k^2 r_{loc}^2 (1 + S^{-1}(k))}{6}\right). \tag{1.10}$$

This is the sought-after microscopic result of the Gaussian theory. Using, e.g., the Percus-Yevick approximation for the liquid structure of hard spheres of diameter σ [6], this equations predicts an ideal glass transition at a volume fraction of $\phi_c \approx 0.432$, beyond which particles are localized with characteristic vibrations on the order a tenth of a particle diameter.

To go beyond this Gaussian theory, the single-particle NLE theory takes the NMCT ideal glass transition to signal the onset of *transient* localization together with a crossover to thermally activated, barrier-hopping-driven transport. The scalar displacement of a tagged

particle from its initial position, $r(t)$, is employed as the primary dynamical variable, and a stochastic equation of motion for its evolution is proposed (of a relaxational or "Model A" [35] form describing a non-conserved order parameter) based on three physically-motivated ideas [31, 32]: (i) NMCT correctly predicts localization in the absence of thermal noise, (ii) particles undergo Fickian diffusion at short times before becoming transiently localized, and (iii) thermal noise destroys the ideal NMCT glass transition, allowing for activated hopping even when $\phi > \phi_c$. The nonlinear Langevin equation embodying condition (iii) in the overdamped regime (i.e. ignoring the inertial term) is

$$\zeta_s \frac{d}{dt} r - \frac{\partial}{\partial r} F_{dyn} + \delta f = 0, \tag{1.11}$$

where the white noise δf satisfies the fluctuation-dissipation relation with respect to the short time friction constant ζ_s. F_{dyn} is a "dynamic" free energy, and Eq. 1.11 is meant to describe single-particle motion at intermediate times, i.e. times during which the particle rattles around in its cage of neighbors and occasionally makes a rare, ergodicity-restoring jump out of that cage. To satisfy condition (i) the dynamic free energy must be constructed so that its minimization with respect to the order parameter recovers the NMCT self-consistent equation for r_{loc} above: $\partial F_{dyn}/\partial r|_{r=r_{loc}} = 0$. To uniquely specify F_{dyn} (up to an irrelevant constant) and satisfy condition (ii), we insist that one of the terms corresponds to Fickian diffusion, with $r^2(t \ll 1) \sim t$. The result is

$$\beta F_{dyn}(r) = -3\ln(r) - \rho \int \frac{d\vec{k}}{(2\pi)^3} C^2(k) S(k) (1 + S^{-1}(k)) \exp\left(\frac{-k^2 r_{loc}^2 (1 + S^{-1}(k))}{6}\right). \tag{1.12}$$

The first term on the right hand side represents the ideal, entropic contribution to fluid motion that describes short-time Fickian motion; the competing term reflects a structural "caging" term that favors particle localization with increasing density. Figure 1.4 shows $F_{dyn}(r)$ for a hard-sphere fluid at different volume fractions. Below ϕ_c the dynamic free

energy is a monotonically decreasing function of particle displacement, corresponding to the absence of any localization and essentially smooth, fluid-like Brownian motion of individual particles. At higher volume fractions, though, an entropic barrier emerges that serves to transiently localize particles over a time scale related to how long it takes to surmount the barrier. As a result of this entropic caging, the dynamics become "exponentially slow," a hallmark of glassy dynamics. This mean first-passage time for barrier crossing has been shown to be connected with the α-relaxation time measured in colloidal suspensions [31].

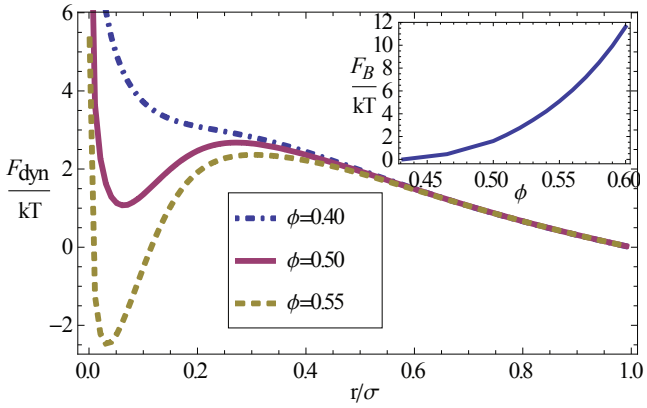

Figure 1.4: Dynamic free energy as a function of particle displacement based on the single-particle NLE theory for hard-sphere fluids at volume fractions above and below ϕ_c. Inset shows the height of the entropic barrier as a function of volume fraction.

To summarize, the intuitive physical picture of this method of describing non-Gaussian fluctuations about a localized state can be described as follows. First, a Gaussian theory is used to derive a self-consistent equation for a dynamical localization length. This self-consistent equation is then physically reinterpreted (in the spirit of a local equilibrium approximation) as arising from a force-balance for the instantaneous displacement of a tagged particle, which can typically be written as the sum of an entropic delocalizing force and an opposing localizing force that depends on the physics of the system in question (e.g. a structural caging term for colloidal suspensions, or a topological entanglement term in polymer melts). The force is then integrated to construct a dynamic free energy, and noise-driven diffusion on this (anharmonic) free energy landscape is then taken to describe the non-Gaussian

character of the fluctuations. This is qualitatively much like treating the inverse localization length of the Gaussian theory as an order parameter of the system and writing down a linear-response Landau-Ginzburg theory for $r^{-1}(t)$ [36], but where the Landau free energy is non-perturbatively expressed instead of approximated as a truncated Taylor expansion of the order parameter. Additionally, in Landau-Ginzburg or Model A theories the effective forces follow from an *equilibrium* free energy; in contrast, the NLE approach considers an F_{dyn} of explicitly *dynamical* origin.

1.4 Plan of the Thesis

The remainder of this dissertation is organized as follows. Chapter 2 presents a comprehensive treatment of dynamically correlated two-particle motion in glassy colloidal suspensions. The focus is on connecting equilibrium structure with the microscopic dynamics, and it formally generalizes the single-particle NLE briefly described in Sec. 1.3. We show that this advance allows one to analytically treat some aspects of dynamic heterogeneity more naturally than the single-particle theory, and in the latter half of the chapter we show that it also allows one to make contact with some of the diverse perspectives and theories for glassy dynamics. Although the material in Chapter 2 stands somewhat apart from the rest of the thesis, Chapter 3 acts as a bridge between the first and second parts of the thesis. It presents a microscopic analysis of an ideal glass-former — a Brownian suspension of three dimensional cross-shaped objects with hard-core interactions — but proceeds by ignoring equilibrium structural considerations and focusing solely on the topological constraints imposed on the system's dynamics by the mutual uncrossability of the arms of colliding crosses. The results of this theory (with added density fluctuations) are then compared with simulations.

Chapters 4 – 7 continue to discuss topological constraints in a wide variety of systems, but generally outside of the glassy regime. Chapter 4 treats the equilibrium dynamics of en-

tangled rigid-rod polymers, presenting a microscopic derivation of the anharmonic transverse confinement potential such objects are subject to, and anticipates the discussion in Chapter 6 of deformation by examining the effect of stress and orientational order on the confinement potential. Chapter 5 boldly generalizes the work on topologically entangled needles to different coarse-grained models of fully flexible polymers. This enables the description of much of the long-time phenomena of flexible chains at a microscopic level without needing to resort to the phenomenological DE model.

Chapter 6 steps back from trying to understand how topological constraints of different macromolecular geometries influence slow dynamics, and instead focuses on entangled rods but under non-equilibrium driven conditions. Specifically the shear rheology of such systems is addressed, under both step-strain and continuous shear deformations. Understanding polymer rheology and processing is, of course, tremendously important for their real-world applications, and such non-equilibrium situations are precisely when we expect our ability to microscopically predict the anharmonic softening of polymer confinement to have the most spectacular consequences. Chapter 7 more speculatively attempts to address a fundamental aspect of the mechanical response of polymeric systems: the origin of the plateau in the elastic modulus (which explains the rubbery response of un-crosslinked polymeric materials at intermediate time scales). In contrast to dense simple liquids, where the stress is dominated by inter-molecular constributions, tube-model theories assume that in entangled polymers the dominant contribution to stored stress via *intra*molecular degrees of freedom. Simulations have challenged this long-held view, and we show that with a microscopic theory in hand one can understand the entanglement modulus vie purely *inter*molecular stress contributions.

Finally, this dissertation concludes in Chapter 8 with a brief summary and outlook for future work. Chapters 2, 3, and 4 were all written so that they could be read as independent units. In contrast, Chapters 5, 6, and 7 all rely to varying degrees on material presented in Chapter 4 and, to a lesser extent, Section 3.6.

Chapter 2

CORRELATED TWO-PARTICLE DYNAMICS IN GLASSY COLLOIDAL SUSPENSIONS

2.1 Introduction

[1]As introduced in Chapter 1, understanding the glassy dynamics of thermal liquids and colloidal suspensions is a challenging problem of wide interest and application [1, 37]. Despite intense theoretical effort, even the problem of highly concentrated overdamped Brownian hard-sphere suspensions remains incompletely understood. The first-principles approach of ideal mode-coupling theory (MCT) [9] approximately describes nonlinear couplings of spatially-resolved collective time-dependent density fluctuations, $S(q,t)$, based on a self-consistent Gaussian closure of a non-Markovian generalized Langevin equation of motion. Local dynamical caging constraints are fully specified by the equilibrium pair structure. Mode coupling theory has had impressive success in the dynamic precursor regime corresponding to the first few orders of magnitude of dynamical slowing down, but a major weakness and limitation of ideal MCT is its prediction of a sharp non-ergodicity transition [9–11]. That this feature is not seen in simulations or in experiments has many qualitatively important implications [5, 38–46]. The origin of the spurious ideal localization transition is the Gaussian-like assumption that dynamics is controlled by collective, but small and continuous, particle displacements. Large amplitude, highly non-Gaussian "activated hopping" events, which restore ergodicity, are not taken into account. Even for the hard sphere fluid, confocal microscopy [5, 44, 46] and computer simulations [41–43, 45] find that particle trajec-

[1]This chapter contains text and figures reprinted with permission from *D. M. Sussman and K. S. Schweizer, J. Chem. Phys.* **134**, 064516 (2011), Copyright AIP 2011; *D. M. Sussman and K. S. Schweizer, Phys. Rev. E* **85**, 061504 (2012), Copyright APS 2012.

tories display intermittent hopping events which destroy the MCT nonergodicity transition. Recent experiments [43] have established the dominance of activated dynamics above an empirically deduced (based on fitting ideal MCT to data) critical volume fraction, ϕ_c, which lies well below random close packing (RCP).

A large number of non-Gaussian dynamic heterogeneity phenomena at the single particle level are also not properly described by ideal MCT, including relaxation-diffusion decoupling, large non-Gaussian parameters, exponential tails in the van Hove function, and highly non-Fickian dependence of the wavevector-dependent relaxation time [38, 40, 42, 45, 47–49]. Moreover, the crucial importance of thermally-induced activated hopping as a mechanism that "breaks" physical bonds in sticky, gel-forming spherical particle fluids has been emphasized in computer simulations [50–52]. These highly nongaussian phenomena are accurately described at the single particle level by the nonlinear Langevin equation (NLE) theory, where ergodicity is restored via activated barrier hopping and ϕ_c represents a dynamic crossover or "onset" volume fraction [31, 32, 38, 53].

The microscopic NLE approach [31, 32] builds on a simplified ("naive") version of mode-coupling theory (NMCT) within a Landau-Ginzburg, or model A [35], type of description. A particle is subjected to a displacement-dependent effective force due to its surroundings described by a dynamic free energy formulated within a non-ensemble-averaged local equilibrium picture. The theory predicts MCT-like critical power laws in the crossover region largely as a result of hopping over relatively low barriers. Deep in the supercooled (or overcompressed) regime the barriers to particle motion grow significantly but without divergence below random close packing. The relative simplicity of the NLE approach has allowed it to be generalized to many systems beyond hard spheres including polymer-particle depletion gels [54], nonspherical particles that translate and rotate [55–58], soft colloids [59], binary mixtures [60, 61], supercooled polymer melts and glasses [62–65] and nonlinear rheological response [65–69]. The microscopic NLE theory is predictive in the same sense that MCT is since it relates structure, interparticle forces, and slow dynamics. Extensive confrontation

with experiment has been pursued in both the dynamical crossover and strongly activated regimes.

An obvious limitation of the NLE approach is that it addresses only single-particle dynamics. Collective dynamic density fluctuations, the centerpiece of ideal MCT, are not directly treated. Space- and time- correlated two-particle mobility directly impacts dynamic heterogeneity phenomena which emerge when motion becomes activated and highly intermittent [3, 5]. The goal of this chapter is to initiate the qualitative extension of the NLE approach to describe the activated dynamics of two tagged particles initially separated by an arbitrary distance in the fluid. The latter aspect is relevant to "structural relaxation" (e.g. how the static pair correlations are dynamically randomized), the onset of irreversibility, and the length scale of dynamic heterogeneity as defined by the separation at which the dynamics of two particles become spatially uncorrelated [70–74]. All these questions are of intense present study in the glass physics community, primarily based on computer simulations or simplified coarse-grained kinetically constrained dynamical facilitation models [70, 75]. This new approach will be illustrated by applying it to the hard sphere fluid, both generically and in the specific context of the "cage breakup" process [76].

The chapter is organized as follows. Section 2.2 presents the two-particle generalizations of NMCT and NLE theory, the single-particle versions of which were discussed in Sec. 1.3. Section 2.3 discusses key features of the dynamic free energy surfaces in the context of hard sphere fluids, and model calculations of various properties are presented in Section 2.4. Section 2.5 presents an application to the problem of cage breakup. Section 2.6 pauses to summarize the status of the theory to that point, and discusses some potential extensions of the work.

Section 2.7 presents new detailed calculations in hard-sphere fluids of dynamic free energy barriers and relaxation times over many more initial separations. This information allows the construction of a lightly coarse-grained picture of correlated-in-space-and-time two-particle hopping, in which particles at an initial separation hop to a new relative separation via

an activated event, are re-trapped in the spirit of a local-equilibrium approximation, hop again after a characteristic time associated with the new relative separation, and so on. In Sec. 2.8 this picture is employed to address the question of irreversible structural relaxation events. The challenge there lies in distinguishing between large-amplitude, stochastic fluctuations that ultimately do not relax the system and those that lead to (statistically) irreversible changes to the configuration. In simulations different coarse-graining schemes have been proposed to address this question from the perspective of changes to lists of nearest-neighbor particles [77–79]. We show that the statistics of such coarse graining schemes can be understood by the statistics of correlated two-particle hops in our NLE theory. Section 2.9 makes contact with a different kind of space-time coarse graining that underlies dynamic facilitation models [80–82] and examines its consequences on time-distribution statistics. KCM-like statistics and relaxation-diffusion decoupling can be derived from a particular coarse-graining over structure in the two-particle hopping picture. In Sec. 2.10 we suggest an extension of our ideas to improve the venerable Vineyard approximation for the distinct part of the van Hove function. The latter half of the chapter is briefly summariezed in Sec. 2.11.

2.2 Two-Particle Theory

2.2.1 Generalized Langevin Equation

Our starting point is the GLE for a pair of tagged particles. Its derivation based on projection operator methods is well documented in the literature, at both the simplest Mori-Zwanzig level (which uses the positions and velocities of the tagged particles as slow variables that are projected onto [83]), and from a more general phase space perspective [84]. The latter starts from the Liouville equation, which takes the slow variable to be the instantaneous reduced phase-space distribution $f(\vec{R},\vec{P},t) = \prod_{i=1}^{2} \delta(\vec{r}_i - \vec{R})\delta(\vec{p}_i - \vec{P})$, where $\vec{R}$ and $\vec{P}$ are the phase space field variables, and the position and momentum coordinates of the particles are $\vec{r}_i$ and

$\vec{p}_i$ [84]. We adopt this more general starting point since it allows nonlinearities associated with structure, such as the potential of mean force (PMF), to be naturally included in the dynamical equations. Our goal is to obtain two coupled evolution equations for $\vec{r}_i$.

We do not repeat derivations in the literature [84, 85], but rather just recall the approximations and physical ideas required for the phase space memory function matrix needed to obtain the starting point of our analysis. Three key points are that (1) momentum relaxes quickly compared to particle displacement, the situation relevant in the high friction regime of interest; (2) the ensemble-averaged time correlation of forces exerted on the two tagged particles by the surrounding fluid evolves via real, not projected, dynamics; and (3) most importantly, the relevant force-force time correlation functions are not dependent on the instantaneous trajectories of the tagged particles [85]. The last two simplifications imply the central dynamical object is the force-force time correlation function matrix, $K_{\alpha\beta}(t) = \langle \vec{F}_\alpha(0) \cdot \vec{F}_\beta(t) \rangle$, which has a "fast" delta-function component, and a "slow part" associated with structural relaxation. With these simplifications the two coupled GLEs governing the correlated dynamics of the two particles in the overdamped regime of interest are [84]:

$$\zeta_s \frac{d\vec{r}_i}{dt} = \frac{-1}{\beta} \frac{\partial \ln g(\vec{r}_{ij})}{\partial \vec{r}_i} + \beta \int_0^t \left(\frac{d\vec{r}_i}{d\tau} K_{ii}(t-\tau) + \frac{d\vec{r}_j}{d\tau} K_{ij}(t-\tau) \right) d\tau + \mathbf{f}^{Q(i)}(t), \tag{2.1}$$

for $i \neq j$. The leading term on the right hand side represents the "systematic" or "thermodynamic" force associated with the equilibrium PMF, while the $K_{ij}(t)$ are the long-time parts of the total memory function, $M_{ij}(t) = \langle \mathbf{f}^i(0) \cdot \mathbf{f}^{Q(j)}(t) \rangle = \zeta_s \delta(t) + K_{ij}(t)$.

We now rewrite Eq. 2.1 in terms of center-of-mass and relative vector coordinates, $\vec{R} = (\vec{r}_1 + \vec{r}_2)/2$ and $\vec{r} = (\vec{r}_1 - \vec{r}_2)/2$, a choice which symmetrizes some of the subsequent equations. By adding and subtracting the GLEs for particles 1 and 2, one has:

$$\zeta_0 \frac{d\vec{R}}{dt} = \beta \int_0^t \frac{d\vec{R}}{d\tau} K_R(\vec{R}, \vec{r}, t) d\tau + \mathbf{f}^{Q(R)}, \tag{2.2}$$

$$\zeta_0 \frac{d\vec{r}}{dt} = -\frac{1}{\beta}\frac{\partial \ln g(2r + r(0))}{\partial r} + \beta \int_0^t \frac{d\vec{r}}{d\tau} K_r(\vec{R}, \vec{r}, t) d\tau + \mathbf{f}^{Q(r)}. \tag{2.3}$$

The PMF term is written in a fashion that exposes the dependence on initial particle separation, $r(0) \equiv 2|\vec{r}(0)| \equiv r_0$, and implicitly defines the dynamical evolution of the relative scalar separation coordinate, r. The two equations are coupled via the center-of-mass and relative memory functions, $K_R(\vec{R}, \vec{r}, t)$ and $K_r(\vec{R}, \vec{r}, t)$.

2.2.2 Naive Mode Coupling Theory

Explicit approximate expressions for the memory functions are obtained by projecting the forces onto bilinear products of the collective fluid density field with the center-of-mass or relative coordinate density. Hence, there are now two slow variables, and the projection process involves well-known matrix manipulations [6, 34, 83–85]. The relevant time correlation functions are factored into a product of time- and space- dependent contributions. For example, defining $\rho_R(q,t) = (e^{i\vec{q}\cdot\vec{r_1}(t)} + e^{i\vec{q}\cdot\vec{r_2}(t)})/2$, $\Delta\vec{R}(t) = \vec{R}(t) - \vec{R}(0)$, and $\Delta\vec{r}(t) = \vec{r}(t) - \vec{r}(0)$ one obtains

$$\begin{aligned}
\langle \rho_R e^{QLt} \rho_R \rangle &= \frac{1}{4}\langle e^{i\vec{q}\cdot\Delta R}\left(e^{i\vec{q}\cdot\Delta r} + e^{-i\vec{q}\cdot\Delta r} + e^{i\vec{q}\cdot(\vec{r}(t)+\vec{r}(0)} + e^{-i\vec{q}\cdot(\vec{r}(t)+\vec{r}(0)}\right)\rangle \\
&\approx \frac{1}{2}\langle e^{i\vec{q}\cdot(\Delta R+\Delta r)}\rangle\langle 1 + e^{i\vec{q}\cdot\vec{r}(0)}\rangle \\
&= \frac{1}{2}(1 + \frac{\sin(qr_0)}{qr_0})\langle e^{i\vec{q}\cdot(\Delta R+\Delta r)}\rangle.
\end{aligned} \tag{2.4}$$

The self-propagator is

$$\langle e^{i\vec{q}\cdot(\Delta R+\Delta r)}\rangle \approx \exp\left(\frac{-q^2(\vec{R}_{loc} + \vec{r}_{loc})^2}{6}\right), \tag{2.5}$$

and its collective analog is of the same form but with the deGennes narrowing factor. The final memory functions are then:

$$K_R(t\to\infty) = \frac{1}{3\beta(2\pi)^3}\int \rho q^2 C^2(q) S(q)\omega(q,r_0)\exp\left(\frac{-q^2(\vec{R}_{loc}+\vec{r}_{loc})^2}{6}(1+S^{-1}(q))\right)d\vec{q}, \tag{2.6}$$

$$K_r(t\to\infty) = \frac{1}{3\beta(2\pi)^3}\int \frac{\rho q^2 C^2(q) S(q)\omega^2(q,r_0)}{1-\sin(qr_0)/(qr_0)}\exp\left(\frac{-q^2(\vec{R}_{loc}+\vec{r}_{loc})^2}{6}(1+S^{-1}(q))\right)d\vec{q} \tag{2.7}$$

where $\omega(q,r_0) = 1+\sin(qr_0)/qr_0$. The initial particle separation thus enters via both memory functions as well as the structural (PMF) term in the GLE for the relative coordinate.

For reasons of tractability, we desire only two coupled self-consistency equations for the scalar variables R and r, which can be written in an intuitive equipartition form as:

$$\frac{1}{2}K_{R,\infty}R_{loc}^2 = \frac{3}{2}k_BT \tag{2.8}$$

$$\frac{1}{2}K_{r,\infty}r_{loc}^2 = \frac{3}{2}k_BT \tag{2.9}$$

To achieve this scalar description, the angular dependence in the memory functions is averaged over. Such a procedure was effectively carried out in the single-particle theory [31,32], where it is a very natural and weak approximation for an isotropic fluid. However, at the two-particle level there is nontrivial relative angular dynamical information, but retaining it would require structural information beyond the usual scalar functions. To be consistent with our neglect of such angular static structure, in addition to the rigorously true statements $\langle\vec{R}(0)\cdot\vec{r}(0)\rangle = \langle\vec{R}(t)\cdot\vec{r}(t)\rangle = 0$, we assume $\langle\vec{R}(0)\cdot\vec{r}(t)\rangle = 0$ in the long-time limit. This simplification implies the neglect of any Rr coupling in the Debye-Waller factors, and with only the vertex carrying Rr coupling information the ability to describe events such as rotation of the tagged particles about their center of mass is lost. The two coupled NMCT

self-consistency relations are then:

$$\begin{aligned} 0 &= \frac{-3}{R} + \frac{3\phi}{\pi^3}\int_0^\infty \frac{q^2C^2(q)S(q)\omega(q,r_0)}{r(1+S^{-1}(q))}V(q,R,r)dq, \\ 0 &= \frac{-3}{r} + \frac{3\phi}{\pi^3}\int_0^\infty \frac{q^2C^2(q)S(q)\omega^2(q,r_0)}{1-\frac{\sin(kr_0)}{kr_0}}\frac{1}{R(1+S^{-1}(q))}V(q,R,r)dq, \end{aligned} \tag{2.10}$$

where $V(q,R,r) = \sinh\left(\frac{q^2Rr}{3}(1+S^{-1}(q))\right)\exp\left(\frac{-q^2(R^2+r^2)}{6}(1+S^{-1}(q))\right)$. As $r_0 \to \infty$, these two equations become identical.

We have numerically solved Eq. 2.10 for a hard sphere fluid to determine the critical (ideal arrest) volume fraction as a function of r_0. We find $\phi_c(r_0)$exhibits decaying oscillations with a period of $\sim \sigma$ which deviate at most by $\sim 1\%$ about $\phi_c(r_0 \to \infty) = 0.432$, precisely the ideal glass transition volume fraction of the single-particle theory [31]. However, the formal difference in self-consistency equations between the single-particle theory and the infinite-separation (or independent-particle) limit of the two-particle theory associated with the angular pre-averaging approximation implies the NLE generalization will not precisely reduce to its single particle analog as $r_0 \to \infty$.

2.2.3 Nonlinear Langevin Equation Theory

Before proceeding to develop the two-particle NLE theory, we comment on some of the primary aims of our work. The initial separation of the two tagged particles, r_0, crucially enters the theory via the PMF and both memory functions. Characterizing its effect on the motion of the tagged particles is a central goal. Such a question can be investigated in computer simulations [39] and via confocal microscopy experiments [5]. For example, recent simulations have studied the "cage breakup" process, defined as when a particle in the first solvation shell leaves the local cage for the first time [76]. Alternatively, one can study the distribution of time scales for a particle to "lose" a specified number of nearest neighbors [77]. One motivation for this question is the desire to quantify "irreversibility" or

"structural relaxation" on a microscopic scale. A length scale of dynamic heterogeneity is often defined as the separation at which the motion of two particles becomes uncorrelated in space and time. The r_0-dependence of two-particle dynamics is relevant to this question. If one is interested in ensemble averaged properties, then the theory must be solved as a function of r_0, and the results then averaged using the equilibrium pair correlation function, $g(r_0)$.

To construct the two coupled NLE's, we proceed per the heuristic implementation of the local equilibrium idea employed to propose the single-particle theory [32]. The NMCT self-consistency equations are utilized to define a field of effective dynamical forces,

$$\vec{f}(R,r) = f_R(R,r)\hat{R} + f_r(R,r)\hat{r}, \tag{2.11}$$

where $f_R \equiv -\partial F_{eff}(r,R)/\partial R$ and $f_r \equiv -\partial F_{eff}(r,R)/\partial r$ are given by the right hand side of Eq. 2.10 and now $R_{loc} \to R$ and $r_{loc} \to r$ are dynamical variables. Knowledge of these forces is all that is required to construct the NLE evolution equations, which, in principle, can then be numerically solved using stochastic Brownian trajectory simulation. However, for both intuitive physical reasons, and practical considerations related to using Kramers theory to compute mean first-passage times for barrier hopping, one also wants to construct the dynamical free energy.

To determine the dynamical free energy surface, the effective forces must be integrated and added to the PMF, $w(r) = \ln g(r)$, to obtain:

$$F_{eff}(R,r) = \int_C \vec{f}(\vec{l}) \cdot d\vec{l} + (w(2r+r_0) - w(r_0)), \tag{2.12}$$

where $\vec{l} = R\hat{R} + r\hat{r}$. Since F_{eff} is not a thermodynamic free energy, the integration is path-dependent. The constraint that the NLE theory should reduce to NMCT in the limit of no thermal noise (i.e. without activated barrier hopping) is sufficient to uniquely specify

an integration path for the one-particle NLE theory [31, 32]. However, this is not true for the two-particle problem, nor for mixtures of particles or nonspherical particles with both translational and rotational degrees of freedom. In previous work on mixtures of hard and sticky spheres [60, 61], and on translation and rotation of hard uniaxial objects [55, 57], the integration path was chosen to be of a sequential form, first along one coordinate, and then the other. The choice of which "orthogonal" two-step path to choose was justified by ruling one of them out on the basis that it yielded unphysical results. For our present two-particle problem one can try a similar approach, but we find that both such two-step paths yield unphysical results in the sense that the resulting dynamic free energy surface is grossly asymmetric, favoring easy particle motion along one coordinate or the other depending on which of the two straight-leg paths are chosen. Additionally, the associated highly asymmetric barriers have an absolute height much smaller than that predicted by the single-particle theory. Since there is no physical reason to expect such asymmetric behavior, we chose to approximately determine $F(R, r)$ by integrating over the maximally symmetric path: a straight-line diagonal trajectory from the NMCT values (R_{loc}, r_{loc}) to the point (R, r).

2.3 Dynamic Free Energy Surface

Figure 2.1a shows a representative dynamic free energy surface for a hard sphere fluid at $\phi = 0.55$ and an initial particle separation of $r_0 = \sigma$, i.e. "at contact." The latter condition is relevant to the question of structural relaxation, or "pair unbinding." The shown surface displays many of the features we find common to all the dynamic free energies we have computed over a wide range of volume fractions ($\phi > \phi_c$) and initial particle pair separations. There are two obvious relaxation channels, one primarily in the R-direction and one primarily along the positive r-direction, which can be thought of as the "eigenvectors" of the two-particle cooperative barrier crossing trajectories. These two relaxation pathways correspond largely to changing the absolute magnitude of R or increasing the magnitude of r. Separating

the escape paths is a very high, rapidly growing barrier that has been truncated in the figure to preserve the scale. This barrier is essentially impassible to particles moving only via thermal noise. If the initial particle separation is large enough ($r_0 > \sigma$ for hard spheres) then a decrease in the relative separation of the particles is also a permissible motion. An example is shown in Fig. 2.1b in a steepest-descent-path representation. Dynamic free energy surfaces can also be constructed corresponding to these motions precisely as outlined above, except now the change in the PMF must be subtracted, not added, to the path integral over the field of forces:

$$F(R, r^-) = \int_C \vec{f}(\vec{l}) \cdot d\vec{l} - (w(2r + r_0) - w(r_0)). \tag{2.13}$$

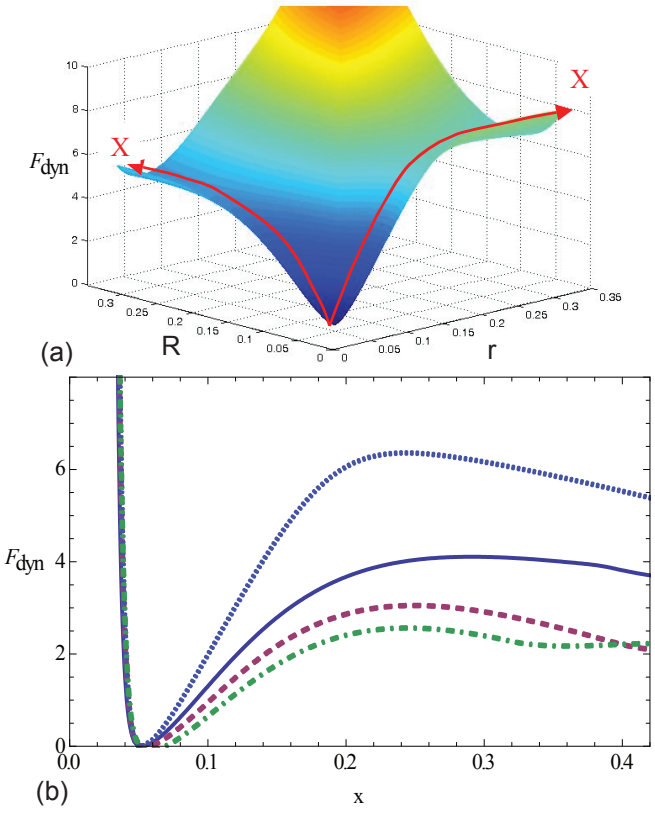

Figure 2.1: (a) Representative dynamic free energy surface, $F(R, r)$, in units of k_BT for a $\phi = 0.55$ hard sphere fluid and initial 2-particle separation of $r_0 = \sigma$. (b) 1-Dimensional cuts along the "escape paths" drawn in the above figure. The red curves designate barriers in the R-direction, blue curves in the r-direction. Solid curves correspond to $r_0 = \sigma$ and dashed curves to $r_0 = 1.4\sigma$.

The three relaxation pathways leading to cage escape and relaxation discussed above have similar, but not identical, features. Systematic differences exist with regards to the barrier region (saddle point) curvature and barrier height as the volume fraction and initial separation are varied. In general, though, increasing volume fraction increases the barrier height at a fixed initial separation. Varying the initial separation non-monotonically modifies the relative difference in height of the R and r barriers, and also causes the location of the r-direction barriers to move in or out, correlated with the distance to the nearest minimum or maximum of $g(r)$.

The paths for easiest escape from the localization well across the saddle points follow additional generic trends. Consistently, we find that crossing an r-directional barrier corresponds to a change in r by approximately $\sigma/4$, which is correlated with variations in distance between consecutive minima and maxima of $g(r)$. Since the variable r is defined as $r \equiv |\vec{r}_1 - \vec{r}_2|/2$, this trend implies that a barrier-crossing event corresponds to a real-space modification of the interparticle separation of approximately one half a particle diameter. This seems to be an intuitive result since it corresponds to a particle hop from the first solvation shell to an "interstitial" site. As a concrete example, to separate two particles that start at contact ($r_0 = \sigma$) when $\phi = 0.55$, a barrier must be crossed that involves increasing their relative separation by 0.41σ; if the two particles are initially separated by a distance corresponding to the second maximum of $g(r)$ ($r_0 = 2.02\sigma$), then barrier crossing involves changing their relative separation by 0.55σ. For comparison, at this volume fraction the distance from the first peak of $g(r)$ to its first minimum is 0.39σ,and the distance from the first minimum to the second maximum is 0.63σ.

The angular averaging approximation made to reduce the NLE equations of motion from a full vector description of the center of mass and relative coordinates to the scalar displacements R and r renders a fully unambiguous physical interpretation of the dynamic free energy surface in terms of real space particle motion difficult. For instance, slaving the displacements of particle 1 and particle 2 corresponds to following a trajectory directly up

the enormous barrier separating the relaxation channels, but not uniquely so; other forms of particle motion map onto the same path. The r coordinate, with our ability to distinguish positive and negative r via the PMF, remains a valid measure of the magnitude of the change in relative separation, which is a classic microscopic metric of structural relaxation. On the other hand, after the absolute value has been taken the R coordinate no longer uniquely tracks the dynamical change in the center of mass. Thus we can identify an r-barrier crossing as a structural relaxation event that will decorrelate $g(r)$, but for the R-barrier crossing trajectory we can only state that it corresponds to some more general relaxation event. Perhaps it is related to simulation and microscopy observations of "cluster motions," i.e. particles that move together in a more-or-less coherent fashion [86, 87]. In any case, in this initial study we focus primarily on the barriers in the positive and negative r-direction.

An additional subtle issue with regards to interpreting the barrier-crossing events is that the trajectories going from the localization well to the saddle point are not perfectly parallel with the axes. That is, the saddle trajectories correspond to some combination of R and r motion. However, we do find that the approximate interpretation of barriers corresponding to "pure" trajectories parallel to the axes in Fig. 2.1a improves as the fluid volume fraction increases. As a measure of trajectory "purity" we define the function $P_{R,r}(\phi, r_0)$ as the ratio of the vector components from the localization well to one barrier or the other. While there is some moderate variation at fixed volume fraction as $r_0$changes, in all cases the purity increases as ϕ is increased. For example, as ϕ grows from 0.5 to 0.6, $P_r(\phi, \sigma)$increases from 3.6 to 5.4, and $P_R(\phi, 2\sigma)$increase from 4.7 to 7.6.

2.4 Model Calculations

2.4.1 Quantitative Analysis of the Dynamic Free Energy Surface

Figure 2.2 shows the total displacement, in units of $x \equiv \sqrt{R^2 + r^2}$, corresponding to the localization well and barrier saddle point in the positive r- and R-directions. The single-

particle theory found that the localization length(i.e. the minimum of $F_{eff}(r)$) is well-described by an exponential decay in volume fraction, $r_{loc} \sim e^{-12.2\phi}$, and a barrier location of $\sim \sigma/3$ that very slowly shifts outwards as volume fraction increases [31]. Here we see the localization well follows this same behavior: the two-particle theory predicts $x_{loc} \sim e^{-12.2\phi}$, albeit with a different constant of proportionality. In both the single- and two-particle theories, the barrier location is a weak function of volume fraction. For the present theory, there are subtle, but small, variations of barrier location with changing volume fraction and initial particle separation, likely due primarily to changes of the PMF. Note that the barrier in the r and R direction relaxation channels are very similar.

Figure 2.3 shows the barrier height for motion in the positive r and R directions as a function of initial particle separation for several volume fractions. The barrier height strongly oscillates in phase with $g(r)$, with an amplitude closely tracking the PMF (see Fig. 2.4). We note that for a given volume fraction the barrier height that is oscillated about is lower than predicted by the single-particle NLE theory. This is consistent with our physical intuition since by allowing two-particle correlated motion a degree of freedom is added and so constraints are more easily avoided. Of course, the single-particle theory does not explicitly address the question of the dynamical separation of a pair of particles.

Limiting analytic analysis of the single-particle theory has shown that the barrier height for hard spheres (but not soft spheres [59]) scales with the inverse of the localization length: $F_B \sim \sigma/r_{loc}$ [31, 88] We find that this scaling works very well for the r-directional barrier when $r_0 = \sigma$, but fails for the R-direction barrier at that initial separation, and for both barriers at all other initial separations. We have not been able to derive, nor numerically find, a simple functional form for the barrier in terms of the two natural length scales available, x_{loc} and r_0.

Figure 2.5 shows barrier heights as a function of volume fraction for fixed initial separation. We empirically find that the barrier heights closely follow the critical power law

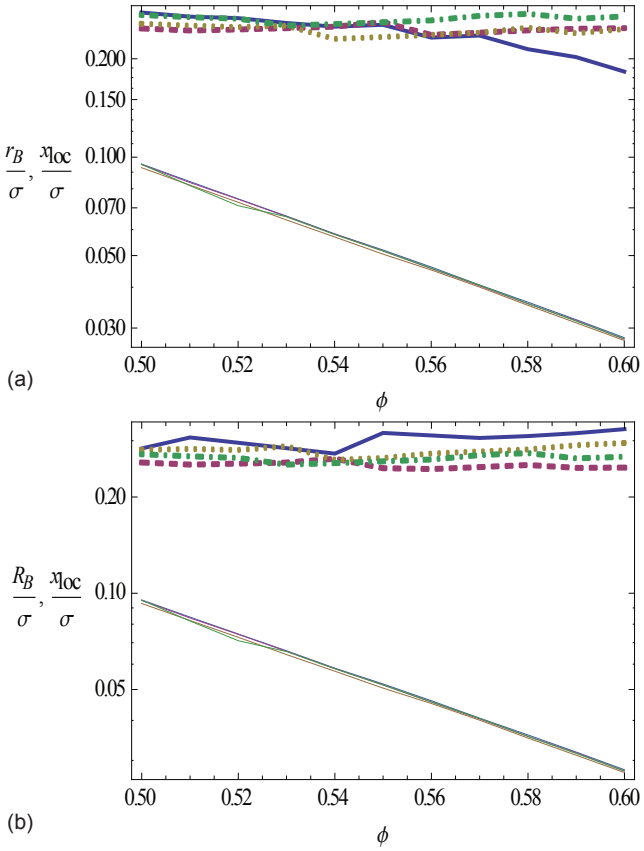

Figure 2.2: Log-linear plot of the location of the saddle point in the (a) relative-coordinate and (b) center-of-mass coordinate ($r_B,\ R_B$) and localization well ($r_{loc} =\ R_{loc} \equiv x_{loc}$) in units of $\sqrt{R^2 + r^2}$ as a function of volume fraction. In both figures the solid blue line corresponds to $r_0 = \sigma$,the dashed line to the first minima of $g(r)$,the dotted line to the second maxima of $g(r)$,and the dot-dashed line to the large $r_0$limit, computed at $r_0 = 10\sigma$. The lower lines show the location of the localization well for these same initial separations, and as can be seen there is very little r_0 dependence.

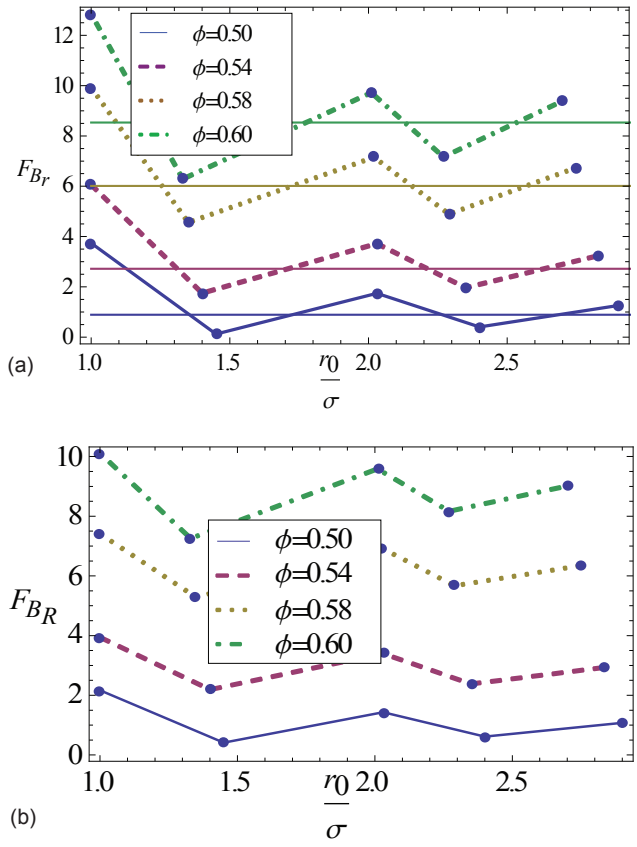

Figure 2.3: Barrier height in the (a) forward r-direction, and (b) R-direction, as a function of initial 2-particle separation for several volume fractions. The lines simply connect the discrete computed points. Horizontal lines in (a) indicate the infinite-separation, independent-particle limit.

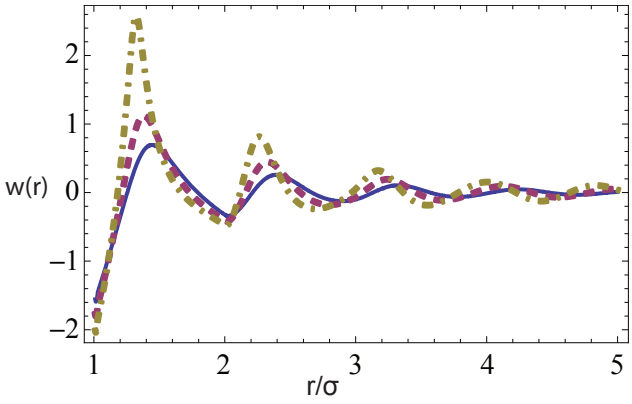

Figure 2.4: The potential of mean force, $w(r)$, in units of k_BT for volume fractions of 0.50 (solid blue), 0.55 (dashed red), and 0.60 (dot-dashed yellow).

form:

$$F_B(\phi, r_0) = A(r_0)(\phi - \phi_c)^{\nu(r_0)}, \tag{2.14}$$

where $\phi_c = 0.432$, and the exponent $\nu(r_0)$ oscillates between 1.5 and 3.0 for barriers in the r-direction, and between 2.0 and 2.8 for barriers in the R-direction (the single-particle theory's result is 2.1), again on the scale of $g(r)$. Note that there is some inherent error in this fitting, since $F_B(\phi, r_0)$ has been computed not at fixed r_0, but rather at initial separations corresponding to the minima and maxima of $g(r)$. As volume fraction changes in the range of $0.50 \leq \phi \leq 0.60$ the position of a local minimum or maximum of $g(r)$ can shift by $\sim 4\%$ relative to the position at $\phi = 0.55$.

2.4.2 Mean Barrier Hopping Time

We now apply multidimensional Kramers' theory to calculate the mean first barrier-crossing time [89, 90]:

$$\frac{\tau}{\tau_0} = \frac{2\pi}{\lambda^+}\left(\frac{|\det \mathbf{K}_B|}{\det \mathbf{K}_0}\right)^{1/2} e^{\beta F_B}. \tag{2.15}$$

Here, $\tau_0 = \beta\zeta_0\sigma^2$ is the elementary Brownian time scale, F_B is the height of the barrier, $\mathbf{K}_B$ and $\mathbf{K}_0$ are the matrices of second derivatives at the saddle point and localization well, respectively, $\lambda^+$is the positive eigenvalue of the matrix $(-\mathbf{D} \cdot \mathbf{K}_B)$, and $\mathbf{D}$ is the matrix of short-time diffusion coefficients in units of the elementary (dilute-limit) diffusion constant D_0. As in prior work [60], $\mathbf{D}$ is taken to be $D_{ij} = \delta_{ij}/g(\sigma)$, based on Enskog binary collision theory [6]. Our calculations find that the exponential pre-factor in Eq. 2.15 varies only weakly with volume fraction and initial separation, and so the mean first passage time is dominated by the barrier heights.

Figure 2.6 presents the Kramers time as a function of volume fraction for several initial separations, along with the results of the single-particle NLE calculation for comparison. The barrier crossing time increases monotonically with volume fraction for any initial separation, although the increase is quantitatively slower than the corresponding single-particle NLE

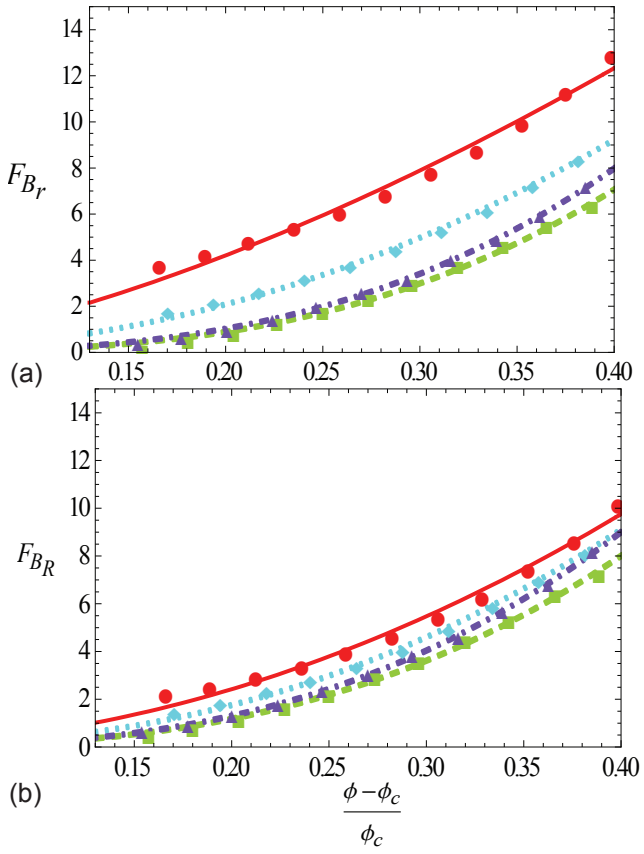

Figure 2.5: Barrier height as a function of differential volume fraction relative to the NMCT crossover in the (a) forward r-direction, and (b) R-direction, for r_0 corresponding to contact, the first minimum of $g(r)$, the second maximum of $g(r)$,and the second minimum of $g(r)$ (the solid red, dashed green, dotted blue, and dot-dashed purple curves, respectively). The numerical calculations are fit to the form $F_B(\phi, r_0) = A(r_0)(\phi - \phi_c)^{\nu(r_0)}$, where the exponent $\nu(r_0)$for the r-barriers is 1.55, 2.99, 2.15, and 2.96, respectively.

calculation. This reinforces the differences between our present theory and the earlier single particle approach. At fixed volume fraction, the Kramers time varies non-monotonically with initial separation, again strongly correlated with the minima and maxima of $g(r)$: the longest mean first-passage time occurs when the particles are at contact ($r_0 = \sigma$), the shortest mean first-passage time occurs when the particles are separated by a distance corresponding to the first minima (interstitial) of the radial distribution function ($r_0 \approx 1.4\sigma$), and $\tau(r_0)$ then continues to oscillate in phase with $g(r)$.

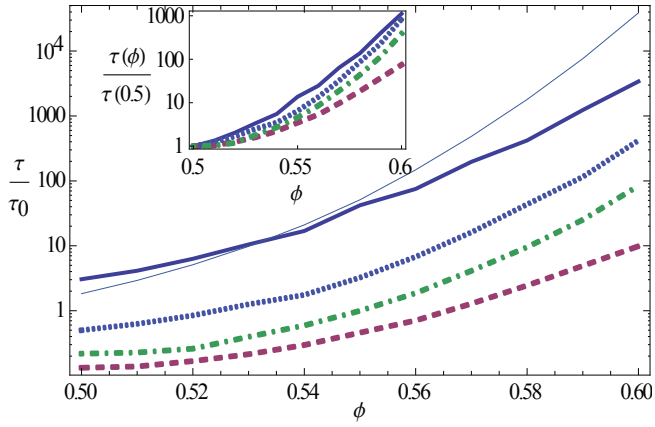

Figure 2.6: Log-linear plot of the dimensionless Kramers mean first passage time, τ/τ_0 , as a function of volume fraction for $r_0 = 1, 1.4, 2$ (blue, red, and yellow curves, respectively). The dashed line shows the single-particle result, and the solid green curve shows the two-particle result in the $r_0 \to \infty$ limit. Inset: The four solid lines of the main plot, normalized by their $\phi = 0.50$ value.

The inset of Fig. 2.6 re-plots the Kramers times in a normalized format to expose the relative rate of increase with volume fraction and r_0, a representation relevant to the question of "dynamic fragility" [37, 57, 59, 91]. The fragility is weakest for an initial interstitial configuration, and strongest when the two particles are initially in contact.

2.4.3 Dynamic Correlation Length

As the hopping times are dominated by the barrier heights, a simple estimate of a two-particle dynamical correlation length can be made by characterizing how quickly the barrier

height oscillations decay with growing initial interparticle separation. This length scale quantifies the interparticle separation at which the activated dynamics of two particles becomes uncorrelated in space and time. The barrier heights at consecutive maxima of $g(r)$ are fit as an exponential decay to the asymptotic value:

$$F_B(r_0) = F_B(r_0 \to \infty) + Ae^{-(r_0-\sigma)/\xi_p}. \tag{2.16}$$

Theoretical analysis has shown the peaks of the radial distribution function can be fit to a Yukawa potential when the initial separation is sufficiently large [6]. In a similar spirit, then, we use the above form to fit the barrier heights at the largest separations we have computed: with initial separations corresponding to the third through sixth maxima of $g(r)$ and the infinite-separation limit. We find (not plotted) that the correlation length computed in this way grows modestly, from $\xi_p \approx 1.3\sigma$ to $\xi_p \approx 1.7\sigma$ as the volume fraction increases from 0.50 to 0.60. This length scale is both modestly smaller and more slowly growing than the result of the analogous procedure applied to $g(r)$.

Including the effects of the hard-core constraints, our results suggest a volume of cooperative, correlated motion whose radius, $\xi_c \cong (\sigma + \xi_p)$, slowly increases from 2.3 to 2.7 particle diameters while the characteristic relaxation time grows by over two orders of magnitude. This is in reasonable agreement with simulations and hard-sphere confocal microscopy experiments, which, using a similar procedure to fit correlation functions to an exponential decay, found dynamic length scales relating to the relative displacement on the order of 2 to 3 particle diameters that were also only weakly dependent on ϕ over a range of volume fractions where the alpha relaxation time grows by 2 order of magnitude, per our present calculations [39, 87]. Moreover, the confocal experiments also found the correlated motion was strongly coupled with the oscillations of the radial distribution function.

2.5 Application to Cage Breakup

2.5.1 Background

We now apply our theory to the problem of a particle escaping from its cage of nearest neighbors, the elementary step of structural relaxation. A simulation study of this problem [76, 79] was based on defining a generalized neighbor list for particle i as a vector with components $(l_i(t))_j = f(r_{ij}(t))$, where $f(r_{ij}(t))$ is a step function equal to 1 if particle j is within the first solvation shell of i, and zero otherwise. The cut-off used is g_{min}, the distance from contact to the first minimum of $g(r)$. Schematically, this process is shown in the inset of Fig. 2.7. There are several ways to define a cage correlation function; one simple choice is [76]

$$C(t) \equiv \langle \Theta(c - n_i^{out}(t)) \rangle, \tag{2.17}$$

where

$$n_i^{out}(t) = |l_i(0)|^2 - l_i(0) \cdot l_i(t) \tag{2.18}$$

quantifies the number of particles that have left the generalized neighbor list of particle i after a time t. The parameter c quantifies the number of particles presumed to be required for a relevant degree of change in the surroundings of particle i. Simulations find that qualitatively the correlation function is not very sensitive to the precise value of c chosen, and $c = 1$ was adopted for convenience [76]. A more recent simulation study has focused on identifying the elementary structural relaxation process underlying irreversability in terms of neighbor exchanges which in the above language corresponds to $c > 1$ [77].

We pause here to note that while we take the model of a cage escape presented by Rabani et al. [76] as inspiration, a direct comparison of our results with their simulations is not applicable since it focused on the Arrhenius-like relaxation regime far from the glass transition. Later work [79] studied colder, one-component Lennard-Jones liquids, but were complicated by the presence of local crystalline order and defects.

2.5.2 Theoretical Results

In the context of our dynamic free energy surface, crossing a barrier in the r-direction leads to a change in interparticle separation on the order of one half a particle diameter. This corresponds to a relative displacement at least as large as that required to move a particle from the first solvation shell to an interstitial site. Thus, any hopping event in the forward r-direction that starts with an initial separation within the first solvation shell leads to new separation where the two particles are not nearest neighbors. Hence, we can use the r^+-barrier crossing times from within the first shell to characterize the same sort of neighbor list cage escape events studied in simulations.

We examine two different cage escape correlation functions. The first,

$$C_1(t) = \langle \exp\left(\frac{-t}{\bar{\tau}}\right) \rangle, \tag{2.19}$$

corresponds to a generic exponential function for the loss of correlation [53, 92]. It is motivated as a toy model of experimental time correlation functions, such as the dynamic structure factor at the cage wavevector, or perhaps dielectric relaxation. The second is

$$C_2(t) = \langle \Theta\left(\bar{\tau} - t\right) \rangle, \tag{2.20}$$

which corresponds to the function defined in Rabani et al. [76] with the choice $c = 1$.

To proceed, we compute the mean first passage time over the r^+-barrier at many initial separations between contact and the first minimum of $g(r)$ at fixed volume fraction. The cage escape time is then averaged over spatial disorder (i.e. over the *initial conditions* as:

$$\left(\tau_{cage}\right)_s = \left\langle \tau(r_0) \right\rangle_s = \frac{24\phi \int_1^{g_{min}} r_0^2 g(r_0) \tau(r_0) dr_0}{24\phi \int_1^{g_{min}} r_0^2 g(r_0) dr_0}. \tag{2.21}$$

Figure 2.7 shows the part of the radial distribution function corresponding to the range of initial separations averaged over. Analogous expressions define the other spatial-disorder-

averaged quantities of interest, $C_1(t)$, $C_2(t)$, and $(\tau_{cage}^{-1})_s$. The latter is a simple surrogate for the self-diffusion constant, and in the presence of heterogeneity it is not expected to be exactly equal to $1/(\tau_{cage})_s$. We initially assume the hopping times are unique for fixed values of the initial separation r_0, in the spirit of Kramers' mean first passage time.

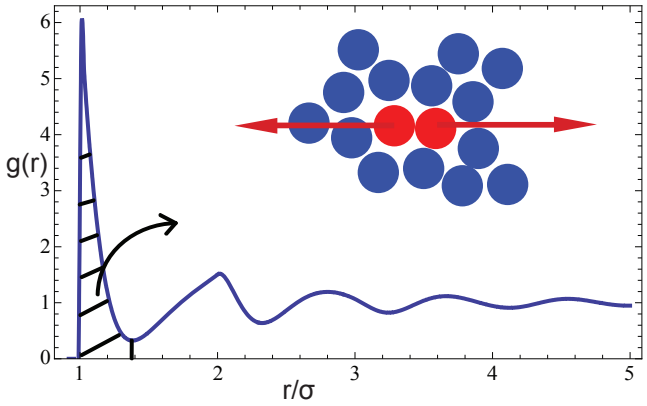

Figure 2.7: Hard sphere fluid radial distribution function at $\phi = 0.55$, with the region controlling cage-escape phenomena shaded. Inset: Schematic of nearest neighbor particles breaking up structure via cage escape.

Figure 2.8 shows an example of the disorder-averaged time correlation functions for $\phi = 0.55$. Note that $(C_2(t))_s$ goes to zero at a finite time because the spatial disorder average involves a longest hopping time (when particles are at contact), and so eventually all of the step functions vanish. On the other hand $(C_1(t))_s$ involves exponential tails and thus has no such finite-time decay.

In reality, barrier hopping is a thermal noise-driven process. Hence, the full solution of the NLE equations yields a distribution of escape times corresponding to pure "dynamic" disorder [92]. This suggests an immediate improvement to our analytic model by introducing a distribution of barrier crossing times for fixed r_0. For barriers greater than a few k_BT, the rare hopping events follow a Poissonian distribution with a mean time given by the calculated Kramers' time [92]:

$$P(\tau) = \frac{\tau}{\bar{\tau}^2} e^{-\tau/\bar{\tau}}. \tag{2.22}$$

In the single-particle theory, this distribution was found to accurately describe the numer-

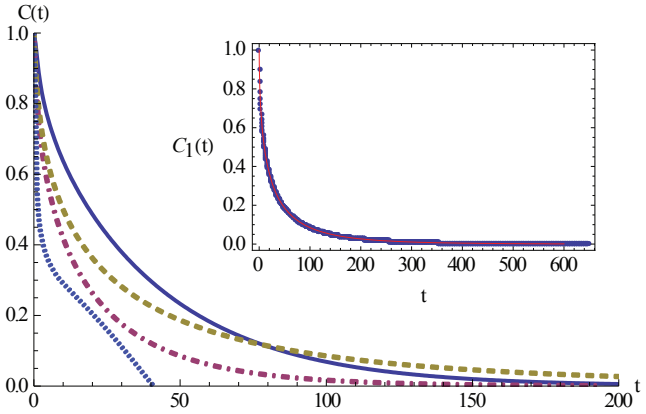

Figure 2.8: Cage correlation functions $C_1(t)$ (in red) and $C_2(t)$ (in blue) for $\phi = 0.55$. Solid curves indicate an average over only the static disorder, whereas the dashed curves include both the static and dynamic disorder. Inset: Representative fit of the full static-plus-dynamic disorder averaged $C_1(t)$ to a stretched exponential function for $\phi = 0.55$.

ical results obtained from Brownian trajectory solutions of the NLE for $\phi = 0.50$ and above. Using the distribution of Eq. 2.22 the dynamic averages can be performed analytically, with the result:

$$\begin{aligned} \tau_{cage} &= \langle \tau(r_0) \rangle = \langle \int_0^\infty \tau P(\tau) d\tau \rangle_s \\ &= \langle \int_0^\infty \left(\frac{\tau}{\bar{\tau}}\right)^2 e^{-\tau/\bar{\tau}} d\tau \rangle_s = 2\langle \tau(r_0) \rangle_s. \end{aligned} \tag{2.23}$$

Similarly,

$$\tau_{cage}^{-1} = \langle (\tau(r_0))^{-1} \rangle_s, \tag{2.24}$$

$$\langle C_1(t) \rangle = \left\langle \frac{2t}{\tau(r_0)} K_2 \left(2\sqrt{\frac{t}{\tau(r_0)}} \right) \right\rangle_s, \tag{2.25}$$

where K_2 refers to the Bessel function of the second kind, and

$$\langle C_2(t) \rangle = \left\langle \frac{t + \tau(r_0)}{\tau(r_0)} e^{-t/\tau(r_0)} \right\rangle_s. \tag{2.26}$$

Note that dynamic disorder of this elementary kind can by itself strongly modify exponential decay.

Figure 2.9 presents results for the full static- and dynamic-disorder averaged cage escape time. The above analysis shows that for this quantity including the dynamic disorder merely introduces a multiplicative factor of two. The cage escape time is both faster and more slowly growing with volume fraction than the mean first passage time calculated in the single particle NLE theory. Intuitively, this seems a reasonable consequence of allowing for two-particle dynamic correlation. In contrast, the cage escape time is longer than the mean hopping time in the large initial separation limit of the two-particle theory. This demonstrates that the cage escape process is largely controlled by the slower-than-average dynamics of particles (near contact) within the first neighbor shell.

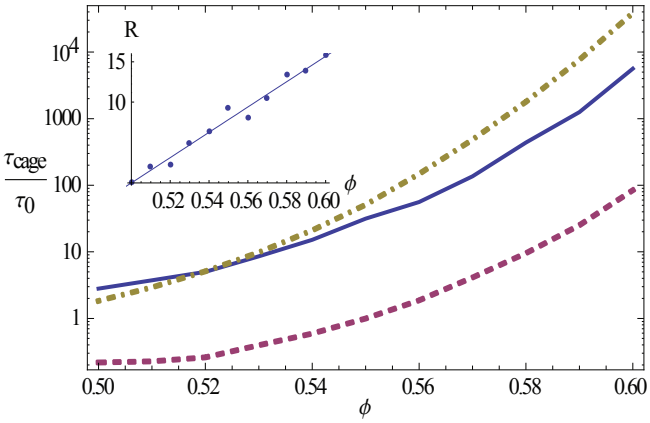

Figure 2.9: Log-linear plot of the dimensionless mean cage escape time as a function of volume fraction (blue curve). For comparison, the mean first passage time of two-particle theory in the $r_0 \to \infty$ limit is shown (dashed red curve), along with the single particle mean first passage time (dashed yellow curve). Inset: Log-linear plot of the decoupling factor R, along with an exponential fit: $R \sim \exp(12.8\phi)$.

2.5.3 Decoupling

By separately calculating $\langle \tau(r_0) \rangle$, qualitatively proportional to the viscosity, and $\langle (\tau(r_0))^{-1} \rangle$, a simple surrogate for the self-diffusion coefficient, we can define an analog of the translation-viscosity (or relaxation) decoupling parameter, $R = \langle \tau(r_0) \rangle \langle (\tau(r_0))^{-1} \rangle$. The inset of Fig. 2.9 shows the decoupling parameter grows strongly with increasing volume fraction. Qualitatively, this is consistent with observations in experiment and simulation of a decoupling of the

viscosity (or rotational diffusion constant) and translational diffusion constant under conditions where activated dynamics are dominant [40, 41, 47, 48, 93]. As shown in the inset, R grows exponentially with the volume fraction, $R \sim \exp(12.8\phi)$, which, remarkably, is essentially identical to how the transient localization length decreases, i.e., $x_{loc} \sim \sigma \exp(-12.2\phi)$. Hence, our two-particle theory predicts a deep connection between the highly localized state and the long time heterogeneous decoupling phenomenon. Such connections between short and long time dynamics are well documented in glass forming liquids, but their microscopic origin has remained largely a mystery [1].

A related question of great interest is how the decoupling factor may be related to a mean structural relaxation time. We find that the square root of R is well fit by

$$\sqrt{R} \sim 2.0 + 0.25 \ln(\tau_{cage}/\tau_0) \tag{2.27}$$

Our numerical data can also be fairly well fit (but not as accurately) by $R \sim 3.2 + 1.5 \ln(\tau_{cage}/\tau_0)$. Hence, the degree of decoupling is predicted to grow in a slow logarithmic manner with increasing relaxation time, not as an effective power law in the "fractional" Stokes-Einstein spirit. Interestingly, experiments also find an apparently weaker-than-power-law relation between the decoupling factor and mean alpha relaxation time [93].

It is interesting to compare our decoupling results with the predictions of the single-particle NLE theory, which found $\langle\tau\rangle\langle\tau^{-1}\rangle \sim \exp(12.3\phi)$ and $R_D \equiv \sqrt{D\tau/(D\tau)_{\phi=0.4}} \sim 0.65 + 0.15 \ln(\tau/\tau_0)$ based on the full trajectory simulation solution, where D is the long time self diffusion constant and τ is the mean alpha relaxation time associated with the incoherent dynamic structure factor at the cage peak wavevector [92]. Qualitatively there is good agreement, but the physics involved is not identical. In our two-particle theory, the essential origin of decoupling is the disorder associated with the initial configuration of two neighboring particles in the first solvation shell, which deeply modifies activation barriers and the escape rate. On the other hand, such physics is not present in the single-particle theory,

where the dynamical free energy has no analog of r_0. There, decoupling emerges as a purely dynamical effect associated with the distribution of time scales for escaping a local trap in an activated manner, with variation of trajectories and escape times being "weighted" differently by the finite length scale relaxation process versus the translational diffusion process [38]. We believe both these mechanisms for the origin of heterogeneous dynamics are generally important, though perhaps their relative importance is system-specific.

Although our present decoupling results are for a hard sphere fluid, they can be expressed in a generic form involving only the cage relaxation time and its "bare" analog, $\tau_0 = \beta\zeta_0\sigma^2 = \sigma^2/D_0$, where σ is the particle diameter and D_0 is the diffusion constant in the "normal" fluid regime. The two thermal liquids where translation-relaxation decoupling has been measured down to T_g are orthoterphenyl (OTP, $\sigma \sim 0.7$ nm) and tris-napthylbenzene (TNB, $\sigma \sim 1$ nm) [93]. Typical values of the normal state self-diffusion constant in small molecule liquids lie in the range $D_0 \approx 10^{-6} - 10^{-4}$ cm^2/s, and hence $\tau_0 \approx 10^{-10} - 10^{-8}$ s for OTP and TNB. The kinetic glass temperature is usually defined as when the alpha relaxation time $\sim 100 - 10,000$ seconds. Assembling these numbers, the ratio $\tau(T_g)/\tau_0 \approx 10^{10} - 10^{14}$. Hence, using Eq. 2.27, we estimate the decoupling factor at T_g for these liquids is $\sim 60 - 100$. Remarkably, this is essentially precisely the range of values experimentally observed for OTP and TNB [94]. The key to obtaining such a sensible result is the logarithmic growth of the decoupling factor, or in a qualitatively equivalent sense, the prediction that the decoupling factor scales linearly with the activation barrier. For multiple reasons we do not wish to over-emphasize the quantitative aspects of the above result, but given that there are no adjustable parameters we do believe this a priori calculation provides significant support for our theory of cage escape and structural relaxation.

2.5.4 Nonexponential Relaxation

We now discuss the time dependence of the relaxation functions and deviations from simple exponential decay. Figure 2.8 shows both the static-disorder-only and the full static-and-

dynamic-disorder-averaged cage correlation functions. As noted above, $(C_2(t))_s$ vanishes at a finite time because the spatial disorder average involves a longest hopping time. However, including dynamic disorder removes this unphysical feature. With the obvious exception of $(C_2(t))_s$, we generally find that the cage correlation functions are very well fit, over at least 2 decades, by a stretched exponential function:

$$C_\alpha(t) \approx \exp\left(-(\gamma t)^{\beta_k}\right), \tag{2.28}$$

where γ is an inverse relaxation time determined by fitting Eq. 2.28 to the numerical calculations. The linear-linear plot in the inset is shown since many experiments are reported in this format, and the measurements are limited to observing only 1-2 orders of magnitude of decay in signal amplitude. In general, the detailed time dependence predicted by our theory is affected by both the "static disorder" associated with initial cage conditions, and the dynamic disorder associated with the Poissonian distribution of hopping times. Hence, uniquely separating the origin of relaxation stretching into independent "static" and "dynamic" contributions does not seem possible.

Figure 2.10 shows results for the stretching exponents, β_k, as a function of volume fraction based on fitting Eq. 2.28 to the numerical calculations. The absolute magnitude of the stretching exponent clearly depends strongly on which correlation function is considered, ranging from $\beta_k \approx 0.56$ for $C_1(t)$, to $\beta_k \approx 0.95$ for $C_2(t)$. On the other hand it is nearly constant, or decreases only weakly with volume fraction, for all cases. The stretching exponent associated with $C_2(t)$, which is relevant to the cage correlation function studied in Rabani et al. [76, 79], is far from the value of $\beta_k = 0.5$ reported [79]. However, interestingly, our value of $\beta_k \approx 0.56$ for the full static- and dynamic-disorder averaged generic relaxation function, $C_1(t)$, is very close to what is observed in dense hard-sphere colloidal suspensions for the alpha process on the cage wavevector scale [94], and also the prediction of ideal MCT [95]. Moreover, this value is close to that observed in the dielectric experiments on TNB [96], the

decoupling behavior for which was discussed in the preceding section.

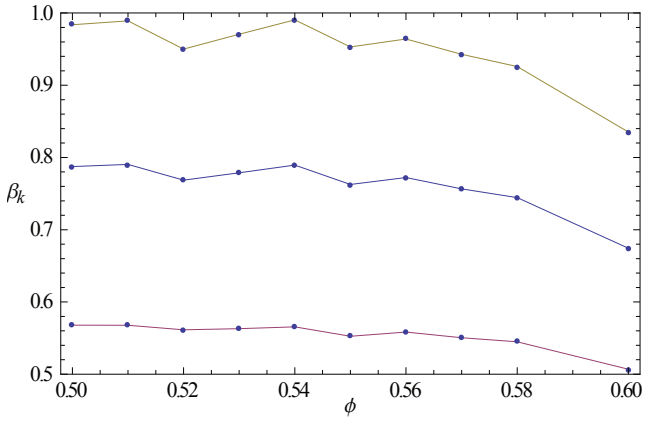

Figure 2.10: Stretching exponent of Eq. 2.28 for the static-disorder-only average of $C_1(t)$ (blue), the full static- and dynamic- disorder average of $C_1(t)$ (red), and the full static- and dynamic-disorder average of $C_2(t)$ (yellow).

Perhaps most significant is our prediction that the stretching exponent is nearly *independent* of volume fraction. This occurs despite the fact that the relaxation time changes by many orders of magnitude and there is significant decoupling. This combination of features is qualitatively what is observed in computer simulations of glassy hard sphere fluids [41], and for experiments on thermal molecular liquids OTP and TNB [94]. Such observations have been characterized as a major "mystery" in the sense that most classic theoretical explanations (for structural and spin glasses) of decoupling involve a postulated static-domain-like model on a mesocopic scale where finite size thermodynamic fluctuations of the relevant local structural variable (e.g. entropy [97], density [98, 99], or free volume [37]) that determines the hopping time is the origin of a distribution of relaxation times. Such models can indeed predict reasonable decoupling, but at the same time will predict strong variations of the stretching exponent with the thermodynamic control variable (temperature or volume fraction) that are not observed in TNB or OTP [94] or hard sphere fluids [41].

2.6 Initial Summary

We have generalized the nonlinear Langevin equation theory of single-particle activated barrier hopping to address correlated two-particle dynamics in a glassy or gel regime. Key technical approximations include the assumption of isotropy and an angular pre-averaging which reduce the problem to two scalar dynamic variables, one corresponding to the relative separation of the two particles, and the other to a center-of mass-like coordinate. The angular averaging approximation, invoked for technical tractability reasons, does raise difficulties, or ambiguities, with regards to the physical meaning of the CM-like variable in terms of the two-particle trajectories. For this reason, our detailed initial studies have focused on the correlated dynamics of two tagged particles approaching or separating from each other, the primary motion relevant to structural relaxation.

We have numerically determined the dynamic free energy surface corresponding to a fluid of hard-spheres, and found they generically display two relaxation channels or reactive trajectory paths, corresponding largely, but not exclusively, to motion parallel to the pure R or r displacement axes. The systematic numerical variation of these barriers was then studied as a function of both volume fraction and the initial separation of the particles, and oscillations related to the pair correlation function are predicted. The latter persists up to a dynamical correlation length beyond which the two-particle dynamics are uncorrelated in space and time. The dynamical length scale is modest in absolute size for the moderate barrier height systems studied ($\lesssim$ 13 k_BT), but does grow significantly with increasing volume fraction and is systematically different from the static correlation length of $g(r)$. Our calculations of mean first-passage times can, in principle, be compared with confocal microscopy experiments or computer simulations which track the motion of a pair of tagged particles [100].

As an application of our new theory, a simplified model of cage escape was presented which addresses the elementary step of structural relaxation. Predictions for characteristic

mean relaxation times, translation-relaxation decoupling, and stretched-exponential behavior of correlation functions were obtained. A consistent picture emerges for the origin of dynamic heterogeneity as encoded in translation-relaxation decoupling and stretched exponential decay of time correlation functions based on a combination of dynamic disorder associated with the noise driven hopping process and "static" disorder associated with the distribution of initial separations of a pair of caged particles. The theoretical results seem to be remarkably consistent with experiments on two thermal molecular liquids and simulations of the hard sphere fluid.

Since our theory requires as input only the equilibrium pair structure, there is nothing restricting its application to systems other than hard spheres. Particularly interesting would be a correlated two-particle study of the interplay between glassy and gel dynamics in very dense fluids where particles (colloids) interact via a strong but short-ranged depletion attraction [101]. Such a system has been found to exhibit a complex "two-step" cage escape process under quiescent "attractive glass" conditions [50], and double yielding behavior is observed in nonlinear rheological experiments [102]. The ability of the two-particle theory to explicitly treat the pair separation dynamics is clearly important for understanding "physical bond" breakage in gel-like systems, especially under high volume fraction conditions where steric blocking is simultaneously present.

Other important topics of future work include: (i) understanding better the physical meaning of the R dynamical variable and its possible connection to "cluster-like" cooperative motions, (ii) employing stochastic Brownian simulation to compute two-particle time-correlation functions of interest including dynamical heterogeneity signatures, and (iii) generalizing the two-particle theory to compute the elastic shear modulus and the full nonlinear mechanical response, as has been achieved based on the single particle NLE approach [69].

Finally, a key parameter of our formulation is the initial interparticle separation, r_0, which was treated as an initial condition to the two coupled NLE's. Both computer simulation and experiment (for colloids) can study two-particle correlated dynamics as a function of

initial particle separation. Given that deep in the glassy regime the particle motions are highly intermittent (undergoing long periods of localized intra-cage vibration interspersed with very rapid, larger amplitude, cage-breaking jumps), one can imagine extending our approach to develop a simple model of multiple correlated caging and hopping (forward and backward) events of a tagged pair of particles. Crossing a barrier in the r direction would take a characteristic time (or distribution of times) and correspond to a change in interparticle separation related to the position of that barrier. Subsequent to this event, the particles can be viewed as "re-caged" at a new value of r_0 via a local equilibration process which has time to occur due to the highly intermittent nature of motion. In such a way, a multi-state Markov model of pair particle motion (e.g. an "unbinding from contact" process) could be built up, which may have rich potential for making connections to existing studies of coarse-grained and phenomenological descriptions such as kinetically constrained models and continuous-time random walks [70, 75, 103].

We now begin a discussion of such a combination of the two-particle activated hopping model derived in the first part of this chapter with such a markovian recaging process can help make contact with a variety of other theories of the glass transition. The purpose being to both extend the two-particle NLE theory to address new questions, and also use the NLE framework to search for connections with other ways of thinking about the glassy dynamics problem. Three topics are addressed. (i) The formulation and application of a multi-state Markov model to describe space-time correlated hopping associated with dynamical interparticle separation (structural relaxation). (ii) A study of the relative importance of neighbor exchange and neighbor loss in distinguishing irreversible relaxation events from reversible ones [77,78,104]. (iii) The proposal of a microscopic, structure-based scenario based on modest coarse graining in which the ideas of persistence and exchange from phenomenological, kinetically constrained models (KCMs) [80–82] can be identified from the correlated motion of pairs of particles.

2.7 Multiple Hopping Events and the Role of the Initial State

Above we reported computations of the dynamic free energy surfaces over a range of volume fractions ($\phi = 0.5 - 0.6$) and at initial separations corresponding to the minima and maxima of the radial distribution function [105]. The primary quantities of interest were the barrier heights and mean first passage times along the direction of CM motion, R, and increasing or decreasing relative separation, r^+ and r^-, respectively. In creating a description of "cage escape," mean first-passage times at many initial separations between the first maximum and first minimum of $g(r)$ were computed. This led to two key predictions: a decoupling between the diffusion constant and the relaxation time (translation-relaxation decoupling) associated with motion in the r-direction of a magnitude and thermodynamic state dependence in semi-quantitative agreement with data on hard sphere suspensions and molecular liquids; and a "cage escape correlation function" that showed stretched-exponential behavior but with a nearly volume-fraction-independent stretching exponent. This qualitative behavior of strong decoupling with no change in the shape of the relaxation function has been observed in hard-sphere simulations [41] and experiments on molecular glass formers [94].

The bulk of the numerical effort relevant for the rest of the chapter involves the extension of the above program to compute barriers and mean first-passage times at many more values of the initial separation for each volume fraction studied. As detailed in the following sections, this permits the construction of a more sophisticated description of relaxation events, which in turn allows us to make contact with different ways of looking at the glassy dynamics problem.

Figure 2.11 presents calculations of the entropic barrier height for motion in the r^+ and r^- directions as a function of initial separation out to the second minima of the radial distribution function. Figure 2.12 shows the corresponding mean first-passage times. Several points are evident. First, the logarithm of the mean first-passage time closely tracks the bar-

rier height. Second, the barrier heights qualitatively track the PMF at different separations, a fact shown explicitly in Ref. [105]. Third, the mean relaxation time calculations are noisier than the barrier height calculations since small numerical inaccuracies in F_{dyn} are amplified in the calculation of the curvatures required in Eq. 2.15. This is a second-order effect which does not affect the general oscillation of barrier heights/relaxation times on the scale of $g(r)$, a key feature of our analysis. In Fig. 2.12, spline interpolations are shown which smooth the discrete numerical hopping-time data; all our subsequent results are only very weakly sensitive to the specific curve-fitting procedure employed.

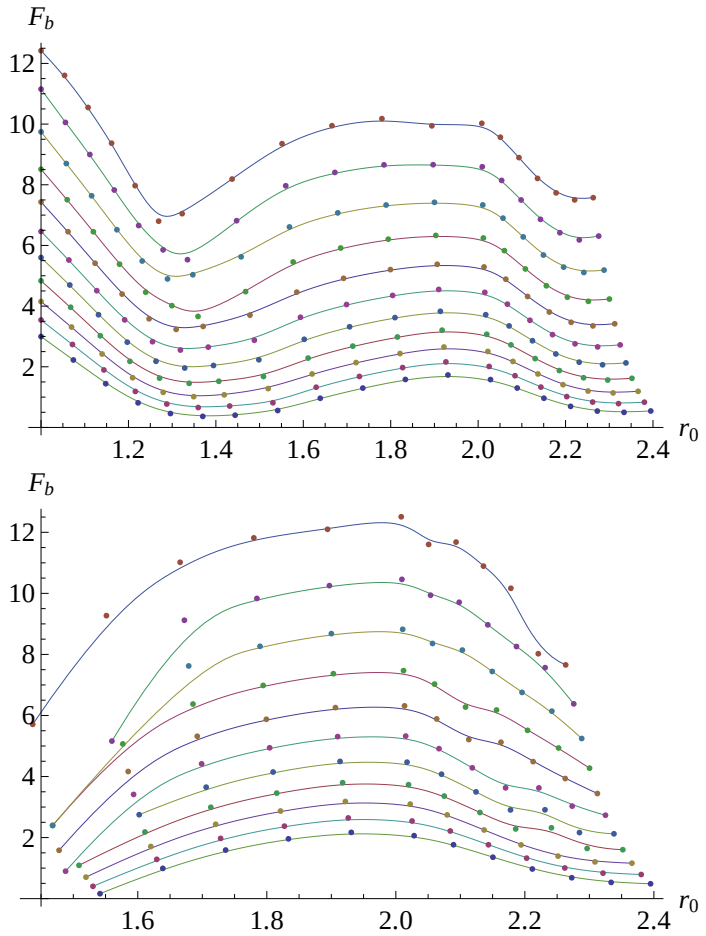

Figure 2.11: Relative-separation barrier heights in the (A) forward (r^+) and (B) backwards (r^-) directions versus initial separation for $\phi = 0.50 - 0.6$ (in increments of 0.01, bottom to top)

In the following sections we adopt a specific jargon and notation to indicate the different

types of changes in the relative separation coordinate of two tagged particles. The "hopping" motion of this relative coordinate is often described in the language of a particle hopping, but in reality this means one of the particles is used to define the origin of an instantaneous radial distribution function in the local-equilibrium approximation centered at that particle. Increases and decreases in the relative separation are referred to as forward and backwards hops, respectively, and (consistent with the above notation) superscripts pluses and minuses are employed on both the coordinate itself and the characteristic time to move in a specific direction $(r^+, \tau^+, r^-, \tau^-)$. Finally, when coarse-graining over shells of the radial distribution function, the characteristic time for the relative coordinate to indicate a change from shell i to shell j is denoted by $\tau_{i\to j}$.

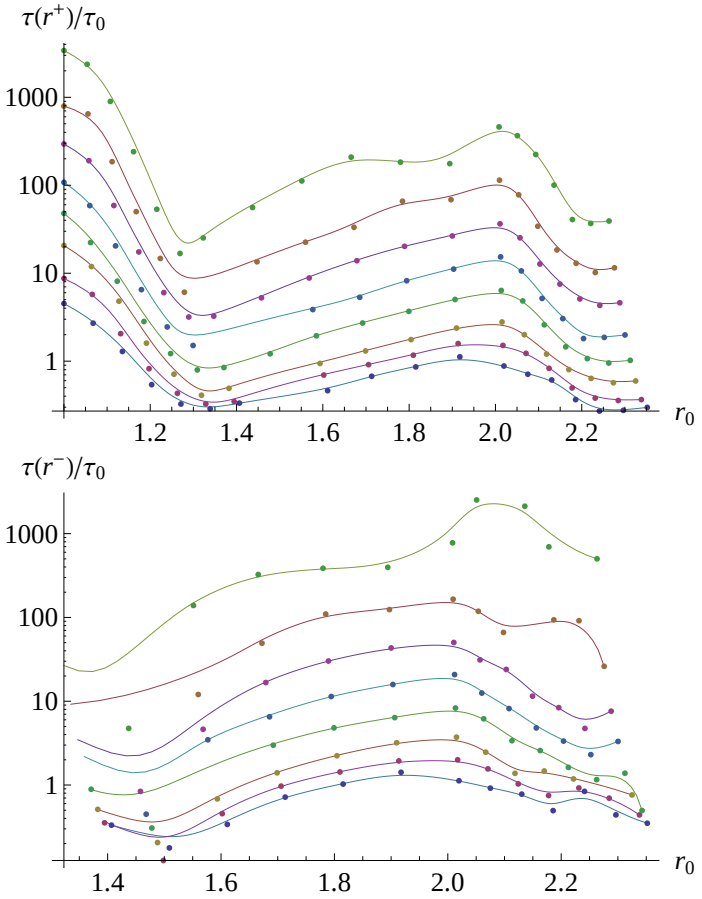

Figure 2.12: Relative-separation hopping times in the (A) forward (r^+) and (B) backwards (r^-) directions versus initial separation for $\phi = 0.53 - 0.6$ (in increments of 0.01, bottom to top), along with the interpolation curves (see text).

2.8 Irreversible Neighbor Loss and Structural Relaxation

2.8.1 Neighbor Loss, Recovery, and Irreversibility

The notion of "irreversibility" in single-particle statistics of glassy systems has long been a thorny problem. At issue is that a tagged particle spends the majority of its time rattling around in its cage, and then occasionally makes a jump of broadly distributed amplitude, including large displacements of order a particle radius, $\sim \sigma/2$ [5, 78]. However, such "cage-breaking" jumps do not always lead to an irreversible change in the configuration of the liquid: when viewing trajectories, sometimes the particle hops further away and the cage closes behind it, but other times the particle fluctuates back into the cage, essentially restoring the initial configuration [40,78,106]. One technique employed in simulations and confocal microscopy experiments on colloids for distinguishing reversible from irreversible rearrangements is to track fluctuations that induce changes in the list of nearest-neighbor particles before and after a tagged particle hops [77, 104, 107].

Our present goal is to address the irreversibility question in the context of the space-time-correlated two-particle hopping model. The physical picture of a particle first hopping some distance and then hopping either further away from or closer to its initial position relative to other particles maps quite intuitively to the combination of our two-particle theory and a local equilibrium idea. The latter means that after a hop the two particles are re-caged and must escape via another activated event. Our ideas are general with regards to the interparticle pair potential, but we analyze the problem in the context of a hard-sphere fluid.

The relative statistics of a given jump being reversible or irreversible will be treated based on a multi-state Markov model. Additionally, we connect our results to the above-mentioned ideas of nearest-neighbor loss. In particular, we initially determine the probability to first

lose some fixed number of neighbors as a function of time, and then study the probability distributions that at time t at least $(x - n)$ nearest neighbors have been irreversibly lost if at some earlier time, $t' < t$, x nearest neighbors were lost. Our results are qualitatively compared to the simulations on model thermal 2D glass formers below the onset temperature [77]. Of course, quantitative comparison between our calculations for a 3D hard sphere fluid and the 2D Lennard-Jones thermal mixture simulations is not possible.

2.8.2 Multi-state Markov Hopping Model

The basic spirit of our model is illustrated in the schematic cartoons of Fig. 2.13. We have previously observed that at all separations a hop in the relative separation coordinate corresponds to a change in r on the order of $\sigma/2$, a natural length scale for defining solvation shells and interstitial configurations [105]. For example, two particles initially at contact can undergo a relative hop that places their separation in an "interstitial"-like configuration, or vice-versa. We use this as motivation to coarse grain over the shells of the radial distribution function, arguing that a forward or backward hop amounts to changing the relative shell the two particles occupy. In this way we track the two-particle separation, computing characteristic times and rates to hop from one shell to the next under the local equilibrium assumption that after a hop the particles temporarily equilibrate and behave as if their new separation serves as the "initial" separation (r_0) of a subsequent hopping event. Since the dynamic free energy surface depends on r_0 via both the PMF and the dynamical forces of the surrounding particles, subsequent forward and backward hopping events are modified relative to the initial activated motion.

As a more general comment, our focus on large amplitude single- and two-particle hopping events should not be interpreted as denying there is more cooperativity involved in the elementary alpha relaxation process. Indeed, the latter no doubt involves the correlated motion, on relatively small scales, of many particles; no microscopic theory exists for such many-particle cooperative dynamics. However, the achievement of irreversibility and struc-

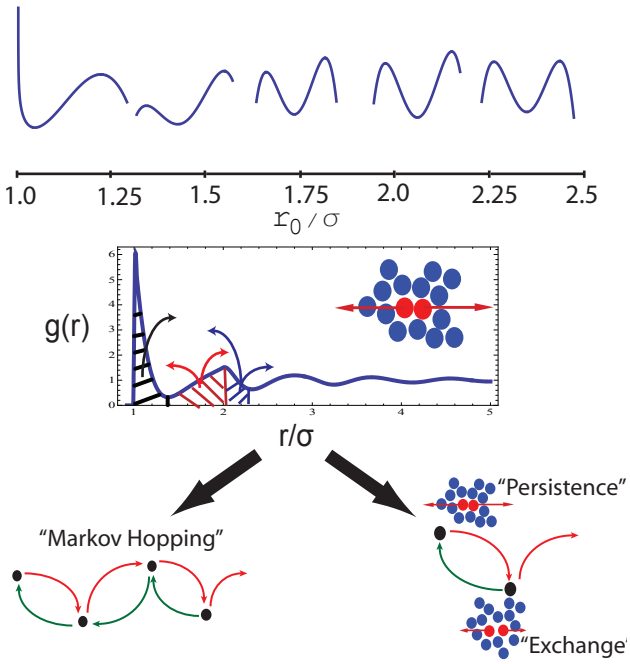

Figure 2.13: (A) Schematic cartoon of forward/backwards barriers at different initial separations. The differently-hatched regions correspond to coarse-grained sites. (B) Schematic cartoon of coarse-graining g(r) into (left) a 4-state Markov model and (right) persistence/exchange events, defined as a near-neighbor pair of particles first separating and then moving farther away, respectively.

tural renewal as defined via neighbor exchange must involve some small number of particles moving a significant fraction of their diameter. It is this latter aspect that we focus on using the NLE approach and our present lightly coarse-grained description. In this regard, we note there is simulation and experimental evidence that on the alpha relaxation time scale the key motions involve compact clusters of particles (not the strings relevant at earlier times) [108,109]. Moreover, irreversible structural rearrangements have been experimentally imaged in glassy hard-sphere colloidal systems, where compact rearranging regions always involve a few particles displacing by distances of order their radius, dressed by small correlated motions of surrounding colloids [107]. The relationship between the smaller and large displacements, and whether "one triggers the other," remains poorly understood.

Previously we evaluated the time for two particles initially at contact (i.e., within the first shell of the radial distribution function, $\sigma \leq r_0 \leq g_{min}$, where g_{min} is the first minima of $g(r)$) to first separate, defining a "cage escape" time, $\tau_{cage} = \tau_{1\to 2}$, analogous to an alpha-relaxation time [105]. We assumed that the white-noise-driven hopping over a (high) barrier is a Poissonian process [53], so that the probability to hop from an initial separation r_0 at time t in either the forward or backwards direction is given by

$$P(t, \tau^{\pm}(r_0)) = \frac{t}{(\tau^{\pm}(r_0))^2} e^{-t/\tau^{\pm}(r_0)}. \tag{2.29}$$

Then, averaging over both the dynamic disorder of this Poisson process, and the static disorder from coarse-graining $g(r)$, the probability to exit the cage of nearest neighbors is

$$\tau_{1\to 2} = \frac{\int_1^{g_{min}} r_0^2 g(r_0) \int_0^{\infty} tP(t, \tau^{+}(r_0))\ dt\ dr_0}{\int_1^{g_{min}} r_0^2 g(r_0)\ dr_0}. \tag{2.30}$$

Similarly, the average hopping time from site 2 to 3 is

$$\tau_{2\to 3} = \frac{\int_{g_{min}}^{g_2} r_0^2 g(r_0) \int_0^{\infty} tP(t, \tau^{+}(r_0)) dt\ dr_0}{\int_{g_{min}}^{g_2} r_0^2 g(r_0)\ dr_0}, \tag{2.31}$$

where g_2 is the location of the second peak of $g(r)$. The other rates are computed analogously, using either the forward or backwards hopping times in $P(t, \tau(r_0))$ as appropriate.

Treating the question of irreversibility requires the determination of how often a particle is recovered after it first jumps away. To do so, we separately consider the probability of first leaving the contact shell, and then the probability of returning given that the particle has left. The first of these questions is straightforward. Defining the function

$$P'(t, \tau^{\pm}(r_0)) = \int_0^t P(t', \tau^{\pm}(r_0))\ dt' = 1 - e^{-t/\tau^{\pm}(r_0)} \left(1 + \frac{t}{\tau^{\pm}(r_0)}\right), \tag{2.32}$$

as the probability for two particles separated by r_0 to have a jump in their relative separation by time t, and averaging over the spatial disorder in the first shell, gives the probability that by time t a particle has escaped from the first (contact) shell:

$$p(t) = \frac{\int_1^{g_{min}} r_0^2 g(r_0) P'(t, \tau^{+}(r_0))\ dr_0}{\int_1^{g_{min}} r_0^2 g(r_0)\ dr_0}. \tag{2.33}$$

To determine whether this escape is irreversible or not we construct a simple 4-site Markov model as schematically illustrated in Fig. 2.13B, with each site corresponding to a shell of the radial distribution function. Particle separations can hop back and forth between three sites corresponding to the two particles being nearest neighbors, next-nearest neighbors, and next-next-nearest neighbors. The fourth shell of $g(r)$ is treated as a semi-absorbing boundary, in that particles can continue to hop further away but cannot hop back to the third shell (schematically shown in Fig. 2.13B and represented in the transfer matrix in Eq. 2.34 below). Over the time scales that we study, this (easily relaxed) approximation makes no quantitative difference to our results. Average hopping rates between these shells are computed in complete analogy with the above, taking the mean rates to be the inverse of the mean hopping times. Concretely, the model assumes that if the particles hop "forward" from the third site then they never return to being nearest-neighbors. That is, particles

can hop back and forth between contact and the second shell, but once they are separated by more than this distance they are never recovered. Rigorously this will not always be true, but on the time scales we consider, and those examined in the simulations (on the order of the mean alpha time, i.e. to hop from the first to the second site), the exceedingly low probability of a recovery makes this a reasonable approximation. We could, of course, use a more sophisticated semi-Markov model that takes into account the Poisson hopping processes instead of using such processes to define the rate constants, but we expect such an improvement to make only a modest quantitative change to our ultimate predictions.

The 4-site Markov model can be easily solved to give the probability, $p_c(t)$, that the particles occupy the "nearest-neighbor" site at time t. We define a transition matrix as

$$T = \begin{pmatrix} -\tau_{1\to2}^{-1} & \tau_{2\to1}^{-1} & 0 & 0 \\ \tau_{1\to2}^{-1} & -(\tau_{2\to3}^{-1} + \tau_{2\to1}^{-1}) & \tau_{3\to2}^{-1} & 0 \\ 0 & \tau_{2\to3}^{-1} & -(\tau_{3\to4}^{-1} + \tau_{3\to2}^{-1}) & 0 \\ 0 & 0 & \tau_{3\to4}^{-1} & -\tau_{4\to5}^{-1} \end{pmatrix} \tag{2.34}$$

and numerically solve for its eigenvalues λ_i and eigenvectors ξ_i. The initial condition is $\sum_{i=1}^{4} a_i\xi_i = \{1,0,0,0\}$, i.e. the two tagged particles are initially nearest neighbors. The probability of occupying the nearest-neighbor site is then just the first element of $\sum_{i=1}^{4} a_i\xi_i e^{\lambda_i t}$. Combining this result with Eq. 2.33 which gives the probability that the particles have ever left contact, $p(t)$, the probability to regain a nearest-neighbor contact given that such a contact was lost (i.e. the probability that a particle was "recovered") is estimated as

$$p_r(t) = \frac{p_c(t) - (1 - p(t))}{p(t)}. \tag{2.35}$$

Addressing irreversibility at the characteristic time to first hop away, the probability of a typical jump being irreversible is $1 - p_r(\tau_{1\to2})$; this quantity is plotted in the inset of Fig. 2.14A. We emphasize that a large hop ($> \sigma/2$) is not necessary for a jump to be

irreversible; even a jump to the interstitial site has a chance to be deemed irreversible with our definition, as we demonstrate in the numerical calculations presented below. The resulting non-monotonicity is a highly non-trivial prediction that results from the complex interplay between forward and backwards hopping times, both of which grow with volume fraction but do so at different rates. We note that such a weak non-monotonicity, and an irreversible-jump-fraction magnitude close to our calculation, has been observed in binary Lennard-Jones mixture simulations as a function of inverse temperature [78]. Our interpretation for irreversibility is then that a particle trying to escape its cage of neighbors must first hop into an "interstitial" site corresponding to the first minimum of the radial distribution function. From there, the average structural constraints determine the relative rates of continuing the cage escape process ("unbinding") or falling back ("recovery") into the nearest-neighbor position.

If one assumes that the different particles forming the cage leave and return in an uncorrelated manner, a simple binomial model suffices for the probability that n lost neighbors were recovered given that x nearest neighbors were at some point lost:

$$P_{n,x}(t) = \binom{x}{n} p_r(t)^n (1 - p(t))^{x-n}. \tag{2.36}$$

The idea that the neighbors can be treated in this uncorrelated manner is perhaps reminiscent of the finding that local density does not correlate well with local dynamic propensity in a constrained lattice gas simulation [110]. Indeed, the distribution of nearest and next-nearest neighbor vacancies found in the simulation is qualitatively quite similar to our $P_{n,x}$ distributions.

Figure 2.14A shows calculations for various x at $t = \tau_{1\to 2}$ and $\phi = 0.55$; qualitatively the results are very similar to the distributions observed in 2D simulations of a binary LJ mixture model below the onset temperature [77]. Figure 2.14B presents calculations at just two different values of neighbors initially lost but for different volume fractions, and the observed

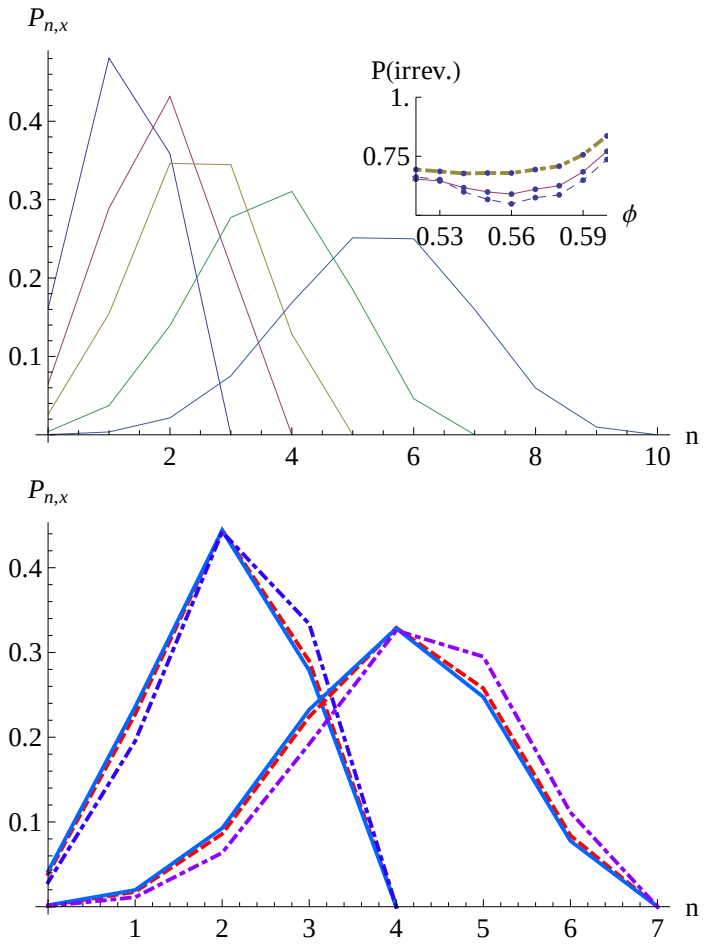

Figure 2.14: (A) Probability of neighbor loss/recovery at the cage-escape time, $P_{n,x}(\tau_{cage})$, for $x = 2, 3, 4, 6, 9$. Inset. Fraction of irreversible jumpers for $\tau = 0.5\tau_{cage}$ (dashed), τ_{cage} (solid), and $\tau = 0.5\tau_{cage},\ \tau_{cage}, 2\tau_{cage}$ (dash-dotted). (B) $P_{n,x}(\tau_{cage})$ for (left) $x = 3$ and (right) $x = 6$ at $\tau = 0.5\tau_{cage},\ \tau_{cage}, 2\tau_{cage}$(dashed, solid, and dash-dotted curves, respectively) at $\phi = 0.52$.

volume fraction dependence of $P_{n,x}$ is rather weak. One can then define, as was done in analyzing the simulation data, an "irreversible" event by finding the x such that probability of recovering all of the lost particles falls below some threshold at the characteristic relaxation time, e.g., $P_{0,x}(\tau_{cage}) < 0.05$. In two dimensions at one specific temperature Widmer-Cooper et al. found $x = 4$ [77], and an experimental study of 2D slices of an ultra-dense 3D hard-sphere colloidal suspension reported $x = 3$ [104]. We estimate that for hard-spheres in three dimensions one also expects $x = 4$ over a broad range of volume fractions, except at the lowest and highest volume fractions we study ($\phi = 0.5 - 0.53,\ \ 0.59,\ \ 0.60$) where a greater fraction of jumps fail to return to contact and the critical x drops to 3. We also find that this distribution often peaks at $n = x - 2$, as has been reported in the 2D simulation, but we expect this is a coincidence and not a general result. Note that a slightly different definition of "recovery" was used in the simulations: a neighbor was counted as "recovered" at time t if it has been recovered at any time prior to t, even if it was then subsequently lost and no longer in the neighbor list at t.

We can also compute quantities like the probability distribution to first lose a fixed number of neighbors, a property that has been studied via the 2D simulations [77]. Results for the probability to first lose the fourth neighbor are presented in Fig. 2.15; the inset shows this quantity up to $t/\tau_{cage} = 2/7$, roughly the range studied in the simulations and over which the probability is a monotonically increasing function. We predict that, for the two volume fractions examined, the distribution peaks soon thereafter, and then quickly decays to zero.

2.9 Facilitation, KCM Statistics, and Decoupling

2.9.1 KCM Picture

In this section we propose a specific spatial coarse-graining over activated two-particle motion to try to connect our microscopic theory that relates structure and slow intermittent

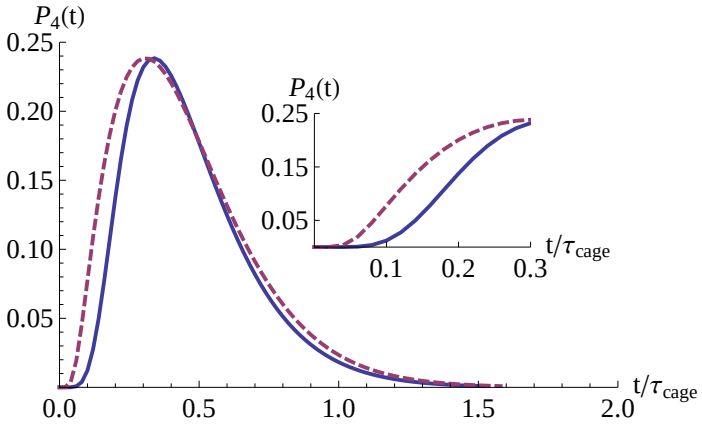

Figure 2.15: Probability distribution to first lose four neighbors, $P_4(t/\tau_{cage})$, for $\phi = 0.52$ (solid curve) and $\phi = 0.55$ (dashed curve). Inset. $P_4(t/\tau_{cage})$ at short times.

activated dynamics with the ideas of dynamic facilitation that form the cornerstone of kinetically constrained models. The KCMs seek to phenomenologically provide a coarse-grained description of glass-formers in the language of lattice spin models. Rules governing the spin flips are chosen so that all configurations are equally likely — resulting in trivial thermodynamics — but where at low temperatures relaxation is governed by increasingly rare diffusing defects, leading to non-trivial dynamically facilitated behavior. Although the microscopic origin of the dynamic rules at the level of atoms and forces is unclear, specific KCMs have been shown to be capable of describing some statistics that result from coarse-graining atomistic MD simulations, and can describe many features of dynamic heterogeneity [82,111,112]. In our opinion, there must be some structural basis for the postulated kinetic rules, and searching for them is our present goal. While a first-principles coarse graining of particle trajectories to recover the facilitation rules of specific KCMs (e.g. the Fredrickson-Andersen or East model) does not seem to be a feasible task, one can ask if the statistics of coarse grained particle mobility are similar to the KCM predictions. Here we take a modest first step towards connecting with KCMs, and do not address the full, most-recently proposed picture [82].

Fundamental to the KCM perspective of diffusion-relaxation decoupling is the division of events into "persistence" and "exchange," which correspond to the first nucleation of particle

mobility and subsequent manifestations of mobility, respectively. The basic insight behind this division is the idea that once particle mobility has been nucleated at a site, further mobility becomes more likely at that site. In the facilitation picture, a particle spends a long time waiting for a (rare) excitation line to sweep past, but once an excitation line is in the particle's vicinity it is likely to diffuse back and forth across the particle's position, triggering further relaxation and diffusion. It is first and foremost this division that we seek to understand at a microscopic level.

2.9.2 Dynamical Mapping and Model Calculations

Current attempts to coarse-grain particle trajectories from molecular dynamics (MD) simulations onto KCM statistics have relied on interpreting the distribution of persistence and exchange times as the first time a particle moves beyond a threshold distance and then subsequent times between further, similarly large particle motions. This characteristic threshold is often taken to be half a particle diameter, $a = \sigma/2$ [111], quite similar to our earlier study of particle escapes from a nearest-neighbor list [105]. Qualitatively similar features are found for a range of choices for this threshold displacement provided that irrelevant small-amplitude vibrational motions are coarse grained out (either by averaging over short vibrational periods or by resolving only inherent structures) and that the displacement is not so large as to obscure a longer time scale associated with broader system relaxation [82].

We adopt the above perspective as inspiration for the analysis of our real-space NLE theory of correlated two-particle hopping. However, we emphasize that the distinction between "persistence" and "exchange" in our microscopic theory arises from the underlying structure of the fluid; spatial correlations imprinted on the hopping times as a function of r_0 make some interparticle separations more favorable for activated events to occur than others. We will take the fundamental persistence event to be the irreversible separation of two particles from the first to the second shell of the radial distribution function (Fig. 2.13B). This definition is in the spirit of recent work on KCMs, where excitations are viewed as

"non-trivial particle displacements associated with transitions between relatively long-lived configurations" [82]. That is, since excitations are not just particles moving but an underlying feature of the structure that promotes mobility, we wish to exclude from our definition of "persistence" events those particles motions which quickly lead to a return to the original configuration. Using the notation of Sec. 2.8, the probability distribution of a persistence event at a fixed initial separation can thus be described as

$$P_{persist}(t, \tau^+(r_0), \tau^-) = \int_0^t P(t', \tau^+(r_0)) \cdot \left(1 - P'(t - t', \tau^-)\right)\ dt', \tag{2.37}$$

where $P(t, \tau^+(r_0))$ as given in Eq. 2.29 is the probability to separate from contact at time t given a mean first-passage time of such an event $\tau^+(r_0)$, and $(1 - P'(t - t', \tau^-))$ from Eq. 2.32 is the probability that the particle pair has not returned to contact in the time interval $(t - t')$ given a mean time for such an event τ^-. As in our previous work [105], this distribution is then averaged over the spatial disorder in the first shell, taking for convenience the backwards-hopping, irreversibility-revoking events to occur at the characteristic rate $\tau_{2\to1}$ as computed in the previous section. Thus, our final estimate for the persistence time distribution is

$$P(\tau_p) = A \int_1^{g_{min}} r_0^2 g(r_0) P_{persist}(\tau_p, \tau^+(r_0), \tau_{2\to1})\ dr_0, \tag{2.38}$$

with A the normalization constant.

The distribution of Eq. 2.38 is plotted in Fig. 2.16 for a variety of hard-sphere-fluid volume fractions, and its first moment is plotted versus volume fraction in Fig. 2.18. We note that the variance of this distribution closely tracks the mean, a feature of many distributions in the exponential family. A key feature of the best-supported facilitated models is a parabolic-law dependence of the relaxation time [113], and this is clearly shown by the fitting curve in Fig. 2.18. Specifically, over the range $\phi = 0.5 - 0.6$ the calculations are very well described by $\ln(\tau_p/\tau_0) \propto (\phi - \phi_c)^2$ for volume fractions greater than an empirical onset $\phi_c \approx 0.47$. This is greater than the NMCT crossover volume fraction of $\phi_{NMCT} \approx 0.43$, and in the

single-particle theory corresponds to a small barrier of $F_b \approx 0.6\ k_B T$.

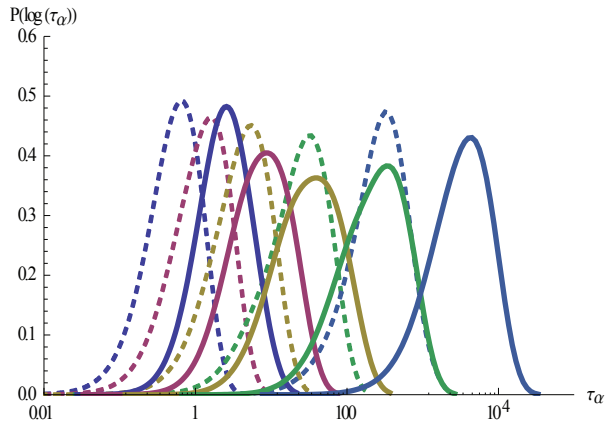

Figure 2.16: Logarithmic probability distributions for the exchange ($P(\log_{10}\tau_x)$, dashed) and persistence times ($P(\log_{10}\tau_p)$, solid) for $\phi = 0.52,\ 0.54,\ 0.56,\ 0.58,\ 0.6$.

Consistent with the above we then define the exchange-time distribution as arising from forward hops out of the second shell (i.e. the probability of hopping away before hopping back to contact), which up to a normalization constant B results in

$$P(\tau_x) = B \int_{g_{min}}^{g_{2nd\,\max}} r_0^2 g(r_0) P(\tau_x, \tau^+(r_0)) \cdot \left(1 - P'(\tau_x, \tau^-(r_0)\right)\ dr_0. \tag{2.39}$$

Numerical results for this distribution are also plotted in Fig. 2.16. We note that the decision to exclude backward hops in the definition of an exchange event makes only a very minor quantitative difference to the distribution, but choosing these irreversible hops to be the fundamental persistence event in Eq. 2.38 is important. This choice results in a small quantitative adjustment to the mean persistence time, but qualitatively suppresses much of the short-time part of the distribution since backward hops can occur more rapidly than the cage-breaking event, and emphasizes the large skew of the distribution, consistent with observed persistence distributions in the literature [111, 112, 114].

Figure 2.17 plots both distributions, normalized by their peak height and position. One sees that the persistence and exchange distributions are significantly different in both their shape and response to increasing volume fraction. Thus, it appears we recover this funda-

mental feature of KCMs, but do note that some details of our distributions are unlike those deduced in the coarse-grained atomistic MD simulations [111]. In particular, in that work the exchange-time distribution acquires a (slight) skewness opposite that of the persistence-time distribution, whereas we find a slight skewness of the same sign. Additionally, at the lowest two temperatures studied in the MD simulations the peak of the exchange distribution showed almost no shift, whereas we find the peak monotonically shifts to longer times with increasing volume fraction.

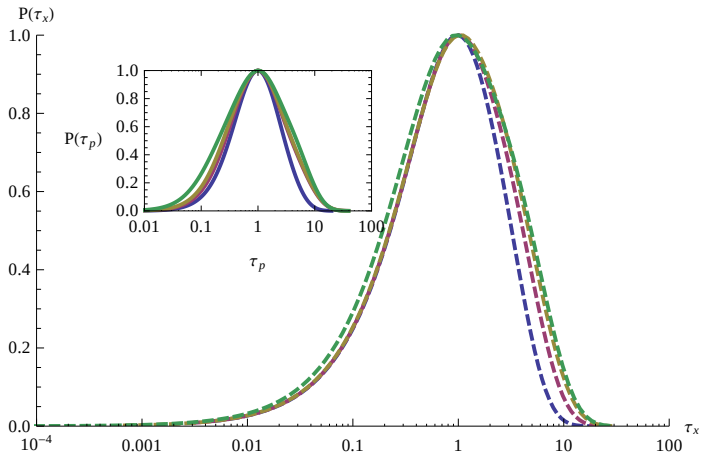

Figure 2.17: $P(\log_{10}\tau_x)$ normalized by its peak height and position. Inset. $P(\log_{10}\tau_p)$ normalized by its peak height and position.

The short-time behavior of the exchange-time distributions exhibit the expected Poissonian behavior, but the rest of the exchange-time distribution is a less-good match to observed distributions in simulations of the thermal liquid model. We expect this is partly a result of including only one type of exchange event: hopping from the second shell to the third. In reality, one should likely include the statistics of all other types of hops in the exchange time distribution: hopping back and forth from the third shell, center-of-mass hops that we have neglected here, and so on. Additionally, particularly for the relatively low barrier hops that characterize the exchange events, it is known that our choice of a Poissonian distribution for the barrier-hopping process is quantitatively inaccurate [92]. All of these factors would serve to broaden our predicted exchange time distribution in line with what is observed com-

putationally, where particles are typically tracked over relatively long time scales thereby allowing for the sampling of long exchange times [111].

Within the KCM perspective the difference between persistence and exchange times has been proposed to explain the Stokes-Einstein decoupling of viscosity (or alpha relaxation time) and diffusion observed in supercooled liquids and also models of hard sphere suspensions [111, 112, 114]. The argument is that while relaxation is governed by the slowest (most local) characteristic time scale of the system, τ_p, mass transport requires multiple hops to become diffusive and is controlled by the faster exchange processes, and hence proceeds on the time scale τ_x. Thus, the ratio $R = \tau_p/\tau_x$ provides a quantitative measure of the decoupling in a given model. For the hard-sphere system, our calculations of this decoupling parameter are plotted against the persistence time in the inset of Fig. 2.18. We find that to within our numerical accuracy the data is well fit by $R \approx 3.95 + 1.0 \log(\tau_p/\tau_0)$. In earlier work using a simpler "cage escape" model [105] we found $R \approx 3.2 + 1.5 \log(\tau_{cage}/\tau_0)$ or $\sqrt{R} \approx 1.0 + 0.25 \log(\tau_{cage}/\tau_0)$. As previously discussed in that reference, the latter agrees well with hard sphere simulations, and also decoupling experiments on molecular liquids at T_g; these forms are also quite similar to earlier estimates based on the single-particle NLE theory which fully took into account trajectory fluctuations (dynamic disorder) by numerically solving the stochastic equation-of-motion [53]. The quantitative similarity between the aforementioned studies again points to the degeneracy of theoretical approaches to the glass problem, and also supports our belief of strong connections between slow single-particle and many-particle activated dynamics.

2.10 New Approximation for the Distinct Van Hove Function

Continuous time random walk (CTRW) models, in which a walker takes a step of random size at random points in continuous time [115], have been used in diverse phenomenological

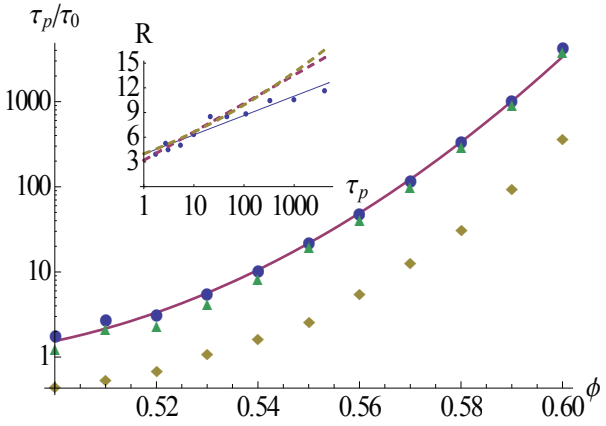

Figure 2.18: Average persistence time (circles), exchange time (diamonds), and cage escape time (triangles) as a function of volume fraction, and an empirical "parabolic law" fit to the persistence time, $\ln(\tau_p/\tau_0) \approx 480(\phi - 0.47)^2$. Inset. Decoupling parameter $R = \tau_p/\tau_x$. Solid line is $R = 3.9 + \log(\tau_p/\tau_0)$, and dashed lines are earlier decoupling predictions based on the "cage escape" model [21], $R = 3.2 + 1.5\log(\tau_p/\tau_0)$ and $R = (2 + 0.25\log(\tau_p/\tau_0))^2$.

descriptions of amorphous materials [116, 117]. Persistence and exchange events have been embedded in this formalism as a way of translating distributions of events into an expression for the self-part of the van Hove function, $G_s(r,t)$, where two distinct time-scales are necessary to recover the correct expression for the van Hove function [118]. The essence of this approach is to take the distribution of displacements associated with persistence and exchange events to be $f_p(r)$ and $f_x(r)$, where $f_p(r)$ is associated with intra-cage local Gaussian vibrations, and the distribution of jump sizes associated with $f_x(r)$ might similarly be drawn from a Gaussian distribution but with a larger characteristic length, e.g., $\sigma/2$. Defining probability distributions for the times at which these events occur, $\phi_p(t)$ and $\phi_x(t)$, the probability that the random variable X of interest (for instance G_s) has the value r at time t is given by

$$X(r,t) = \sum_{n=0}^{\infty} p(n,t) f(n,r), \tag{2.40}$$

where $p(n,t)$ is the probability that the variable undergoes exactly n jumps in time t, and $f(n,r)$ is the probability that in n jumps the displacement is r. With the above distributions the CTRW framework allows one to carry out the sum in Fourier-Laplace space, with the

result [118]

$$X(q,s) = f_p(q)\frac{1-\phi_p(s)}{s} + f_p^2(q)f_x(q)\frac{\phi_p(s)(1-\phi_x(s))}{s(1-\phi_x(s)f_p(q)f_x(q))}. \tag{2.41}$$

This sort of formula can be (and has been [70, 119]) used to write down an expression for $G_s(r,t)$ or $F_s(k,t)$ given information from a single-particle theory about localization, jump distances, and average hopping and reaction times. In the KCM perspective of persistence and exchange events the expression is largely the same, except the distributions of persistence and exchange jumps are both taken to be drawn from the same (Gaussian) distribution [70].

Our theory of two-particle hopping is not suitable for studying the *self* part of the van Hove function because the jumps are not single particle events. However, if the analysis in Sec. 2.9 is embedded in a CTRW framework one could construct a theory for a variable $X(r,t)$ that gives the probability that two particles with initial separation r_0 are separated by $r_0 + r$ at time t. Here we sketch an idea for how information of this sort might be used to improve on the standard Vineyard approximation and estimate the distinct part of the van Hove function, $G_d(r,t)$.

First, one imagines coarse graining over the shells of the radial distribution and proceeds as outlined in Sec. 2.9, defining the set $X(r,t;i)$ for each shell i. Vineyard's original idea was to write the convolution [120]

$$G_d(r,t) = \int d\vec{r'} g(\vec{r'}) H(\vec{r},\vec{r'},t), \tag{2.42}$$

defining the unknown function G_d in terms of the unknown function H, and then making the approximation $H(\vec{r},\vec{r'},t) \approx G_s(\vec{r}-\vec{r'},t)$. As a first step, motivated by the above discussion, one could alternatively approximate

$$H(\vec{r},\vec{r'},t) \approx X(|\vec{r}-\vec{r'}|,t;\mathrm{i}_{|\vec{r}-\vec{r'}|}). \tag{2.43}$$

where i is the shell of $g(r)$ indicated by the value of $|\vec{r} - \vec{r}'|$. Indeed, one could coarse grain to any desired degree - doing so exploits the observation that relative particle hops take (on average) particles from one shell to the next. This improves on the usual Vineyard approximation in two ways: first, the convoluting function for the radial distribution function is not identical to the single-particle time evolution, G_s, but rather is a genuine two-particle function, and second the convolution function itself varies with displacement. While the numerical work necessary to carry out this scheme is non-trivial, it may nevertheless prove useful to go beyond the venerable Vineyard approximation.

2.11 Summary

The second half of this chapter extended the two-particle NLE formalism to study the relative motion of two tagged particles over many correlated hopping and caging motions. This picture closely corresponds to the intuition embedded in the local-equilibrium approximation, that after a hop the fluid quickly re-equilibrates and tagged particles once again find themselves caged by local neighbors at a new spatial position. Qualitatively, this advance uncovers connection between dynamical statistics predicted by kinetically constrained models and microscopic structural correlations, for instance by finding persistence/exchange decoupling in close agreement with simulations. Working at a more sophisticated level of neighbor-loss creates a probe of the notion of irreversible particle motions that contribute to system relaxation and reversible hops that do not. Identifying such irreversible rearrangements has long been considered an especially thorny problem in understanding supercooled and glassy materials. Quantitative comparisons of our theoretical results with experiments and simulations are presently limited for several reasons, including the fact that our theory has been developed for 3D fluids while the former have been largely focused on 2D systems.

Future work could generalize the theory to two dimensions, and new 3D simulations could also be performed to more critically test our ideas. Additionally, while the focus here

has been on hard spheres for simplicity, extension to other potentials for spherical particles is in principle straightforward, as has been extensively achieved in diverse contexts based on the single particle NLE approach [121]. In colloidal systems, the presence of short-range attractive forces and/or shape anisotropy can result in qualitatively new behaviors, and it could be interesting to study such systems from the perspective proposed here. Additionally, at present the multi-state Markov framework has been developed only out to the third shell of the radial distribution function, but in principle it can be extended much further. In addition to suggesting a new approximation for the distinct van Hove function as outlined in Sec. 2.10, this would allow new questions to be addressed. A natural next step might be to continue building up the Markov model to fully address the problem of 2-particle "unbinding." That is, the process of two particles starting at contact and then separating to such a point that their motion becomes dynamically uncorrelated. The length and time scales over which that occurs are a key metric of dynamic heterogeneity.

Chapter 3

DYNAMICS IN SYSTEMS WITH TOPOLOGICAL CONSTRAINTS: THREE-DIMENSIONAL CROSSES

[1]This chapter forms a convenient bridge between the two parts of this thesis. The divisions are between glassy dynamics and macromolecular entanglement dynamics, between systems where equilibrium structure controls dynamical behavior and where the equilibrium structure is trivial and cannot influence the dynamics. The bridging systems discussed in this chapter are dense Brownian suspensions of non-rotating three-dimensional crosses composed of three orthogonal infinitely thin arms joined at their midpoint and interacting only via binary arm collisions. Such crosses were previously studied in a series of simulations, albeit using Newtonian instead of Brownian dynamics [122, 123]. The motivation behind the simulations was an attempt to get at one of the ongoing disputes in the glass-physics community mentioned in Chapter 1: whether it is possible to have purely dynamically-driven glass-like behavior, without complicated nonlinear feedback from liquid structure [8]. By construction the crosses are an ideal test system. They move isotropically as in the case of spherical particles, but as objects with zero excluded volume they always have trivial, ideal-gas-like structure and thermodynamics. Thus the only influence on their dynamics are the non-trivial topological constraints that arise from the uncrossability of the the cross arms. Not surprisingly, these topological constraints become crucially important for the system dynamics with increasing cross number density. As model glass-formers there are real differences between their phenomenology and that of real glass-formers, for instance the apparent absence of any decoupling phenomena [123].

Understanding the simulations from a theoretical perspective requires the ability to mi-

[1]This chapter contains text and figures reprinted with permission from *D. M. Sussman and K. S. Schweizer, Physical Review E* **83** *061501 (2011)*, Copyright APS 2011

croscopically account for the topological constraints represented here by arm-arm collisions; historically, describing such constraints has been an open and quite challenging problem [12]. Here we generalize a Gaussian theory that respects topological constraints to understand this model glass former. In later chapters we will exploit the combination of this formalism with the NLE to microscopically study a rather different phenomena: entangled polymer dynamics, where topological constraints show up as "entanglements."

3.1 Introduction

Understanding the uniquely slow motion of fluids of extended synthetic and biological macromolecules that experience dynamic constraints due to so-called "topological entanglements" is a problem of broad theoretical and practical interest. Topological constraints are the dynamical consequence of macromolecular connectivity and uncrossability, and they become relevant when polymers are large enough and/or dense enough. Their emergence is signaled by a dramatic change of the intermediate and macromolecular length scale viscoelasticity in a manner that generally depends on polymer architecture. The current theoretical state-of-the-art description for such systems is the phenomenological tube model and its many extensions [12, 15, 16], which have been quite successful in describing quiescent entanglement dynamics for various architectures (e.g., chains and many-armed stars). However, different extensions of the basic theory can sometimes appear to be mutually incompatible [23]. More importantly, the entire approach is phenomenological since a "confining tube," and the motional mechanisms to escape it (e.g., reptation or arm retraction), are postulated rather than derived from first principles. The need for foundational advances in our theoretical understanding of entangled polymers has been recently emphasized, and is being actively pursued via computer simulation [22, 23, 124].

In the glassy dynamics area, phenomenological kinetically constrained models (KCMs), formulated in terms of coarse-grained mobility fields (not molecules or forces) and postulated

rules, are able to account for many aspects of slow dynamics without invoking nontrivial structure or thermodynamics [75, 80]. In some sense, this is the spirit of the reptation/tube models which postulate the real space motional mechanisms that control entangled dynamics. However, it is unclear how to specifically coarse-grain any given system (let alone entangled polymer solutions or melts) onto a specific set of rules for the kinetic constraints within the KCM framework.

A different microscopic approach to describing entangled polymer liquids builds on the mode-coupling theory of glassy dynamics [125] generalized to linear chain polymers [85, 126]. The polymer mode coupling theory (PMCT) predicts many aspects of entangled polymer chain melt and solution dynamics rather well as a consequence of a specific macromolecular structural feature: the long range correlation hole which emerges due to segmental-scale finite excluded volume repulsions between connected chains that are "long enough." However, although this approach accounts for chain connectivity and local excluded volume constraints, its formulation at the pair correlation function level implies it does not explicitly respect the topological constraints that rigorously preclude chain crossing (or bond cutting). Such constraints can only be captured by higher order dynamical correlations. For this reason, the applicability of PMCT to the entanglement regime in molten polymers is controversial, particularly in light of simulation studies which find that two different systems with identical static structure, differing only in whether chain crossing is allowed or not, have globally different dynamical properties if the chains in the simulation are sufficiently long [127].

The only truly first-principles microscopic theory for fluids of strongly entangling objects formulated at the level of forces that does account for uncrossability is Szamel's dynamic mean-field theory [17, 24]. In this approach a solution of infinitely thin, non-rotating rigid rods was studied by self-consistently renormalizing exact binary collisions to take into account many-body effects. In the very long rod (or high reduced density) limit, the theory predicts not only tube localization and anisotropic motion, but also scaling laws for the tube diameter and long-time transverse diffusion constant, which all agree with the pre-

dictions of a reptationlike tube theory. Szamel's theory was later shown to be related to a MCT-based microscopic approach that goes beyond the standard "Gaussian approximation" of factorizing 4-point dynamic correlations into a product of 2-point functions. While the Szamel theory necessarily then invokes other uncontrolled approximations, keeping 4-point correlations is a necessary step to explicitly account for polymer uncrossability [128].

Recently there have been simulation studies of the system mentioned above: an ideal gas of non-rotating three-dimensional crosses, formed by three mutually orthogonal infinitely thin rods joined at their midpoints, studied as a function of density [122, 123]. Since these crosses have zero excluded volume their equilibrium structure and thermodynamics is trivial, and dynamics are controlled solely by the fact that two crosses cannot pass through each other. Standard MCT-based approaches, which account for dynamical correlations as a consequence of static correlations, are inapplicable to this system. Nevertheless, at a qualitative level many of the classic predictions of MCT are observed in the simulations [123], a provocative and puzzling situation that is not understood. In contrast to fragile glass formers, but consistent with the behavior of strong glass formers, the cross fluid simulations find little or no "decoupling" between translational diffusion and relaxation. This is consistent with the polymer physics view that entanglement dynamics is a "local" effect that occurs on the single-polymer length scale of interpenetrating objects, with center-of-mass diffusion and rotational (or longest) relaxation slaved to essentially the same elementary physical process [12].

Most recently, computer simulations were carried out on an extended tangent-bead model of a cross, i.e. a similar shape as discussed above but with finite excluded volume and where rotations were allowed [129]. Qualitative agreement between these simulations and the analogous topological model was found. This provides zeroth-order support for the classic polymer physics view that, when the aspect ratio of the macromolecule is large, local excluded volume effects are not the primary origin of the dynamical slowing-down phenomenon called "entanglement."

In this section we generalize the dynamic mean-field theory approach of Szamel to study a solution of non-rotating crosses. In addition to providing one more example in what is currently a vanishingly small library of molecular architectures for which topological constraints have been rigorously included at some nontrivial level, our hope is that the understanding gained will provide a foundation for deeper insight into the relationship between topological constraints and macromolecular dynamics. We shall also consider the consequences of a specific local-density-fluctuation effect in qualitatively modifying a dynamic arrest transition that we predict.

The rest of the chapter is organized as follows. In Sec. 3.2 we recall the relevant results of Szamel's dynamic mean-field theory for infinitely thin, non-rotating rods that provides the starting point for our work. This material will be recalled throughout much of the rest of this thesis as we discuss rods and chains in a variety of quiescent and rheological conditions. Section 3.3 generalizes this theory beyond the prior asymptotic analysis for rods, and also presents the new extension to treat non-rotating crosses. Results are derived for the long-time diffusion constant of the fluid, as well as a characteristic localization length of the entangled crosses in a dynamically frozen phase. Section 3.4 compares the results of these calculations with simulations, and proposes corrections from (Gaussian) local density fluctuations to explain the exponential suppression of diffusion and strong-glass behavior observed in the simulations. Section 3.5 contains a summary and discussion of this present work, and outline plans for future studies. Some technical details relating to the mathematical calculations in Sec. 3.3 are relegated to Sec. 3.6.

3.2 Dynamic Mean-Field Theory for Rods

3.2.1 Derivation of the Effective Diffusion Tensor

The mathematical framework underpinning the dynamic mean-field theory of Szamel is the N-particle generalized Smoluchowski equation [17, 24]. From this equation one can derive

an infinite (in the $N \to \infty$ limit) hierarchy of equations that relate the time evolution of the reduced m-body distribution function to an integral over the reduced $(m+1)$-body distribution function. Defining $\rho_1(\vec{r}_1, \vec{u}_1; t)$ as the density of a tagged rod at position $\vec{r}_1$ oriented along the unit vector $\vec{u}_1$, and $\rho_2(\vec{r}_1, \vec{u}_1, \vec{r}_2, \vec{u}_2; t)$ as the two-particle distribution of the tagged rod and a second rod, the first two levels of the infinite hierarchy are

$$\frac{\partial \rho_1}{\partial t} = \nabla_1 \cdot \left(\overleftrightarrow{D}_0 (\vec{u}_1) \cdot \nabla_1 \rho_1 - \overleftrightarrow{D}_0 (\vec{u}_1) \cdot \int d2 \, \overleftrightarrow{T} (12) \rho_2 \right), \tag{3.1}$$

$$\begin{aligned} \frac{\partial \rho_2}{\partial t} &= \left(\nabla_1 \cdot \overleftrightarrow{D}_0 (\vec{u}_1) \cdot \left[\nabla_1 - \overleftrightarrow{T} (12) \right] + \nabla_2 \cdot \overleftrightarrow{D}_0 (\vec{u}_2) \cdot \left[\nabla_2 - \overleftrightarrow{T} (21) \right] \right) \rho_2 \\ &\quad - \sum_{i=1}^{2} \nabla_i \cdot \overleftrightarrow{D}_0 (\vec{u}_i) \cdot \int d3 \, \overleftrightarrow{T} (i3) \rho_3, \end{aligned} \tag{3.2}$$

where for brevity we have suppressed the arguments of the reduced distribution functions and abbreviated the variables of integration as $d\# = (4\pi)^{-1} d\vec{r}_\# d\vec{u}_\#$. In the above equations $\overleftrightarrow{D}_0$ is the diffusion tensor in the limit of zero concentration which describes Brownian short time motion in an implicit solvent; it can be written in terms of the bare longitudinal and transverse diffusion coefficients of the rod as $\overleftrightarrow{D}_0 (\vec{u}_1) = D_{\parallel,0} \vec{u}_1^T \vec{u}_1 + D_{\perp,0} (\overleftrightarrow{I} - \vec{u}_1^T \vec{u}_1)$. Playing the role of "forces" in the Smoluchowski equations are the T-operators, which directly encode into the evolution equations for the reduced distribution functions the constraint that the infinitely hard rods cannot overlap and that rod-rod collisions occur impulsively. The T-operators can be thought of as exactly describing the classical mechanics of two colliding hard objects, and rigorously enforcing the uncrossability constraint at all times. For hard, infinitely thin rods of length L the T-operator is given by [130]

$$\overleftrightarrow{T} (12) = \hat{w}_{12} T(12) = \hat{w}_{12} \lim_{b \to 0^+} \delta(\vec{w}_{12} - b) \Theta(L/2 - |\alpha|) \Theta(L/2 - |\beta|), \tag{3.3}$$

where b is the radius of the rod, $\vec{w}$ is the component of the relative CM separation of the two rods, $\vec{r}$, along the vector $\vec{u}_1 \times \vec{u}_2$, and

$$\alpha = \frac{\vec{r}\cdot\vec{u}_1 - (\vec{r}\cdot\vec{u}_2)(\vec{u}_1\cdot\vec{u}_2)}{1-(\vec{u}_1\cdot\vec{u}_2)^2}, \tag{3.4}$$

$$\beta = \frac{\vec{r}\cdot\vec{u}_2 - (\vec{r}\cdot\vec{u}_1)(\vec{u}_1\cdot\vec{u}_2)}{1-(\vec{u}_1\cdot\vec{u}_2)^2}. \tag{3.5}$$

Two approximations are now introduced to self-consistently close the infinite hierarchy. First it is assumed that the right hand side of Eq. 3.1 can be written in terms of a tagged-rod current density, $\vec{j}$, that involves only one-body terms (not, that is, an explicit integral over two-body terms). Thus, one defines $\partial_t \rho_1 = -\nabla_1 \cdot \vec{j}(\vec{r}_1, \vec{u}_1; t)$, with a current density

$$\vec{j}(\vec{r}_1, \vec{u}_1; t) = -\overleftrightarrow{D}_e(\vec{r}_1, \vec{u}_1; t) * \nabla_1 \rho_1(\vec{r}_1, \vec{u}_1; t), \tag{3.6}$$

where the asterisk denotes a time- and space-convolution, and $\overleftrightarrow{D}_e$ is a non-local effective diffusion tensor. Second, a dynamic mean-field approximation is made to the second level of the Smoluchowski hierarchy. Specifically, the integral over the three-body term is dropped and the bare diffusion tensors are replaced with the same effective diffusion tensor defined above. Hence, based on this approximation, the time evolution of the reduced two-body distribution obeys the closed equation

$$\frac{\partial \rho_2}{\partial t} = \left(\nabla_1 \cdot \overleftrightarrow{D}_e(\vec{u}_1) * \left[\nabla_1 - \overleftrightarrow{T}(12)\right] + \nabla_2 \cdot \overleftrightarrow{D}_e(\vec{u}_2) * \left[\nabla_2 - \overleftrightarrow{T}(21)\right]\right) \rho_2. \tag{3.7}$$

This type of self-consistent approximation is in the spirit of ideal MCT in that three- and higher-body dynamic correlations are replaced by a self-consistent calculation involving only one- and two-body dynamics. From this perspective, one can perhaps view the present approach as a Gaussianlike dynamical theory, which is known to have strong limitations in its glassy ideal MCT context [45, 131].

With these approximations one can formulate a self-consistent equation for the effective diffusion tensor. The two-particle correlations,

$$\delta\rho_2(\vec{r}_1,\vec{u}_1,\vec{r}_2,\vec{u}_2;t) = \rho_2(\vec{r}_1,\vec{u}_1,\vec{r}_2,\vec{u}_2;t) - \rho g(\vec{r},\vec{u}_1,\vec{u}_2)\rho_1(\vec{r}_1,\vec{u}_1;t) \tag{3.8}$$

where ρ is the mean number density of the fluid and $g(\vec{r},\vec{u}_1,\vec{u}_2)$ is the equilibrium pair correlation function (equal to one almost everywhere for these objects with no excluded volume), can be written in terms of the single-particle current density. Equating the resulting expression with that of Eq. 3.6 yields, in Fourier-Laplace space,

$$\overleftrightarrow{D}_e^{-1}(\vec{k},\vec{u}_1;z) = \overleftrightarrow{D}_0^{-1}(\vec{u}_1) + \frac{\rho}{V}\int d2d\vec{r}_1 e^{-i\vec{k}\cdot\vec{r}_1}\overleftrightarrow{T}(12)\frac{1}{z-\Omega_e(12;z)}\overleftrightarrow{T}(12)g(\vec{r},\vec{u}_1,\vec{u}_2)e^{i\vec{k}\cdot\vec{r}_1}, \tag{3.9}$$

where z is the reciprocal time variable and the effective Smoluchowski operator is

$$\Omega_e(12;z) = \left(\nabla_{\vec{r}}\cdot\left[\overleftrightarrow{D}_e(\vec{u}_1;z) + \overleftrightarrow{D}_e(\vec{u}_2;z)\right]\cdot\left[\nabla_{\vec{r}} - \overleftrightarrow{T}(12)\right]\right). \tag{3.10}$$

A final technical approximation adopted to allow an analytic treatment is to ignore the $\vec{k}$-dependence of the effective diffusion tensors in Eq. 3.9 and set $\overleftrightarrow{D}_e(\vec{k},\vec{u}_1;z) \approx \overleftrightarrow{D}_e(\vec{k}=0,\vec{u}_1;z)$. Such an approximation, combined with the use of the same effective diffusion tensor to capture the effect of the surroundings on both the tagged and the untagged rod in Eq. 3.7, can be thought of as approximating the collective diffusion tensor by an effective self-diffusion tensor [17]. This is reminiscent of a Vineyard-type approximation for self- and collective propagators in simplified "naive" mode-coupling theories [31, 33]. Such a simplification might be argued to be reasonable in the present context since disentanglement dynamics are believed to be local, i.e. controlled by physics on the single macromolecule scale. Finally, using the above approximation and writing the equation in terms of the effective adjoint

Smoluchowski operator,

$$\Omega_e^\dagger(z) = \left(\left[\nabla_{\vec{r}} + \overleftrightarrow{T}\,(12) \right] \cdot \left[\overleftrightarrow{D}_e(\vec{u}_1; z) + \overleftrightarrow{D}_e(\vec{u}_2; z) \right] \cdot \nabla_{\vec{r}} \right), \tag{3.11}$$

so that no derivatives act on the pair correlation function, one arrives at the self-consistent equation defining the effective diffusion tensor:

$$\overleftrightarrow{D}_e^{-1}\,(\vec{u}_1; z) = \overleftrightarrow{D}_0^{-1}\,(\vec{u}_1) + \frac{\rho}{4\pi} \int d\vec{u}_2 d\vec{r}\; g(\vec{r}, \vec{u}_1, \vec{u}_2)\, \overleftrightarrow{T}\,(12) \frac{1}{z - \Omega_e^\dagger(z)}\, \overleftrightarrow{T}\,(12). \tag{3.12}$$

Two specific results that emerge from Eq. 3.12 are the long-time diffusion constant and the transverse localization length in a dynamically "frozen" phase of the rods. These are discussed in the following subsections.

3.2.2 Long-Time Transverse Diffusion

To derive the long-time transverse diffusion constant for rods (the longitudinal component always equals the bare value for infinitely thin needles), the $z = 0$ limit of Eq. 3.12 is considered. A function $f(\vec{r}, \vec{u}_1, \vec{u}_2)$ is introduced as the solution to the differential equation

$$\Omega_e^\dagger(z = 0) f(\vec{r}, \vec{u}_1, \vec{u}_2) \hat{w}_{12} = \hat{w}_{12} T(12), \tag{3.13}$$

and the long-time limit of the self-consistent equation can then be written as

$$\overleftrightarrow{D}_e^{-1}\,(\vec{u}_1; z = 0) = \overleftrightarrow{D}_0^{-1}\,(\vec{u}_1) + \frac{\rho}{4\pi} \int d\vec{u}_2 \hat{w}_{12}^T \hat{w}_{12} \int d\vec{r}\; g(\vec{r}, \vec{u}_1, \vec{u}_2) T(12) f(\vec{r}, \vec{u}_1, \vec{u}_2). \tag{3.14}$$

The differential equation defining f can be broken up into a singular part (proportional to the delta-function in $T(12)$) and a regular part. These equations are, respectively,

$$\begin{aligned} \hat{w}_{12} \cdot \left[\overleftrightarrow{D}_e (\vec{u}_1) + \overleftrightarrow{D}_e (\vec{u}_2) \right] \cdot \nabla_{\vec{r}} f(\vec{r}, \vec{u}_1, \vec{u}_2) &= 1, \\ \nabla_{\vec{r}} \cdot \left[\overleftrightarrow{D}_e (\vec{u}_1) + \overleftrightarrow{D}_e (\vec{u}_2) \right] \cdot \nabla_{\vec{r}} f(\vec{r}, \vec{u}_1, \vec{u}_2) &= 0 \end{aligned} \tag{3.15}$$

One can analytically solve for f by first changing from the Cartesian coordinate system to the "natural," non-orthogonal coordinates defined by the orientations of rods 1 and 2 ($\vec{r} \rightarrow \alpha\vec{u}_1 + \beta\vec{u}_2 + \gamma\hat{w}_{12}$), and then changing variables a second time to $x = A(\alpha + \beta)$, $y = B(\alpha - \beta)$, $z = c\gamma$, for certain constants A, B, and c. After these transformations the regular part of the differential equation for f is a Laplace equation, and the singular part corresponds to a boundary condition in a rhombus-shaped region of the $z = 0$ plane. If one specifies the remaining boundary conditions by assuming f vanishes outside of the rhombus in the $z = 0$ plane then a "hydrodynamic analogy" [17] holds: the differential equation and the boundary conditions are the same as for the velocity potential of an ideal, incompressible fluid in which a flat rhombus moves in a direction normal to its surface [132]. The spatial integral that needs to be performed in the self-consistent equation for the diffusion tensor is thus proportional to the kinetic energy of the fluid.

An analytic solution for the above problem does not exist, so as a final technical approximation the rhombus is replaced by an ellipse of equal area. The transverse component of the long-time diffusion tensor is then finally shown to be [17]

$$D_\perp = \frac{D_{\perp,0}}{1 + \rho L^3 F(D_\perp / D_{\parallel,0}) \sqrt{D_{\perp,0}^2 / D_\perp D_{\parallel,0}}}. \tag{3.16}$$

In the high-density regime this simplifies to

$$D_\perp \approx 18\pi \frac{D_{\parallel,0}}{(\rho L^3)^2}. \tag{3.17}$$

Remarkably, this is precisely the scaling predicted by reptation/tube theory (c.f. Eq, 1.1). The function $F(x)$ is a known (but complicated) monotonically decaying function between $x = 0$ and $x = 1$ [17], the details of which are dependent on the technical approximations used to solve the hydrodynamic problem outline above. However, the general form of the above equation for $D_\perp$ is independent of those details, and so for the high-density scaling the technical approximations used to solve for f affect only the numerical prefactor. As discussed by Szamel [17], one can further estimate the rotational relaxation time within the reptation/tube picture via a Fick's law type argument:

$$\tau_{rot} \propto L^2/D_{\parallel,0}. \tag{3.18}$$

3.2.3 Localization Length

To investigate the emergence of a new dynamical length scale, directly related to the effective radius of a confining tube in reptation theories, a slightly simpler system is considered: the rods are still assumed to be infinitely thin and non-rotating, but now their longitudinal motion is frozen. This procedure is precisely how modern simulations are now employed to perform so-called "primitive path" analysis to deduce the tube diameter [30, 124]. Formally, the $D_{\parallel,0} \to 0^+$ limit of Eq. 3.16 is taken, resulting in $D_\perp = D_{\perp,0}(1 - \rho \mathrm{L}^3/(\rho_c L^3))$, where $\rho_c L^3 \approx 9.29$. Thus, the theory predicts that above this critical density the system enters a dynamically frozen phase. To study the corresponding localization length, d, one assumes that for small z the transverse diffusion is $D_{\perp,e}(z) \approx zd^2/4$. The resulting self-consistent equation is

$$\frac{4}{d^2} = \frac{-\rho}{8\pi}(\overleftrightarrow{I} - \vec{u}_1^T\vec{u}_1) : \int d\vec{r}d\vec{u}_2 \overleftrightarrow{T}(12)(\Omega_{loc}^\dagger)^{-1} \overleftrightarrow{T}(12), \tag{3.19}$$

where the colon denotes a double contraction of tensorial indices and

$$\Omega_{loc}^\dagger = -1 + \frac{d^2}{4}\left[\nabla_{\vec{r}} + \overleftrightarrow{T}(12)\right] \cdot \left(2\overleftrightarrow{I} - \vec{u}_1^T\vec{u}_1 - \vec{u}_2^T\vec{u}_2\right) \cdot \nabla_{\vec{r}}. \tag{3.20}$$

Defining a function f_{loc} by

$$\Omega^{\dagger}_{loc} f_{loc} \hat{w}_{12} = \overleftrightarrow{T}(12) \tag{3.21}$$

and making variable changes analogous with those above, one finds f_{loc} obeys a Helmholtz equation with boundary conditions. Szamel solved the resulting problem in the $d \ll L$ limit. In this very high-density regime the boundary conditions in the $z = 0$ plane coming from the singular part of Eq. 3.21 can be taken to cover the entire plane, and thus the problem is effectively 1-dimensional. The asymptotic result is [17]

$$\frac{d}{L} \approx \frac{8\sqrt{2}}{\pi} \frac{1}{\rho L^3}. \tag{3.22}$$

This localization length, which has a purely *dynamic* origin, has the same asymptotic scaling as the tube radius in reptation theory where it is imagined to be (and is computed as) a *static* quantity.

3.3 Dynamic Mean-Field Theory for Crosses

3.3.1 Self-Consistent Equation and Technical Approximations

Extending the dynamic mean-field theory to treat infinitely thin, non-rotating crosses is conceptually straightforward, although a tractable model requires additional technical approximations. Describing for convenience the orientation of each cross by two variables, the orientation of an arbitrarily chosen arm $\vec{u}$ and an additional (scalar) angle γ to specify how the other two arms are oriented in the plane orthogonal to $\vec{u}$, the self-consistent equation for the diffusion tensor is quite similar to what was derived earlier:

$$\overleftrightarrow{D}_e^{-1}(\vec{u}_1, \gamma_1; z) = \overleftrightarrow{D}_0^{-1}(\vec{u}_1, \gamma_1) + \frac{\rho}{8\pi^2} \int d\vec{u}_2 d\gamma_2 d\vec{r}\ \overleftrightarrow{T}(12) \frac{1}{z - \Omega^{\dagger}_e(z)} \overleftrightarrow{T}(12). \tag{3.23}$$

For brevity we have omitted the pair distribution function, as it is again equal to one almost everywhere. The major difference is that the T-operators in Eq. 3.23, including the one implicit in $\Omega_e^\dagger(z)$, are now T-operators for crosses. Thinking of each cross as being composed of three mutually orthogonal rods of length L joined at their midpoints, it is easiest to express the cross T-operator as a sum over the nine rod T-operators corresponding to the nine possible rod-rod collisions that could be involved in the interaction of two crosses. So, if $i = 1, 2, 3$ labels the rods composing the tagged cross and $j = 1, 2, 3$ labels the rods of the second cross, then

$$\overleftrightarrow{T}\,(12) = \sum_{i,j=1}^{3} \overleftrightarrow{T}_{rod}(ij). \tag{3.24}$$

Our method of analyzing Eq. 3.23 mirrors what was done for rods and involves defining a set of functions f_{ij} as the solutions to the differential equations

$$\Omega_e^\dagger(z) f_{ij}(\vec{r}, \vec{u}_i, \vec{u}_j)\hat{w}_{ij} = T_{rod}(ij)\hat{w}_{ij}, \tag{3.25}$$

where $\hat{w}_{ij} = \vec{u}_i \times \vec{u}_j / |\vec{u}_i \times \vec{u}_j|$ and the adjoint effective Smoluchowski operator,

$$\Omega_e^\dagger(z) = \left(\left[\nabla_{\vec{r}} + \overleftrightarrow{T}\,(12) \right] \cdot \left[\overleftrightarrow{D}_e(\vec{u}_1; z) + \overleftrightarrow{D}_e(\vec{u}_2; z) \right] \cdot \nabla_{\vec{r}} \right), \tag{3.26}$$

contains the cross T-operator, not that of a rod.

As motivation for the additional technical approximations needed in this section, at $z = 0$ the integral in Eq. 3.23 is expressed as

$$\frac{-\rho}{8\pi^2} \int d\vec{u}_2 d\gamma_2 d\vec{r} \sum_{i,j,k,l=1}^{3} \hat{w}_{ij}^T \hat{w}_{kl} T_{rod}(kl) f_{ij}(\vec{r}, \vec{u}_i, \vec{u}_j). \tag{3.27}$$

Since the $\hat{w}_{ij}$ are not orthogonal, there are two sources of "off-diagonal" contributions in the above expression that, for tractability, we will ignore. First, the left hand side of Eq. 3.25 defining the f_{ij} contains contributions from multiple rod T-operators. This prevents the

neat division of the differential equation for each of the f_{ij} into simple regular and singular parts, and thus the exploitation of the hydrodynamic analogy. Second, there are the obvious integrals to be done in Eq. 3.27 when $(ij) \neq (kl)$.

The neglect of the first type of off-diagonal term in the definition of the f_{ij} is related to a physical assumption that only one pair of arms is involved in the collision of two crosses. That is, f_{ij} describes the influence of a collision of rods i and j on the two colliding crosses. Dropping the off-diagonal terms in Eq. 3.25 assumes the collision of rods i and j is unaffected by the collision of any other rod pairs. In a sense, this amounts to ignoring those events that involve multiple-arm collisions, and in fact this type of event was disregarded in simulations of the crosses [122, 123] since it is expected to make a contribution of measure zero for these objects. Having made this assumption, the f_{ij} are straightforward to define (as demonstrated in the next sections), but there are still the off-diagonal integrals in Eq. 3.27, and the above argument says nothing about whether those should equal zero. We have numerically computed these integrals under the assumption that the first type of off-diagonal contribution is negligible, and find they do indeed vanish. This seems to be a consequence of the fact that although the $\hat{w}_{ij}$ are not orthogonal for any arbitrary relative orientation of the crosses, on average they are. That is, a full angular average over $\hat{w}_{ij} \cdot \hat{w}_{kl}$ is equal to zero when $(ij) \neq (kl)$. Thus, the neglect of this second type of off-diagonal contribution is apparently intimately related to the geometry of the objects we are studying, a fact that limits the range of shapes that this formalism can be easily extended to cover.

3.3.2 Long-Time Diffusion Constant

After making the approximations described above in Eq. 3.23, the long-time, $z = 0$ limit of the self-consistent equation for the diffusion tensor can be written as

$$\overleftrightarrow{D}_e^{-1}(\vec{u}_1, \gamma_1; z) = \overleftrightarrow{D}_0^{-1}(\vec{u}_1, \gamma_1) - \frac{\rho}{8\pi^2} \int d\vec{u}_2 d\gamma_2 d\vec{r} \sum_{i,j=1}^{3} \hat{w}_{ij}^T \hat{w}_{ij} T_{rod}(ij) f(ij). \tag{3.28}$$

The diffusion tensor for these objects is isotropic, and so the long time diffusion constant is $D = \overleftrightarrow{D}_e : \overleftrightarrow{I}\ /3$. Under the angular averaging over $\vec{u}_2$ and ν in the integral of Eq. 3.28 all nine of the rod-rod pairs are equivalent, so to evaluate the second term on the right-hand side of Eq. 3.28 we simply work out the total integral for any one pair of rods and multiply by nine. The coordinate system is first changed as $\vec{r} \to \alpha\hat{u}_i + \beta\hat{u}_j + \gamma\hat{w}_{ij}$, followed by a second variable change to

$$x = \sqrt{\frac{1+\mu}{2}}(\alpha+\beta),\ y = \sqrt{\frac{1-\mu}{2}}(\alpha-\beta),\ z = \gamma, \tag{3.29}$$

where $\mu = \vec{u}_i \cdot \vec{u}_j$. The f_{ij} are then defined by the differential equations

$$\begin{aligned} \left(\frac{\partial^2}{\partial x^2} + \frac{\partial^2}{\partial y^2} + \frac{\partial^2}{\partial z^2}\right) f_{ij}(x,y,z) &= 0, \\ \frac{\partial}{\partial z} f_{ij}(x,y,z) &= \frac{1}{2D}, \end{aligned} \tag{3.30}$$

where the second equation holds on the rhombus in the $z = 0$ plane which is the $x,\ y$ transformation of the square defined by $|\alpha|,\ |\beta| \leq L/2$. This is precisely the hydrodynamic analogy mentioned in the previous section, with the above two equations describing the velocity potential of a rhombus moving with velocity $1/2D$ normal to its surface through an ideal, incompressible fluid. Replacing the rhombus with an equal-area ellipse (with minor and major axes $g = L\sqrt{(1-\mu)/\pi},\ h = L\sqrt{(1+\mu)/\pi}$) we exploit this hydrodynamic analogy to approximate

$$-\int_{\text{rhombus}} dxdy\ f_{ij}(x,y,z=0) \approx -2D \int_{\text{ellipse}} dxdy\ f_{ij}\frac{\partial f_{ij}}{\partial z}. \tag{3.31}$$

The negative of the second integral is twice the kinetic energy of the fluid through which the ellipse moves [132], and so using that result we get

$$-\int dxdydz\ T_{rod}(ij)f_{ij} \approx \frac{2L^3(1-\mu^2)}{3D\sqrt{\pi}}\psi(\mu), \tag{3.32}$$

where

$$\psi(\mu) = \left(\int_0^{\pi/2} d\theta \sqrt{(1-\mu)\sin^2\theta + (1+\mu)\cos^2\theta}\right)^{-1}. \tag{3.33}$$

Since the same analysis applies for any pair of $i,\ j$, we are essentially done. Contracting both sides of Eq. 3.28 with $\overset{\leftrightarrow}{I}$ /3, accounting for the Jacobian determinants of the variable transformations employed, and making use of the approximate hydrodynamic result in Eq. 3.32, the final expression for the long-time diffusion constant for an ideal gas of these crosses is:

$$\frac{1}{D} = \frac{1}{D_0} + \frac{\rho L^3}{D\sqrt{\pi}}\int_{-1}^{1} d\mu\ (1-\mu^2)\psi(\mu). \tag{3.34}$$

Numerically performing the last integral yields

$$\frac{D}{D_0} = 1 - \frac{\rho}{\rho_c} \quad , \qquad \rho_c L^3 = 2.06. \tag{3.35}$$

Thus, much like the "longitudinally frozen rod" calculation, above a critical dimensionless density the system enters a dynamically frozen state. Note the critical density is a factor of $\sim$4.5 smaller than required for transverse localization of rods, but the functional dependence of the diffusion constant on reduced density is identical.

3.3.3 Full Localization Length

To study cross localization above the critical density, we write for small reciprocal time z the 3-dimensional isotropic diffusion constant as $D(z) \approx zr_{loc}^2/6$. With this expression for

$D(z)$, contracting both sides of Eq. 3.23 with $\overleftrightarrow{I}$ /3 yields

$$\frac{6}{r_{loc}^2} = \frac{-\rho}{24\pi^2} \overleftrightarrow{I} : \int d\vec{u}_2 d\gamma_2 d\vec{r} \overleftrightarrow{T}(12)(\Omega_{loc}^{\dagger})^{-1} \overleftrightarrow{T}(12), \tag{3.36}$$

where

$$\Omega_{loc}^{\dagger} = -1 + \frac{r_{loc}^2}{3}\left[\nabla_{\vec{r}} + \overleftrightarrow{T}(12)\right] \cdot \overleftrightarrow{I} \cdot \nabla_{\vec{r}}. \tag{3.37}$$

The functions $g_{ij}(\vec{r}, \vec{u}_i, \vec{u}_j)$ are now defined as the solutions to $\Omega_{loc}^{\dagger} g_{ij} \hat{w}_{ij} = \hat{w}_{ij} T_{rod}(ij)$, and we make all the same approximations involving the neglect of "off-diagonal" terms as when calculating the diffusion constant. The resulting self-consistent equation for r_{loc} is then

$$\frac{1}{r_{loc}^2} = \frac{-\rho}{144\pi^2} \overleftrightarrow{I} : \int d\vec{u}_2 d\gamma_2 d\vec{r} \sum_{i,j=1}^{3} \hat{w}_{ij}^T \hat{w}_{ij} T_{rod}(ij) g_{ij}(\vec{r}, \vec{u}_i, \vec{u}_j). \tag{3.38}$$

As mentioned in Sec. 3.2, the earlier rod work evaluated the analogous spatial integral over g_{ij} only in the high-density limit [17, 24]. With the aid of a slightly different technical approximation on the g_{ij} we are able to extend the analytic calculation of r_{loc} to any density. The details of the analysis are given in Sec. 3.6, where the full self-consistent equation for the localization length is shown to be

$$\frac{L^2}{r_{loc}^2} = \frac{6\pi\rho L^3}{4\sqrt{3}} \frac{L^2}{r_{loc}^2} F\left(\frac{L}{r_{loc}}\right), \tag{3.39}$$

where

$$F(x) = \int_0^1 \int_0^{\infty} \frac{J_1(m) J_0(rm)}{\sqrt{m^2 + x^2}} r dm dr = \frac{x - I_1(2x) + L_1(2x)}{2x^2}. \tag{3.40}$$

Here, J_0 and J_1 are Bessel functions, I_1 is the first modified Bessel function of the first kind, and L_1 is the first modified Struve function.

The inset of Fig. 3.1 shows an order parameter plot for the inverse localization length predicted by Eq. 3.39 versus the dimensionless density. In the highly localized limit ($L >>$

r_{loc}) the asymptotic result is

$$r_{loc} = \frac{4\sqrt{3}}{3\pi\rho L^2}. \tag{3.41}$$

For positive x the function $F(x)$ monotonically decays from $4/3\pi$ at $x = 0$ and asymptotically approaches $F(x) \sim 1/2x$ for $x \gg 1$. This behavior implies there is a critical density, $\rho_c L^3 = \sqrt{3}/2$, below which the only solution to Eq. 3.39 is $r_{loc} \to \infty$. In addition, the large-x scaling of $F(x)$ ensures that our result for the localization length has the same high-density scaling as in Eq. 3.22. This estimate of the critical density is not identical to that in Eq. 3.35 due to a different set of boundary conditions used in the mathematical analysis. As discussed in Sec. 3.6, applying the same boundary conditions as in Sec. 3.3.2 here would lead to a predicted critical density of $\rho_c L^3 = \sqrt{3}$, but would leave the $L >> r_{loc}$ behavior unchanged. The quantitative similarity ($\sim$ 15% numerical prefactor deviation) of this estimate of the critical density compared to Eq. 3.35, together with the recovery of the same high-density scaling of the localization length, suggests that the technical approximations adopted to extend the calculation beyond the high-density regime are not severe. The fact that the predicted critical density is not identical when determined from the diffusion constant or the localization length "routes" is a common inconsistency of approximate theories, including the simplified MCT and density functional approach [33]. Note that the monotonic decay of $F(x)$ implies an unusual behavior for the localization length. Rather than jumping from zero to a finite value at some critical density, as might be expected for a transition to an amorphous glassy state, instead the localization length continuously decreases from infinity as the critical density threshold is crossed. Qualitatively, this prediction of localization on a scale much larger than the cross itself near the critical density seems unlikely, and the stability of this result to improvements in the theory and/or its mathematical analysis is presently unknown.

For interest, we also mention that the mathematical techniques used to solve for the localization length outside of the asymptotic regime do not depend on the diffusion tensor

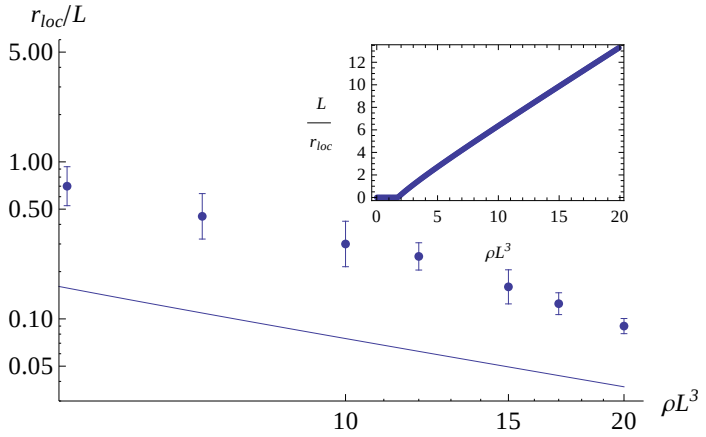

Figure 3.1: Log-log plot of r_{loc} vs. dimensionless density. Circles identify the value of the root-mean-square displacement at the inflection point of the MSD vs time plots, taken from the data in Ref. [123]. The inset shows the order parameter plot of inverse localization length vs dimensionless density.

being isotropic, nor on any of the technical approximations related to the shape of the three-dimensional crosses. As such, with only a few changes we can extend the localization length calculation for longitudinally frozen rods beyond the asymptotic limit considered by Szamel. Starting from Eq. 3.19 and applying the techniques outlined in Sec. 3.6, the result is the extremely similar-looking

$$\frac{L^2}{r_{loc}^2} = \frac{\pi\rho L^3}{4\sqrt{2}}\frac{L^2}{r_{loc}^2}F\left(\frac{L}{r_{loc}}\right), \tag{3.42}$$

where the function $F(x)$ is the same as defined in Eq. 3.40. Note that taking the $r_{loc} \ll L$ limit of this function, for which $F(x) \approx 1/2x$, exactly recovers the high-density result in Eq. 3.22 derived by Szamel.

A calculation of the localization length for a system of rods that are assumed to diffuse *isotropically* in three dimensions can be similarly performed, resulting in

$$\frac{L^2}{r_{loc}^2} = \frac{\pi\rho L^3}{6\sqrt{3}}\frac{L^2}{r_{loc}^2}F\left(\frac{L}{r_{loc}}\right). \tag{3.43}$$

Here, the critical density is $\rho_c L^3 = 9\sqrt{3}/2$, a factor $3^2 = 9$ larger than for the cross, and the

asymptotic limit of the localization length is

$$r_{loc} = \frac{12\sqrt{3}}{\pi\rho L^2}. \tag{3.44}$$

An essential point of the above analysis is that with (i) the neglect of the second type of off-diagonal terms in Eq. 3.27, and (ii) the assumption of isotropic diffusion in either 2 or 3 dimensions, the scaling predictions of the theory for both the localization length and long-time diffusion constant becomes architecture independent. For the special class of shapes where approximation (i) is valid (linear rods and crosses composed of 2 or 3 orthogonal rods), shape only changes the predicted value of the critical density. Thus, plotting our results against ρ/ρ_c would collapse the curves corresponding to different shapes or different dimensionalities of isotropic diffusion. On the other hand, anisotropic diffusion can lead to different scaling laws, as seen in Sec. 3.2.2.

3.4 Comparison with Simulation

3.4.1 Diffusion Constant at Low Densities and the Localization Length

Since the present theory permits not just a scaling analysis but a quantitative computation of the diffusion constant and dynamical localization length at all densities, we wish to compare with the molecular dynamics simulations in Refs. [122,123]. However, these simulations were performed using purely Newtonian dynamics, while our theory adopts a Brownian description of short time motion (as relevant for a solution) and a Newtonian (impulsive) description of cross-cross interactions. The implications of different microscopic dynamics have been studied in depth in the glassy dynamics area, both theoretically [133] and via simulation [134]. Physically, one expects that the slow long-time diffusion and its associated transient localization length are not sensitive to the form of the short time dynamics (Newtonian versus

Brownian). Indeed, for systems with non-trivial equilibrium structure it has been shown that the ideal MCT non-ergodicity transition is independent of whether the microscopic dynamics are Newtonian or Brownian [133]. Moreover, computer simulations find that while the short-time (β-) relaxation of a simple liquid is sensitive to the chosen microscopic dynamics, in the glassy regime the long-time (α-) relaxation is essentially independent of them [134].

Given the above discussion, the only point that needs to be addressed to confront our theoretical results with simulation is how the diffusion constant is nondimensionalized. In Refs. [122, 123] the diffusion constant is reported in units of a bare diffusivity, $D_0 = \sqrt{kTL^2/m}$, which is the average thermal velocity (the initial velocity of the simulated crosses was drawn from a Maxwell-Boltzmann distribution) multiplied not by the mean free path, but rather by the characteristic size of the cross. Thus, at high densities D/D_0 has the meaning of the average time for a cross to move a fixed distance at zero density (in this case, inertially) relative to the average time for a cross to move the same distance via the long-time relaxation process (i.e., diffusively due to inter-cross collisions) at a nonzero density. More generally, the time scales for Brownian and Newtonian athermal systems are related by a density-dependent scaling factor. At low densities this factor varies as the inverse of density and hence formally diverges as $\rho \to 0$ since a diffusion constant is not defined based on Newtonian dynamics in this limit. However, at high densities, when inter-particle collisions become dominant, the scale factor becomes increasingly density-independent (since the mean-free path becomes relatively short). It is in this sense that with increasing density the simulation D/D_0 becomes analogous to the D/D_0 we compute for our Brownian system.

Given this ambiguity in the density-dependent time rescaling between Newtonian and Brownian systems, our result for the diffusion constant, $D/D_0 = 1 - \rho/\rho_c$, is difficult to directly compare with the simulation. On the one hand, it is reasonable that at low densities the diffusion constant decays linearly for the Brownian system, and our result of $D/D_0 = 0.51$ at $\rho L^3 = 1$ is within an order of magnitude of the simulation result of $D/D_0 = 0.34$. This is a qualitatively sensible result since at that density inter-cross collision effects are important

and thus the time re-scaling factor is expected to be of order unity. However, the prediction of a critical density at which the diffusion literally goes to zero is expected to be an artifact of the theoretical approximations made. The simulations do clearly show a rapidly decreasing diffusion constant, but one that is non-zero at all densities simulated (up to $\rho L^3 = 20$, well beyond our $\rho_c L^3$). Naively, it is perhaps not surprising that the dy mic mean-field theory predicts this kind of non-ergodicity transition, given that it has been shown to be related to a MCT [128], and MCT is well known to predict spurious non-ergodicity transitions [11]. However, this dynamical transition was not guaranteed to occur for the present topological model. Indeed, it does not exist for the system of anisotropically diffusing infinitely thin rods. Miyazaki and Yethiraj [128] have demonstrated that Szamel's dynamic mean-field theory is recovered in a MCT approach only by going beyond the Gaussian approximation (commonly taken to be the origin of the ideal MCT non-ergodicity transition) by including 4-body dynamical correlations that explicitly encode information about polymer uncrossability. Just as in the MCT work, then, we interpret our critical density as signaling the onset of a new microscopic transport mechanism. Moreover, the density value predicted seems reasonably consistent with the simulation finding of a change in density dependence of D around $\rho L^3 \sim 2$.

Below we will describe a simple model for calculating the diffusion constant beyond the critical density based on finite-sized density fluctuations of the local environment of the cross. However, we first compare our prediction for the localization length in Eq. 3.39 with the simulation data. Of course, the simulations do not have an exact analog of our localization length, since at all densities the dynamics are ergodic. Nevertheless, we can take inspiration from the glassy physics field where a theoretically predicted localization length is viewed as a transient quantity. As was found based on the nonlinear Langevin equation (NLE) theory of hard-sphere suspensions, we expect that the localization length should be qualitatively related to the dynamic localization length defined to be the root-mean-square displacement of the tagged particle at the inflection point of a log-log plot of the mean-square

displacement (MSD) vs. time [53]; equivalently, this corresponds to the displacement at the time of most anomalous non-Fickian diffusion. We employ the MSD simulation results in Figure 2 of Ref. [123] to extract this transient localization length, and the results are shown in Fig. 3.1. Within the simulation error bars, this transient localization length and its theoretical analog are nearly proportional, with the latter being a factor of ~ 3 smaller than the former. We note that the data at low densities are quite noisy; the minimum value of the slope is well-determined but the precise time at which it occurs is relatively uncertain. However, at the highest densities the scaling of the simulation data agrees unambiguously with the predicted localization length, with both length scales proportional to the inverse of the dimensionless density.

3.4.2 Local Density Fluctuations and Activated Diffusion

The prediction of strict arrest beyond a critical density very likely reflects a dynamical crossover to a rare-event mechanism of transport that relies on some kind of finite length scale fluctuation process not captured in a Gaussian theory. For glassy systems, MCT has been generalized to address noise-driven activated barrier hopping within the NLE approach based on the concept of a dynamic free energy or confinement potential [31, 32]. For these topologically entangled objects, though, we find that the dynamic free energy has an *infinite* barrier, as seen in Fig. 3.2 (the NLE extension for topological systems will be discussed in much greater detail in Chapter 4, where it is more relevant). This results from the detailed technical approximations we made, which break down at very large displacements. As seen in the inset to Fig. 3.2, the barrier to move a fixed amount generally grows linearly at large displacements, and so we intuitively expect an exponential suppression of the diffusion constant. To motivate an alternate model, consider the following argument.

Schematically, we start with the NLE equation of motion,

$$\zeta_s \frac{d}{dt} r - \frac{\partial}{\partial r} F_{dyn} + \delta f = 0, \tag{3.45}$$

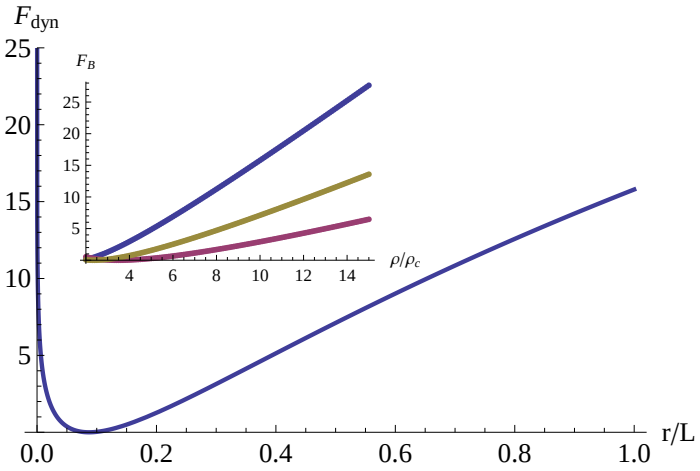

Figure 3.2: F_{dyn} vs scalar displacement for crosses at $\rho/\rho_c = 10$. Inset. Height of the dynamic free energy relative to the well depth at (top to bottom) $r = L$, $r = L/2$, and $r = L/\sqrt{12}$ (the cross radius of gyration).

and take the $r(t \to \infty)$ limit. For large cross displacements ($r \gg L$) we enter the easily-analyzed asymptotic regime of the free energy corresponding to the $x \ll 1$ limit of $F(x)$, which in the case of isotropic diffusion reduces to $\beta F_{dyn}(r \gg L) \approx -3\ln(r/L) + 3\rho\ln(R)/\rho_c$. Thus the NLE is

$$\zeta_s \frac{dr}{dt} = \frac{3}{r}\left(1 - \frac{\rho}{\rho_c}\right) + \delta f(t) \tag{3.46}$$

$$\to \zeta_s \frac{d}{dt} r^2 = 6\left(1 - \frac{\rho}{\rho_c}\right) + 2r\delta f(t). \tag{3.47}$$

We then take an ensemble average (where, by orthogonality of the noise and the position variable the last term vanishes) and integrate in time to get our expression for the mean-squared displacement. This equation for the MSD is nonsensical if the term in parentheses is negative, so we assume that the mean-squared displacement is simply zero for $\rho > \rho_c$, in the sense that $\langle r^2(t \to \infty)\rangle$ is some time-independent constant. On the other hand, if we assume that the system includes density fluctuations that occasionally bring the local

density below the critical density then we have

$$\langle r^2(t)\rangle = 6D_s \left\langle \left(1 - \frac{\rho}{\rho_c}\right) \right\rangle t, \tag{3.48}$$

where the diffusion constant D_s has been introduced to give proper units. The key point is that we can relate an effective diffusion constant to an ensemble average over density fluctuations, $\langle 1 - \rho/\rho_c \rangle$.

Another motivation to study such density fluctuations comes by recalling some of the approximations made in the derivation of the self-consistent equation for the diffusion tensor in Sec. 3.2. In particular, the effective collective-diffusion tensor (generally length scale dependent) was replaced by the effective self-diffusion analog. In kinetic theories of fluids with volume-excluding particles such approximations are usually found to be reasonably accurate up to length scales associated with the cage of nearby particles [33]. In effect, we can imagine that our theory accurately predicts the diffusion constant in some finite region of the fluid surrounding the tagged cross. On this scale there are spontaneous density fluctuations, which thereby modulate the strength of confining entanglements. Such an idea is common in diverse theories of structural glasses, where activation barriers are distributed due to finite-size thermodynamic fluctuations of the relevant property (e.g., configurational entropy in the random first order phase transition theory [98], density fluctuations in the NLE theory [93], free volume [135], etc.). Interestingly, for entangled polymers it is known based on primitive path analysis that what is meant by a localization length (tube diameter) is not uniquely defined even at the level of a single polymer, but rather has a distribution arising from the underlying static disorder [30, 124].

What we specifically assume, then, is that Eq. 3.35 correctly describes the diffusion constant in regions with local density as high as the critical density, and that in higher-density regions the local diffusion is zero. The ideal gas of crosses is subject to finite-size Gaussian density fluctuations, and we expect their lifetime is effectively as long as the

relaxation timescale of the diffusing crosses. Hence, we estimate the self-diffusion constant at any density by averaging Eq. 3.35 over the probability that a region of a fluid with mean density $\bar{\rho}L^3$ has local density ρL^3 :

$$\frac{D(\bar{\rho}L^3)}{D_0} = \int_0^{\rho_c} \left(1 - \frac{\rho}{\rho_c}\right) \mathcal{P}(\rho, \bar{\rho})\ d\rho, \tag{3.49}$$

with

$$\mathcal{P}(\rho, \bar{\rho}) = \sqrt{\frac{2V_c}{\pi\bar{\rho}}} \frac{1}{1 + \mathrm{Erf}(\sqrt{\bar{\rho}V_c/2})} \exp\left(\frac{-V_c}{2\bar{\rho}}(\rho - \bar{\rho})^2)\right). \tag{3.50}$$

The amplitude of the square density fluctuations follows from the bulk compressibility, $\left\langle(\delta\rho)^2\right\rangle = \rho S_0/V_c$, where for an ideal gas of crosses of trivial structure $S_0 = 1$ [93]. We emphasize these regions of high and low density are not envisioned as literally static, but rather fade in and out as a result of dynamic fluctuations on the macromolecular scale with the low-density regions having a lifetime comparable to or longer than the timescale for a cross to diffuse through them. This picture is partially motivated by the physical interpretation of the cross simulations [123].

We do not have a rigorous criterion for choosing the size of the critical region, beyond the earlier observation that we expect our approximations are reasonable up to a length scale commensurate with the cage of nearby particles (a macromolecular scale for the present system). A natural choice for the critical volume is a sphere that would enclose one cross, $V_c = \pi L^3/6$. This choice for the critical volume is in some ways analogous to the idea that "tube escape" for rods or chain polymers — the onset of center-of-mass Fickian diffusion — takes place after a displacement equal to the end-to-end vector [12]. In any case, with this V_c our theory predicts an exponential decay of the diffusion constant at high densities, qualitatively similar to the observation that the simulation data is well fit by $D \sim \exp(-0.42\rho L^3)$ for $\rho L^3 > 5$. Figure 3.3 compares the results of this finite-sized density-fluctuation calculation for the diffusion constant with the simulation data. We note that Eq. 3.49 is fairly

sensitive to the chosen size of the critical volume, and that very modestly increasing the size of the critical region to be a sphere of radius $0.57L$ results in a quantitatively good fit of the simulation data at all densities beyond the critical density. Significantly, Fig. 3.3 also shows that the exponential fit used to describe the simulation data at high densities works quite well nearly all the way down to the theoretically predicted critical or onset density of $\rho L^3 \approx 2$. This finding is again consistent with the expectation that the crossover density to an ultra-slow activated-like relaxation regime should be independent of the microscopic dynamics (Brownian versus Newtonian).

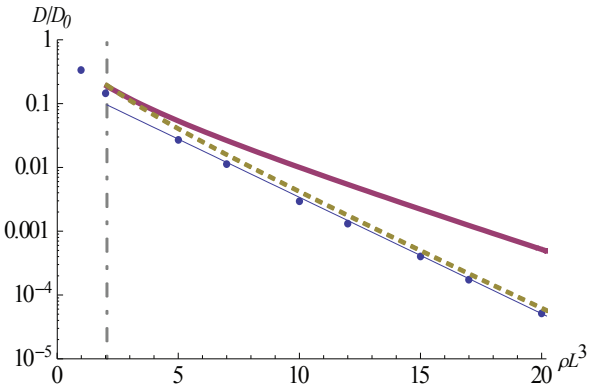

Figure 3.3: Log-linear plot of the three-dimensional cross long-time isotropic diffusion constant vs. dimensionless density. Points are simulation data from Ref. [123], the thin curve is the exponential fit to the simulation date at high densities [123], the solid curve is the prediction of Eq. 3.49 with $V_c = \pi L^3/6$, and the dashed curve is Eq. 3.49 with finite-size density fluctuations in a critical region of radius $0.57L$. The vertical dash-dotted line is our theoretical estimate of the critical dimensionless density.

In the context of this model of diffusion via rare local density fluctuations we can use our result for the long-time diffusion constant to also estimate the relaxation time in a Fickian manner as $\tau_r(\rho) \approx L^2/D(\rho)$. Although a somewhat trivial estimate, this is consistent with the observed strong-glass-former behavior this system exhibits [122], as by construction it avoids any translation-relaxation decoupling. In this way the relaxation time grows exponentially with ρL^3 at high reduced densities.

Finally, given how radically this model of local density fluctuations alters the entangled cross dynamics (effectively destroying a non-ergodicity transition), it is worth mentioning

that when applied to other models or systems characterized by a non-zero diffusivity at all densities the consequences of local density fluctuations are much less pronounced. For example, using the same Eq. 3.50 for local density fluctuations but studying their effect on the transverse diffusion constant under the assumption of anisotropic rod motion as originally derived by Szamel — Eq. 3.16 — we find that the high-density "reptationlike" power-law scaling is perfectly preserved. Additionally, the model becomes much less sensitive to the choice of critical volume. Taking the radius of the critical region to be anything from $0.4L$ to $5L$, not only is the asymptotic scaling prediction unchanged, but the value of $D_\perp/D_{\perp,0}$ predicted by the local-density-fluctuation model is almost quantitatively identical to Eq. 3.16 over the full range of density.

3.5 Summary and Discussion

We have generalized the dynamic mean-field theory of Szamel [17] for infinitely thin non-rotating rods to a new model architecture, non-rotating three-dimensional crosses, and also extended the calculation of the localization length for rods beyond the high-density asymptotic regime. The initial theoretical results for the long-time diffusion constant and the localization length of crosses are in reasonable agreement with simulation. Key technical approximations include a neglect of certain types of off-diagonal mathematical terms, as well as minor modifications to the boundary conditions of Laplace and Helmholtz differential equations. Numerical analysis indicates that many of these technical approximations are of a relatively minor quantitative nature.

More severe, though, is the essentially local range of validity that the approximation of the collective-diffusion tensor by an effective self-diffusion tensor imposes on the resulting self-consistent equation for $\overleftrightarrow{D}_e$. This limitation was invoked as physical motivation for going beyond the literal non-ergodicity transition the theory predicts, reasoning that we have neglected rare fluctuations that would permit long-time transport processes. We then

imagined partitioning the fluid into regions, with size comparable to the crosses themselves, of local density drawn from the thermodynamically correct ideal gas Gaussian distribution. Although the prediction for the long-time diffusion constant obtained by averaging over these regions was sensitive to the choice of critical region size, natural choices for this size led to excellent reproduction of the simulated long-time diffusion at densities above $\rho_c L^3$. The resulting picture of mobile regions of enhanced motion diffusing through the fluid is perhaps qualitatively reminiscent of the general ideas underlying kinetically constrained models [75, 80]. And, indeed, in addition to the generic "strong glass former" behavior observed, some of the more advanced features seen in the simulations seem consistent with facilitated models, such as the behavior of the multi-point dynamical susceptibility [123]. However, connecting either our theory or the simulations concretely to a specific KCM is an open and daunting challenge.

The simulations have also quantified many other dynamical features of the gas of ideal crosses that we hope to address in future work. In particular, the wavevector-dependent incoherent dynamic scattering function, mean-square displacement, nongaussian parameter, and dynamical susceptibility all present more sensitive tests of the fundamental validity of our theoretical approach. Particularly desirable, although presenting significant theoretical challenges, would be a self-consistent treatment of the collective diffusion tensor, rather than the simple approximation of it by the self-diffusion tensor. In addition to resolving the unphysical nonergodicity transition in a consistent manner rather than via the physically-motivated but heuristic approach of Sec. 3.4, this might shed light on the origin of a dynamical length scale much larger than the system size discovered in the simulations [123]. Building directly on the progress reported in this article, the extension of the NLE approach to the topological entanglement problem, combined with Brownian trajectory simulations, is presently under study as a means of accomplishing many of the above goals. We anticipate that this advance will also be relevant to the quiescent and stress-driven dynamics of entangled liquids of non-rigid polymers including semiflexible F-actin, random coils, and star branched

polymers.

3.6 Analytic Solution for the Localization Length

In this section we expand on our presentation of the approximations and mathematical techniques used to derive an analytic expression for the localization length of fluids of crosses at all density. The starting point is Eq. 3.38,

$$\frac{1}{r_{loc}^2} = \frac{-\rho}{144\pi^2} \overset{\leftrightarrow}{I} : \int d\vec{u}_2 d\gamma_2 d\vec{r} \sum_{i,j=1}^{3} \hat{w}_{ij}^T \hat{w}_{ij} T_{rod}(ij) g_{ij}(\vec{r}, \vec{u}_i, \vec{u}_j), \tag{3.51}$$

where the g_{ij} are the solutions to

$$\left(-1 + \frac{r_{loc}^2}{3} \left[\nabla_{\vec{r}} + \overset{\leftrightarrow}{T}(12) \right] \cdot \overset{\leftrightarrow}{I} \cdot \nabla_{\vec{r}} \right) g_{ij} \hat{w}_{ij} = \hat{w}_{ij} T_{rod}(ij). \tag{3.52}$$

Since each of the arm-arm interactions is identical after angular averaging, the sum is replaced by nine times the value of the integral for any particular g_{ij}. Performing one of the angular integrals and contracting the identity matrix with $\hat{w}_{ij}^T \hat{w}_{ij}$ gives

$$\frac{1}{r_{loc}^2} = \frac{-\rho}{8\pi} \int d\vec{u}_2 d\vec{r}\, T_{rod}(ij) g_{ij}(\vec{r}, \vec{u}_i, \vec{u}_j). \tag{3.53}$$

We now transform the coordinate system as $\vec{r} \to \alpha \hat{u}_i + \beta \hat{u}_j + \gamma \hat{w}_{ij}$, and change variables to

$$x = \sqrt{\frac{3(1+\mu)}{2L^2}}(\alpha + \beta),\ y = \sqrt{\frac{3(1-\mu)}{2L^2}}(\alpha - \beta),\ z = \frac{\sqrt{3}}{L}\gamma, \tag{3.54}$$

which have Jacobians of $|J_1| = \sqrt{1-\mu^2}$ and $|J_2| = L^3/(3\sqrt{3}\sqrt{1-\mu^2})$, respectively, for $\mu = \hat{u}_i \cdot \hat{u}_j$. Defining a new function $G(x,y,z) = \frac{r_{loc}^2}{L\sqrt{3}} g_{ij}(x,y,z)$, in terms of these variables

G satisfies the equations

$$\begin{aligned}\left(\frac{\partial^2}{\partial x^2}+\frac{\partial^2}{\partial y^2}+\frac{\partial^2}{\partial z^2}\right)G(x,y,z) &= \left(\frac{L}{r_{loc}}\right)^2 G(x,y,z)\\ \frac{\partial}{\partial z}G(x,y,z) &= 1,\end{aligned} \tag{3.55}$$

where the second equation is a boundary condition that holds on a rhombus of area $A_{rhomb.} = 3\sqrt{1-\mu^2}$ in the $z=0$ plane.

To make further progress, two new technical approximations are invoked, both related to the boundary conditions that G must satisfy. Recall that in the computation of the long-time diffusion constant the rhombus in the $z=0$ plane was replaced with an equal-area ellipse. Here we replace the rhombus by a circle of equal area, that is, a circle with radius $a=\sqrt{3\sqrt{1-\mu^2}/\pi}$. If we were to make this approximation in the calculation of the long-time diffusion constant, analysis shows the critical density becomes $\rho_c L^3 = 1.94$ instead of $\rho_c L^3 = 2.06$. We thus conclude that for the isotropically diffusing crosses this first different approximation is of very minor quantitative importance. Second, and more importantly, rather than assuming that the function G vanishes in the $z=0$ plane outside of the circle (the "hydrodynamic-like" choice of boundary conditions), we instead assume it is the z-derivative of G that vanishes in that region of the plane. Numerically carrying out these calculations with the hydrodynamic-like boundary conditions at several densities indicates that the implications of this choice are irrelevant at very high densities (i.e., when r_{loc} is small), and make only a minor quantitative difference as long as the self-consistent equation ultimately results in $r_{loc} \lesssim L$. At larger r_{loc} the difference is more significant, though, so that when using the hydrodynamic boundary conditions the critical density increases by a factor of two: $(\rho_c L^3)_{hd} = \sqrt{3}$.

Proceeding, we transform to scaled cylindrical coordinates, $x = ar\cos\theta$, $y = ar\sin\theta$, $z = aZ$, and find the problem reduces to that of a spatial integral over a function with circular symmetry satisfying the Helmholtz differential equation $\nabla^2 G = (L/r_{loc})^2 G$, whose

boundary conditions are a Z-derivative of $\partial_Z G = 1/a$ inside a circle of radius 1 in the $Z = 0$ plane and zero outside of it in the plane. The generic solution for G given the circular symmetry of the problem is

$$G(r, Z) = \int_0^\infty A(n) e^{nZ} J_0\left(r\sqrt{n^2 - \frac{L^2}{r_{loc}^2}}\right) \, dn, \tag{3.56}$$

where the $A(n)$ are the weighting coefficients that will be determined by the boundary conditions. Changing variables to $m = \sqrt{n^2 - L^2/r_{loc}^2}$, one obtains

$$\left.\frac{\partial G(r, Z)}{\partial Z}\right|_{Z=0} = \int_{iL/r_{loc}}^\infty mA(m) J_0(rm) \, dm = w(r), \tag{3.57}$$

where $w(r) = 1/a$ for $r < 1$ and $w(r) = 0$ otherwise. The variable of integration in Eq. 3.57 runs from iL/r_{loc} to 0 along the imaginary axis, and then from 0 to ∞ along the real axis. Recall that the present goal is only to choose the factors $A(m)$ such that the boundary condition is satisfied. Assuming that this can be achieved with $A(m) = 0$ for all $m \notin \mathbb{R}$, we exploit standard Bessel function orthogonality relations by multiplying both sides of Eq. 3.57 by $rJ_0(rm')$ and integrating over r. We then find that the boundary conditions can be satisfied by choosing

$$A(m) = \begin{cases} J_1(m)/am & m \geq 0 \\ 0 & \mathrm{Im}(m) \neq 0 \end{cases} \tag{3.58}$$

Thus, the solution to the given Helmholtz problem in cylindrical polar coordinates is

$$G(r, z) = \frac{1}{a} \int_0^\infty \frac{J_0(rm) J_1(m) e^{z\sqrt{m^2 + L^2/r_{loc}^2}}}{\sqrt{m^2 + L^2/r_{loc}^2}} dm. \tag{3.59}$$

Substituting this result into Eq. 3.53, integrating over both sides of the circle, and taking into account the factors arising from all the variable transformations, the self-consistent equation

for the localization length finally reads

$$\frac{L^2}{r_{loc}^2} = \frac{6\pi\rho L^3}{4\sqrt{3}} \frac{L^2}{r_{loc}^2} F\left(\frac{L}{r_{loc}}\right), \tag{3.60}$$

where

$$F(x) = \int_0^1 \int_0^\infty \frac{J_1(m)J_0(rm)}{\sqrt{m^2+x^2}} r dm dr = \frac{x - I_1(2x) + L_1(2x)}{2x^2}. \tag{3.61}$$

Chapter 4

RIGID RODS: EQUILIBRIUM DYNAMICS

4.1 Introduction

[1]As briefly discussed in Chapter 1, achieving a first-principles theoretical understanding of the spectacular viscoelasticity of strongly entangled synthetic and biological polymer liquids is a very challenging problem in time-dependent statistical mechanics [12]. The key concept that must be addressed is the emergence of "topological constraints," the dynamical consequence of polymer connectivity and uncrossability in liquids of interpenetrating macromolecules that are sufficiently large and/or concentrated. For many decades the primary theoretical approach for linear entangled polymer solutions and melts has been the phenomenological reptation-tube model [12, 15]. Its central postulate is that the dynamical effect of many surrounding macromolecules on single polymer motion can be represented as an effectively static confining potential that strictly prohibits motion transverse to the polymer backbone beyond a mesoscopic length scale, the tube diameter. At zeroth order, this single material parameter is assumed to fully quantify the lateral dynamical constraints and consequences of intermolecular forces. For random-coil chains, long-time transport proceeds via one-dimensional curvilinear diffusion, and scaling laws close (but not equal to) experimental observations are predicted. In practice, many competing non-reptative processes are of high importance (e.g., contour-length fluctuations, dynamic dilution, and constraint release), all of which reduce motional anisotropy and are required to understand experi-

[1]This chapter contains text and figures reprinted with permission from: *D. M. Sussman and K. S. Schweizer, Physical Review Letters.* **107** *078102 (2011)*, Copyright APS 2011; *D. M. Sussman and K. S. Schweizer, Journal of Chemical Physics* **135** *131104 (2011)*, Copyright AIP 2011; *D. M. Sussman and K. S. Schweizer, Macromolecules* **45** *3270 (2012)*, Copyright ACS 2012

ment [16].

The reptation-tube approach has been undeniably very useful for polymers of diverse architecture. However, the confining tube concept is a bold ansatz that is not deduced from the statistical mechanics of the fundamental inter-polymer interactions in a first-principles, self-consistent manner. Recent perspective and opinion articles [22, 23] emphasize that the tube model lacks a microscopic foundation, and a "bottom up" conceptual breakthrough on the crucial tube diameter length scale is needed to address open questions, some of which were mentioned in chapter 1. In particular we recall the following: (i) What is the nature of an entanglement and of the tube confinement field, and can it be derived theoretically? (ii) What is the microscopic basis of constraint release? (iii) Can the connection between polymer chemistry, concentration, and the tube diameter be understood from first principles? (iv) How does the branch point in a star polymer diffuse subject to the tube constraint?

Several recent studies, both experimental and simulation-based, have challenged the commonly postulated one-parameter harmonic approximation for the tube confinement field. Particularly relevant for our work are experiments and complementary theoretical work on entangled solutions of the semiflexible biopolymer F-actin [25, 26], and simulations of F-actin and rigid rod model polymers [27]. By studying displacement distributions at intermediate times, or averaging mean-square displacements over many trajectories, these studies have revealed an effective transverse confining potential that is significantly softer than harmonic. Evidence of strong anharmonic softening has also been observed in DNA solutions [28] and in primitive-path simulations of entangled flexible chain melts [29, 30]. Hybrid Monte-Carlo/primitive-path simulations of polyethylene melts have found highly non-gaussian distributions of effective tube diameters [136, 137], which could be indicative of an underlying softer-than-harmonic confining potential. We note that some alternative simulation methods of extracting probability distributions of the radial displacement of a monomer from its mean position in a flexible polymer melt appear to find an effectively harmonic confinement potential over the (limited) displacement range studied [138], but the

bulk of the evidence points towards ubiquitous anharmonicities. The latter are relevant for a deeper understanding of quiescent non-reptative motions involving lateral motion, and even more importantly can have qualitative consequences for large-deformation response.

We have very recently proposed a new microscopic approach for the quiescent and stressed dynamics of entangled, non-rotating rigid rod fluids [139, 140]. Its centerpiece is the self-consistent construction of an anharmonic transverse confinement (tube) field based solely on topological entanglements. Under quiescent equilibrium conditions, the theory is consistent with the DE model for how the tube diameter and rotational/transverse center-of-mass (CM) diffusion constants vary with rod density. It also predicts a strongly anharmonic confinement field with key features in quantitative accord with highly entangled F-actin experiments [25,139], and qualitatively consistent with chain melt simulations [29] and DNA solution measurements [28]. The single most important feature of our theory is that the dynamic entanglement force localizing a polymer in a tube is of finite strength, which results in multiple novel consequences for the role of applied stress on the tube diameter, diffusion, and relaxation [140] that are not anticipated by existing reptation-tube models.

In this chapter we present a detailed exposition of our theory. Questions (i)-(iii) above are directly addressed, and question (iv) was partially treated in Chapter 3 by studying fluctuation-driven activated hopping of the center-of-mass of topologically entangled 3D crosses, a potential analog for the branch-point motion of rigid six-arm stars [141]. Our aim is a unified presentation of the new ideas; we thus repeat some of the material from Sec. 3.2, but supplemented with additional physical discussion.

The rest of the chapter — in which we present the key theoretical aspects for both quiescent and stressed conditions (self-diffusion constant; tube diameter; dynamic confinement potential; incorporation of stress and orientation; and the concept and definition of "microscopic yielding") — is organized as follow. Sections 4.2 and 4.3 review some of the more technical aspects of the prior work we build on, deriving expressions for the long-time diffusion constant and a characteristic localization length for a needle in a tube, respectively.

These first two sections also comment on the limitations of approximations used and present a different analysis of the critical entanglement density than was presented in Chapter 3. Section 4.4 combines this formal starting point with the NLE theory to construct the tube confinement potential, and Sec. 4.5 discusses stochastic trajectory simulations on the quiescent transverse confinement potential to gain additional insight into the anharmonicities of the tube. Section 4.6 generalizes the confinement potential to treat applied shear stress. Section 4.7 allows for the confinement potential to be modified by an anisotropic distribution of needle orientations, important both in considering liquid crystalline order but also of potential relevance for our later rheological applications, where external deformations can induce orientational order on the polymer system. Section 4.8 briefly summarizes the material in the chapter.

4.2 Quiescent Long-Time Diffusion

Our starting point is the self-consistent dynamic mean-field theory of Szamel, which describes a solution of infinitely thin, non-rotating rigid rods or needles of length L [17, 24]. The rod fluid has ideal-gas structure and thermodynamics, so the dynamics are determined *solely* by topological constraints. For heavily entangled rods that are allowed to rotate the long-time rotational diffusion constant is proportional to its transverse CM diffusion analog ($D_\perp$), and is inversely related to the terminal rotational relaxation time [17]; thus, knowledge of $D_\perp$ captures all long-time dynamics [17,24]. Polymer connectivity and uncrossability are exactly enforced at the two-rod-collision level, in contrast to the usual mode coupling theories which do not rigorously forbid polymer backbone crossing at any level due to a factorization of multipoint dynamic correlations [128]. In both Szamel's and our approach, beyond-two-body effects are described via a self-consistent renormalization. A schematic illustrating the spirit of the approach is presented in Fig. 4.1.

The Szamel theory is formulated in terms of coupled equations for reduced distribution

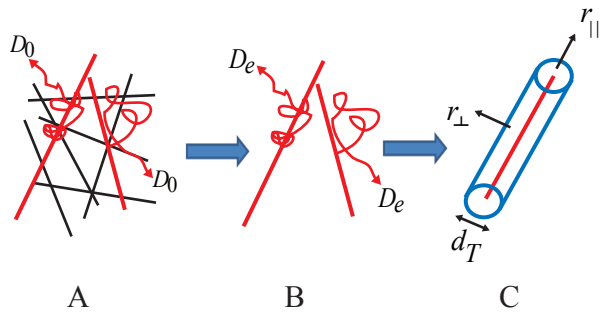

Figure 4.1: (a) Uncrossable rods diffusing with bare dynamics in between impulsive hard-core collisions. (b) Self-consistent renormalization of many-body effects into an effective diffusion tensor at the two-rod-dynamics level. (c) Analysis of the short-time structure of $\overleftrightarrow{D}_e$ determines the full transverse dynamic tube confinement potential.

functions, ρ_i, derived from the N-particle generalized Smoluchowski equation, the first two of which are [24]

$$\frac{\partial \rho_1}{\partial t} = \nabla_1 \cdot \left(\overleftrightarrow{D}_0 (\vec{u}_1) \cdot \nabla_1 \rho_1 - \overleftrightarrow{D}_0 (\vec{u}_1) \cdot \int d2 \, \overleftrightarrow{T} (12) \rho_2 \right), \tag{4.1}$$

$$\begin{aligned} \frac{\partial \rho_2}{\partial t} &= \left(\nabla_1 \cdot \overleftrightarrow{D}_0 (\vec{u}_1) \cdot \left[\nabla_1 - \overleftrightarrow{T} (12) \right] + \nabla_2 \cdot \overleftrightarrow{D}_0 (\vec{u}_2) \cdot \left[\nabla_2 - \overleftrightarrow{T} (21) \right] \right) \rho_2 \\ &\quad - \sum_{i=1}^{2} \nabla_i \cdot \overleftrightarrow{D}_0 (\vec{u}_i) \cdot \int d3 \, \overleftrightarrow{T} (i3) \rho_3, \end{aligned} \tag{4.2}$$

where the arguments of the reduced distribution functions have been suppressed, the variables of integration are denoted as $dl = (4\pi)^{-1} d\vec{r}_l d\vec{u}_l$, and $\vec{u}_l$ is the orientation of rod l. Here $\overleftrightarrow{D}_0$ is the bare diffusion tensor in the limit of zero concentration describing Brownian short-time motion in an implicit solvent, which in terms of the longitudinal and transverse components can be written as $\overleftrightarrow{D}_0 (\vec{u}_1) = D_{\parallel,0} \vec{u}_1^T \vec{u}_1 + D_{\perp,0} (\overleftrightarrow{I} - \vec{u}_1^T \vec{u}_1)$. The key features are the T-operators, which exactly describe binary collisions and rigorously enforce rod uncrossability at all times. They correspond to an impulsive "entanglement force" perpendicular to the plane formed by the orientations of the two colliding rods. For hard, infinitely thin rods

of length L the T-operator is [130]

$$\overleftrightarrow{T}(12) = \hat{w}_{12} T(12) = \hat{w}_{12} \lim_{b \to 0^+} \delta(\vec{w}_{12} - b)\Theta(L/2 - |\alpha|)\Theta(L/2 - |\beta|) \tag{4.3}$$

where $b \to 0$ is the rod radius, $\vec{w}$ is the component of the relative CM separation of the two rods, $\vec{r}$, along the vector $\vec{u}_1 \times \vec{u}_2$, and

$$\alpha = \frac{\vec{r} \cdot \vec{u}_1 - (\vec{r} \cdot \vec{u}_2)(\vec{u}_1 \cdot \vec{u}_2)}{1 - (\vec{u}_1 \cdot \vec{u}_2)^2}, \quad \beta = \frac{\vec{r} \cdot \vec{u}_2 - (\vec{r} \cdot \vec{u}_1)(\vec{u}_1 \cdot \vec{u}_2)}{1 - (\vec{u}_1 \cdot \vec{u}_2)^2}. \tag{4.4}$$

The infinite dynamic hierarchy is closed by writing a self-consistent equation for $\overleftrightarrow{D}_e$, a non-local in space and time effective diffusion tensor. This is achieved by dropping the integral over the three-body term in Eq. 4.2, and replacing the bare diffusion tensor with this same effective self-diffusion tensor. By comparing the definition of the test-rod current with a derived expression, one obtains in Fourier-Laplace space the self-consistent equation [17]:

$$\overleftrightarrow{D}_e^{-1}(\vec{u}_1; z) = \overleftrightarrow{D}_0^{-1}(\vec{u}_1; z) + \frac{\rho}{4\pi} \int d\vec{u}_2 d\vec{r} g(\vec{r}, \vec{u}_1, \vec{u}_2) \overleftrightarrow{T}(12) \frac{1}{z - \Omega_e^\dagger(z)} \overleftrightarrow{T}(12). \tag{4.5}$$

Here z is the reciprocal time variable, $g(\vec{r}, \vec{u}_1, \vec{u}_2)$ is the 2-rod equilibrium pair correlation function (equal to unity almost everywhere for an isotropic solution of infinitely thin needles), and the effective adjoint Smoluchowski operator is given by:

$$\Omega_e^\dagger(z) = \left[\nabla_{\vec{r}} + \overleftrightarrow{T}(12)\right] \cdot \left[\overleftrightarrow{D}_e(\vec{u}_1; z) + \overleftrightarrow{D}_e(\vec{u}_2; z)\right] \cdot \nabla_{\vec{r}}. \tag{4.6}$$

Two main approximations have been used to derive this expression: (i) neglect of the $\vec{k}$-dependence of the effective diffusion tensor, $\overleftrightarrow{D}_e(\vec{k}, \vec{u}_1; z) \approx \overleftrightarrow{D}_e(\vec{k} = 0, \vec{u}_1; z)$, and (ii) use of the same effective diffusion tensor to capture the effect of the surroundings on both the tagged and the untagged rod. Together these approximations can be thought of as replacing the wavevector-dependent collective diffusion tensor by an effective self-diffusion

tensor [17], reminiscent of a Vineyard-like approximation successfully employed in glassy-dynamics contexts [31,33]. Szamel's theory has been shown to be related to a sophisticated version of a MCT-like approach that avoids factorizing four-point correlation functions into products of two-point correlations [128], the crucial feature required to capture dynamical polymer backbone uncrossability.

Equations 4.5, 4.6 are infinite order in the effective diffusion constant and T-operator. Hence, an infinite sequence of correlated collisions of a tagged rod with its surroundings is approximately taken into account. If the effective diffusion constant in Eq. 4.6 is replaced by its dilute solution value, then an independent binary collision (IBC) theory [6] is recovered, akin to dynamic second-order perturbation theory. The IBC description can describe the initial consequences of inter-rod collisions, but cannot predict tube localization, a non-perturbative phenomenon.

The self-consistent dynamic mean field theory makes several notable predictions. The most elementary comes from asking what happens if one assumes that rods diffuse isotropically. By ignoring the distinction between transverse and longitudinal motion, and employing the same mathematical methods discussed previously [17,141], we find $D/D_0 = 1-(\rho/\rho_{c,iso})$, corresponding to a non-ergodicity transition at $\rho_{c,iso}L^3 \approx 18.2$. This quenching of isotropic motion, or formation of a "topological glass," occurs at an eminently reasonable density in the sense that it requires $(18.2/L^3)(\pi L^3/6) \approx 10$ interpenetrating rods to occupy a sphere of diameter L. Of course, such an isotropic glass is not expected to be realized since the system can exploit anisotropic modes of transport.

Carrying out the full anisotropic calculation, wherein $D_{||} = D_{||,0}$ (unconstrained longitudinal reptation) and $D_\perp$ is self-consistently computed [24], agreement with the asymptotic high-density scaling law of the static tube-reptation theory is obtained, $D_\perp/D_0 \propto (\rho L^3)^{-2}$. A full numerical analysis from the IBC to the reptative scaling regime yields a dynamical crossover at $\rho_e L^3 \approx 10.1$ [139]. Recall that the underlying physics controlling long-time transverse center-of-mass and rotational diffusion is qualitatively identical: each proceeds

via a small lateral displacement or a rotation when a rod reptates out of its local tube [17]. The practical estimate of the entanglement crossover above agrees quite well with what is predicted if reptation as a mode of motion is removed by hand. Doing so (i.e., setting $D_{||,0} = 0$) one finds $D_\perp/D_0 = 1 - (\rho/\rho_c^*)$, corresponding to strict transverse localization at $\rho_c^* L^3 = 9.29$ [17]. After rescaling ρ by its crossover value the full anisotropic theory agrees quantitatively with simulations for both the rotational and transverse translational diffusion constants over the entire density range [20, 21], as seen in Fig. 4.2.

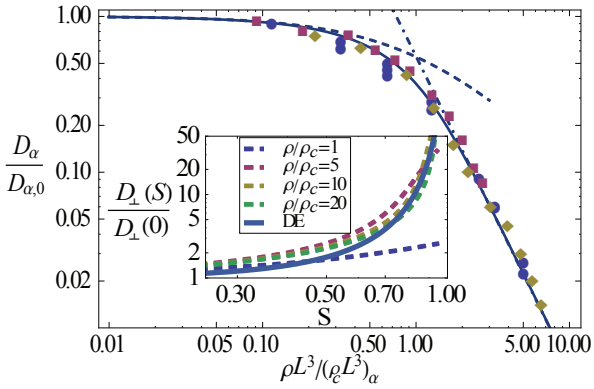

Figure 4.2: Dimensionless diffusion constant vs. rescaled density. Solid line: $D_\perp/D_{\perp,0}$ as predicted by Eq. (15) of Ref. [24], with $\rho_c L^3 \approx 10.1$. Circles, squares and diamonds are simulation data for $D_r/D_{r,0}$ taken from Fig. (9.7) of Ref. [20] and $D_r/D_{r,0}$ and $D_\perp/D_{\perp,0}$ from [21], with $\rho_c L^3 \approx 34,\ 55,$ and 23, respectively. Dashed and dot-dashed lines are the IBC and high-density scaling. Inset: Normalized transverse diffusion versus orientational order parameter at several reduced densities, along with the Doi-Edwards (DE) result [12].

4.3 Gaussian Transverse Localization

The possibility of tube localization can be addressed by taking the low-frequency limit of the effective self-diffusion tensor, $D_e(z \to 0)$, and assuming Gaussian localization characterized by a mean harmonic localization radius, r_l. A self-consistent expression for the transverse localization length (half of the mean tube diameter) can thus be derived [17]:

$$\frac{4}{r_l^2} = \frac{-\rho}{8\pi}(\overleftrightarrow{I} - \vec{u}_1^T \vec{u}_1) : \int d\vec{r} d\vec{u}_2 \overleftrightarrow{T}(12)(\Omega_{loc}^\dagger)^{-1} \overleftrightarrow{T}(12), \tag{4.7}$$

where the colon denotes a double contraction of tensorial indices, and

$$\Omega^{\dagger}_{loc} = -1 + \frac{{r_l}^2}{4}\left[\nabla_{\vec{r}} + \overleftrightarrow{T}\,(12)\right] \cdot \left(2\,\overleftrightarrow{I} - \vec{u}_1^{T}\vec{u}_1 - \vec{u}_2^{T}\vec{u}_2\right) \cdot \nabla_{\vec{r}}. \tag{4.8}$$

Equation 4.7 is derived by analyzing a system where the longitudinal (reptative) motion of all rods is quenched. Conceptually this is similar to how simulations perform primitive path analyses to deduce the tube diameter [124]. We re-emphasize that no equilibrium structural-correlation information enters Eqs. 4.7, 4.8, since thermodynamically the rods are an ideal gas. Note that since r_l and the T-operators enter the adjoint "localized" Smoluchowski operator, Eq. 4.7 corresponds to an infinite-order re-summation of the multiple correlated collisions which are the microscopic origin of tube localization.

With a particular choice of boundary conditions for the Helmholtz differential equation (discussed in Sec. 3.6) used to solve Eq. 4.7 for r_l, transverse localization is found to emerge at a critical density $\rho_c L^3 = 3\sqrt{2}$ [141]. The numerical discrepancy between this critical density and the entanglement crossover for the long-time diffusion constant discussed above is partly a result of the technical mathematical approximations used to solve the Helmholtz equation, and partly a result of the inaccuracy of the theory at very large displacements [141]. Specifically, at ρ_c the theory predicts that the inverse localization length increases continuously from zero, and $r_l^{-1} \ll L^{-1}$ is precisely the regime in which the Vineyard-like replacement of the collective-diffusion tensor with a k-independent self-diffusion tensor is expected to be least accurate. However, we emphasize that the theory predicts sensible localization lengths ($r_l < L$) at all rod densities greater than $2.3\rho_c \approx \rho_e$. Our focus here is $\rho \gg \rho_c$, where the theory is not sensitive to the approximations discussed above. In the heavily entangled limit one finds [24] $d_t \equiv 2r_l = 16\sqrt{2}/\left(\pi\rho L^2\right)$. This is in agreement with the DE scaling law for the tube diameter [12], and is quantitatively close to the result found in simulations of rotating and translating needles at high density [142], $d_t \approx 5/\rho L^2$.

4.4 Quiescent Transverse Confinement Potential

Starting from the microscopic dynamics of a fluid of entangled needles of length L, the previous sections derive results for the long-time longitudinal and transverse diffusion constants of a tagged needle and for a localization length that characterizes the spatial extent of fluctuations transverse to the needle when it is inside the confining tube (i.e., a tube diameter). The theory predicts the distinctive connection between the transverse localization length and long-time transport, $D_\perp/D_{\parallel,0} \propto (\rho L^3)^{-2} \propto (d_t/L)^2$, which is also the result of the real space reptation-tube ansatz for entangled rod solutions. The key result for our purposes here is Eq. 4.7, which is a self-consistent equation for the localization length r_l assuming purely gaussian fluctuations. The above approach has been qualitatively extended [139] to create a microscopic theory of the full dynamic transverse confinement potential as a function of the instantaneous CM transverse displacement, $r_\perp$, that goes beyond a Gaussian description. We start by re-writing the explicit form of Eq. 4.7 as a force balance:

$$f(r_l) = \frac{2k_BT}{r_l} - 2r_lK_\perp(r_l) = 0, \tag{4.9}$$

$$K_\perp(r_l) = \frac{\pi\rho L k_BT}{8\sqrt{2}}(L/r_l - I_1(2L/r_l) + \mathbf{L}_1(2L/r_l)) \equiv \frac{\pi\rho L k_BT}{8\sqrt{2}}g(L/r_l), \tag{4.10}$$

where $\mathbf{L}_1$ (I_1) is the first Struve function (modified Bessel function of the first kind). Equation 4.9 suggests interpreting the derived tube localization result as a competition between a delocalizing entropic driving force and a localizing entanglement force. The fact that the entanglement force takes the form of a highly nonlinear spring with the displacement-dependent coefficient $K_\perp(r_l)$ is an early hint that the confining tube is more complicated than a simple harmonic potential. The basis for reinterpreting the localization length equation as a force balance stems from recent theoretical work in glass physics, where a self-consistent localization result of the form of Eq. 4.7 emerges from a dynamical-Gaussian-approximation treatment of kinetic vitrification within an amorphous solid model [31]. It is well known for

structural glasses that such strict-localization results are an artifact of the Gaussian approximations used (common to both ideal MCT and the Szamel approach), which only address the stability of kinetic arrest to small-amplitude fluctuations and ignore large-amplitude, ergodicity-restoring, barrier hopping events. We thus use some of the microscopic methods and concepts developed in the glass physics community for describing such large-amplitude events to probe the stability of the confining tube to non-gaussian fluctuations.

One such highly developed microscopic approach to treat activated dynamics at the single-particle level is the nonlinear Langevin equation (NLE) theory [31,32]. Its key insight is to interpret Eq. 4.9 as a force balance at the instantaneous tagged-particle-displacement level, coupled with a non-ensemble-averaged version of the local equilibrium concept, so that the tagged needle stochastically samples transverse displacements in a way consistent with the forces prescribed by Eq. 4.9. Predicting tagged particle trajectories requires additional noise and short-time friction terms, and in the overdamped limit this leads to the stochastic NLE for the transverse rod center-of-mass displacement

$$-\zeta_s \frac{dr_\perp}{dt} - \frac{\partial}{\partial r_\perp} F_{dyn}(r_\perp) + \delta f_s = 0, \tag{4.11}$$

where ζ_s is the short-time friction constant, δf_s the corresponding white noise random force, and

$$F_{dyn}(r_\perp) = \int_{r_l}^{r_\perp} f(r) dr \tag{4.12}$$

is a "dynamic free energy." This corresponds to the transverse tube potential that captures the effects of entanglement forces, including an exact accounting of two-rod uncrossability. Unlike in the phenomenological tube theory, the resulting confinement field is not a static, geometrically determined object, but is rather the consequence of dynamic intermolecular correlations [32].

We note that the NLE framework has been derived from microscopic statistical mechanics for sphere fluids, and can describe activated relaxation via highly non-gaussian trajectory

fluctuations [32]. The underlying physical ideas are not tied to the precise nature of the Gaussian self-consistent theory that serves as its starting point (here, Eq. 4.7), and thus can be applied to topologically entangled liquids. For numerical convenience, in subsequent calculations $g(x)$ in Eq. 4.10 is replaced with a Pade approximation that correctly recovers its asymptotic behavior:

$$\frac{r^2}{2L^2} g\left(\frac{L}{r}\right) \approx \frac{r\left(a + 48\pi\frac{r}{L}\right)}{2L\left(a + 48\pi\frac{r}{L} + 18\pi^2\frac{r^2}{L^2}\right)} \simeq \begin{cases} \frac{r}{2L}, & r \ll L \\ \frac{4}{3\pi} - \frac{L}{4r}, & r \gg L \end{cases} , \tag{4.13}$$

where $a = 128 - 9\pi^2$.

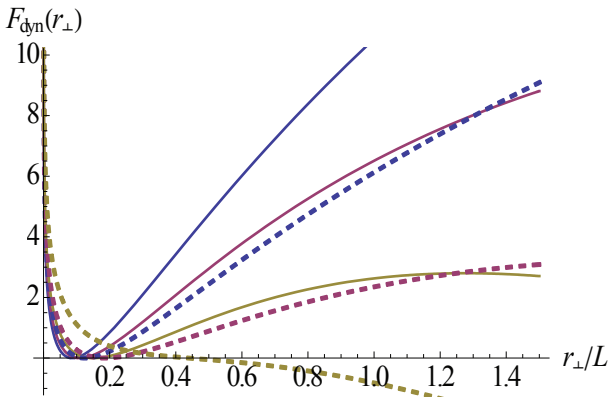

Figure 4.3: Transverse tube confinement potential (in units of the thermal energy) as a function of the dimensionless rod CM transverse displacement at fixed reduced density, $\rho/\rho_c = 10$. From top to bottom the solid curves correspond to $S = 0$ and $\sigma/\sigma_y = 0,\ 1/3\ ,\ 2/3$. From top to bottom the dashed curves correspond to $S = 1/2$ and $\sigma/\sigma_y = 0,\ 1/3\ ,\ 2/3$.

There are many interesting features of the dynamic tube confinement potential (see Fig. 4.3 for examples). In qualitative contrast with particle glasses where activation barriers are finite [31,32], for all densities $\rho > \rho_c$ the topological confinement potential is predicted to be infinitely deep. This would seem to provide some justification for the most basic aspect of the reptation-tube ansatz, that is, the quenching of unbounded lateral motion or the idea that polymers must reptatively "diffuse around" entanglement constraints. However, in contrast to phenomenological harmonic tube models which typically postulate a confinement field

characterized by a single parameter, the tube diameter (e.g., spring or slip-link models [143]), the dynamic free energy is only parabolic up to $\sim k_B T$ above its minimum. It then crosses over to a weaker quasi-linear regime out to displacements of order the rod length, and finally grows logarithmically for very large displacements. The predicted harmonic and quasi-linear regimes are in very good accord with experiments on heavily-entangled F-actin solutions, which observe long exponential tails in the rod displacement distribution on time scales short compared to the reptation time [25].

The large-displacement form of the tube potential follows from Eqs. 4.10, 4.12 as

$$F_{dyn}(r_\perp \gg L) \sim (\rho/\rho_c - 2)\log(r_\perp/L). \tag{4.14}$$

We caution that this logarithmic growth, and hence our prediction that the transverse barrier is infinitely high, is a technically subtle result that we believe is sensitive to the Vineyard-like and local-equilibrium approximations of the theory. One might have physically expected a large, but finite, entropic barrier at $r_\perp \approx L$. However, the very-large-displacement form of the transverse tube confinement potential is not relevant in practice. The reason is that in strongly entangled systems its height at $r_\perp \approx L$ (before the crossover to logarithmic growth) is already enormous relative to the thermal energy, and thus a tagged rod reptates out of the local tube by longitudinal motion long before its transverse displacement ever approaches the logarithmic regime.

To quantitatively test our theory, we compare with recent experiments on heavily entangled solutions of the biopolymer F-actin [25] which measured the probability distribution of transverse displacements from the mean position (tube axis), $P(r_\perp)$, on intermediate time scales when reptation is not active. A lateral tube confinement potential was deduced as $V(r_\perp)/k_B T = -\ln\left(P(r_\perp)/P(0)\right)$, and the results reported in terms of a "restoring force," $f(r_\perp) = -dV_\perp/dr_\perp$. We employ the experimental conditions of $L = 23\ \mu m$ and room temperature. Since the F-actin's semiflexibility results in a tube radius with a density scaling

($r_l \sim \rho^{-3/5}$) different than in our rigid-rod theory, we choose ρ such that the r_l predicted by Eq. 4.9 equals the measured most probable tube radius. This choice connects experimental and theoretical measures of the harmonic portion of the confinement potential, but all anharmonic features are then predicted in an a priori manner.

Figure 4.4 presents the theory-experiment comparison for the restoring force as a function of dimensionless transverse displacement at three concentrations. The bold curves are the theory, while the dashed curves indicate the range of density mappings corresponding to the measurement error bars[2] of r_l. The theory agrees in all aspects with the observations.[3] This quantitative comparison, and the observations of a nearly linear form of F_{dyn} at intermediate displacements in DNA solutions [28] and simulations of flexible chain melts [29], provide further support for our theoretical approach and its generality.

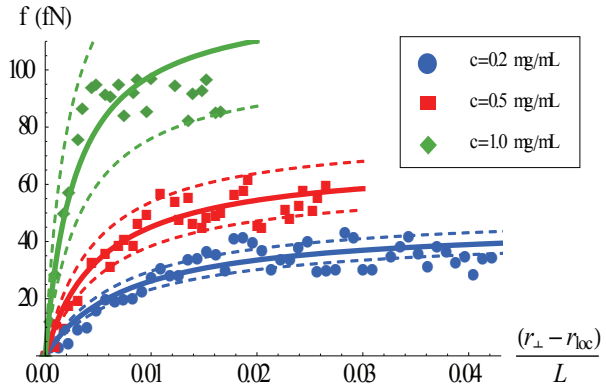

Figure 4.4: Transverse displacement force versus dimensionless displacement from the most probably localization position. Curves correspond to Eq. 4.9 at different reduced densities, points are experimental data from Ref. [25] at the 3 concentrations indicated.

We emphasize that the key to this quantitative agreement with F-actin experiments [25] (and, qualitatively, the consistency of our approach with DNA experiments [28] and the entangled-chain-melt primitive-path simulations [29, 30]) is the harmonic and quasi-linear

[2]Not shown are the error bars associated with each experimental data point: $\sim$ 1fN in the harmonic regime, and $\sim$ 10fN outside of it [Bo Wang (private communication)].

[3]Two alternative phenomenological explanations of F-actin data have been recently presented. Both make use of binary collision approximation ideas where topological interactions are replaced by ansatz with a harmonic potential, which is then either exploited [25] or self-consistently renormalized [26]. Since we begin with bare rod-rod collisions our theory makes no assumptions about the form of the effective potential prior to the renormalization of the diffusion tensor.

part of the dynamic tube potential and the concomitant prediction of a maximum entanglement restoring force. Such confinement softening emerges from a self-consistent treatment of nonlinear feedback between lateral polymer displacements and the transverse dynamic localization constraints. As a speculative comment, this feature can perhaps be qualitatively viewed as a microscopic realization of local constraint release or a "double reptation"-like process in the language of the classic tube model [16]. Szamel previously showed that the needle theory captures some constraint-release-like effects at the CM self-diffusion level [17], and we here propose that our theory for the dynamic confinement potential similarly self-consistently captures some matrix-mobility effects. That is, as the tagged rod displaces the dynamical constraints it experiences are also relaxed via the motion of the other polymers entangled with it (since $\overleftrightarrow{D}_e$ is responsible for the dynamic evolution of both the one- and two-body density distributions), resulting in a dynamical softening of the tube constraint. Note this is certainly not the textbook global constraint release mechanism tied to the reptative motion of a matrix rod end past a tagged polymer [12]; it is fundamentally more general since it exists when reptation is quenched. A generalized constraint release motion not tied to reptation has also been suggested based on primitive path simulations of chain melts [142].

Indirect, but we believe significant, evidence for the anharmonic nature of the tube confinement field for thin, rigid macromolecules can also be found in recent Brownian simulation studies of heavily entangled semiflexible chains constructed to mimic F-actin [27] and rigid needles [142]. These studies investigated the lateral mean square displacement (MSD) of the center of a polymer defined in a way that ignored contributions from the longitudinal motion. The classic tube idea predicts that this MSD would saturate at quite early times after a displacement of order d_T^2. However, even at very high degrees of entanglement this was not found, neither for stiff semiflexible chains nor rigid rods [142]. Instead a slow, seemingly unbounded increase (at lower densities) or steadily upwards creep (at high densities) of the lateral MSD was detected, and significant lateral displacements beyond the putative mean

tube diameter occurred on time scales less than the reptation-controlled rotational relaxation time. Moreover, by varying the longitudinal friction the simulations determined that this "tube leakage" is not due to a simple constraint-release effect of one polymer reptating past a local entanglement [142], and that it can be eliminated if all polymers surrounding the tagged one are frozen, per a network. Hence, these tube-leakage phenomena appear to be an intrinsic, many-polymer property of lateral dynamical constraints, and their essence seems qualitatively consistent with our prediction of an anharmonic confinement potential.

In the heavily entangled regime, the displacement at which a rod feels the maximum confining force, r_m, is much less than L. A series expansion of Eq. 4.10 in inverse density can be carried out to obtain

$$\begin{aligned} f_{max} &\simeq \frac{k_B T}{L}\left(\frac{\pi\rho L^3}{4\sqrt{2}} - 2\sqrt{\rho L^3/\sqrt{2}} + \cdots\right) = 2\ k_B T\left(\frac{1}{r_l} + \frac{-2\sqrt{2}}{\sqrt{\pi r_l}} + \cdots\right) \\ &= 2k_B T(r_l^{-1} - 2r_m^{-1}), \end{aligned} \tag{4.15}$$

where in the second equality the high-density approximation for the localization length is used. The displacement at which the maximum force occurs is

$$r_m^{-1} \simeq \sqrt{\rho L/(4\sqrt{2})} \quad \ll \quad r_l^{-1} \simeq \pi\rho L^2/(8\sqrt{2}) \tag{4.16}$$

At high densities r_m is small compared to L, and hence is unaffected by the long-range logarithmic growth of the confinement potential, but is large compared to the localization length. In the heavily entangled limit we obtain $f_{max} = 2k_B T/r_l$, a direct connection between the maximum entanglement force and the tube diameter. Although we derive this result only for rigid needles, it perhaps provides a theoretical basis for a speculative argument by Wang et.al. based on dimensional analysis concerning the finite strength of tube localization for entangled flexible chain liquids [144].

4.5 Stochastic Trajectories on the Transverse Confinement Potential

To probe alternate measures of the tube's anharmonicity we solve the equation of motion for the transverse displacement of a rod in the confinement potential, Eq. 4.11, at the level of stochastic trajectories. This amounts to integrating this equation starting with the initial condition $r_\perp(t = 0) = 0$ over many instantiations of the Gaussian white noise, and then taking ensemble averages of these trajectories to address questions of interest. In colloidal glasses the stochastic integration of the NLE was a key method for addressing questions of dynamical heterogeneity [53, 92, 119]. Here the polymers are not in a glassy state and our free energy permits no activated barrier hopping processes in equilbrium, and so our goals are more limited. Implementing the Brownian trajectory algorithm is a standard exercise, and we refer the more curious reader to a favorite text [145].

The first question we address is the ensemble-averaged transverse mean square displacement (MSD) as a function of time. In the absence of a microscopic treatment of the tube, the standard cartoon for rods would simply be diffusive ($r_\perp^2(t) \sim t$) behavior at very short times before the rod "discovers" that there is a confining tube, followed by either a sharp, instantaneous transition to a constant plateau or an exponential decay to the plateau, depending on whether the confinement is assumed to be of a step-potential or harmonic form [12].

Our prediction for the MSD is show in Fig. 4.5 for reduced densities ranging from $\rho/\rho_c = 10$ to $\rho/\rho_c = 1000$, obtained by simulating 50000 trajectories at each density. Several points are immediately evident. First, we find a complete collapse of the MSD curves by normalizing both displacement *and* time by a quantity related to the plateau value of the MSD (i.e. $\tau_e = \tau_0 L^2/\langle r_\perp^2 \rangle$). Such a joint normalization would be expected for Brownian motion in a purely harmonic potential, so the fact that it works here is surprising. However, instead of an exponential decay of $(1 - \mathrm{MSD}(t))$ to the plateau value, the curves transition from a diffusive regime to one of modestly *stretched* exponential decay to the plateau. This

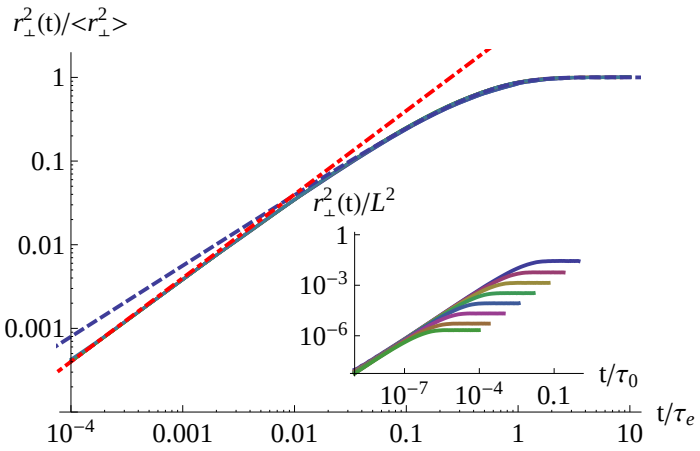

Figure 4.5: Transverse MSD vs. time normalized by plateau values. Dash-dotted curve represents the short-time diffusive behavior $r_\perp^2 = 4t/\tau_e$: the dashed curve corresponds to stretched exponential decay to the plateau, $r_\perp^2 = 1 - \exp\left(-2(t/\tau_e)^{0.86}\right)$. Inset: Transverse MSD vs time for $\rho/\rho_c = 10, 20, 40, 80, 160, 320, 640, 1000$ (top to bottom).

reflects the anharmonic nature of the tube confinement potential. Our predicted collapse of the MSD curves agrees with recent simulations of rigid and semi-flexible rods [27, 142], and the universal "approach to entanglement" curve we predict is, in principle, also directly testable.

The predicted stretched-exponential behavior should remind the reader of the signature correlation functions in glassy systems. For interest we also study so-called "non-Gaussian parameters" (NGP), of which there are two primary definitions. The classic definition is [6]

$$\alpha_2(t) = \frac{3}{5}\frac{\langle r_\perp^4(t)\rangle}{\langle r_\perp^2(t)\rangle^2} - 1, \tag{4.17}$$

and a recently proposed alternative is [47]

$$\gamma = \frac{1}{3}\langle r_\perp^2(t)\rangle \left\langle \frac{1}{r_\perp^2(t)} \right\rangle - 1. \tag{4.18}$$

The classic NGP emphasizes departures from diffusive motion at short times and small displacements, whereas the alternate NGP emphasizes deviations at relatively longer times or larger displacements. In glassy particle fluids the "maximum non-gaussian state" —

in which nongaussian fluctuations, activated events, and dynamic heterogeneity are most important — can be identified by the peak of these functions, and in particular simulations have found that the peak of the alternate NGP closely tracks the alpha relaxation time [47].

In the present topologically entangled case the NGPs are somewhat less revealing. The dynamic free energy associated with Eq. 4.11 features an infinitely deep potential well, so activated hopping events are completely suppressed and both NGPs will simply approach a plateau value associated with the Boltzmann distribution $P \sim \exp(-\beta F_{dyn})$ as the rod equilibrates within the tube. However, the nongaussian parameters still serve as a more sensitive probe of anharmonicities than considering just the MSD. This is shown in Fig. 4.6: despite the complete collapse of the MSD curves under the above normalization, we see that even given the large noise (for the same number of simulated trajectories) a complete collapse of the NGPs requires going to higher rod densities. The classic NGP exhibits a power law scaling of $\alpha_2(t < \tau_e) \sim \sqrt{t}$ over roughly two decades before saturating at the plateau. The alternate NGP looks qualitatively similar, but is too noisy to reliably extract a power law exponent without running more simulations.

4.6 Applied Stress and Microscopic Yielding

To include the effect of applied deformation at the single-polymer level in the framework of NLE theory, a stress-based microrheology approach is employed as previously formulated for finite-excluded-volume complex liquids that interact via conservative forces [65,67–69]. This treatment is significantly less microscopically rigorous than our theory for quiescent dynamics, but the stress-generalized NLE theory has been successfully applied to quantitatively understand many aspects of nonlinear activated relaxation and mechanics in colloidal and polymer glasses. The appropriate stress-generalization of the NLE is expected to depend on the particular deformation of interest, and here we focus specifically on shear stresses. For both simplicity (and consistency with the scalar localization length derived above) we

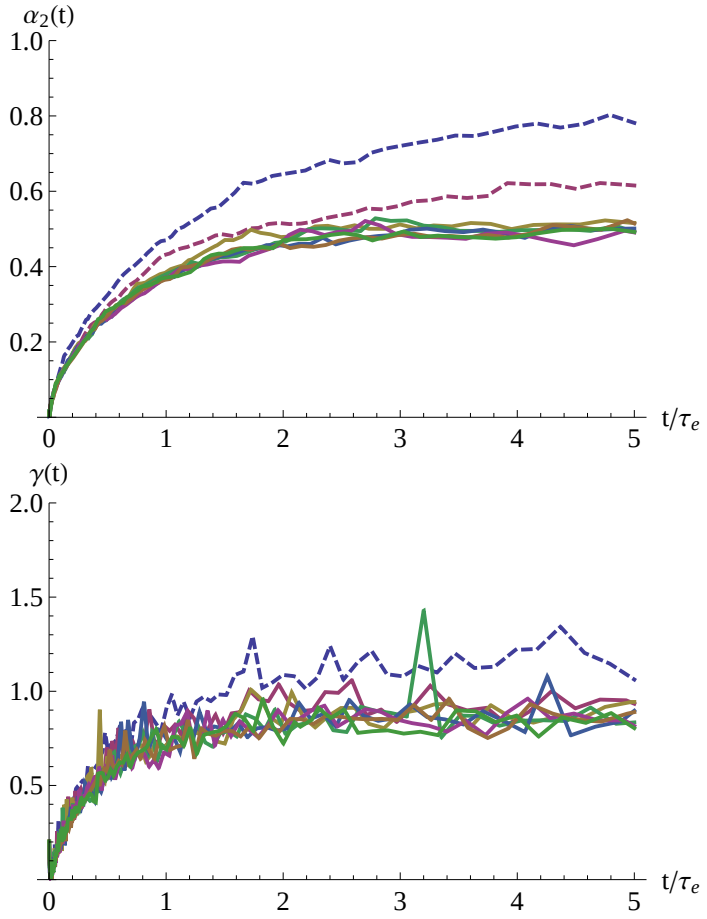

Figure 4.6: Classic and alternate NGP vs normalized time. Dashed curves correspond to $\rho/\rho_c = 10, 20$ (top plot) and $\rho/\rho_c = 10$ (bottom plot), solid curves correspond to $\rho/\rho_c = 40, 80, 160, 320, 640, 1000$.

neglect the tensorial nature of the deformation and formulate a theory in terms of a scalar stress, σ. The key physical idea is that the macroscopic stress results in a constant effective force on the CM of a particle, molecule, or polymer (a microrheological-like perspective). This external force weakens the dynamical constraints encoded in F_{dyn}, which thus acquires a mechanical-work-like contribution that is linear in both stress and instantaneous transverse displacement:

$$F_{dyn}(r_\perp, \sigma) = F_{dyn}(r_\perp, \sigma = 0) - \pi L^2 \sigma r_\perp / 4. \tag{4.19}$$

Since the theory treats the ensemble-averaged confinement potential, we neglect the fact that the transverse displacement of any given tagged rod may not be in the direction of the stress plane; that is, Eq. 4.19 conceptually represents the effect of constructing the confinement potential and averaging it over (an isotropic distribution of) all rod orientations. Breaking the assumption of isotropy and treating orientational ordering effects will be presented in the following section.

The relevant cross-sectional area, A, for converting macroscopic stress to microscopic force is taken to be a circle of diameter L. For spheres the relevant area seems obvious, i.e. proportional to the square of the particle diameter [68, 69]. For needles the choice is less obvious, but since L is the only intrapolymer length scale choosing $A \sim L^2$ seems a natural and inevitable choice. The only plausible alternative would be to employ an area determined by the localization length (tube diameter). This is an emergent length scale that in some way quantifies how the surrounding interpenetrating polymers transmit stress (and hence applied force) to the tagged rod. However, for this needle system we find that such a choice leads to seemingly unphysical or counterintuitive predictions, e.g. the ability of the fluid to support arbitrarily large strains at high density (cf. Eqs. 4.22, 4.23 below).

A general consequence of our theory, also true for glasses and gels within the NLE framework [65, 68, 69], is the existence of an "absolute yield" stress at which the transverse entropic barrier first vanishes and hence tube localization is destroyed, $\sigma_y \equiv f_{\max}/A$. One

can think of it as the onset of an imbalance between the larger applied force experienced by a tagged macromolecule and the intrinsic entanglement force that keeps it in a tube. Beyond this critical stress, lateral motion occurs spontaneously in a barrier-free manner.

We note that our subsequent numerical results are quantitatively sensitive to the choice of A, but qualitatively depend only on adopting $A \propto L^2$. We also point out that stress directly effects only the transverse motion. So far, deformation is assumed not to modify the (isotropic) rod orientation distribution; this restriction is relaxed later.

In general, the stress dependence of key features of the tube confinement potential must be determined numerically. A critical general finding is that *any* nonzero value of σ destroys the infinitely deep nature of the lateral confining field, resulting in a stress-induced finite entropic barrier. This is a direct consequence of the fragile logarithmic localization predicted for large displacements in the quiescent theory. The two extreme limits for the entropic barrier can be analytically analyzed. For relatively low values of stress the barrier is given by

$$F_B \approx 2(1 - \rho/\rho_c) \log \tilde{\sigma}, \tag{4.20}$$

where $\tilde{\sigma} \equiv \sigma L^3/k_B T$. In the opposite extreme where the stress is close to its absolute yield value (defined microscopically here as when the localization well and entropic barrier first vanish), the dynamic confinement potential exhibits a "fold catastrophe" form with

$$F_B \propto (1 - \sigma/\sigma_y)^{3/2}. \tag{4.21}$$

This result can be derived in the limit of large density using Eqs. 4.15, 4.16 and the small-displacement approximation for F_{dyn} obtained from Eqs. 4.9 – 4.13. However, we find that the practical relevance of these two limiting results is small, for different physical reasons, as will be discussed when we take up rheology in a later chapter.

The explicit expression for the absolute yield stress at very high densities follows from

Eq. 4.15 (keeping only the dominant term) as

$$\sigma_y = \frac{4f_{\max}}{\pi L^2} \simeq \frac{\rho k_B T}{\sqrt{2}} = \frac{5}{3\sqrt{2}} G_e, \tag{4.22}$$

where $G_e = 3\rho k_B T/5$ is the needle-fluid shear modulus [12]. Adopting an elastic solid perspective of the entanglement network, one estimates a corresponding absolute yield strain as

$$\gamma_y = \frac{\sigma_y}{G_e} \simeq \frac{5}{3\sqrt{2}} \approx 1.18, \quad \rho \gg \rho_c. \tag{4.23}$$

Although the precise numerical results are sensitive to our choice of cross-sectional area, a yield strain of order unity seems to be at least qualitatively consistent with recent experiments on entangled microtubulin (rigid rod) networks [146]. Intriguingly, yield strains of order unity have also been reported in entangled flexible chain liquids [144, 147, 148].

Two features of the stress-dependent confinement potential can have dramatic consequences for the long-time dynamics. First, as is implicit in the above and explicitly shown in the inset of Fig. 4.7, at fixed density the most probable (and the mean) transient localization length grows with increasing σ, corresponding to deformation-induced tube dilation. Within the phenomenological tube framework, conflicting arguments have been advanced that the tube diameter grows, shrinks, or remains unchanged under deformation [16]. For shear deformations we predict tube dilation, and the ratio of the tube radius at absolute yield to its quiescent value grows as $r_{l,yield}/r_l \sim \sqrt{\rho L^3}$ for $\rho \gg \rho_c$. Since in the static tube model (and dynamic theory [17, 24, 139]) the rotational diffusion constant $D_{rot} \propto D_\perp \propto (r_l/L)^2$, tube dilation results in a significant acceleration of reptative relaxation, especially for heavily-entangled solutions near σ_y. Second, as shown in Fig. 4.7, since F_B decreases rapidly with stress, a deformation-assisted transverse barrier hopping process emerges as a parallel relaxation channel which competes with reptation. These relaxation times will be discussed in much greater detail in Chapter 6 when we take up the rheology of entangled rods. There the competing relaxation channels and their differing responses to stress and orientation can

radically change system relaxation.

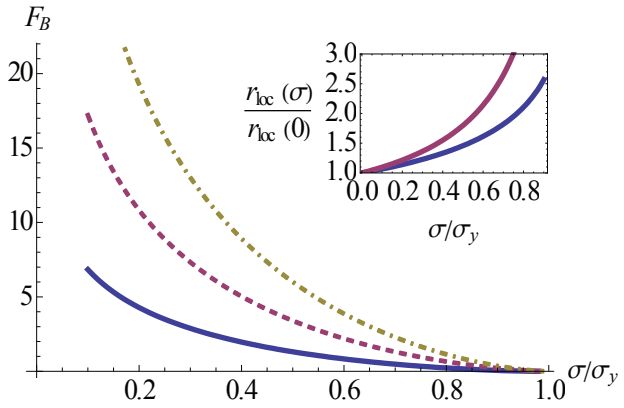

Figure 4.7: Barrier height in units of k_BT vs normalized stress for $\rho/\rho_c = 3,\ 6,\ 10$ (bottom to top). Inset: normalized tube radius vs. normalized stress for $\rho/\rho_c =\ 10$ (lower curve) and $\rho/\rho_c =\ 100$ (upper). At these four densities, the estimated absolute yield strains are $\sigma_y/G_e \approx 0.28,\ 0.52,\ 0.67,$ and 1.04, respectively.

4.7 Effect of Orientational Order

Since we consider zero-excluded-volume rods, spontaneous nematic ordering cannot occur. However, the dynamical consequences of externally-induced rod alignment can still be treated as long as the distribution of rod centers of mass remains random, since in that case all the technical approximations employed for the isotropic fluid are still valid [139]. Specifically, the effect of rod alignment on entanglement dynamics for both the Szamel and NLE theories can be captured by modifying the pair correlation function in Eq. 4.5 with an Onsager-like distribution [12] for the relative orientation of two rods: $f(\mu,\alpha) = \alpha\cosh(\mu\alpha)/4\pi\sinh\alpha$, where α parameterizes the degree of orientation relative to some axis and $\mu = \vec{u}_1 \cdot \vec{u}_2$ Expressing our results in terms of the nematic order parameter, $S = \langle(3\cos^2\theta - 1)/2\rangle$, we find [139]

$$D_\perp(S)/D_\perp(0) \approx (1-S)^{-1}, \tag{4.24}$$

$$r_l(S)/r_l(0) \approx (1-S)^{-1/2}. \tag{4.25}$$

Orientation reduces inter-rod collisions, thereby enhancing lateral and rotational diffusion. The inset of Fig. 4.2 demonstrates the density-dependent enhancement of diffusion and compares it with the standard Doi-Edwards expression. A reduction of collisions also results in the tube diameter increasing with orientation (see Fig. 4.3. The predicted rod-alignment effects are qualitatively similar to the Doi-Edwards calculation for rod densities beyond the purely topological regime, where nonzero-excluded-volume physics enters [12]. We also find that the predicted tube-model scaling of $D_\perp \propto (r_l/L)^2$ continues to hold in the presence of rod orientation. Moreover, all features of the tube confinement potential, including the maximum entanglement force, soften with orientation and stress (see Fig. 4.3).

The above results suggest, and we have numerically verified, that to a very good approximation the effect of orientational order can be thought of as modifying the effective fluid density as $\rho \to \rho\sqrt{1-S}$, and hence

$$F_{dyn}(r_\perp, \rho, \sigma, S) = F_{dyn}(r_\perp, \rho\sqrt{1-S}, \sigma = 0) - \pi L^2 \sigma r_\perp/4. \tag{4.26}$$

This expression succinctly captures how the consequences of macroscopic stress and orientation are microscopically included at the tagged-rod level. The approach is self-consistent in the sense that stress modifies the tube confinement potential and hence polymer dynamics, but polymer displacement weakens the confining force and also determines stress relaxation. The effects of stress and orientation on r_l follow from this dynamic tube potential. For example, one can derive the high-density result

$$\left(\frac{r_l(\rho, 0, 0)}{r_l(\rho, S, \sigma)}\right)^2 \approx \left(\sqrt{1-S} - \tilde{\sigma}/3(\rho/\rho_c)\right)^2, \tag{4.27}$$

an expression valid as long as the localization length is finite (i.e., for stresses not too high). This result follows by expanding Eq. 4.26 in powers of inverse density, and combining Eqs. 4.9-4.12 to write the quiescent dynamic confining potential in limit when the localization

length is small, $r_l \ll L$. Then, employing the full stress- and orientation-dependent F_{dyn}, differentiating, and solving for the minimum yields Eq. 4.27. At the highest density considered in this paper ($\rho/\rho_c = 1000$), we find Eq. 4.27 is reasonably accurate all the way up to the absolute yield stress. However, for only modestly entangled systems (e.g., $\rho/\rho_c = 10$), this expression grossly underestimates tube dilation. Combining Eqs. 4.15 and 4.27, the reduction of the maximum entanglement force by rod alignment in the heavily entangled regime is

$$f_{\max} \simeq \frac{2k_BT}{r_l(\rho,0,0)}\sqrt{1-S}. \tag{4.28}$$

This implies the absolute yield stress (and strain) decrease with increasing rod alignment. Figure 4.3 shows sample dynamic tube confinement potentials computed numerically at fixed density and various levels of applied stress and orientational order. Both can massively weaken the entropic barrier to transverse motion. Note that all the effects of stress and orientation on the tube potential, and the dynamical consequences discussed above and in subsequent sections, are absent by assumption in the Doi-Edwards theory of purely topologically entangled rods [12].

4.8 Summary

In summary, by combining recent extensions of a dynamical theory for topologically entangled rigid rods with a dynamic free energy perspective inspired from the field of glass physics, we have formulated a microscopic theory for the transverse confinement potential. In essence we have attempted to statistically describe what an entanglement is and where a confining tube comes from at the level of (impulsive) forces arising from an exact accounting of polymer uncrossability at the two-rod level combined with a self-consistent renormalization to account for many-body terms. Above a critical reduced density (whose value corresponds to an eminently sensible number of interpentrating rods occupying the same local volume) an infinite barrier to lateral motion emerges, qualitatively supporting the idea that unbounded

transverse displacements are suppressed. However, in contrast to phenomenological tube models we predict a highly anharmonic confining potential, key features of which are in quantitative agreement with experiment [25].The anharmonic nature of the transverse dynamical confinement potential implies that there is a maximum restoring force keeping a tagged rod in its tube due to topological interactions with its surroundings, i.e., physical entanglements cannot always be literally treated as chemical crosslinks in rubber networks. In this sense, the theory might be viewed as having some features in common with venerable "transient network" models [149–151]. The consequences of a finite entanglement force are especially dramatic under applied deformation, leading to phenomena such as stress- and orientation-driven tube dilation, transverse entropic barrier reduction, and ultimately tube destruction beyond a critical level of stress or strain when the external force on a tagged rod exceeds the intrinsic entanglement force localizing the polymer in a tube. This last feature may be akin to empirical attempts to describe stress-dependent crosslinks in transient network models [150, 151], and recent experimentally-motivated physical ideas about force imbalance in entangled chain liquids [144, 148].

Our prediction that the confining tube has a finite strength has many dramatic and novel consequences. Applied stress and induced polymer alignment can result in a dramatic acceleration of terminal relaxation not anticipated by the reptation-tube approach. With increasing stress we predict: (i) the tube widens, resulting in reduced entanglement and faster reptative relaxation, in qualitative agreement with a recent chain polymer simulation [152], (ii) a transverse activated barrier hopping relaxation process emerges that can become faster than reptation, and (iii) the tube is completely destroyed (microscopic absolute yielding) for $\sigma > \sigma_y$. The latter two regimes appear to be qualitatively consistent (at zeroth order) with recent experimentally-based suggestions that tubes can become severely weakened or destroyed by stress [144, 148, 153], and also the observation of yield strains of order unity for rigid rod (microtubules) [146] and flexible chain liquids [144]. Although at present there is a dearth of data on isotropic, high-aspect-ratio rod solutions under deformation, new simula-

tions of entangled needle fluids based on primitive path methods [124] can be performed to critically test all aspects of our predicted dynamic tube confinement potential. The ability to construct this potential sets the stage for developing a first-principles treatment of nonlinear rheology where applied stress may qualitatively modify the confinement potential. Moreover, many open issues can be addressed such as: the time [29] and deformation [16] dependence of the tube diameter, possible destruction of entanglement localization when polymers become strongly aligned and/or deformed [144], and construction of a self-consistent description of constraint release under both quiescent and strongly sheared (convective [16]) conditions. Our development of molecular-based constitutive equations for rheological response under step-strain and startup continuous shear conditions are discussed in Chapter 6.

Chapter 5

COARSE GRAININGS OF FLEXIBLE CHAIN POLYMERS

5.1 Introduction

[1]Understanding the fascinating and complex dynamics of concentrated liquids of flexible polymer coils has been an ongoing challenge spanning many decades. From the point of view of simulations the vast range of length and time scales associated with dense melts of long chains poses a formidable challenge to studying the long-time dynamics [154]. The theoretical difficulty is that when polymers become sufficiently long "entanglements," the topological constraints arising from chain connectivity and uncrossability, dominate intermediate and long-time elasticity, relaxation, and transport. These singular interactions, combined with the statistical nature of polymer conformations, render a first-principles theory exceptionally challenging to formulate. Since its introduction the phenomenological reptation-tube model of deGennes, Doi, and Edwards [12, 15] has been the most common starting point for theoretical analysis. This single-chain approach is based on assuming the existence of transverse localization beyond a mesoscopic material-specific length scale, the tube diameter d_T. By ansatz the localization arises as the dynamical consequences of the many interpenetrating chains on tagged polymer motion, and is modeled by an infinitely strong (e.g., harmonic) confinement field which permits long-time diffusion only via anisotropic curvilinear motion or "reptation."

The phenomenological nature of the reptation-tube theory, including its diverse elaborations which help explain a broad class of experimental data [16], renders the connec-

[1]This chapter contains text and figures from *D. M. Sussman and K. S. Schweizer, Phys. Rev. Lett.; submitted 2012.*

tion between its mathematical foundation and real-space polymer motions somewhat unclear [23]. Particularly desirable is a theoretical explanation of the tube diameter, the full spatially-resolved dynamic confinement potential, and the critical chain length that signals the crossover from unentangled to entangled dynamics, N_e [23].

In this chapter we adopt the classic Doi-Edwards picture of a single entangled chain of N segments as an ideal random walk of $Z = N/N_e$ "primitive path" (PP) steps of length $L_e = \sigma\sqrt{N_e}$, where σ is the statistical segment length such that $R_{ee} = \sigma\sqrt{N}$ is the mean polymer end-to-end distance. This picture has been extensively used in simulations to numerically compute properties of the confining tube [29,124]. By building on and qualitatively generalizing our recently developed and quantitatively accurate theory for the dynamics of entangled rigid needles [139] to treat the topological interactions between PP steps on different chains, we construct a microscopic theory for the full tube confinement potential governing the distribution of transverse segment displacement relative to the nearest PP step. We also examine the theory's consequences on long time diffusion and relaxation. Intriguingly, and surprisingly, we find that the results from studying chains at the level of interacting PP steps are very similar to a "super coarse-graining" procedure [154] which replaces the entire chain with its end-to-end vector and applies the topological needle theory to that object. Traditionally, the goal of such coarse-graining schemes has been to create a fast computational model for larger-scale rheological applications. In contrast, here we will explore the coarse-graining idea from the perspective of the fundamental physics.

5.2 Coarse-Grained Chains

We begin by considering our microscopic theory for the transverse confinement of a single PP step α on a tagged polymer in a melt with chain number density ρ, schematically depicted in the inset of Fig. 5.1. We initially treat transverse localization as a Gaussian distribution with a mean characteristic length $\bar{r}_l$ (the tube radius). Generalizing the dynamic mean-field

theory of Szamel for non-rotating needles [17, 24], the formal expression for this localization length under the condition that the longitudinal reptative motion is turned off ("quenched") is:

$$\frac{4}{\bar{r}_l^2} = \frac{-\rho}{16\pi}(\overleftrightarrow{I} - \vec{u}_1\vec{u}_1) : \sum_{j,k=1}^{Z} \int d\vec{v}d\gamma d\vec{r}_{\alpha 2}\, \overleftrightarrow{T}(\alpha j)(\Omega_{loc}^{\dagger})^{-1}\, \overleftrightarrow{T}\,(\alpha k). \tag{5.1}$$

Here $\vec{u}_i$ is the orientation of the PP step i, $\vec{v}$ and γ describe the orientation of an instantaneous conformation of a second chain, $\vec{r}_{\alpha 2}$ is the center of mass (CM) separation between α and the second chain, and the colon denotes a double contraction of tensorial indices. $\overleftrightarrow{T}\,(\alpha j)$ represents an impulsive interaction (the uncrossability constraint) between α and the PP segment j on the second chain treated at the needle-level (the form of which is given by [130]), and the "localized" two-chain evolution operator governing transverse PP motion is.

$$\Omega_{loc}^{\dagger} = -1 + \frac{\bar{r}_l^2}{4} \sum_{n,m=1}^{Z} \left(\nabla + \vec{T}(nm)\right) \cdot \left(2\vec{I} - \vec{u}_n\vec{u}_n - \vec{u}_m\vec{u}_m\right) \cdot \nabla. \tag{5.2}$$

Further progress requires approximations to treat the Z^2 possible time-dependent collisional correlations between a tagged PP unit and those on a different interpenetrating chain. We assume that the off-diagonal elements in Eq. 5.1 (i.e. where $j \neq k$) vanish, and that when evaluating the integral over diagonal elements the terms in $\Omega_{loc}^{\dagger}$ with $n \neq \alpha,\ m \neq j$ can also be neglected. These approximations are consistent with our theory for infinitely thin, non-rotating 3D crosses [141], which was favorably compared with simulation [122, 123]. Physically, under quenched-reptation conditions we interpret the first assumption as both neglecting simultaneous three-body collisions and assuming that on average there is no angular correlation between steps at the primitive path level. The second assumption is also consistent with the quenching of reptation, i.e., during the time scales of interest to describe localization in a tube the chain does not displace enough to change the pair of interacting PP steps.

After these approximations, Eq. 5.1 is a sum over Z identical terms, each of which can be

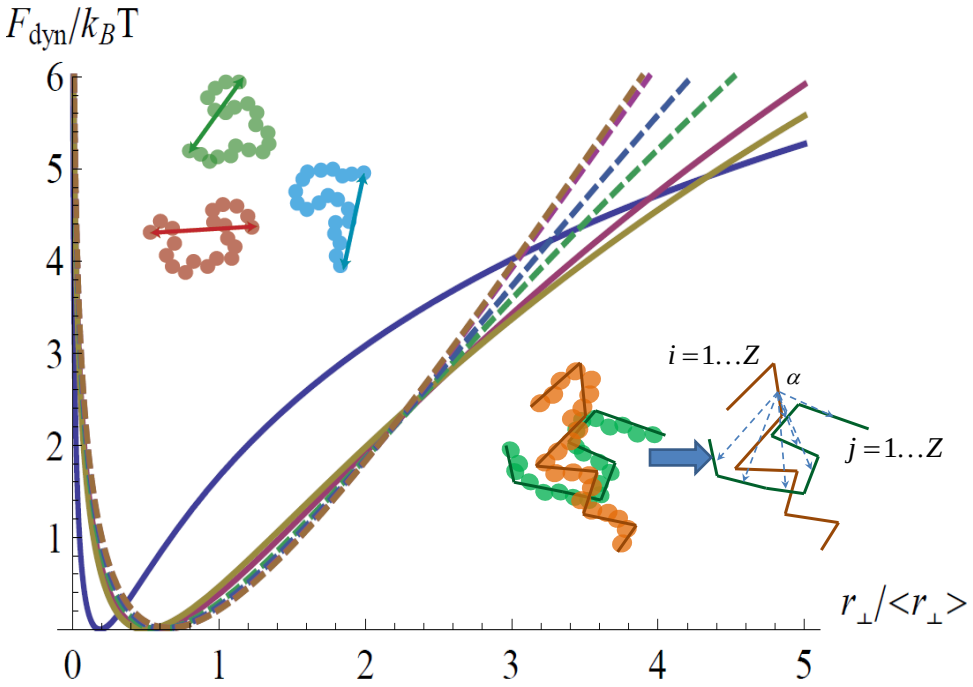

Figure 5.1: Normalized tube confinement potential for the PP mapping vs. transverse displacement (solid curves, $A^{-1} = 0.5,\ \ 0.22,\ \ 0.18$, left to right), and for the super coarse-grained needle limit with $N/N_e = 10,\ 20,\ 100,\ 200$ (dashed curves, bottom to top) Cartoons above and below curves schematically depict the two mappings.

evaluated according to previous work [17, 139, 141]. This yields the self-consistent relation

$$\bar{r_l}^{-2} = F(L_e/\bar{r_l}) Z \pi \rho L_e^3 / (\bar{r_l}^2 4\sqrt{2})^{-1}, \tag{5.3}$$

where $F(x)$ is a combination of modified Bessel and Struve functions determined by approximately evaluating the integral [141]. The length of the PP steps is commonly taken to be related to the tube diameter, $L_e = \sigma\sqrt{N_e} = A\overline{r_l}$, where typically one expects $A = 2$. Writing the expression for the localization length in terms of the invariant packing length (which quantifies the system-specific way different polymer chains fill space [155]), $p = (N\rho\sigma^2)^{-1} \equiv (\rho_s\sigma)^{-1}$, the evaluation of the self-consistent expression with $A = 2$ leads to

$$\bar{r_l} = \frac{4\sqrt{2}}{A\pi F(A)} \rightarrow L_e = 2r_l = 9.99p \tag{5.4}$$

The level of quantitative agreement between Eq. 5.4 and the experimental result of $d_T \approx 17.7p$ [155] seems remarkable given the simplified nature of the approximations employed. This tube-diameter scaling can be viewed as a first-principles derivation of the Lin-Noolandi conjecture for polymer melts, which asserts that the number n of primitive path segments that can fit inside a volume d_t^3 is a fixed, universal number [156, 157]. Our estimate of $n = d_t/p$ is roughly a factor of two smaller than experiment, consistent with the fact that quenching the rotational PP degree of freedom should lead to an overestimate of the confining constraints.

Just as in the needle-theory, one can go beyond the above Gaussian analysis to construct the full anharmonic tube-confinement potential using the nonlinear-Langevin-equation (NLE) approach [139]. The NLE stochastic equation of motion for the transverse CM displacement of a PP ($r_\perp$) step is $-\zeta_s \frac{dr_\perp}{dt} - \frac{\partial}{\partial r_\perp} F_{dyn}(r_\perp) + \delta f_s = 0$. Here, ζ_s is the short-time (bare) friction constant, δf_s is the corresponding white noise random force, and $F_{dyn}(r_\perp)$ is a dynamic confinement potential that follows from integrating the displacement-dependent

force,

$$f(r_\perp) = \frac{-2}{r_\perp} + \frac{2}{r_\perp F(A)} F\left(\frac{L_e}{r_\perp}\right). \tag{5.5}$$

For rigid needles we successfully compared the relatively small-displacement limit of the NLE theory (but large enough to include a strongly anharmonic, exponential-tail regime) with experiments on heavily entangled semiflexible f-actin solutions [25]. Here we predict that this function depends only on the ratio of the PP step size to the average transverse displacement, and Fig. 5.1 shows confinement potentials for three values of A. Exponentiating the negative of $F_{dyn}(r_\perp)$ and normalizing yields the probability distribution of transverse displacements relative to the primitive path on time scales when the polymer has equilibrated inside the tube but not yet relaxed via reptative motions of the primitive path.

Figure 5.2 presents a comparison between our predicted transverse-displacement probability distribution, $P(r_\perp)$, and the distribution of individual segments from their primitive-path-step center in units of the average tube radius deduced via simulation [30]. A modest quantitative complication is that the simulations report the displacement of beads relative to the PP step containing the bead, whereas it is most natural for us to predict the distribution of transverse primitive path displacements from their initial position. To perform the comparison we assume the bead displacement distribution can be modeled taking $\bar{r}_l/L_e$ to be the ratio of the average bead displacement to primitive path length; the polyethylene (PE) melt data in Table 1 of Ref. [30] implies $\bar{r}_l/L_e = A^{-1} \approx 0.18$. The agreement between theory and simulation using this value, while imperfect, is striking. Not only is the shape of the distribution quite accurate, but the exponential tail is very well reproduced. Additionally, the simulations find that when normalized by $\bar{r}_l$ the distribution is universal, and the confinement potential we predict is similarly universal (up to the value of $\approx 0.18 - 0.22$ for PE and polybutadiene (PB) [30]).

Within the classic tube-model framework one could then argue that the rigid PP needle must take $(L/d_T)^2 \propto N/N_e$ "steps" to exit the tube and for the mapped chain to

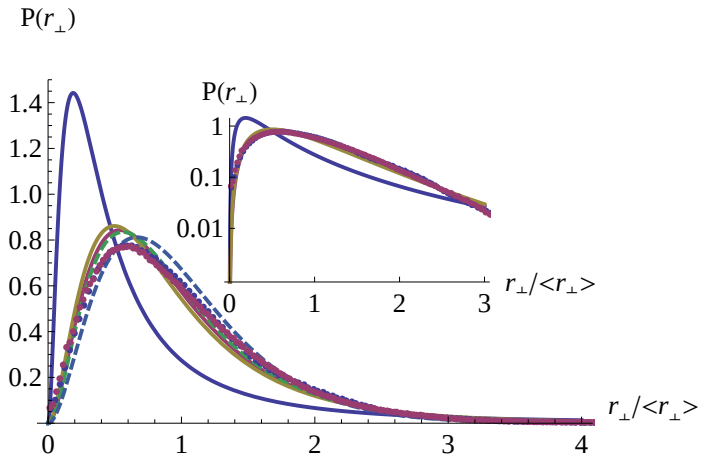

Figure 5.2: Probability distribution comparison with simulation [30] (points). Solid curves are predicted PP distributions with $A^{-1} = 0.5,\ \ 0.22,\ \ 0.18$ (left to right, corresponding to PP and monomer displacements); dashed curves are the chain-to-needle results for$N/N_e =$ 6, 18000 (left and right). Inset: Log plot of PP distribution with $A^{-1} = 0.5,\ \ 0.22,\ \ 0.18$ overlaid on the simulation data.

fully randomize its orientation. One thus expects the terminal relaxation time to scale as $\tau_{rot} \propto \tau_{Rouse}(N/N_e) \propto N^3/N_e$, where the standard result for the Rouse time has been employed, and that by invoking a Fickian perspective the CM diffusion constant would be $D \propto L^2/\tau_{rot} \propto N_e/N^2$. However, it is possible to extend our approach to directly predict these scaling relations, rather than resorting to a deGennes-like argument. First, making the same approximations involving the neglect of off-diagonal terms above, the formal result for the isotropic, long-time CM diffusion of the chain is

$$D_{CM}^{-1} = D_0^{-1} - \frac{\rho}{24\pi} \overleftrightarrow{I} : \int d\vec{v} d\gamma d\vec{r}_{12}\, \overleftrightarrow{T}(ij)(\Omega_e^{\dagger})^{-1}\, \overleftrightarrow{T}\,(ij), \tag{5.6}$$

where now each T-operator describes all Z^2 possible PP collisions between a pair of chains. The bare diffusion constant corresponds to Rouse diffusion of a single PP step of length N_e, and hence $D_0 = D_{mon}/N_e$, where D_{mon} is the segmental diffusion constant. Eq. 5.6 describes the effective diffusion of a chain represented by an instantaneous conformation of PP steps interacting with other instantaneous conformations of PP steps, subject to the constraint that the conformations are allowed to neither change nor rotate. Evaluating the terms in

the integral leads to $D_{CM}/D_{mon} \approx N_e^{-1} - 0.54N/N_e^2$. Hence, based on our computation of prefactors, we predict that isotropic motion vanishes when the chain is roughly twice the entanglement length.

There seems to be no way to rigorously include anisotropic, reptative-like diffusion in this framework due to the geometric complexities of many connected primitive paths. In contrast to the needle theory where one can straightforwardly decompose the motion into fast longitudinal (reptative) motion and constrained transverse motion, for chains the direction of longitudinal motion along different PP step adds incoherently in the laboratory frame. However, one can invoke the physically-motivated idea that reptative diffusion is controlled by the coherent motion of PP steps due to chain connectivity. Using Szamel's theory for transverse PP motion as a sensible surrogate for the rotational relaxation of the PP steps [17], and assuming that long-time CM chain diffusion proceeds only when all steps have relaxed in this way, the self-consistent equation for the diffusion constant becomes

$$\frac{D_{CM}}{D_0} \approx \left(1 + 9.99\frac{N}{N_e}\sqrt{\frac{D_0}{D_{CM}}}F_D\left(\frac{D_{CM}}{D_0}\right)\right)^{-1}, \tag{5.7}$$

where the function F_D is defined in the Appendix of Ref. [17]. In the limit of $N \gg N_e$ this simplifies considerably; expressed relative to the Rouse diffusion constant ($D_R = D_{mon}/N$) we find $D_{CM}/D_R \approx 0.567N_e/N$, almost exactly the classic result of $D_{CM}/D_R \approx N_e/3N$ [12].

To check our interpretation of the physical meaning of the off-diagonal terms discarded above, we consider another, even simpler model: mapping the chains to a fluid of disconnected primitive path segments. The needle theory [17, 139] is then applied to a fluid of segments of length L_e and number density $\rho_{pp} = Z\rho$. We find that the mean tube radius and effective confining forces for a given primitive path step are identical to the calculation presented above. This concurs with the physical intuition that on the time-scale of interest, primitive-path localization is "aware" of intra-chain connectivity only as a second-order effect. In contrast, computing the PP transverse diffusion constant at asymptotically high-

densities (hence, long chains) for this model results in $D_\perp/D_{\perp,0} \approx 18\pi p^2/L_e^2$, a factor of Z^{-2} different from the chain CM diffusion constant obtained above. This is again sensible, since by disconnecting the chain diffusive motion has been massively (and artificially) enhanced.

We now demonstrate that the results from mapping chains to connected primitive-path steps are, surprisingly, quite similar to a much simpler mapping: replacing the entire chain by a single uncrossable needle representing its end-to-end vector. Clearly, at this level of description internal chain modes are ignored. The idea of replacing an entire chain with one degree of freedom is in the spirit of recent "super coarse-graining" methods that substitute a single fictitious particle for the entire polymer chain [154]. For short chains, soft ellipsoidal particles are able to accurately predict long-time unentangled Rouse dynamics [158], but as the chains get longer correctly modeling the interparticle interactions to recover both the equilibrium structure and the dynamics is very difficult [154, 159]. Our goal is to investigate whether such a radical reduction of degrees of freedom is able to accurately predict, from first principles, various entanglement phenomena. Certainly for studying the crossover from unentangled to entangled behavior such an approach is well known to be sensible from simulation-based primitive-path analyses of the topology-preserving network that defines the melt. In such analyses each chain is represented by rod-like primitive path segments, and entanglements correspond to the intersection of these rod-like segments as different polymers wrap around each other. Crucially, in a melt of chains with $N < N_e$ there are no entanglements and a primitive path analysis results in a liquid of rigid rods with mean length equal to the average polymer end-to-end distance [160, 161]. In the same spirit as the PP-step-based calculation above, one would expect this mapping to correctly capture the crossover behavior of relatively short chains.

Our specific implementation of the super coarse-graining idea is to identify the average long axis of an instantaneous chain conformation with the mean rod length, schematically illustrated in the inset of Fig. 5.1. This acknowledges that instantaneous polymer conformations are quite anisotropic. Using simulation data from Ref. [162] to quantify this anisotropy,

a flexible chain is coarse-grained to a needle of length $L \approx \sigma\sqrt{N/1.3}$. The dimensionless coupling constant of the needle theory can thus be expressed as $\rho L^3 \approx \sigma\sqrt{N}/(1.481p)$. The number of segments in an entanglement strand follows from our prior prediction for the crossover density $\rho_e L^3 \approx 10.1$, defined as the intersection between a regime of independent binary collisions and a regime of reptative scaling behavior [139]. We note that this value of the crossover density corresponds to having of order 10 entangled chains within an end-to-end distance of a given chain. Combining the calculated crossover density with the relation between length and number of segments yields $N_e \approx 244(p/\sigma)^2 = 244\rho_s p^3$, very close to the experimental finding of $N_e \approx 313\rho_s p^3$ [155]. The tube diameter can be independently predicted when $N >> N_e$ by identifying the tube radius with the transverse localization length of the rod CM [17, 139], a surrogate for the localization of a PP step. The result is $d_T = 2r_l = 2\frac{8\sqrt{2}}{\pi\rho L^2} \approx 9.36p$, very similar to the PP analysis presented above. Finally, and perhaps most remarkably, this chain-to-needle mapping also results in an accurate tube confinement potential, as shown in Fig. 5.2, although here the normalized potential is weakly N/N_e-dependent, apparently in contrast to the simulations [30].

One additional issue needs consideration here, and that is the meaning of the bare diffusion constant, $D_{\perp,0}$, in this needle mapping. Since the theory already accounts for the topological uncrossability we need not worry about "entanglement friction" terms, but it is nonetheless true that the bare friction of a needle in solution and the mapped chain in a melt or solution should differ. Thus, we make the assumption that our theory treats additional effects due to topological uncrossability, and that the bare dynamics are Rouse-like: $D_{\perp,0} \to D_{Rouse}$. With this one can directly convert the diffusion constant as calculated for rods in Chapter 4 to predict the long-time CM diffusion of chains by using the transverse diffusion of a needle as a surrogate for the rotational diffusion of the chain. Since the theory for needles predicts in the high-density limit that $D_\perp/D_{\perp,0} \simeq 18\pi(\rho L^3)^{-2} \to 0.55N_e/N$, one obtains $D_{CM} = 0.55D_{Rouse} \cdot N_e/N$. This is remarkably close to the Doi-Edwards result $D_{CM} = D_{Rouse}N_e/3N$, [Doi1986] where the error is consistent with our underprediction

of N_e. Again making a Fickian assumption that there is no decoupling between diffusion and viscosity one gets back $\tau_{rot}/\tau_{Rouse} = D_{Rouse}/D_{CM} \approx 1.8N/N_e$, again just as would be expected by the phenomenological model and with the same slight prefactor error. This ansatz suggests a possible simulation-based test of our proposed mapping: one could study the dynamics of fluids of entangled rods whose length is allowed to fluctuate according to the statistics of the end-to-end vector of an ideal chain, $L \to L(t)$, and compare them with known data on flexible chains.

5.3 Coarse-Grained Star Polymers

One of the great successes of tube theories is that they can be extended to polymer architectures other than linear chains, in particular to branched macromolecules [16]; one can ask if our formalism is similarly flexible. Previously we showed that the Szamel theory can be successfully extended to topologically entangled 3D crosses, a rigid coarse-grained analog of a six-arm star-branched polymer [141]. Combining the exact results from simulations, $D_{CM,cross} \sim \exp(-0.42\rho L^3)$ [122, 123], with the super coarse-grained mapping proposed above, we can study stars composed of six flexible chain arms. However, one would expect our prediction for the self-diffusion of a star to be wrong since tube theories argue that it is dominated by branch point hopping events triggered by arm-retraction, leading to $D_{CM,cross} \sim \exp(-\nu N_a/N_e)$, where $\nu \approx 0.6$ and the important quantity is the degree of entanglement of *the arms* [16]. Re-expressing the reduced cross density in terms of the arm-lengths, and applying our mapping, we predict a density-fluctuation-mediated activated star CM diffusion constant of:

$$D_{CM,cross} \sim \exp(-0.42(\rho L^3)_{cross}) \sim \exp\left(-0.42\frac{\rho_s}{6N_a}\left(\frac{2\sigma\sqrt{N_a}}{\sqrt{1.3}}\right)^3\right) \sim \exp\left(-0.38\frac{\sigma}{p}\sqrt{N_a}\right). \tag{5.8}$$

Using the experimental $\sigma/p \approx \sqrt{313/N_e}$ [155], this implies $D_{CM,cross} \sim \exp\left(-6.7\sqrt{N_a/N_e}\right)$. Formally this shows a weaker dependence on arm length than is experimentally observed, but the large prefactor in the exponent implies this new mode of motion is unimportant until $6.7\sqrt{N_a/N_e} \approx \nu N/N_e$. The latter condition corresponds to arm lengths with $N_a/N_e \geq 100$, well beyond the experimentally-studied regime of exponentially slow dynamics [163]. In this sense the mapping is not inconsistent: our secondary branch-point-hopping mechanism is hidden by a faster relaxation mechanism not yet taken into account in our theoretical approach.

5.4 Summary

In summary, we have constructed a first-principles microscopic theory for the dynamics of entangled polymers at the primitive-path level, self-consistently renormalizing interchain PP interactions to define an effective dynamic confining potential. This advance responds to a major outstanding theoretical challenge in the understanding of highly entangled polymer chain dynamics [23]. Furthermore, we have gone beyond computing only a particular moment of the transverse displacement distribution to construct the full anharmonic confinement potential. The close agreement between the theoretical confining potential and simulation at the primitive-path level suggests a potential application of our work in improving slip-link model simulations by replacing the harmonic springs typically employed to mimic entanglement constraints. This direction may be particularly important for nonlinear rheology, where the question of how large deformations soften, or even destroy, the confining tube is a frontier issue [140, 144, 147, 152, 164]. Another potential application of our present work is a microscopic investigation of the "rubbery plateau" modulus, one of the key experimental manifestations of entanglement in long chains. Here, a long-standing and theoretically difficult issue is the relative importance of bonded and non-bonded stresses (or intra- and inter-chain interactions) in determining the plateau modulus and stress relaxation

functions [12, 165–167]. Different decompositions of the stress appear to all be proportional to the total stress at long enough times, suggesting that the usual Doi-Edwards assumption that intrachain terms dominate might be reasonable up to a (large) numerical prefactor. However, simulations also find that the magnitude and sign of the interchain terms is much more compatible with the total contribution to the stress [167], and how these different stress storage contributions change under deformation could be quite different. We discuss this issue in some detail in Chapter 7.

Finally, a potential advantage of our mapping perspective is that the underlying microscopic theory provides a tractable conceptual and computational framework to implement specific modifications to the basic tube-reptation model. For instance, the effect of contour length fluctuations can be modeled by allowing the length of the PP steps (or the mapped needle in the super coarse-graining) to be stochastically sampled from Gaussian length fluctuations, while keeping the mean value fixed at the equilibrium length. We also anticipate that our prediction of anharmonic transverse confinement may have deep implications for how the tube model is modified when large stresses or shear rates are applied to flexible chain liquids, as we demonstrated recently under large amplitude step-strain for entangled needle fluids [168].

Chapter 6

SHEAR RHEOLOGY OF RODS

6.1 Introduction

[1]In this chapter we build upon our quiescent theory for the transverse, topologically-induced confinement of rigid rods to try to study such systems under applied deformations. Understanding the rheological behavior of heavily-entangled polymer melts and solutions has been an outstanding theoretical challenge for many decades. The key issue is that when the polymers become sufficiently long and/or dense the dominant obstacles to relaxation are "topological entanglements," the dynamical constraints that arise from polymer connectivity and uncrossability. As discussed in previous chapters, encoding these constraints in a rigorous microscopic theory is exceptionally challenging. For many decades, the primary framework for studying entangled polymer dynamics has been the phenomenological reptation-tube model of de Gennes [15], Doi and Edwards [12], and its many recent extensions [16]. This single-chain approach is based on an ansatz for a mean-field that encodes the effect of the surrounding chains with an infinitely strong confining tube around the tagged chain, but it is not self-consistently constructed. Constrained in this way, long time relaxation and mass transport can only proceed via one-dimensional curvilinear diffusion of the polymer (a chain or rigid rod) along the tube axis, and from this starting point one can go on to predict a variety of viscoelastic and time-dependent phenomena.

For monodisperse melts and concentrated solutions of chains in equilibrium the reptation-

[1]This chapter contains text and figures reprinted with permission from *D. M. Sussman and K. S. Schweizer, Macromolecules* **45** *3270 (2012)*, Copyright ACS 2012; *D. M. Sussman and K. S. Schweizer, J. Rheology; submitted 2012.*

tube model has had many successes. The simplest version of the theory predicts, for instance, scaling laws for the relaxation time and the self-diffusion with increasing chain length that are close to experimental observations in the heavily-entangled regime. Elaborations on the theory that incorporate additional competing relaxation processes, such as constraint release and contour length fluctuations [169], can bring the theory into essentially quantitative agreement with many linear response experiments and some non-linear rheology measurements, based on employing a few adjustable parameters. Impressively, the tube approach can be generalized to treat a variety of polymeric architectures, from rigid rods to branched macromolecules such as stars and combs [16]. However, when applied to nonlinear rheology the reptation-tube approach must invoke additional strong assumptions and approximations. These effectively involve making guesses for the true nature of entanglements and tube confinement potentials. For example, nonlinear step-strain experiments are treated by picturing physical entanglements as chemical crosslink of effectively infinite strength, allowing very rapid retraction of stretched chains, and assuming a quiescent reptation process relaxes chain orientation. A notable success of the theory for this deformation is the prediction of an accurate damping function, defined as $h(\gamma) = G(t > \tau_x, \gamma)/G(t > \tau_x, \gamma_0 << 1)$, where $G(t, \gamma) = \sigma(t, \gamma)/\gamma$ is the ratio between the shear stress σ and the applied strain γ, and τ_x is a crossover time often cited as of order the longest Rouse relaxation time [12].

In continuous shear, the original Doi-Edwards theory predicts an unphysically large degree of shear thinning at high deformation rates due to affine-deformation polymer "over-orientation." To address this issue, additional qualitative modifications to the theory must be invoked. The most promising is "convective constraint release" (CCR), which posits that that fast flows can mechanically convect the many entangled chains surrounding a tagged polymer at a rate set by the imposed shear rate, effectively releasing constraints to its motion faster than the bare tube theory would predict based on quiescent reptation. The essential idea behind CCR, schematically, is to modify the polymer relaxation rate under flow as $\tau^{-1} = \tau_q^{-1} + \dot{\gamma}$, where τ_q is the quiescent relaxation time and $\dot{\gamma}$ is the flow rate [170].

Present implementations of CCR include more sophisticated changes to the relaxation time that depend on deformation time and history, contour length fluctuations, and other factors [16, 169, 170]. The CCR idea can "cure" the shear-thinning problem in the original reptation-tube theory at the cost of an additional fitting parameter, but issues still remain. For instance, many of the ideas that have worked so well in describing simple shear flow seem to fail to describe experimental data in extensional flow, a rather puzzling situation [171]. Additionally, there is some ambiguity about the physical meaning of the mathematical terms CCR adds to the tube model [23].

Another set of poorly understood issues concerns the strength of the physical entanglements that collectively define the confining tube potential. The standard tube-model assumption that the tube can provide an infinite restoring force, i.e. mimic unbreakable chemical crosslinks, cannot be literally true, but the relevant question is whether such an approximation is physically reasonable under deformation conditions of interest. Infinitely strong constraints would imply a tube diameter that does not change under deformation [12]. Subsequent work by others argued for the other two postulates: stress increases [16, 172] or decreases (for extensional deformation) [173] the tube diameter. This issue remains unresolved within the phenomenological tube-model framework, but recent simulations have found evidence for stress-induced tube widening ("dilation") or the reduction of entanglement upon extensional [152] or shear [164] deformation. There is also a growing body of evidence that the finite size of the entropic barrier to transverse motion is important [144, 174]. The most spectacular consequence of tube breakability under stress would be "microscopic yielding," in analogy with this well-accepted phenomena as observed in colloidal gels and glasses of all types [67, 69, 144, 175]. Even before tube destruction may occur, recent simulations support the idea that the tube is strongly and nonperturbatively deformed under flow conditions. For instance, atomistic simulations and primitive chain network slip-link studies of shear and extensional flows have found power-law reductions of steady-state number of entanglements and increased effective tube diameters [152, 164, 176]. This may be

a consequence of an effectively softer-than-harmonic tube, a feature observed in quiescent primitive-path simulation analysis of entangled chain melts [29] and experiments on biopolymers [25, 28]. Anharmonic softening may also be important for the power-law scaling of the "yield strain" (the value of strain at the stress overshoot), $\gamma_y \sim (\dot{\gamma}\tau_R)^{1/3}$, observed for Rouse Weissenberg numbers in excess of unity, $\dot{\gamma}\tau_R > 1$. This observation, first seen in solutions [144] and recently independently confirmed in melts [177], remains unexplained by any statistical mechanical theory, although a phenomenological force-imbalance-based scenario has been constructed [144].

In addition to the concerns they raised under quiescent conditions mentioned in previous chapters, recent perspective articles [22, 23] have emphasized the need for conceptual advances nonlinear driven conditions as well, particularly for the microscopic foundation of CCR and the way entanglements and tubes are modified by large deformations. To address such issues theoretically we choose to study a simpler model system - a solution of infinitely thin, non-rotating rods of length L. The Doi-Edwards (DE) theory for entangled rod-like polymers [12, 178] shares many features and predictions with the full flexible chain tube-based rheological theory, including an excessive shear thinning behavior at high shear rates, but to our knowledge CCR elaborations have not been developed for rigid-rod polymers. We find that by starting from a first-principles, microscopic perspective we naturally arrive at (i) a highly anharmonic transverse confining potential, and (ii) a way to include the effects of shear stress that leads to an emergent CCR-like behavior in continuous shear flows *without* the need to explicitly include additional relaxation mechanisms by hand. A key new feature is that under stress our microscopic theory involves relaxation in parallel via longitudinal reptative motion and transverse activated barrier hopping.

This chapter discusses the shear rheology of rigid rods under the two most important deformation conditions: instantaneous step-strains and continuous shear deformations. The remainder of the chapter is organized as follows. Chapter 4 has already discussed the key theoretical aspects for both quiescent and stressed conditions (self-diffusion constant, tube

diameter, dynamic confinement potential, incorporation of stress and orientation, concept and definition of "microscopic yielding"), including a full exposition of various analytically-derivable results and a new analysis of entanglement onset. Section 6.2 briefly discusses the initial consequences of stress and orientation immediately after an instantaneous step-shear strain, including how the tube dilates and is possibly destroyed. Section 6.3 presents calculations of the two competing relaxation times (relevant for all shear deformations) from knowledge of the dynamic confinement potential's dependence on degree of entanglement and strain amplitude. Our theory for the time evolution of stress and rod orientation under nonlinear step-strain deformations is given in Section 6.4, along with numerical calculations. We emphasize that our treatment of nonlinear rheology is carried out under the assumption of homogeneous deformation, which ignores the possibility of constitutive instabilities (such as strain localization or shear banding) and macroscopically non-quiescent relaxation. A summary of our findings for instantaneous step strains is presented in Section 6.5.

Section 6.6 generalizes the step-strain model to continuous shear deformations. Our rheological theory has formal mathematical similiarities with the Doi-Edwards model, but there are qualitative physical differences associated with our ability to compute a time-, stress-, and strain-dependent effective relaxation time from the dynamic tube confinement potential. The model also introduces a second evolution equation governing the relaxation of orientation, which is nonlinearly coupled with stress relaxation, based on a modified version of the generalized Maxwell model used to study step strain deformations [168]. Section 6.7 presents calculations for different degrees of entanglement and constant deformation rates. We conclude in Sec. 6.8 with a brief summary and discussion.

6.2 Step-Strain Deformation: Initial State

An applied stress or strain results in both an effective force on the polymer CM and an external torque that orients rods. For a step shear strain, the initial induced stress and

orientation are treated via the standard assumption of affine deformation: an instantaneous shear strain of dimensionless amplitude γ results in a stress [12]

$$\sigma(t = 0^+) = \frac{3\rho k_B T \gamma}{(5 + \gamma^2)} = G_e \gamma h(\gamma), \tag{6.1}$$

where an approximate, but accurate, analytic form of the DE damping function, $h(\gamma)$, is utilized. The Lodge-Meissner relation is then used to relate the alignment angle to shear and normal stresses [12], resulting in an initial orientational order of

$$S(t = 0^+) = \frac{2}{-1 + 3\sqrt{1 + 4\gamma^{-2}}}. \tag{6.2}$$

Combining Eqs. 6.1 and 6.2 with 4.26, the combined effects of stress and orientation on the dynamic confinement potential can be determined as a function of applied strain.

Using Eqs. 4.22, 4.23, 4.28, the absolute yield strain corresponding to tube destruction then becomes a self-consistent equation which in the heavily entangled limit is:

$$\gamma_y = \frac{\sigma_y(S(\gamma_y))}{G_e} \simeq \frac{5}{3\sqrt{2}} \sqrt{1 - S(\gamma_y)}. \tag{6.3}$$

Employing Eq. 6.2 in Eq. 6.3, one finds $\gamma_y \approx 0.96$, which is modestly smaller than the result in Eq. 4.23 due to rod-alignment-induced weakening of the maximum tube confinement force. We note this precise value is subject to small errors owing to the approximations that enter the calculation of σ_y (cf. yield strain numbers below).

Figure 6.1 plots calculations of the initial change ($t = 0^+$) in the normalized localization length as a function of strain. The tube diameter is monotonically widened (dilated) by deformation due to the combined effect of applied stress and rod alignment. The inverse tube diameter decreases roughly linearly with strain over an extended range until the absolute yield strain is approached, beyond which the tube no longer exists. For a relatively modest degree of entanglement ($\rho/\rho_c = 10$), the tube is stable up $\gamma_y \sim 0.6$, and at higher degrees of

entanglement ($\rho/\rho_c = 1000$) it is stable up to $\gamma_y \approx 1.12$, comparable to the estimate in Sec. 4.6 based on an elastic solid model. The normalized initial tube radius can be analytically estimated from Eqs. 4.27, 6.1, 6.2; the result is shown as the uppermost curve in Fig. 6.1, and is an increasingly good approximation as rod density increases. The analytic form predicts a density-independent yield strain of $\gamma_y = 1.16$, quite close to the estimate in Sec. 4.6.

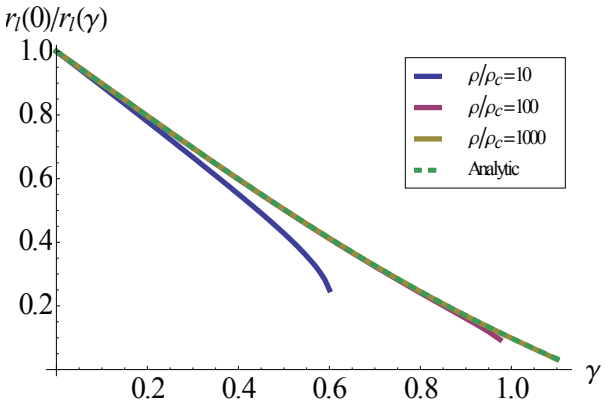

Figure 6.1: Inverse localization length (normalized by its quiescent value) at $t = 0^+$ after an instantaneous step strain of amplitude γ. From left to right the curves correspond to calculations at $\rho/\rho_c = 10,\ 100,\ 1000$, and the dashed curve (indistinguishable on the scale of this plot with the $\rho/\rho_c = 1000$ calculation) is the approximate prediction based on Eqs. 4.27, 6.1, 6.2.

6.3 Parallel Relaxation Mechanisms

Recall that the Doi-Edwards tube model assumes that for a step strain deformation of any amplitude, affinely-oriented rods relax via unperturbed quiescent reptation. As described below, our theory agrees with this picture for very low strain amplitudes. However, as the strain amplitude grows the initial stress and rod orientation increase, which we predict triggers tube dilation and thus speeds up reptation-driven rotational relaxation. In addition, the transverse entropic barrier is decreased, effectively "turning on" a competing activated hopping process where the lateral tube confinement can be dynamically surmounted. Moreover, the entire transverse confinement potential evolves in time in a manner that depends

on the degree of entanglement and strain.

6.3.1 Stress-Accelerated Reptation

Knowledge of the confinement potential allows microscopic predictions to be made for the two longest relaxation times as a function of density, stress and orientational order — the critical information required to describe nonlinear stress relaxation after a step-strain in our theory. In the quiescent heavily entangled state the terminal rotational relaxation time (which is controlled by the reptative process) is inversely proportional to the transverse diffusion constant [17, 139] $D_\perp/D_{\perp,0} \propto D_{rot}/D_{rot,0}$, and in the absence of stress one has

$$\tau_{rot}(\rho) = \frac{\tau_0}{36} \cdot \frac{D_{\perp,0}}{D_\perp(\rho)}, \tag{6.4}$$

where $\tau_0 = L^2/D_{||,0}$ is proportional to the fast (dilute-solution-like for rods [12]) CM longitudinal "reptation time." For notational clarity we will occasionally refer to the quiescent value of the terminal relaxation time (unmodified by stress or orienatation) by $\tau_{rot,q}$.

Including stress in the full dynamical calculation of the long-time transverse diffusion constant is a daunting task. For simplicity, we exploit the connection between τ_{rot}, $D_\perp$, and r_l to express the reptation-controlled rotational relaxation time in terms of the localization length, $\tau_{rot} \propto r_l^{-2}$. The effects of stress and orientation on r_l are then obtained from the confinement potential and related back to τ_{rot}. Since the tube dilates with increasing stress, the terminal rotational relaxation time is reduced as

$$\frac{\tau_{rot}(\rho, S, \sigma)}{\tau_{rot}(\rho, 0, 0)} = \left(\frac{r_l(\rho, 0, 0)}{r_l(\rho, S, \sigma)} \right)^2 \approx \left(\sqrt{1 - S} - \tilde{\sigma}/3(\rho/\rho_c) \right)^2, \tag{6.5}$$

where the limitations of the final approximate equality were discussed in section 4.7. The stress- and orientation-dependence of the tube potential can have dramatic consequences for the long-time dynamics because the transient localization length grows with S and σ. Specif-

ically, since $D_{rot} \propto D_{\perp} \propto \tau_{rot}^{-1} \propto (r_l/L)^2$, tube dilation can significantly accelerate reptative rotational relaxation and transverse diffusion, especially for heavily-entangled solutions near the absolute yield stress, σ_y.

Sample rotational relaxation times immediately after an instantaneous step-strain are plotted in Fig. 6.2 for three degrees of entanglement. The degree of stress-accelerated relaxation is heavily density-dependent, since $r_l(\rho, \sigma_y)/r_l(\rho, 0) \sim \sqrt{\rho L^3}$ at $\rho \gg \rho_c$, and hence the maximum enhancement of τ_{rot} increases linearly with ρ. As the absolute yield strain is approached the rotational relaxation time is predicted to accelerate by over two orders of magnitude for the most heavily entangled system. Figure 6.2 also shows the quantitative increase of the absolute yield strain with degree of entanglement, which ultimately saturates as $\rho/\rho_c \to \infty$.

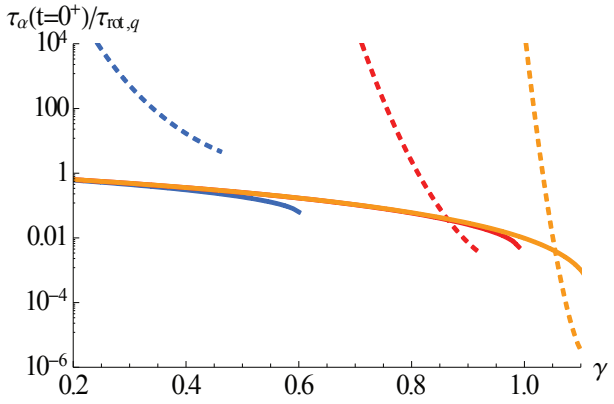

Figure 6.2: Log-linear plot of the initial mean transverse hopping (dashed) and terminal rotational relaxation (solid) times normalized by the quiescent terminal relaxation time given by Eq. 6.4. From left to right the curves correspond to calculations at $\rho/\rho_c = 10,\ 100,\ 1000$. The yield strains at these rod densities are $\gamma_y = 0.6,\ 1.0,\ 1.12$, respectively.

6.3.2 Activated Transverse Barrier Hopping

We also predict the emergence of a qualitatively new relaxation channel due to stress-reduction of the transverse entropic barrier. The characteristic rate of lateral barrier hopping

can be computed from Kramers' result for the mean first-passage time [90]:

$$\frac{\tau_{\perp,hop}(\rho,S,\sigma)}{\tau_0} = \frac{2\pi}{\sqrt{K_0 K_B}} e^{\beta F_B(\rho,S,\sigma)}, \tag{6.6}$$

where K_0 and K_B are the absolute magnitudes of the local curvatures at the confinement potential minimum and barrier location, respectively. We find that lateral hopping times become comparable to the reptation-controlled terminal relaxation process only when the barrier is relatively small (i.e. at high stress). In these cases, the relevant part of the quiescent tube potential is not the large-displacement logarithmic part, but rather the well-validated [139] quasi-linear regime. Nevertheless, analytic analysis of the low-stress regime is straightforward and yields important insight.

Recall that as a consequence of Eq. 4.14, for relatively low stresses the barrier is given by Eq. 4.20. Hence, for $\sigma \ll \sigma_y$ the hopping time decreases as a power law with an exponent determined by the degree of entanglement:

$$\tau_{\perp,hop} \propto (\sigma/\sigma_y)^{-\theta}, \tag{6.7}$$

where $\theta = 2(\rho/\rho_c - 1)$. Thus, while the lateral hopping time is astronomically long for low stress and high density, it decreases with stress at an enormously faster rate than the acceleration of τ_{rot}. Sample calculations of the hopping time as a function of strain amplitude are shown in Fig. 6.2.

Physically, as the strain approaches its absolute yield value entanglements and tube localization are destroyed, $F_B \to 0$, and the transverse hopping time must smoothly recover its "bare" value [92], $\tau_{\perp,hop} \to \tau_0$. In practice it is well known that Eq. 6.6 is a poor approximation as the barrier height approaches the thermal energy, and thus in Fig. 6.2 curves are shown only for $F_B \geq 1.5\ k_B T$. In the calculations below, when an activated hopping time is required under conditions where the barrier is lower than this threshold, as

a practical numerical approach we fix S and use a simple linear interpolation between the hopping time at the stress value that gives a barrier of 2 k_BT and the bare time τ_0 relevant at $\sigma = \sigma_y(S)$.

6.3.3 Stress-Modified Relaxation: Reptation Versus Transverse Barrier Hopping

Figure 6.2 compares the mean initial transverse barrier hopping (a tube-breaking event) and terminal rotational relaxation times after a step strain of variable amplitude, each normalized by the quiescent relaxation time, $\tau_{rot}(\rho)$, given by Eq. 6.4. The massive reduction of $\tau_{\perp,hop}$ relative to the comparatively weak tube-dilation effect on the rotational relaxation time is evident. Even for $\rho/\rho_c \sim 100-1000$, very high degrees of entanglement relevant to synthetic rods or stiff biopolymers (e.g., long PBLG synthetic rods and F-actin [25–27, 142]), entropic barriers can become sufficiently low that transverse hopping becomes faster than (tube-dilated) reptation at strains of order unity, which is well below the classic "over-orientation" stress maximum [12] at $\gamma = \sqrt{5}$.

Due to the strain-dependent competition between tube-dilated reptation and activated transverse hopping, three distinct dynamical regimes are predicted. (i) For γ/γ_y sufficiently less than unity, the hopping time is astronomically long relative to τ_{rot}, the transverse confinement is dynamically stable, and hence the quiescent reptation-tube picture remains essentially unchanged in accord with the Doi-Edwards theory. (ii) In the opposite limit of $\gamma > \gamma_y$, a microscopic instability-like, or "absolute yielding," phenomenon is predicted, defined by the complete destruction of the transverse barrier and hence the tube constraints. (iii) A third dynamical regime emerges at high-enough densities over an intermediate range of strains, in which the entropic barrier still exists but it is small enough that $\tau_{\perp,hop} < \tau_{rot}$. This regime occurs when, on average, the strain causes the entanglement network to collapse via transverse barrier hopping before reptative relaxation is completed. In the context of

structural glasses and gels, this behavior is often called "dynamic yielding" corresponding to achieving irreversible motion and flow via thermally-induced activation on the experimental time scale [65, 67–69]. These latter two regimes have no analog in classic tube theories.

6.4 Generalized Maxwell Model for Instantaneous Step Strains

6.4.1 Coupled Evolution Equations

We now consider the coupled nonlinear stress and orientational relaxation following an instantaneous shear strain. A minimalist generalized Maxwell model is adopted in which relaxation can proceed in parallel via reptation-controlled terminal rotational motion and transverse barrier hopping. Thus, at any moment we take the effective relaxation rate to be

$$\tau_{eff}^{-1}(t) = \tau_{rot}^{-1}(\rho, S(t), \sigma(t)) + \tau_{hop}^{-1}(\rho, S(t), \sigma(t)). \tag{6.8}$$

The coupling between the relaxation time and the system stress and orientational order renders the non-local-in-time integral representation of evolution equations unwieldy. Hence, we employ a time-local differential formulation. The evolution equations are formally first order in time, but highly nonlinear in stress and orientation due to the coupling via τ_{eff}:

$$\frac{d\sigma}{dt} = \frac{-\sigma(t)}{\tau_{eff}(t)}, \tag{6.9}$$

$$\frac{dS}{dt} = \frac{-S(t)}{\tau_{eff}(t)}. \tag{6.10}$$

Eqs. 6.8, 6.9, 6.10 assume a $1/e$ increment of stress and orientational relaxation associated with each type of dynamical event. While one can image countless variations on this assumption, as a first approximation it should correctly capture the qualitative implica-

tions of having two competing terminal relaxation processes. Eqs. 6.9 and 6.10 imply the logarithmic derivatives of the time dependent stress and orientation are equal, and hence $d(\log(\sigma/S))/dt = 0$. Thus, stress and S are proportional at all times, a type of stress-optical relation [12].

The key input to the evolution equations is the time evolution of the tube diameter, rotational reptation time, and transverse barrier-hopping time, which are all nonlinear functions of strain (their detailed properties were discussed in section 6.3. Extensive calculations of all aspects of the dynamic tube confinement potential and stress and orientational relaxation after step-strains have been performed over a wide range of strain amplitudes and degrees of entanglement. Results will be presented for $\rho/\rho_c = 10,\ 100,\ 1000$. The essential new physics emerges from the self-consistent, microscopically-computed connection between time-dependent stress, orientational order parameter, and characteristic single-rod relaxation times. The latter are directly connected to the dynamic confinement potential, most notably the tube diameter and entropic barrier height.

6.4.2 Nonequilibrium Relaxation of the Dynamic Confinement Potential

Figure 6.3 shows the time-dependence of the tube diameter after various step strains, both above and below the absolute yield strain. For very low strain amplitudes the tube diameter remains essentially unperturbed. At intermediate strain amplitudes below absolute yield there is a period of nearly constant tube dilation at short times, followed by a decrease to its quiescent value at long times. For large deformations the tube is initially completely destroyed (i.e. there is no lateral confinement force), and this state persists for some finite period of time. As stress and orientation are relaxed the tube then eventually re-emerges and slowly grows back in ("heals") with increasing time, with the localization length monotonically approaching the quiescent value from above. Similarly, since the terminal rotational

time is linked to the tube diameter, $\tau_{rot} \sim r_l^{-2}$, it is initially much smaller than its quiescent value, which it approaches from below at long times. Since the rotational relaxation time and tube diameter are directly related, the former is plotted only for the highest degree of entanglement in Fig. 6.4a; for the other cases, τ_{rot} can be inferred from the behavior of the tube diameter. In contrast, the mean transverse barrier hopping time is initially very fast for large enough strains. Indeed, Fig. 6.4b shows that if the barrier initially vanishes after a large step strain the hopping time approaches the bare time, but then grows to astronomical values rather quickly as stress and rod orientation decay and entanglements are restored over short time scales. Note that Fig. 6.4b contains only two representative curves, both above the yield strain; the mean hopping time for lower strains is far off the scale of this plot (cf. Fig. 6.2).

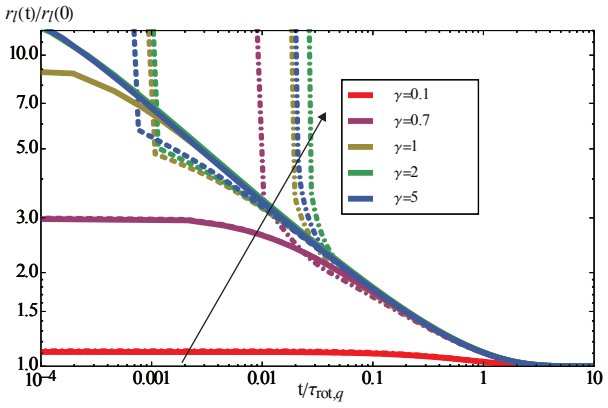

Figure 6.3: Time evolution of the normalized localization length or tube diameter for various initial strain amplitudes. Solid curves correspond to $\rho/\rho_c = 1000$, dashed curves to $\rho/\rho_c = 100$, and dash-dotted curves to $\rho/\rho_c = 10$. Read in the direction of the arrow, strain amplitudes are $\gamma = 0.1,\ 0.7,\ 1,\ 5,\ 2$.

Intriguingly, when the tube is initially either strongly dilated or destroyed, the temporal manner in which the tube diameter approaches its equilibrium value has an apparent power-law behavior, roughly independent of strain amplitude and degree of entanglement, over an intermediate time window (Fig. 6.3. The scaling is roughly $r_l \sim t^{-0.3}$, with higher densities supporting this behavior over an ever-larger time regime. This behavior implies a regime of power-law growth of the terminal reptative rotational relaxation time ($\tau_{rot} \sim t^{0.6}$) as the

entanglement network reforms, as seen in Fig. 6.4a.

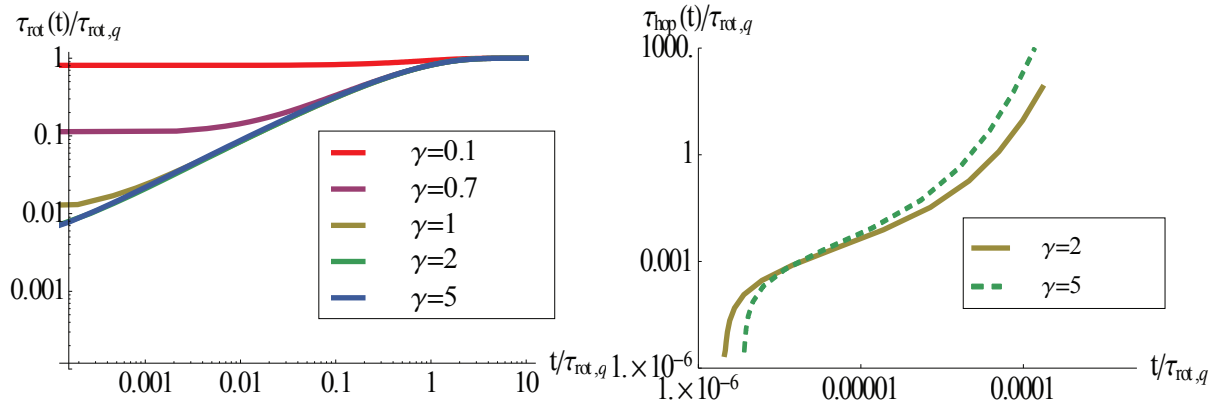

Figure 6.4: (A) Time evolution of the terminal rotational relaxation time (nondimensionalized by the quiescent terminal relaxation time) with increasing strain (top to bottom) at $\rho/\rho_c = 1000$. (B) Time evolution of normalized transverse hopping time for $\gamma = 2$ (solid curve) and $\gamma = 5$ (dashed curve) at $\rho/\rho_c = 1000$.

In those cases where the initial deformation is sufficient to destroy the entanglement network ("microscopic yielding"), the transverse hopping relaxation channel, which now proceeds on the short time scale of the bare relaxation time (Fig. 6.4b), rapidly relaxes both stress and orientation and allows the entanglement network to reform. The time t^* at which a tube first re-emerges when $\gamma > \gamma_y$ is plotted in Fig. 6.5. This time is a non-monotonic function of strain that reflects the non-monotonicity of the initial stress, $\sigma(t = 0^+)$. However, in all cases tube reformation occurs at a short time of order τ_0. The radius of the newly-reformed tube at t^* can be implicitly read off from Fig. 6.3. The main trends are that $r_l(t^*)$ becomes much larger with increasing rod density since (as discussed in section 4.6) at higher degrees of entanglement the tube can grow to a larger radius before being destroyed, i.e., $r_l(\rho, \sigma_y)/r_l(\rho, 0) \sim \sqrt{\rho L^3}$. Above the absolute yield strain there is a comparatively modest variation in $r_l(t^*)$ with increasing γ.

Entanglement-constraint healing can also be characterized by the growing back in of the maximum lateral confinement force after the tube has been initially destroyed by a large step strain. Even though the relation $f_{max} \sim k_B T/r_l$ in Eq. 4.22 was derived under equilibrium conditions, we find that it continues to be reasonably accurate numerically at high densities

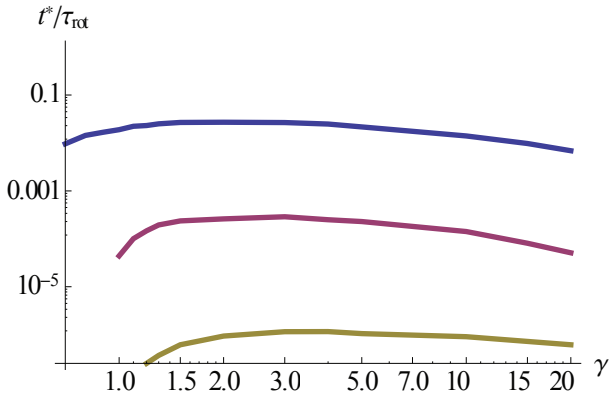

Figure 6.5: Normalized time at which the tube constraints first re-emerge for deformations $\gamma > \gamma_y$. From top to bottom the curves correspond $\rho/\rho_c = 10,\ 100,\ 1000$.

under large deformation conditions:

$$f_{max}\left(\rho \gg \rho_c, S(t), \sigma(t)\right) \sim r_l(\rho, S(t), \sigma(t))^{-1}. \tag{6.11}$$

Thus, the maximum transverse force also exhibits intermediate-time power-law healing kinetics, $f_{max} \sim t^{0.3}$, until enough time elapses for it to approach its quiescent value.

6.4.3 Nonlinear Stress and Orientation Relaxation

Figure 6.6 presents calculations of orientational relaxation, and Fig. 6.7 shows the dynamic nonlinear relaxation modulus, for three degrees of entanglement. Given that a stress-optical-like relation is obeyed by our theory, these two quantities are directly connected. Thus, we plot the orientational order in a log-linear fashion to highlight the return to single-exponential decay with time, and the modulus in a log-log plot to highlight the ultra-fast, short-time relaxation at high strains. Several trends are evident. For low dimensionless strains ($\gamma \ll 1$), the effective relaxation time is only very weakly perturbed from its equilibrium reptation value, resulting in essentially unmodified exponential decay of both $S(t)$ and $G(t)$. Note that if the time scale is nondimensionalized by the quiescent relaxation time there is only a very weak dependence on degree of entanglement, most readily seen in Fig. 6.6. This corresponds

to the Doi-Edwards scenario. However, we predict this behavior eventually breaks down due to modification of the tube potential by the imposed deformation.

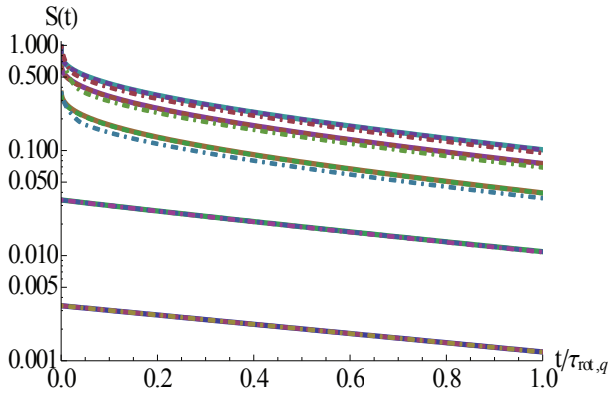

Figure 6.6: Log-linear plot of the decay of orientational order parameter after step strains of (top to bottom) γ =10, 5, 1, 0.5, 0.1, 0.01. Dash-dotted, dashed, and solid curves correspond to $\rho/\rho_c = 10,\ 100,\ 1000$, respectively.

At intermediate strains (but still $\gamma < \gamma_y$), acceleration of the terminal reptative rotational time is the first observable correction to quiescent relaxation, and at even higher strains much more dramatic effects emerge. In the latter case, a significant amount of stress and orientation relax on the bare time scale, τ_0, since the large deformation temporarily removes the transverse barrier and thereby allows very rapid relaxation until stress and orientation decrease sufficiently for the tube to reform. The separation in time scales between the quiescent terminal and bare times is greatest for larger degrees of entanglement, thereby allowing a clear short-time plateau in the relaxation modulus to be observed (Fig. 6.7a). This feature emerges due to an ultra-fast relaxation of stress, which then necessitates much slower rotational (or transverse diffusive) motions for further relaxation to continue as the entanglement constraints are re-established (cf. the very rapid growth of τ_{hop} in Fig. 6.4b). For weaker degrees of entanglement (Fig. 6.7b and 6.7c) well-developed stress plateaus are less apparent. Note that the apparent non-monotonicity of the height of the stress plateau as a function of strain for the two highest strain values in Fig. 6.7 is the result of our choice to normalize the curves by the strain-dependent $G(t = 0)$ instead of the entanglement

modulus G_e. Thus, in the results for the damping function discussed below no such non-monotonicity is present. In any event, in all cases of nonperturbative strain amplitude, Fig. 6.7 demonstrates that the relaxation of stress and orientation is strongly modified from the quiescent reptation behavior, in contrast to the Doi-Edwards model. Moreover, stress and orientation relaxation is highly nonexponential in time for two physical reasons: the tube constraints are time-dependent and there are two competing relaxation mechanisms.

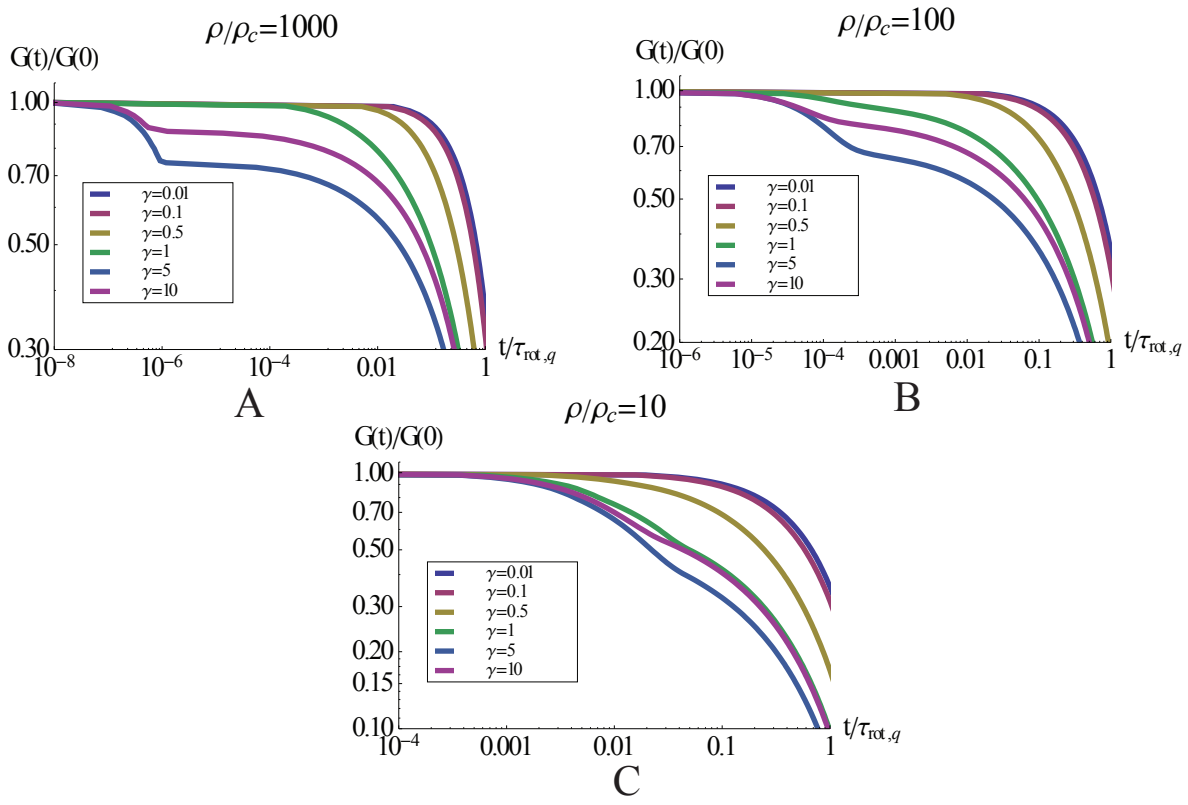

Figure 6.7: (A) Log-log plot of normalized stress relaxation modulus as a function of time at six strain amplitudes for (A) $\rho/\rho_c = 1000$ (B) $\rho/\rho_c = 100$ (C) $\rho/\rho_c = 10$.

6.4.4 Damping Function

Regardless of the strain amplitude or rod density, at long times both stress and orientation relax to low enough values that the tube reforms and purely exponential decay of stress and S occurs, characterized by the quiescent terminal relaxation time (inset of Fig. 6.8). This

allows an apparent damping function to be defined via superposition at long times as

$$h(\gamma) = G(t \to \infty, \gamma)/G(t \to \infty, \gamma_0), \tag{6.12}$$

where we have used $\gamma_0 = 10^{-3}$, and "$t \to \infty$" indicates a long enough time that superposition can be achieved. As seen in Fig. 6.8, since there are additional fast relaxation processes, qualitative departures from the classic DE damping function appear [12]. In particular, our damping function is not well-described as a Lorentzian, and decays with strain amplitude much faster due to stress- and orientation-induced dynamical softening of the tube potential. As a secondary effect, there is a very weak dependence of the damping function on density.

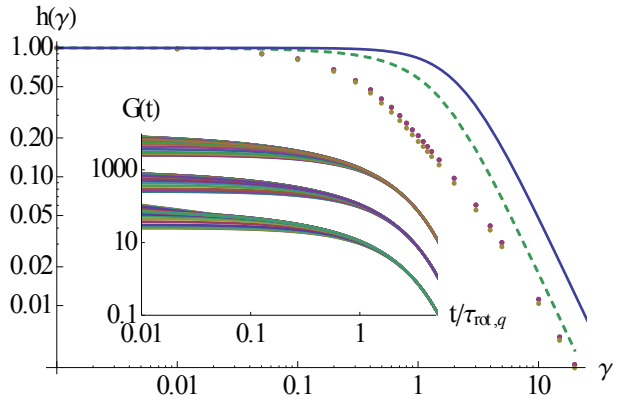

Figure 6.8: Log-log plot of the damping function (Eq. 6.12) at $\rho/\rho_c = 10,\ 100,\ 1000$ (points). The solid curve is the original DE $h = 5/(5+\gamma^2)$, and the dashed curve corresponds to the modified classic tube model that includes an orientation-dependent tube diameter (see text). Inset. Log-log superposition plot of the nonlinear relaxation modulus from which the damping function is determined.

To more thoroughly understand the physical origin of our predicted deviations from the Doi-Edwards theory, the calculations were repeated with modified input but still within an effective tube model framework. Specifically, in the original DE theory of entangled rods, a tube dilation effect can arise from orientational considerations in the more concentrated nematic-liquid-crystal regime [12]. This effect does not enter in the pure topologically entangled "semi-dilute" regime [178], but we can adopt this orientational-tube-dilation effect

to take into account transient, deformation-induced orientational order as discussed above. We have performed numerical calculations of a modified classic tube model analogous to the calculations in Sec. 6.4.1 where: (a) transverse activated barrier hopping was turned off by hand ($\tau_{hop} \to \infty$), but (b) the terminal rotational time was modified by orientation-dependent tube-dilation. We emphasize that in the context of our NLE theory, point (b) is equivalent to assuming that orientation modifies the tube confinement potential but stress does not. The damping function that results is shown in Fig. 6.8 as the dashed curve. While it differs from the classic DE prediction, functionally it is very similar in the sense that it is again well-described by a Lorentzian, $h(\gamma) \approx 2/(2+\gamma^2)$. The corresponding time evolution of stress is also more like the original DE model than our full theory since the nonlinear relaxation modulus never develops a plateau at short times. This is a consequence of τ_{rot} being accelerated via orientation but not including tube-breaking, transverse hopping events.

Given the above analysis, we can unambiguously conclude that the most dramatic new effects predicted by our theory of nonlinear stress relaxation are the direct result of the explicit and self-consistent coupling of the tube confinement field to stress, which results in both strongly accelerated reptative rotational relaxation and barrier-free lateral motion for deformations beyond the absolute yield strain. It is interesting to note that this explicit coupling of stress and confinement potential also underlies distinctive aspects of nonlinear relaxation and mechanical response in polymer and colloidal glasses within the NLE theory framework [65, 69].

6.5 Step-Strain Summary

We have now presented our self-consistent microscopic theory for the transverse tube confinement potential and dynamics of topologically entangled needle solutions under both equilibrium quiescent and nonequilibrium stressed conditions. In essence, we have attempted to statistically describe at the level of (impulsive) forces what an entanglement is and where a

confining tube comes from. The key physics of polymer connectivity and uncrossability is exactly taken into account at the 2-rod level, with three and higher body dynamical effects renormalizing the 2-rod entanglement problem in a self-consistent manner via single polymer diffusive motion [17,24]. An explicit accounting of dynamical uncrossability at the 2-rod level is the minimum level of description required to discuss entanglement, and is already beyond the single-chain reptation model where tube localization is postulated, not deduced.

Under quiescent conditions, and as discussed in Chapter 4, the theory predicts with quantitative accuracy: (i) a very sensible value of the number of interpenetrating rods required for the onset of entanglements and tube localization, (ii) perpendicular and rotational diffusion over the full range of rod densities [139] including agreement with the Doi-Edwards asymptotic scaling laws [12] and several computer simulations [20, 21], and (iii) key anharmonic features of the confinement field [139] observed in recent experiments on heavily entangled F-actin solutions [25] and more qualitatively in both DNA experiments [28] and primitive-path simulations of chain melts [29]. The anharmonicity of the confinement field is an emergent, not assumed, feature of our NLE approach which predicts that lateral tube constraints continuously weaken as a tagged polymer and its neighbors move.

The anharmonic nature of the transverse dynamical confinement potential has the important qualitative implication that there is a maximum restoring force keeping a tagged rod in its tube due to topological interactions with its surroundings, i.e., physical entanglements cannot always be literally treated as chemical crosslinks in rubber networks. In this sense, the theory might be viewed as having some features in common with venerable "transient network" models [149–151]. The consequences of a finite entanglement force are especially dramatic under applied deformation, leading to phenomena such as stress- and orientation-driven tube dilation, transverse entropic barrier reduction, and ultimately tube destruction beyond a critical level of stress or strain when the external force on a tagged rod exceeds the intrinsic entanglement force localizing the polymer in a tube. This last feature may be akin to empirical attempts to describe stress-dependent crosslinks in transient network

models [150,151], and recent experimentally-motivated physical ideas about force imbalance in entangled chain liquids [144,148].

By building on the above advances, we formulated a minimalist, generalized Maxwell model theory for stress and orientational relaxation after an instantaneous (and homogeneous) step-strain deformation. The richness of this theory arises from taking into account nonlinear couplings to a time- and deformation-dependent tube diameter, a maximum confinement force, and an entropic barrier. As a consequence, time- and deformation-dependent reptative rotational relaxation and transverse activated barrier hopping processes emerge as competing relaxation mechanisms. We predict both the acceleration of the terminal rotational time due to stress- and orientation-dependent tube dilation, and the emergence at sufficiently high deformations of a transverse barrier-hopping (tube breaking) relaxation process as a consequence of the highly anharmonic form of the dynamic confinement potential. These features result in an extended regime of strongly nonexponential stress relaxation after a step strain of sufficient magnitude. All these aspects are not present in classic reptation-tube models of topologically entangled rods.

An important finding is that beyond a large enough step strain, the tube is destroyed in a manner that can be thought of as an elastic instability or microscopic yielding event [144]. This results in a regime of ultra-fast relaxation of stress and orientation on a time scale much shorter than the (reptation-controlled) terminal relaxation time. After this initially very fast relaxation we predict that, as a consequence of the reduced levels of stress and orientation, the entanglement constraints re-emerge, resulting in the slower, reptative relaxation process again becoming dominant at long times. The approach to this state of quiescent reptation-tube dynamics is characterized by intriguing apparent power-law evolution, or healing kinetics, of the tube diameter, maximum entanglement force, and rotational relaxation time towards their quiescent values. An important consequence of including the stress-assisted transverse hopping process is the prediction of a qualitatively different damping function compared to the Doi-Edwards model.

For entangled chain solutions and melts, there has been a long ongoing debate about whether the tube diameter should couple to deformation [16]. Some researchers argue that in a step-strain deformation the competition between tube dilation and contraction should cancel and leave the tube diameter unchanged [170], the original simplifying assumption of Doi and Edwards [12]. Clearly, for rods we do not have the processes thought to govern one side of that competition - chain retraction dilating the tube. Other workers have proposed either tube dilation or contraction, which might depend on deformation type for flexible chains (e.g., shear versus extension), based on qualitatively different ansatzes [16, 173]. Our microscopic theory for rigid rods always predicts tube dilation under applied shear stress or strain as a direct consequence of the anharmonic nature of the quiescent dynamic tube potential. This result, and others we have obtained, suggests it is essential to self-consistently couple stress to the microscopic construction of the tube field, in analogy with the situation for colloid and polymer glasses [65, 68, 175, 179].

Unfortunately, there is a dearth of experimental data on the nonlinear rheological response (especially for step-strains) of high-aspect-ratio rod solutions in the isotropic state which could serve to test our theory. This presumably is in part due to the difficulty of studying such systems while avoiding the liquid crystalline regime. Nevertheless, this problem seems experimentally addressable based on synthetic or biological (e.g., microtubules) rigid rod polymers that interact via short range repulsive forces, and we encourage new measurements to be undertaken.

There is also very little computer simulation data for Brownian solutions of entangled rigid needles that can be used to incisively test our ideas, especially under nonlinear step strain conditions. For the quiescent topologically entangled needle system, there is a tentative study long ago by Doi [178] and a more recent work by Ramanathan and Morse [142]. This is surely a tractable problem for simulation, including the application of primitive path analysis under both quiescent [29] and highly deformed [164] conditions. We suggest that new simulations of the topologically entangled needle system be performed to critically test

the key features of our quiescent tube confinement potential, and its response to prescribed applied stress and imposed rod orientation. Our many predicted consequences of the latter on entanglement dynamics are also testable, such as how the terminal rotational relaxation time and tube diameter respond to stress and rod orientation, and the detailed time dependence of stress relaxation and various dynamical properties after a nonlinear step strain. Perhaps the most penetrating test would be to determine whether the tube can be completely destroyed beyond a critical strain (microscopic yielding), and, if so, the nature of its reformation-kinetics.

We note that some of our results seem intriguingly similar to the physical interpretations given by Wang and coworkers of recent rheology/microscopy studies of step-strain, startup shear, and creep nonlinear response of heavily entangled chain polymer liquids [144,147,148]. Specifically, the concept of a tube or entanglement network that has a finite strength related to the tube diameter (including the functional dependence of f_{max} on d_T), and the possibility of stress- or strain-induced microscopic yielding [144]. Of course, the nonlinear rheology of such systems is presumably influenced by processes not present in rigid rods, most notably chain stretch and retraction. However, it is interesting to recall that Doi and Edwards, in their seminal work, emphasized that most of the nonlinear rheological response predicted by their tube model is essentially the same for rods and chains based on the assumed rapid equilibration of chain stretch via fast Rouse dynamics [12, 178]. Efforts are underway to generalize our theory to apply to entangled flexible chains. Although this is a theoretically formidable task, preliminary results in equilibrium are discussed in Chapter 5.

6.6 Theory of Continuous Shear Deformations

Here we generalize this model to time-dependent shear deformations, where we must switch to an integral representation for the shear stress. Closely following the standard Doi-Edwards

prescription for a time-continuous shear deformation in the xy-plane [12,180], we begin with

$$\sigma(t) = G_e \int_{-\infty}^{t} dt' \left(\frac{d\psi(t-t')}{dt'} \right) Q[E(t,t')], \tag{6.13}$$

The plateau modulus for rigid rods is $G_e = 3\rho k_B T/5$, a very simple result that stems from the decay of single-rod orientational autocorrelations [12]. The key point is that even though the tube diameter is a function of orientation and stress, the elastic modulus is not; this contrasts sharply with what we expect for entangled flexible-chain liquids. The quantity $Q(x) \approx 5x/(5+x^2)$ is the classic deformation "over-orientation" factor, and E is the accumulated deformation that, for start-up shear deformations, is

$$E(t,t') = \int_{t'}^{t} dt'' \dot{\gamma}(t'') = \begin{cases} \dot{\gamma}(t-t'), & t' > 0 \\ \dot{\gamma}(t), & t' < 0 \end{cases}. \tag{6.14}$$

The normalized "tube survival" relaxation function ψ is taken to be the accumulated exponential relaxations along the two parallel channels:

$$\psi(t-t') = \exp\left(- \int_{t'}^{t} \frac{dt''}{\tau_{eff}(\rho, S(t''), \sigma(t''))} \right). \tag{6.15}$$

Note this "tube survival" function does not in general decay exponentially in time due to the orientation and stress dependence of the effective relaxation time. This is the crucial difference between our theory and the DE model. Undoing an integration-by-parts used to get to the above equation for σ gives

$$\sigma(t) = -G_e \int_{-\infty}^{t} dt' \psi(t-t') \frac{d}{dt'} Q[E(t,t')], \tag{6.16}$$

$$\frac{d}{dt'} Q(t,t') = \begin{cases} \dot{\gamma} - \dot{\gamma} dQ(x)/dx|_{x=\dot{\gamma}(t-t')}, & t' > 0 \\ 0, & t' < 0 \end{cases}. \tag{6.17}$$

Combining these expressions, the final expression for the stress of the system as a function of time is then:

$$\sigma(t) = G_e \dot{\gamma} \int_0^t dt' \left(\psi(t-t') \left[\frac{d}{dx} \left(\frac{5x}{x^2+5} \right) \right]_{x=\dot{\gamma}(t-t')} \right). \tag{6.18}$$

We now must generalize the evolution equation governing orientational order for time-dependent deformations, and we employ a simple, physically intuitive extension that reduces to our step-strain formalism in the limit of a very rapid, interrupted continuous shear deformation (physically distinguished from a step strain as a delta-function deformation). The initial value of the orientation following a step-strain is the result of a purely geometric (affine deformation) argument. For an arbitrary $\dot{\gamma}(t)$ in the absence of relaxation (i.e. in the limit where deformation occurs much faster than any relaxation process) one expects that after a total strain of $\gamma = \int_0^t \dot{\gamma}(t')dt'$ the orientation has built up to the same value it would have had after a step-strain of equal total amplitude. Evidently, then, in the absence of relaxation one has

$$\frac{dS}{dt} = \left(\left. \frac{dS_a}{d\gamma} \right|_{\gamma=\int_0^t \dot{\gamma}(t')dt'} \right) \dot{\gamma}(t) \tag{6.19}$$

where $S_a(\gamma)$ is the orientation that results from an affine deformation of strain γ,

$$S_a(\gamma) = \frac{-2\gamma}{\gamma - 3\sqrt{\gamma^2+4}}. \tag{6.20}$$

To reintroduce orientational relaxation we posit the following evolution equation:

$$\frac{dS}{dt} = \frac{-S(t)}{\tau_{eff}(\rho, S(t), \sigma(t))} + \left(\left. \frac{dS_a}{d\gamma} \right|_{\gamma=\gamma_{eff}} \right) \dot{\gamma}(t). \tag{6.21}$$

Here we have included the "relaxation" term exactly as in the previous step-strain calculation, but instead of evaluating the derivative of S_a at the total strain as in Eq. 6.19, it is evaluated at an *effective* value of the strain. This allows one to capture the intuition that,

as the orientation relaxes, the amount by which the deformation re-orients the rods depends more on the current state of the system than on some hypothetical state that exists in the absence of relaxation. As such, the theory is closed via the approximation of introducing an effective strain, γ_{eff}, which satisfies $S_a(\gamma_{eff}) = S(t)$. Explicitly inverting Eq. 6.20 gives

$$\gamma_{eff}(t) = \frac{3S(t)}{\sqrt{1 + S(t) - 2S^2(t)}}. \tag{6.22}$$

Note that, as desired, in the limit of $\tau_{eff}^{-1} \ll \dot{\gamma}$ one has $\gamma_{eff} \to \gamma = \int_0^t \dot{\gamma}(t')dt'$, and so Eq. 6.21 reduces to Eq. 6.19. Together Eqs. 6.18, 6.21, 6.22 form a set of coupled nonlinear equations, functionally coupled to the dynamic tube confinement potential, which govern the evolution of an entangled needle system under a general time-dependent shear deformation. These equations are solved numerically below for a constant deformation rate, $\dot{\gamma}(t) \to \dot{\gamma}$, and hence a strain $\gamma = \dot{\gamma}t$. The full transient response is obtained, during which stress, orientation, relaxation time, and tube confinement potential all evolve in a dynamically coupled and self-consistent manner.

6.7 Continuous Shear Results

6.7.1 Approach to Steady State

We now present numerical calculations of stress and orientational relaxation during a continuous startup shear deformation for two reduced densities which correspond to modestly ($\rho/\rho_c = 10$) and heavily-entangled ($\rho/\rho_c = 1000$) rod systems, at a variety of deformation rates. These reduced densities are relevant, e.g., to entangled solutions of long synthetic PBLG rods and semiflexible f-actin or rigid microtubules, respectively [12, 25]. An important limitation is the range of deformation rates we expect to be able to describe given that our theory has no mechanism for single rod motion to proceed faster than the "bare" time scale set by τ_0. In light of this, the computations are restricted to a range of flow rates

$\dot{\gamma}\tau_{rot,q} \lesssim (\tau_{rot,q}/\tau_0)$. Under quiescent conditions the separation in time scales between the terminal rotational relaxation time and the bare time is controlled by the ratio $D_\perp/D_{\perp,0}$, as in Eq. 6.4. This ratio is highly density-dependent: at $\rho/\rho_c = 10$, $(D_\perp/D_{\perp,0})^{-1} \approx 30$, whereas for $\rho/\rho_c = 1000$, $(D_\perp/D_{\perp,0})^{-1} \approx 1.6 \times 10^5$. Thus, we study the lower-density system at Weissenberg numbers up to $\mathrm{Wi} \equiv \dot{\gamma}\tau_{rot,q} = 50$ and the higher-density system up to $\mathrm{Wi} = 1000$.

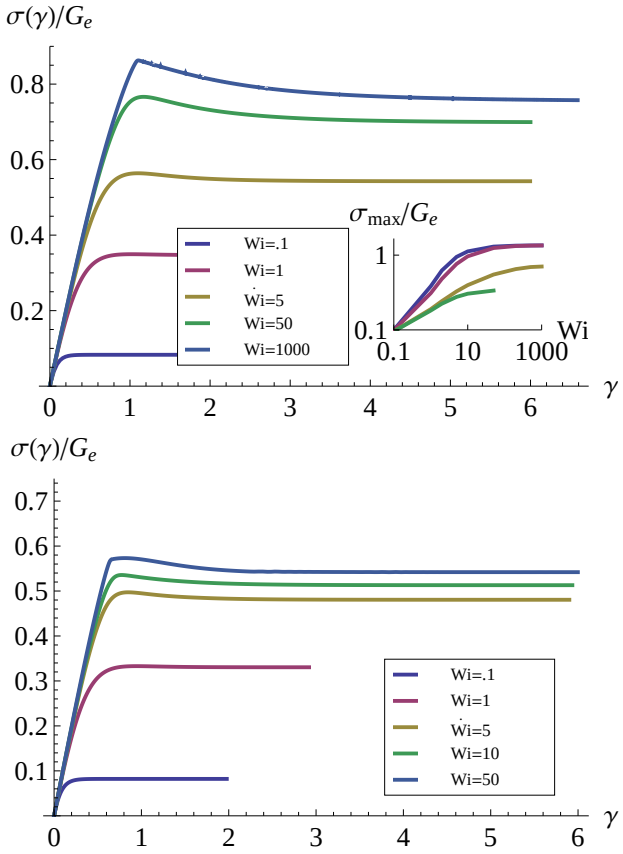

Figure 6.9: Stress normalized by the equilibrium shear modulus vs. strain at increasing deformation rates (bottom to top) for (A) $\rho/\rho_c = 1000$ and (B) $\rho/\rho_c = 10$. Inset of (A): Value of stress at the yield peak normalized by the entanglement modulus as a function of deformation rate. Curves are the calculation according to Doi-Edwards [12], orientation-modified Doi-Edwards, and the present work at high and low densities (top to bottom).

Figure 6.9 shows the stress normalized by the shear modulus as a function of accumulated strain curves for different shear rates. As the Weissenberg number exceeds a value of order unity, one sees the weak overshoot characteristic of entangled rod solutions; recall that in the

absence of chain stretch the stress overshoot is expected to be weaker here than for flexible chains [178]. The stress normalized curves in Fig. 6.9A and 6.9B at the two densities are very similar: at the lowest rate the normalized calculations would overlap, and at higher rates (subject to $\dot{\gamma}\tau_{rot,q} \lesssim (\tau_{rot,q}/\tau_0)$) there are only relatively minor differences in the region of crossover to steady state. In the inset to Fig. 6.9A the magnitude of the stress (overshoot or yield) peak vs. shear rate is plotted as a function of Weissenberg number. Qualitatively, a strong increase is predicted at low shear rates, followed by a slower approach to saturation at high Wi numbers. Overall, the behavior is very similar to the usual Doi-Edwards result [12], which is also shown in the figure, although with a lower magnitude due to our prediction that the tube confinement potential softens with increasing deformation. The corresponding "yield strain" is a weakly non-monotonic (concave down) function of imposed shear rate (not shown). For the high-density system we find $\gamma_y \approx 1 - 1.1$, quite close to the "absolute yield strain" estimated for this system for step-strain deformations [168]. For the lower-density fluid the peak is at $\gamma_y \approx 0.8 - 0.9$, slightly higher than the corresponding step-strain yield strain [168]. In all cases, the strain at the overshoot is smaller than the DE result of $\sqrt{5}$.

Figure 6.10 shows the growth of orientational order during the deformation. In contrast to the stress curves, there is no overshoot. This raises an important point: in our prior step-strain work the form of the generalized Maxwell model guaranteed a type of stress-optical law relation between stress and orientation [168], but here our use of γ_{eff} suggests that no such relationship will hold. Although the orientation does not go through a maximum, there does seem to be a qualitative change in its rate of growth at an accumulated strain close to the stress maximum. The absolute magnitude of S at high strains is also significantly smaller than predicted by Doi-Edwards theory (not shown), a trend that follows from our prediction that tube confinement self-consistently weakens with growing stress and rod alignment.

One can also study the microscopic dynamical state of the sheared fluid. In Fig. 6.11 calculations of the effective relaxation time normalized by its quiescent (reptation-controlled) value are shown. Strong acceleration of relaxation is generically predicted, which is more

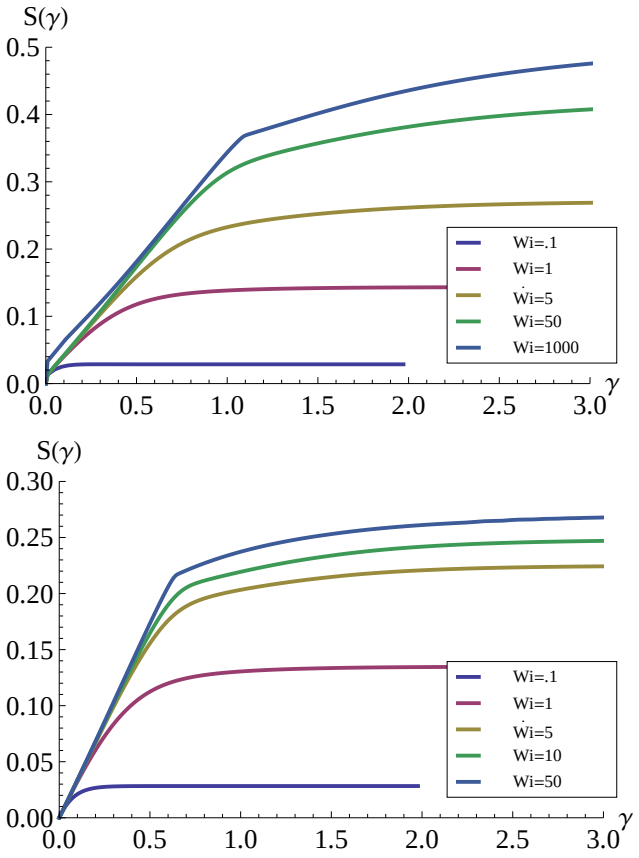

Figure 6.10: Orientational order parameter vs. strain at increasing deformation rates (bottom to top) for (A) $\rho/\rho_c = 1000$, and (B) $\rho/\rho_c = 10$

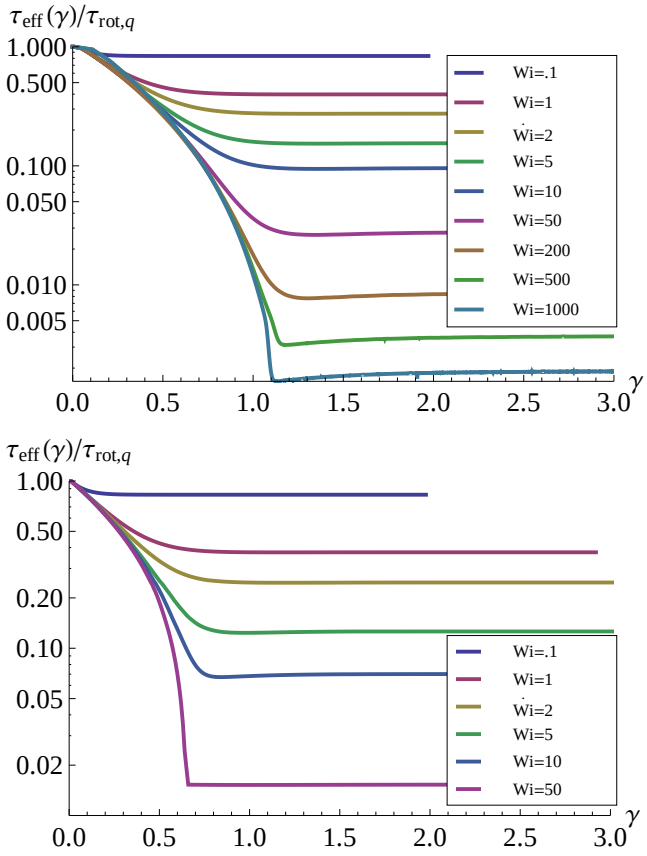

Figure 6.11: Effective relaxation time normalized by the quiescent terminal relaxation time as a function of strain at increasing deformation rates (top to bottom) for (A) $\rho/\rho_c = 1000$, and (B) $\rho/\rho_c = 10$

pronounced as the Weissenberg number increases. One also sees a weak undershoot at a strain close to the stress maximum for high Wi number. Figure 6.12 shows the relative importance of (accelerated) reptative relaxation and transverse barrier hopping. For the high density fluid, even up to very large rates there is still a substantial entropic barrier, and only at the highest rate is transverse activated hopping competitive with reptation. In contrast, the entanglement constraints are much weaker for the lower density fluid, and as a consequence at the fastest deformation rate studied we find the barrier to transverse motion (the tube) is completely destroyed. This is akin to a microscopic "absolute" yielding event, in the spirit of recent experimentally-motivated discussions for entangled chain polymer solutions and melts [144].

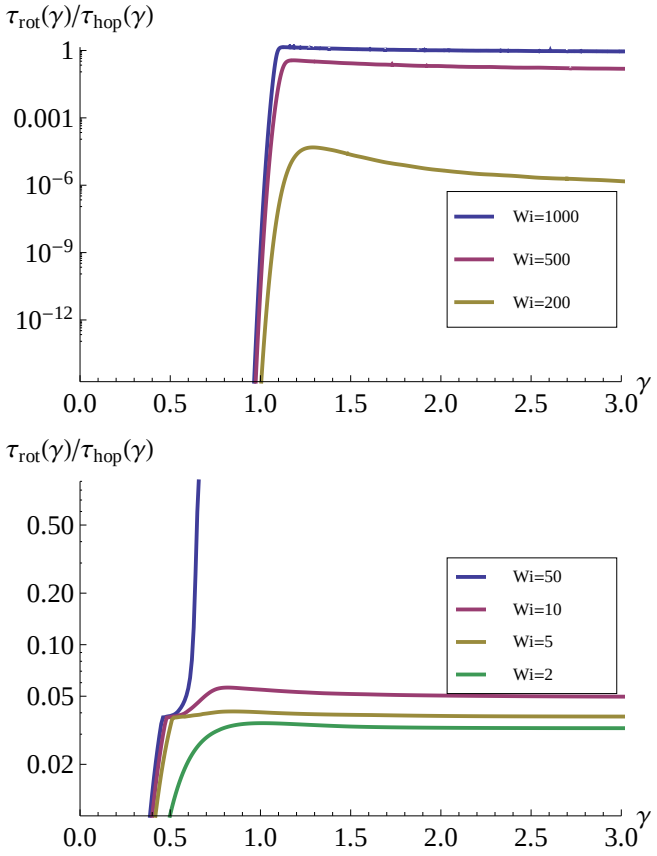

Figure 6.12: Ratio of mean transverse (tube breaking) hopping time to terminal reptative rotational relaxation time, τ_h/τ_{rot}, as a function of strain at increasing deformation rates (bottom to top) for (A) $\rho/\rho_c = 1000$, and (B) $\rho/\rho_c = 10$

The behavior described above is more explicitly documented in Figs. 6.13 and 6.14 in the context of key features of the tube confinement potential. Figure 6.13 shows the strain-evolution of the barrier height for a wide range of shear rates. The entropic barrier generically drops by orders of magnitude with increasing deformation rate. However, at the shear rates we study the high-density system always exhibits a transverse barrier large compared to thermal energy, in contrast to the more weakly entangled fluid. Figure 6.14 shows the concomitant widening (and breaking at high Wi for the lower density system) of the effective tube diameter during the deformation. Again, the long-time steady state value is achieved at a strain roughly equal to, or just beyond, the stress overshoot. Quantitatively, the tube diameter can widen by a highly nonperturbative factor depending on rod density and Wi number.

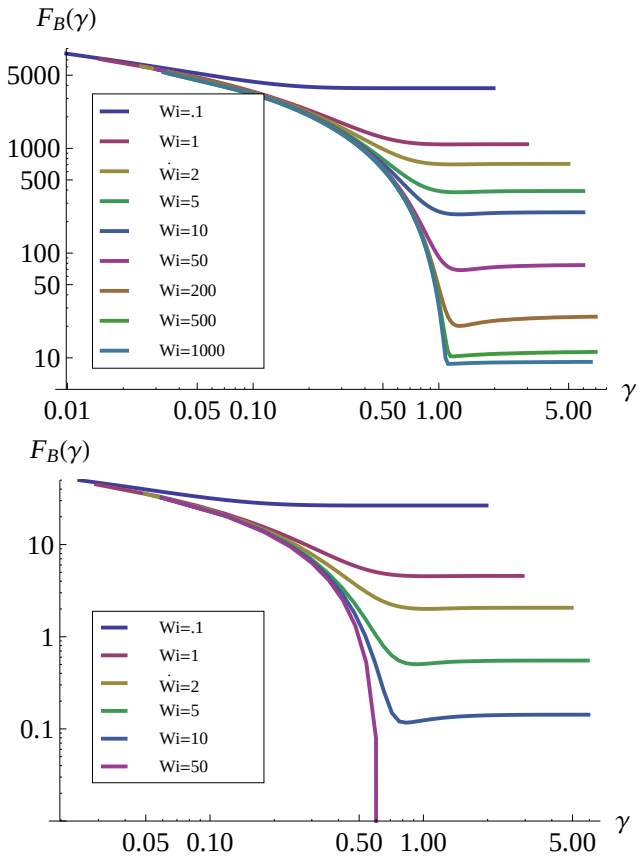

Figure 6.13: Entropic barrier height (in units of thermal energy) vs. strain at increasing deformation rates (top to bottom) for (A) $\rho/\rho_c = 1000$, and (B) $\rho/\rho_c = 10$

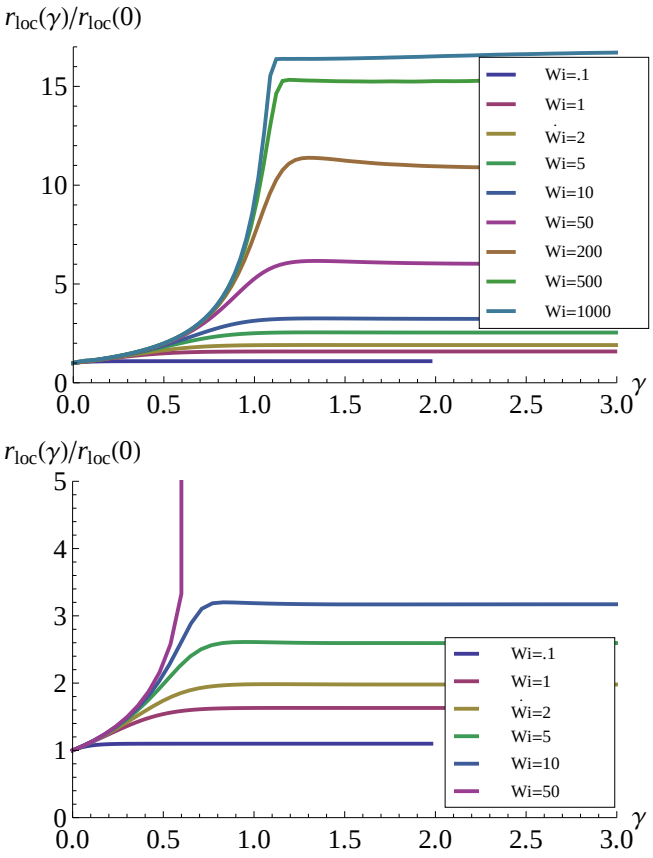

Figure 6.14: Ratio of the tube or localization length at fixed strain to its undeformed value,$r_l(\gamma)/r_l(0)$, as a function of strain at increasing deformation rates (bottom to top) for (A) $\rho/\rho_c = 1000$, and (B) $\rho/\rho_c = 10$

6.7.2 Steady State Properties

We now turn to the long-time, nonequilibrium steady-state properties. Perhaps our most dramatic finding is the flow curve shown in Fig. 6.15. In contrast to the Doi-Edwards model which displays an unphysical non-monotonicity at high deformation rate [12, 178], we predict a sensible plateau in the stress at both rod densities studied; the modulus-normalized limiting stress is only weakly dependent on rod density or quiescent degree of entanglement. This stress-plateau behavior is an emergent aspect of the theory that is a consequence of our microscopic, self-consistent construction of a deformation-dependent tube confinement field. Hence, it is quite different than the phenomenological CCR approach where an ansatz concerning many chain physics in strong flows is inserted into the single chain DE model. As previously done in our investigation of step-strain deformations [168], a Doi-Edwards-like calculation is also shown in Fig. 6.15 where the tube is allowed to dilate with orientation but which remains insensitive to stress. This delays the non-monotonicity to higher deformation rates, but does not remove the unphysical behavior. Thus, we conclude that the most dramatic predictions of our theory are primarily due to the self-consistent coupling of the macroscopic stress to the microscopic dynamical state of the tube confinement potential. Figure 6.16 shows the corresponding long-time orientational order parameter, which monotonically grows with strain rate. Though qualitatively similar, we note that our theory predicts much less steady state alignment under shear than the Doi-Edwards model, consistent with expectations based on Fig. 6.10.

The form of the stress plateau here is in some ways qualitatively similar to the modification of the tube-model to include CCR effects in systems of flexible chains. For example, in Fig. 6.17 the long-time value of the effective Weissenberg number, defined by $Wi_{eff} = \dot{\gamma}\tau_{eff}$, is plotted and a plateau is evident at Wi_{eff} of order unity. This suggests that the long-time value of the effective relaxation time scales roughly as $\tau_{eff,\infty} \sim \dot{\gamma}^{-1}$. Such a relation is essentially assumed in models of CCR [16], but here it is an emergent feature of our self-consistent

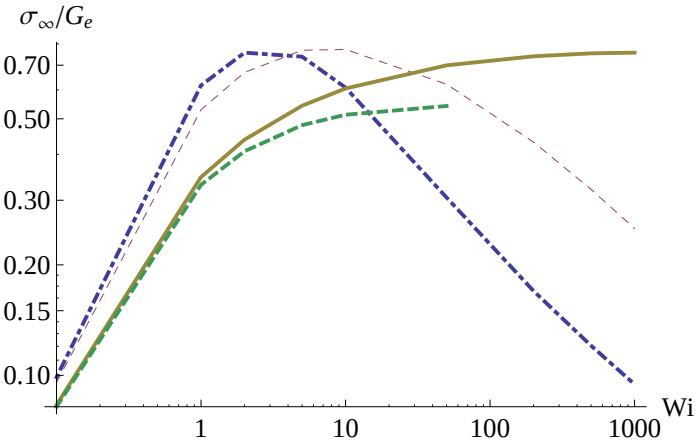

Figure 6.15: Normalized steady-state shear stress vs. strain rate. Curves are the calculation according to Doi-Edwards [12], orientation-modified Doi-Edwards (thin, dashed), and the present work at high (thick) and low densities (thick, dashed).

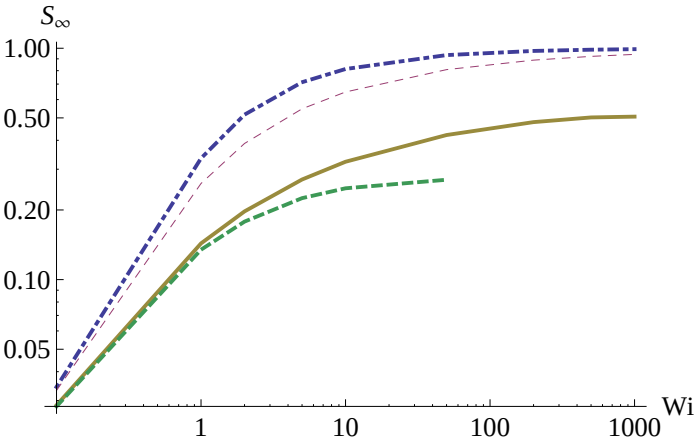

Figure 6.16: Steady-state orientational order vs. strain rate. Curves are the calculation according to Doi-Edwards [12], orientation-modified Doi-Edwards (thin, dashed), and the present work at high (thick) and low densities (thick, dashed).

treatment which allows the tube confinement field to evolve dynamically. To get a sense of when this CCR behavior emerges, in Fig. 6.18 the effective Weissenberg number is plotted as a function of strain for the high-density system. In all cases it is clear that the qualitative change in the behavior of Wi_{eff} from the initial behavior to the steady-state behavior occurs at a strain comparable in magnitude to the location of the yield or stress overshoot peak. Note that the full flow-induced modification of the relaxation time is not complete until a strain of order γ_y.

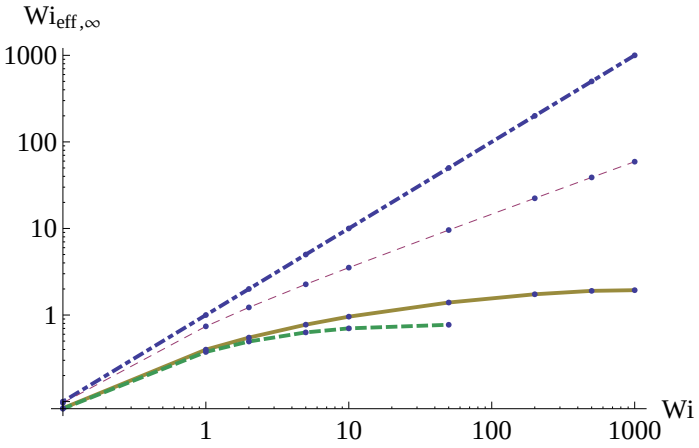

Figure 6.17: Effective Weissenberg number vs. strain rate. Curves are the calculation according to Doi-Edwards [12], orientation-modified Doi-Edwards (thin, dashed), and the present work at high (thick) and low densities (thick, dashed).

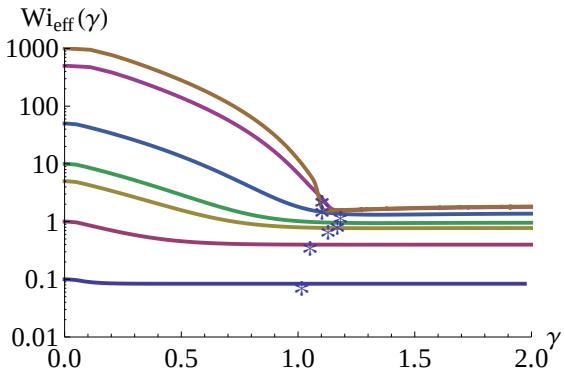

Figure 6.18: Effective Weissenberg number vs. accumulated strain for $\rho/\rho_c = 1000$. From bottom to top curves correspond to Wi $= 0.1, 1, 5, 10, 50, 500, 1000$, and the stars correspond to the value of strain at the stress maximum at each of those rates.

Figure 6.19 examines the steady-state tube diameter as a function of deformation rate.

After an initial complicated regime of tube widening, the transverse localization length continues to dilate in a power-law fashion, $r_l \sim Wi^{-0.4}$. Computing the localization length using the full calculation's steady-state degree of orientational order but neglecting the effects of stress, we can probe the relative importance of flow-induced orientation vs direct stress effects in dilating the tube. We find that the dominant effect comes from the direct stress effect - using only orientational order results in a power-law tube dilation with much smaller exponent, $r_l \sim Wi^{-0.05}$. Taking standard tube-model relationships between the tube diameter and the number of entanglements [12], this could similarly be interpreted as a power-law reduction in the number of effective entanglements, shown in the inset to Fig. 6.19. Intriguingly, precisely such power-law entanglement-reduction behaviors have been observed in simulations of flexible and semi-flexible chains under both shear and extensional deformation, although for these flexible-chain systems the observed power laws have smaller exponents than the ones we predict here [152, 164, 176].

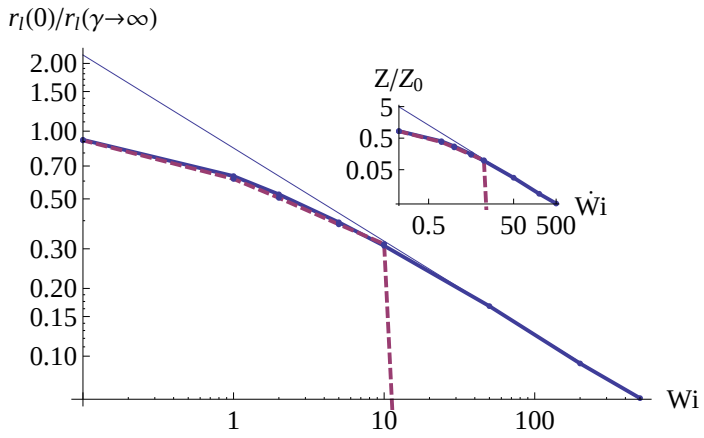

Figure 6.19: Inverse normalized steady-state localization length vs. strain rate. Curves are the high-density (thick) and low-density (dashed) calculations, plus a power-law guide to the eye with -0.4 Inset. Effective entanglement density vs. strain rate. Curves are the high-density (thick) and low-density (dashed) calculations, plus a power-law guide to the eye with -0.8

From the above discussion and the various figures showing both transient and steady-state properties, it is clear that there is a regime of flow rates for which the tube is no longer present: the stresses induced by the flow are sufficient to destroy it. This is seen for

the upper range of rates at $\rho/\rho_c = 10$, and would also be seen for the high-density fluid at higher rates. Interestingly, the behavior of the stress peak implies that there would be a (very narrow) range of flow rates at which the tube would be only *transiently* destroyed in the vicinity of the stress peak, but then would reform at a very weak level in steady state. However, we emphasize that the possibility of transient or permanent tube destruction are of only modest importance for the quantities we study. In the range of rates prescribed above, the main finding is that the tube is sufficiently softened for transverse activated barrier hopping to become competitive with (stress- and orientation-accelerated) longitudinal reptative relaxation. Even without tube destruction, it is this feature that underlies the qualitatively sensible CCR-like behavior seen in Fig. 6.15. For other quantities, such as the Wi-scaling of the location of the yield peak [144, 177], whether the tube is destroyed or not may be a more important question to address, but at least in the lower-density system in which we have studied a high-enough shear rate to destroy the tube, this occurs beyond the $\dot{\gamma}\tau_{rot} \lesssim (\tau_{rot}/\tau_0)$ limit we have imposed on our model.

6.8 Summary

We have generalized our microscopic theory of rigid macromolecules interacting via topological constraints to predict their nonlinear response under continuous shear deformation. Our earlier results for instantaneous step strains [168] are recovered in the limit of an interrupted continuous shear deformation that proceeds at very high rates for a small but nonzero amount of time. As a consequence of (i) the nonlinear coupling between stress, orientation, and effective relaxation rate via the tube confinement potential, and (ii) the introduction of a competing "transverse tube hopping" relaxation channel, a variety of novel phenomena are predicted. These include: (a) the strain and Weissenberg number dependent dilation of the tube in shear flows, (b) a purely monotonic growth, and ultimate apparent saturation, of the steady state stress with shear rate, (c) an emergent CCR-like phenomena

in which the terminal relaxation time is (nearly) inversely related to the shear rate, and (d) a decrease in the effective entanglement density under flow. Qualitatively these effects all seem consistent with recent experiments and simulations of entangled flexible chain polymer liquids [144, 164, 176]. Extending our theory to explicitly address flexible polymers instead of the rigid macromolecules is a formidable theoretical task but is presently under study.

Unfortunately, there is relatively little experimental data characterizing the response of high-aspect-ratio rod solutions in the isotropic state to continuous shear deformations. This would seem to be an experimentally accessible problem based on synthetic or biological rigid rod polymers (e.g., microtubule solutions [146,181]). Similarly there is little simulation data for the nonlinear rheology of Brownian solutions of entangled rigid needles. This is undoubtedly a tractable problem for computer simulation, and we suggest that new simulations of the topologically entangled needle system be performed to critically probe the key features of our quiescent tube confinement potential, its response to prescribed applied stress and rod orientation, and other predicted consequences of deformation on entanglement dynamics.

The next natural step in the development of our theory is to consider the relaxation of rigid-rod solutions under different deformation protocols. In particular, given the mysteries surrounding the observed differences between shear and extensional deformation experiments and simulations [12,152,171,176], formulating the theory to treat extensional deformation is a worthwhile direction of future study. However, we believe the task of highest importance is to extend of our approach to treat entangled flexible chain liquids. We have begun work in this direction based on a microscopic version of the classic DE ansatz of treating ideal coils as random walks of primitive path steps under equilibrium conditions (as discussed in Chapter 5). Generalization to nonlinear rheological conditions will at a minimum require introducing ideas about how chain stretching enters the problem. We anticipate it may also require a critical evaluation of how stress is stored, both at the intra- and inter-polymer level [165, 167].

Chapter 7

INTERMOLECULAR STRESS IN ENTANGLED POLYMER MELTS

7.1 Introduction

In adopting the classic Doi-Edwards expressions [12] for polymer stress under deformation in Chapter 6 a crucial question was glossed over. Namely, how is stress stored in dense liquids of extended macromolecules? There are many ways to pose this more specifically, but classic theories understand stress storage as a fundamentally *intra*molecular phenomena [12, 182]. Polymers are modeled as beads connected by entropic springs, and it is the deformation of these springs, or persistent orientational correlations of nearest-neighbor bond vectors, that contribute to the stress. The assumption is that entanglements do not themselves store stress, but that they do slow the relaxation of intrapolymer conformations. So, the direct effect of *inter*molecular interactions is taken to be negligible, but they can indirectly change stress storage by modifying the distribution and relaxation of polymer conformations. It has been suggested that the theoretical justification for neglecting the direct contribution stems from an incorrectly taken limit of an intermolecular separation vanishing while the bond vectors connecting the nearby beads remains finite [165]. More generally, from a historical perspective the problem of microscopically accounting for interchain forces has been viewed as intractable; thus, the possible role of direct interchain contributions to stress storage has generally been discarded a priori as a first step towards any theoretical description.

More concretely, in dense polymer melts the tube model [12] imagines the effect of interpolymer interactions to be the construction of the transverse confining tube, and in the rubbery plateau region of viscoelastic polymer response this tube significantly restricts how

a polymer can change from its initial orientation. Thus, in melts the tube model predicts that the $\alpha, \beta = x, y$, or z component of the stress tensor can be approximated by dyadic products of the bond vectors $b_i, \quad i = 1 \ldots N$ connecting the beads along a chain:

$$\sigma_{\alpha\beta} \approx \frac{3}{d_t^2 \beta} \sum_{j=1}^{N} b_i^\alpha b_j^\beta, \tag{7.1}$$

and the tube plays an important role in the behavior of the bond correlations. All of the predictions that the tube-model makes for the viscoelastic response of polymers to deformation rest upon this assumption, effectively adopting by ansatz the classic view of rubbery elasticity despite the absence of permanent chemical crosslinks. As an aside, it is interesting to note that the tube model was originally invented by Edwards and others to describe the interchain contributions to the elasticity of rubbers [183].

However, there is mounting evidence from simulations that this assumption may be deeply problematic. A series of MD simulations by Gao and Weiner revealed that for deviatoric stresses following a volume-preserving uniaxial extension the bond-vector contribution to the total stress was the minority contribution to the total stress (see, e.g., Refs. [166,184]). In fact, not only was the non-bonded contribution to the stress much larger and more commensurate with the total stress — at high, melt-like densities they found that the bonded contribution became negative [166]. Taking a slightly different perspective, Fixman divided the stress not into bonded and non-bonded contributions but rather into inter- and intramolecular components. This allows one to think about entangled polymers in the same conceptual framework as simple liquids, but generalized to have an intramolecular component. Contrary to the classical expectation, it was the intermolecular contribution that dominated [165].

More recent simulations have also been carried out, and the result is unambiguous: the bonded contribution to the stress in all (melt-density) cases is the minority component, and its sign is often wrong [167]. A natural question is how the theoretical situation could persist

— if the classic theories are approximating the stress storage with what seem from the above discussion to be inappropriate terms, why have the theories been able to describe any results at all? The answer lies is in another revelation of the simulations: even though the bonded contribution to the total stress is small and often of the wrong sign, at the intermediate and long times of interest (e.g. those times that correspond to the rubbery stress plateau) the bonded stress is *proportional* to the total stress [165–167]. Since the phenomenological tube theory has an arbitrary prefactor built into it (the tube diameter), this proportionality can easily be absorbed into the theory. Certainly in the small-deformation, linear-response regime one might thus still expect the classic theory to be able to account for experimental observations, but for nonlinear deformations it is not at all clear that the way the stress is changed in the bonded (or intramolecular) terms at all follows the change in the non-bonded (or intermolecular) terms. Perhaps, then, the fact that the tube model needs so many additional ad hoc assumptions in the nonlinear regime [12, 16, 144] is not an accident.

In this chapter we explore the possibility of understanding stress at the intermolecular level as an alternative to adopting the classic tube-theory perspective of intramolecular dominance. The key quantity to compute is the stress relaxation modulus, $G(t)$, and as a first step we will be particularly interested in the "plateau" value of the modulus, G_e. We strive for a first-principles derivation of the experimental result that for flexible chain melts the plateau modulus can be written as $G_e \propto k_B T/p^3$, where $p = (\rho_s \sigma^2)^{-1}$ is again the invariant packing length. To date this result has been deduced from a scaling-law argument and as an experimental [155] or simulation-based [185] empiricism.

The rest of this chapter is organized as follows. Section 7.2 quickly reviews Fixman's expressions for $G(t)$, dividing it into intramolecular, intermolecular, and cross-correlation terms. Section 7.3 calculates the intermolecular stress contribution in four entangled systems: chains mapped to needles, chains mapped to random walks of primitive-path steps, rigid rods, and rigid three-dimensional crosses. Section 7.4 discusses a way to study the effects of orientational order via a general deformation tensor, demonstrating the technique with

a calculation of potential relevance to polymer thin films. Section 7.5 closes with a brief discussion.

7.2 Microscopic Shear Stress Relaxation Modulus

At the molecular level the modulus can be written as [165]

$$G(t) = \beta^{-1}\rho N_b C_\infty(t), \tag{7.2}$$

where β is the inverse thermal energy, ρ is the number of molecules per unit volume, N_b is the number of bonds per molecule, and $C_\infty(t)$ is the $K \to \infty$ limit of

$$C_K(t) = \frac{\beta^2}{KN_b}\sum_{\nu,\lambda=1}^{K}\langle\sigma_\nu(0)\sigma_\lambda(t)\rangle_e. \tag{7.3}$$

In this expression ν, λ label different molecules and $\langle\cdots\rangle_e$ refers to an equilibrium ensemble average. We will restrict our attention to shear deformations, and so σ_α is the xy component of the stress associated with molecule α.

We adopt the Fixman stress perspective and begin by formally dividing the total stress into "internal" (intramolecular) and "external" (intermolecular) parts, $\sigma_\alpha = \sigma_\alpha^I + \sigma_\alpha^E$. At the center-of-mass (CM) level these contributions can be written as [165]

$$\sigma_\alpha^I = -\sum_{i=1}^{N}(\vec{r}_{\alpha,i} - \vec{r}_{\alpha_{CM}})\vec{F}_{i\alpha} \tag{7.4}$$

$$\sigma_\alpha^E = -\frac{1}{2}\sum_{\gamma=1}^{K}\vec{r}_{\alpha\gamma}\vec{F}_{\gamma,\alpha}. \tag{7.5}$$

Here $\vec{r}_{\alpha,i}$ is the position of monomer i on chain α, $\vec{r}_{\alpha_{CM}}$ is the CM position of chain α, $\vec{F}_{i\alpha}$ is the total force acting on monomer i of chain α, $\vec{r}_{\alpha\gamma}$ is the relative CM separation of chains α and γ, and $\vec{F}_{\gamma,\alpha}$ is the total force exerted on chain γ *by* chain α. Note that since $\vec{F}_{i\alpha}$ is

a *total* force acting on a monomer it implicitly includes some forces acting on the monomer from a different chain (and thus has both an intramolecular and intermolecular character; it is similar to a total deformational stress on the single chain), but that $\vec{F}_{\gamma,\alpha}$ is purely intermolecular. Since we are interested in the xy component of the stress tensor it is the x component of the forces and the y component of CM separations that we must calculated, denoted as $F^x_{\gamma\alpha}$ and $Y_{\alpha\gamma}$, respectively.

An expanded expression for $C_K(t)$ is then

$$C_K(t) = \frac{\beta^2}{KN_b} \sum_{\nu,\lambda=1}^{K} \langle \left(\sigma^I_\nu(0) + \sigma^E_\nu(0)\right) \left(\sigma^I_\lambda(t) + \sigma^E_\lambda(t)\right) \rangle_e. \tag{7.6}$$

We divide the modulus into the three physically distinct terms:

$$G(t) = G^{EE}(t) + G^{II}(t) + 2G^{IE}(t), \tag{7.7}$$

where

$$G^{EE}(t) = \frac{\rho\beta}{K} \sum_{\nu,\lambda=1}^{K} \langle \sigma^E_\nu(0)\sigma^E_\lambda(t) \rangle_e \tag{7.8}$$

$$G^{II}(t) = \frac{\rho\beta}{K} \sum_{\nu,\lambda=1}^{K} \langle \sigma^I_\nu(0)\sigma^I_\lambda(t) \rangle_e \tag{7.9}$$

$$G^{IE}(t) = \frac{\rho\beta}{K} \sum_{\nu,\lambda=1}^{K} \langle \sigma^I_\nu(0)\sigma^E_\lambda(t) \rangle_e. \tag{7.10}$$

These correspond to the direct intermolecular stress contributions, the direct internal chain stress contributions, and the intra-inter cross-correlations, respectively. In simulations that divided stress into bonded (b) and non-bonded (nb) contributions a ranking of relative importance in stress storage implied that nb-nb correlations dominated, nb-b cross terms were of intermediate importance, and finally b-b correlations contributed much less to the total stress [167]. Fixman's simulations for the relative importance of intra- and intermolec-

ular contributions did not explicitly study the cross terms, but nevertheless found that $G^{EE} \gg G^{II}$. In that spirit, we will approximate the total modulus by considering *solely* the intermolecular correlations, writing $G(t) \approx G^{EE}(t)$.

7.3 Calculating Intermolecular Stress Correlations

Our task is now the evaluation of the inter-chain stress correlations, starting from Eq. 7.8. The most immediate simplification comes from recognizing that under the ensemble average each chain contributes equally to the stress. Hence, one of the sums returns K identical terms; choosing $\nu = \alpha$ we have

$$\begin{aligned} G^{EE}(t) &= \rho\beta \sum_{\lambda=1}^{K} \langle \sigma_\alpha^E(0)\sigma_\lambda^E(t)\rangle_e \\ &= \rho\beta \sum_{\lambda=1}^{K} \left\langle \left[\frac{-1}{2}\sum_{\gamma=1}^{K} Y_{\alpha\gamma}(0)F_{\gamma\alpha}^x(0)\right] \cdot \left[\frac{-1}{2}\sum_{\mu=1}^{K} Y_{\lambda\mu}(t)F_{\mu\lambda}^x(t)\right] \right\rangle_e . \end{aligned} \tag{7.11}$$

This is a rather daunting number of terms, but under natural assumptions (together with the approximation of treating the polymers as infinitely thin PP segments) most of them can be ignored. To illustrate this, it is convenient to break up the sum as follows:

$$\begin{aligned} G^{EE}(t) = \frac{\rho\beta}{4} \Bigg[& 2\left\langle \sum_{\gamma,\mu} Y_{\alpha\gamma}(0)F_{\gamma\alpha}^x(0)Y_{\alpha\mu}(t)F_{\mu\alpha}^x(t)\right\rangle_e \\ & +2\left\langle \sum_{\substack{\lambda,\mu \\ \lambda,\mu\neq\alpha}} Y_{\alpha\mu}(0)F_{\mu\alpha}^x(0)Y_{\lambda\mu}(t)F_{\mu\lambda}^x(t)\right\rangle_e \\ & +\left\langle \sum_{\substack{\gamma,\lambda,\mu, \quad \gamma\neq\lambda,\mu \\ \lambda,\mu\neq\alpha; \ \lambda\neq\mu}} Y_{\alpha\gamma}(0)F_{\gamma\alpha}^x(0)Y_{\lambda\mu}(t)F_{\mu\lambda}^x(t)\right\rangle_e \Bigg] . \end{aligned} \tag{7.12}$$

The first sum comes from setting $\lambda = \alpha$ or $\mu = \alpha$ (hence the factor of two); the second sum contains terms where $\gamma = \lambda$ or $\gamma = \mu$; the third sum is everything else. A cartoon of

these different types of correlations is shown in Fig. 7.1. Physically, the first sum is a self-consistent renormalization of strictly binary (two-chain) interactions, the second sum treats the correlations of a tagged chain with different nearby chains at different times, and the third sum involves the correlation between a collision at $t = 0$ with a collision of *a different pair of chains* at a later time.

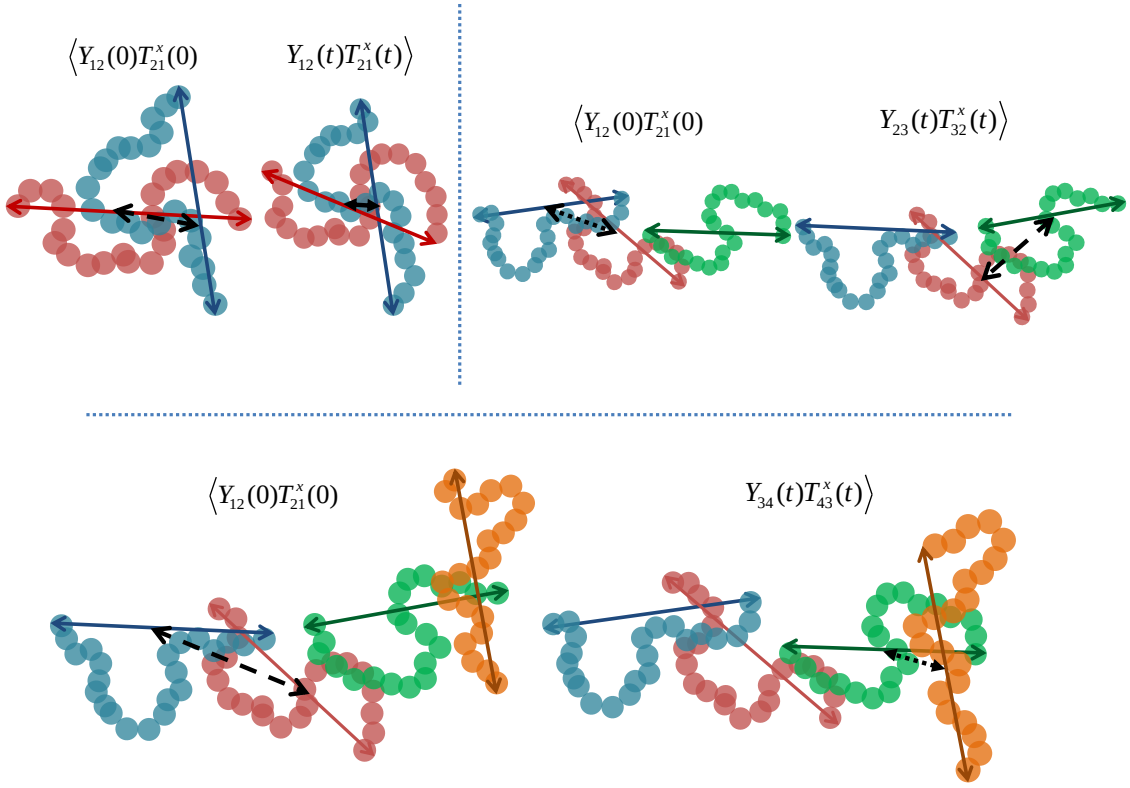

Figure 7.1: Cartoon schematically corresponding to the terms in the first (top left), second (top right), and third (bottom) sums in Eq. 7.12. Cartoons on the left and right of each box correspond to $t = 0$ and some later t, respectively. Colored lines represent polymer end-to-end vectors, and black lines connect polymers whose y-component CM separation and x-component interchain forces must be calculated.

To get a physical and mathematical intuition for why, given the approximations we make, the second and third set of sums vanish (i.e. decay before the plateau regime), it helps to observe that later we will make a Gaussian-like closure of factorizing the four-point correlation functions into products of two-point functions. Most simply, then, terms like

$\langle Y_{\alpha\beta}(0)Y_{\gamma\delta}(t)\rangle\langle F^x_{\alpha\beta}(0)F^x_{\gamma\delta}(t)\rangle = 0$ vanish if $\alpha,\ \beta,\ \gamma,\ \delta$ are all different: even in the rubbery stress-plateau regimes, the relative separations of *different pairs* of molecules become uncorrelated over the time-scale to explore the tube, τ_e, and the topological interactions are similarly uncorrelated. Crucially, this time scale is shorter than the plateau regime of interest, and so the third sum in Eq. 7.12 vanishes. The second sum is also negligible: $\langle F^x_{\alpha\beta}(0)F^x_{\alpha\gamma}(t)\rangle$=0 because in the "thread" limit of purely topological interactions we neglect 3-rod (3-chain) interactions, thus $F^x_{\alpha\beta}$ and $F^x_{\alpha\gamma}$ are again uncorrelated over timescales related to τ_e. This consideration of the force correlations of course also applies to the 4-rod interactions in the third sum. We note that simulations of thin but finite-excluded-volume chains suggest that the terms we are neglecting here are indeed quantitatively small compared the terms we keep [165, 186].

We are left with the first sum, but for the same reason just outlined we need only consider the terms for which $\gamma = \mu$:

$$G^{EE}(t) = \frac{\rho\beta}{2}\left\langle \sum_{\gamma=1}^{K} Y_{\alpha\gamma}(0)Y_{\alpha\gamma}(t)F^x_{\gamma\alpha}(0)F^x_{\gamma\alpha}(t)\right\rangle_e . \tag{7.13}$$

Each term in this sum is identical, so to simplify we bring out a factor of K and we replace the now-fixed Greek indices with (arbitrarily) molecules 1 and 2. Finally, we factorize the four-point correlation into a product of two-point correlations, but we must be careful about how we define the averages. Naively splitting $\langle Y_{12}(0)Y_{12}(t)F^x_{12}(0)F^x_{12}(t)\rangle_e = \langle Y_{12}(0)Y_{12}(t)\rangle_e \langle F^x_{12}(0)F^x_{12}(t)\rangle_e$ would be incorrect: the ensemble average of $Y_{12}(0)Y_{12}(t)$ vanishes because most of the average would be involve considering two molecules arbitrarily far apart (whose motion would be uncorrelated over short times) and thus not part of the colliding processes (with nonzero intermolecular force terms) in which correlations persist. Hence we factorize the expression as

$$G^{EE}(t) \approx \frac{\rho K\beta}{2}\langle Y_{12}(0)Y_{12}(t)\rangle_c \langle F^x_{12}(0)F^x_{12}(t)\rangle_e , \tag{7.14}$$

where the conditional average over the CM separation, denoted by $\langle \cdots \rangle_c$, is an ensemble average over the configurations in which the molecules are colliding, i.e. in contact with each other. This consideration respects the fact that the true $G(t)$ contains "beyond two-point-correlator" information. This result is now specialized (i.e. the constrained and ensemble averages are evaluated) for coarse-grained linear and star polymers; for rigid rod suspensions it is shown that this intermolecular contribution is unimportant. The essential argument that will be made in those systems is that the intermolecular terms, Eq. 7.8, actually decay *more quickly* than the intramolecular contribution, Eq. 7.9. The fact that intermolecular correlations may persist just as long as intramolecular ones for entangled flexible polymers [165–167,186] is an essential physical motivation for our considering the intermolecular terms in the above analysis.

Mapping chains to needles

Invoking the chain-to-rod mapping from Chapter 5 allows us to explicitly calculate the G^{EE} modulus in the localized regime under quenched-reptation conditions. We now calculate the two-point correlation functions from Eq. 7.14 individually.

At first the calculation of $\langle Y_{12}(0)Y_{12}(t\to\infty)\rangle_c \approx \langle Y_{12}^2(0)\rangle_c$ might seem to be a tractable-but-ungainly geometry problem ("What is the average y-component CM separation of two lines of length L that touch at any point?"), but fortunately we can use the T-operators themselves to impose the requirement in the constrained average that the two rods be in contact. That is,

$$\left\langle Y_{12}^2(0)\right\rangle_c = \frac{\int d\vec{u}_1 d\vec{u}_2 d\vec{r}\ \ (\hat{y}\cdot\vec{r})^2 T(12)}{\int d\vec{u}_1 d\vec{u}_2 d\vec{r}\ \ T(12)} \equiv \frac{A}{B} \tag{7.15}$$

The denominator is easiest to calculate. Recall that (in units where $L=1$) the T-operator is $T(12) = \delta(\vec{r}\cdot\hat{w})\Theta(1/2-|\alpha|)\Theta(1/2-|\beta|)$ expressed in coordinates where $\vec{r} = \alpha\vec{u}_1 + \beta\vec{u}_2 + \gamma\vec{w}$, a transformation with Jacobian $|J_1| = \sqrt{1-(\vec{u}_1\cdot\vec{u}_2)^2}$. The denominator can be expressed

and numerically calculated as

$$B = \int d\vec{u}_1 d\vec{u}_2 \; |J_1| \int_{-1/2}^{1/2} d\alpha \int_{-1/2}^{1/2} d\beta \approx 124.02. \tag{7.16}$$

With this formalism the numerator is not much more challenging:

$$A = \int d\vec{u}_1 d\vec{u}_2 \; |J_1| \int_{-1/2}^{1/2} d\alpha \int_{-1/2}^{1/2} d\beta \left(\alpha \vec{u}_1 \cdot \hat{y} + \beta \vec{u}_2 \cdot \hat{y}\right)^2 \approx 6.885, \tag{7.17}$$

and restoring units the result is

$$\left\langle Y_{12}^2(0) \right\rangle_c \approx \frac{A}{B} = 0.0555 L^2. \tag{7.18}$$

Calculating $\left\langle F_{12}^x(0) F_{12}^x(t) \right\rangle_e$ requires a bit more work, but is still straightforward. By definition of the ensemble average we start with

$$\begin{aligned} \left\langle F_{12}^x(0) F_{12}^x(t) \right\rangle_e &= \frac{\int d\vec{u}_1 d\vec{u}_2 d\vec{r} d\vec{R} \left[\hat{x} \cdot \overleftrightarrow{T} \left(\Omega_{loc}^{\dagger} \right)^{-1} \overleftrightarrow{T} \cdot \hat{x} \right]}{\int d\vec{u}_1 d\vec{u}_2 d\vec{r} d\vec{R}} \\ &= \frac{1}{\beta^2 16 \pi^2 V} \int d\vec{u}_1 d\vec{u}_2 d\vec{r} \left[\hat{x} \cdot \overleftrightarrow{T} \left(\Omega_{loc}^{\dagger} \right)^{-1} \overleftrightarrow{T} \cdot \hat{x} \right]. \end{aligned} \tag{7.19}$$

In this expression $\vec{R}$ is the CM of the two rods and $\overleftrightarrow{T} \, /\beta = \hat{w} T / \beta$ represents the force.

Making use of the variable transformations and approximations of Sec. 3.6 we can write

$$\begin{aligned}
&\int d\vec{u}_1 d\vec{u}_2 d\vec{r} \left[\hat{x} \cdot \overleftrightarrow{T} \left(\Omega_{loc}^{\dagger} \right)^{-1} \overleftrightarrow{T} \cdot \hat{x} \right] \\
&\qquad = \int d\vec{u}_1 d\vec{u}_2 (\hat{x} \cdot \hat{w})^2 \int d\vec{r}\, T \left(\Omega_{loc}^{\dagger} \right)^{-1} T \\
&\qquad = \int d\vec{u}_1 d\vec{u}_2 (\hat{x} \cdot \hat{w})^2 |J_1||J_2| \frac{L\sqrt{2}}{r_l^2} 2\frac{\sqrt{2}}{L} \int_{rhomb} G(x,y,0) dx dy \qquad (7.20) \\
&\qquad = \frac{4\sqrt{2}L^3}{r_l^2} F\left(\frac{L}{r_l}\right) \int d\vec{u}_1 d\vec{u}_2 (\hat{x} \cdot \hat{w})^2 |J_1| \\
&\qquad = \frac{4\sqrt{2}L^3}{r_l^2} F\left(\frac{L}{r_l}\right) \cdot (41.34)\,,
\end{aligned}$$

where in the above $|J_2| = L^2/4\sqrt{2}$, G and F are the functions described in Sec. 3.6, and the last integral has been done numerically. Combining this with with Eq. 7.19 yields

$$\left\langle F_{12}^x(0) F_{12}^x(t) \right\rangle_e = 4\sqrt{2} \frac{41.34 L^3}{16\beta^2\pi^2 V r_l^2} F\left(\frac{L}{r_l}\right) = \frac{1.481 L^3}{\beta^2 V r_l^2} F\left(\frac{L}{r_l}\right). \qquad (7.21)$$

Finally, combining Eqs. 7.14, 7.18, and 7.21 leads to this intermolecular-perspective's prediction for the entanglement modulus. Absorbing the factor K/V as another power of density gives

$$\begin{aligned}
G_e^{EE} &\approx \frac{\rho K \beta}{2} \left\langle Y_{12}(0) Y_{12}(t) \right\rangle_c \left\langle F_{12}^x(0) F_{12}^x(t) \right\rangle_e \\
&= \frac{\rho^2 \beta}{2} \left(0.0555 L^2\right) \left(\frac{1.481 L^3}{\beta^2 V r_l^2} F\left(\frac{L}{r_l}\right) \right) \\
&\underset{r_l \ll L}{\approx} (0.0205) k_B T \frac{(\rho L^2)^2}{r_l}, \qquad (7.22)
\end{aligned}$$

where in the last approximate equality the high-density limit $F\left(\frac{L}{r_l}\right) \approx r_l/(2L)$ from Chapters 3 and 4 has been invoked. The mapping results described in Chapter 5 give $r_l \approx 4.68p$ and $\rho L^2 \approx \rho_s \sigma^2/(1.3) \approx 1/(1.3p)$, where p is the invariant packing length, so the modulus

can be expressed as

$$G_e^{EE} \approx (0.0205)\frac{k_BT}{4.68 \times (1.3)^2 p^3} = 0.00259\frac{k_BT}{p^3}. \tag{7.23}$$

This is extremely close to experimental observations; Fetters et al. report the value of the plateau modulus to be $G_N^0 \approx 4B^2 k_BT/(5p^3) = 0.00256 k_BT/p^3$. We do not wish to overstate the quantitative accuracy of this result, especially given the approximations made and numerous neglected terms in Eq. 7.7. Nevertheless, we believe this to be a powerful demonstration of the predictive power of the microscopic, topological theory we have developed, and that it thus is a promising starting point for future investigations of nonlinear rheology.

We also note that a key prediction of our microscopic theory, the inverse relationship between the localization length and density, helps understand why the phenomenological single-chain picture leads to the correct scaling relation vis-a-vis experiments. Specifically, the high-density intermolecular contribution scales as

$$G_e^{EE} \propto \frac{k_BT\rho^2 L^4}{r_l} \propto \frac{k_BT\rho\sigma^2}{r_l^2} \propto \rho k_BT/N_e, \tag{7.24}$$

where in the second proportionality the crucial inverse relationship between density and the predicted localization length has been invoked. This allows the result to be cast in a single-chain form of an entirely *intra*molecular nature that is linear in the density and apparently involves a harmonic spring confining the chain on the scale of the tube diameter; in actuality the result stems from a detailed analysis of the intermolecular stress terms. This situation is analogous to the situation in colloidal glasses and gels, where the plateau modulus is entirely determined by intermolecular contributions (since there are no intramolecular terms!), but the result can nevertheless be written as $G_e \sim \rho k_BT(\sigma/r_l)^2$ [54, 68].

Coarse-grained chains as random walks of primitive paths

We here show that the above pleasing result is not merely the result of an accidental cancellation of errors arising from a vastly oversimplified coarse-graining. Making use of the results of the primitive path mapping from Chapter 5, it is straightforward to calculate the intermolecular entanglement modulus for a chain mapped to a random walk of PP steps, subject to all of the same approximations and discared terms above. The main result from the previous section is the factorized expression

$$G_e^{EE} \approx \frac{\rho K \beta}{2} \left\langle Y_{12}(0) Y_{12}(t) \right\rangle_c \left\langle F_{12}^x(0) F_{12}^x(t) \right\rangle . \tag{7.25}$$

The first term is again the y-component of the CM separation between two random walks subject to the constraint that they intersect. We make the assumption that these two random walks intersect in only one place (an approximation consistent with our earlier neglect of ternary PP interactions), in which case the result is

$$\left\langle Y_{12}(0) Y_{12}(t) \right\rangle_c \approx \left\langle Y_{12}^2 \right\rangle_c = \frac{Z L_e^2}{9}. \tag{7.26}$$

Deriving this is a straightforward exercise in the statistical mechanics of random walks; to first order, the square center of mass separation between the two chains is twice thesquare of the radius of gyration of a single chain ($R_g^2 = Z L_e^2/6$), and then the y component is one third of that.

The force-force correlation is more directly related to the calculation in the needle mapping. Consistent with the "single-intersection" approximation (or, alternately, with the idea that chain 2 only contributes to the confinement of one PP segment of chain 1, say, segment

i) one can write

$$\langle F_{12}^x(0)F_{12}^x(t)\rangle = \frac{1}{\beta^2 16\pi^2 V}\int d\vec{u}_i \sum_{j=1}^{Z} d\vec{u}_j d\vec{r}_{ij}\hat{x}\cdot \overleftrightarrow{T}(ij)(\Omega_{loc}^{\dagger})^{-1}\overleftrightarrow{T}(ij)\cdot\hat{x}. \quad (7.27)$$

$$= Z\frac{1.48L_e^3}{\beta^2 V r_l^2}F\left(\frac{L_e}{r_l}\right), \quad (7.28)$$

where the second line follows from noting that each term in the sum is identical and then evaluating the integral for rods of length L_e. As in Chapter 5, L_e and r_l are self consistently related, so combining this result with Eq. 7.26 yields

$$\begin{aligned}\frac{G_e^{EE}}{k_B T} &= \frac{\rho^2}{2}\frac{ZL_e^2}{9}Z\frac{1.481\times L_e^3}{r_l^2}F(A)\\ &= \frac{1.481}{18}\frac{\pi(AF(A))^2}{4\sqrt{2}}\frac{1}{p^3}\\ &= \frac{0.00593}{p^3},\end{aligned} \quad (7.29)$$

where in the last line the intuitive choice of $A = 2$ (primitive path step length equal to the tube diameter and hence twice the localization length) has been used. That is, whereas in Chapter 5 we used a different value to understand the distribution of monomers relative to the primitive path, here there is no need to mix and match monomer displacement and PP step length — we simply imagine the stress to be stored by the primitive path links. The result is, as before, strikingly close to the experimental result, and it is reassuring that this more detailed model leads to a quantitative *over*prediction of the stored stress (by roughly a factor of two): just as the neglect of rotational motions led us to overpredict the transverse confinement (i.e. underpredict the localization length), the same set of approximations should overpredict the value of the stress plateau.

Stress modulus for rigid crosses

We can apply the same formalism to work out the intermolecular entanglement modulus for crosses. Our model for the T-operator of a cross is the sum of the nine possible rod-rod interactions of two colliding crosses (precisely as in Chapter 3), and we again ignore all off-diagonal terms. From there it is straightforward to carry out calculations analogous to the above. The results are

$$\langle Y_{12}(0)Y_{12}(t)\rangle_c \approx 0.0555L^2, \tag{7.30}$$

$$\langle F^x_{12}(0)F^x_{12}(t)\rangle_e \approx \frac{8.2}{\beta^2 V}\frac{L^2}{r_l}, \tag{7.31}$$

where for crosses the localization length is $r_l = 4\sqrt{3}/(3\pi\rho L^2)$. Combining everything yields

$$G^E_{e,cross}E \approx 0.23k_BT\frac{(\rho L^2)^2}{r_l} = 0.3(\rho L^2)^3. \tag{7.32}$$

Can this calculation say anything about the linear response of star polymers? We use the proposed mapping between crosses and six-armed stars from Chapter 5, with $\rho L^2 = \frac{\rho_s}{6N_A}\left(2\sigma\sqrt{N_a/1.3}\right) \approx \frac{0.51}{p}$, to predict

$$G^{EE}_{e,6-star} \approx \frac{0.04k_BT}{p^3} \approx 16G^{EE}_{e,rod}. \tag{7.33}$$

This is quite far from the canonical $G_{e,6-star} \sim (N_e/N_a)G_{e,chain}$ relevant at the terminal time [187]. This is, however, consistent with the observation that our theory for a mapped cross neglects the primary motions which dominate transport (in Chapter 5) and here serve to relax the stress, and so we grossly over-predict the modulus. Unfortunately, the shear rheology of rigid crosses is an understudied problem, and so even this more straightforward prediction of our theory for crosses is untested. However, future simulations can directly address this issue.

Stress modulus in rigid rods

We close this section by briefly commenting on why this consideration of intermolecular stress is not important in suspensions of actual rigid rods, per the classic Doi-Edwards model. Of course the formalism of the Fixman stress tensor is still valid, and all of the terms we discarded in the sums over G_e^{II} are all still negligible. The question is why we can now also neglect the terms that were so important in the chain system, i.e. the $\langle Y_{12}(0)Y_{12}(t)F_{12}^x(0)F_{12}^x(t)\rangle_e$ terms. The important point here is that for mapped chains in the localized state, CM separation is still slow; reptation along the primitive path (which is the motional process on the timescale of interest) has very little effect on the CM separation of the two chains.

More specifically, the CM motion of a given chain in the tube is (from DE theory and experiments) both weaker than the segmental motion and still subdiffusive: $\langle r_{CM}^2(t)\rangle \sim t^{1/2}$. This weak time-dependence allows us to approximate $\langle Y_{12}(0)Y_{12}(t)\rangle \approx \langle Y_{12}(0)^2\rangle$. Consider by contrast the situation for thin rigid rods. Localization is enforced in the transverse direction, but longitudinal motion remains a bare diffusion process. Thus, for rods the intermolecular part decays rapidly as $\langle Y_{12}(0)Y_{12}(t)\rangle \sim \exp(-t/\tau_0)$, the *bare* diffusion time.

On the other hand, for rods we still must consider the *intra*molecular part of the stress tensor. A standard result [12, 142] is that one can split the intramolecular stress tensor for rods as

$$\sigma_{intra} = \sigma_{tens} + \sigma_{orient} = \rho \left\langle \int_0^t ds\ \mathcal{T}(s,t)\vec{u}(t)\vec{u}(t) \right\rangle + 3\rho k_B T \left\langle \vec{u}(t)\vec{u}(t- \overleftrightarrow{I}/3 \right\rangle. \quad (7.34)$$

The first term is tension in the rod induced by fluid flow (viscous stress), and the second term reflects orientational order (elastic stress). The shear stress modulus corresponding to these terms is

$$G(t) = \frac{\zeta_\parallel L^3}{180}\delta(t) + \frac{3}{5}\rho k_B T e^{-t/\tau_{rot}}. \quad (7.35)$$

The crucial point is that inter-rod interactions do not contribute directly to the stress, since they relax on a time scale $\tau_0 \ll \tau_{rot}$, but they indirectly enter by massively lengthening the rotational relaxation time. In a dilute solution τ_{rot} is proportional to the bare time, but it grows with density as $(\rho L^3)^2$. Thus, for dense rod suspensions there can be a plateau regime from this part of the modulus that decays much slower than the intermolecular contribution to the modulus does, and we have simply

$$G_{e,rod} = \frac{3}{5}\rho k_B T. \tag{7.36}$$

7.4 Polymer Films: A Toy Model

We now introduce a simple toy model of polymer thin films. Understanding how entanglements change under confinement is an active topic of research, and rheological measurements of the modulus are often the most straightforward way to probe the system [188]. In real films there is a complicated spatial dependence of chain orientation and conformation on the position of the polymer within the thin film. Our approach will be to calculate a film-averaged polymer behavior and then study a *bulk* reference fluid whose polymers all adopt this film-averaged anisotropic conformation and orientational order. This allows us to exploit our ability to describe the effect such changes have as in Chapters 4 – 6. We also make use of a more general deformation-tensor approach to describe these changes [12].

Simple models of random walks in confinement treat thin films by modifying the distribution of the out-of-plane component of the chain end-to-end vectors [189], and also sometimes treat confinement as inducing an effective discotic liquid-crystalline order [190]. Here we study the former model. The essential idea is that in the presence of a reflecting boundary the components of a random walk parallel to that boundary (which we take to be the x and y components) is unaffected, but the component perpendicular to the boundary (the z component) are reduced. The "principle of conformation transfer" [189] quantify-

ing this effect is depicted in Fig. 7.2A. The random walk through the points $ABCD'E'$ is equally probable with the walk through the points $A'B'CDE$, but both walks violate the constraint at the surface. Exchanging the sections $CD'E'$ and CDE between this pair of conformations leaves the local melt structure unchanged while returning two random walks that now respect the boundary condition imposed by the surface. Performing this procedure for every boundary-violating chain leads to an analytic prediction for the average change in the component of the end-to-end vector of the chain in the z-direction as a function of the position of the start of the chain (i.e. the chain endpoint closest to the wall at $z = 0$). Evidence from simulations and experiments suggests that this model of the changes to polymer conformation is an excellent first-order approximation [190–192]. The physical picture is schematically shown in Fig. 7.2B; the reduced spatial extent of chain conformations reduces the effective degree of entanglement between chains.

It is simplest to work out the consequences of such confinement effects on the modulus in the chain-to-needle mapping, where it instigates two changes. First, the magnitude of the end-to-end vector changes relative to its equilibrium value as

$$\frac{L(\alpha)}{L_{eq}} = \sqrt{\frac{2+\alpha^2}{3}}, \tag{7.37}$$

where α is defined by $R_{ee,z}(\alpha) = \alpha R_{ee,z}^{bulk}$. That is, the end-to-end vector shrinks a bit, and note that in G_e^{EE} four powers of L enter the final result. In real thin films the z-component of the end-to-end vector is a function of the position of the polymer CM relative to the film boundaries but again, in the spirit of trying to capture the first-order physics, we will average over this distribution and compute a single film-averaged value of α for the whole film.

Second, the changes in the end-to-end vectors induce a change in the angular distribution of the rods (i.e. if all of the z components are reduced the angular distribution is no longer isotropic). We can encode this using the "deformation tensor" formalism invoked

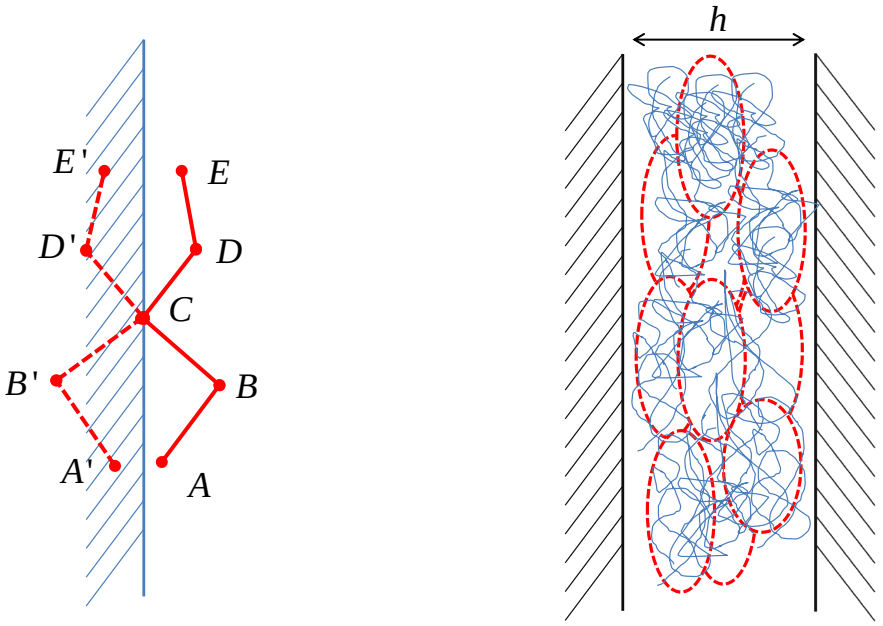

Figure 7.2: (Left) Silberberg's principle of conformational swapping near a wall (see text). Cartoon adapted from [189]. (Right) Cartoon of conformational change induced by a film of thickness h. On average, the polymers extend less in the direction of film thinness (qualitatively shown with the dotted ellipses), and there is a lower degree of chain overlap (i.e. entanglements) as a result.

to study the change of angular distribution under shear and extensional deformations in polymer liquids [12]. There the ensemble average of the vectors $\vec{u}$ are transformed by tensor $\overleftrightarrow{E}$ as $\vec{u} \rightarrow \overleftrightarrow{E} \cdot \vec{u}/|\overleftrightarrow{E} \cdot \vec{u}|$. Although analytic progress is possible only with particular forms of the deformation tensor, numerically carrying out the angular integrals in Sec. 7.3 over distributions of arbitrarily deformed orientations whose undeformed distribution was isotropic is straightforward. That is, $d\vec{u}$ is still $\sin\theta d\theta d\phi$, but the vectors $\vec{u}$ themselves in the integrals are replaced by the deformed vectors and the integral done with standard numerical techniques.

In the specific model of thin-film confinement the deformation tensor we need is

$$\overleftrightarrow{E}(\alpha) = \begin{pmatrix} 1 & 0 & 0 \\ 0 & 1 & 0 \\ 0 & 0 & \alpha \end{pmatrix}. \tag{7.38}$$

Note that this is *not* an affine deformation, as it is not volume preserving (i.e. in making the z component shrink we are not enforcing any kind of expansion of the x or y components). In any event, this allows us to numerically compute the modulus as a function of α. The final task is to relate α to an experimentally measurable/controllable quantity, the thickness of the film. For this we employ and extend the Silberberg approach.

Silberberg's original model was intended for relatively thick films, exactly solving a polymer random walk model with one reflecting boundary and then assuming the film was thick enough that the behavior in the center mimicked the bulk behavior (allowing the same calculation to apply to both halves of the film) [189]. That calculation solves for the z-component of the end-to-end vector as a function of polymer position; averaging it over the film thickness gives

$$\alpha(h) = \frac{6h - 8\sqrt{\frac{2}{\pi}} - 2e^{-\frac{h^2}{8}}\left(-4+h^2\right)\sqrt{\frac{2}{\pi}} + h^3 \mathrm{Erfc}\left[\frac{h}{2\sqrt{2}}\right]}{6h}, \tag{7.39}$$

where h is the total film thickness in units of the bulk $R_{ee,z}$. The full problem of two reflecting

boundaries can be solved by the method of images with an infinite series of images [193]. Computing the first correction is simple (if tedious), with the result

$$\begin{aligned}\alpha(h) &= \frac{e^{-2h^2}\sqrt{2}}{3h\sqrt{\pi}}\left(6 - e^{\frac{7h^2}{8}}\left(4 + 4e^{\frac{9h^2}{8}} - 3h^2 + e^{h^2}\left(-4 + h^2\right) + e^{\frac{5h^2}{8}}\left(2 + 4h^2\right)\right)\right) + 1 \\ &+ \frac{h^2}{6}\mathrm{Erfc}\left[\frac{h}{2\sqrt{2}}\right] + \left(1 + \frac{4h^2}{3}\right)\mathrm{Erfc}\left[\frac{h}{\sqrt{2}}\right] - \frac{3h^2}{2}\mathrm{Erfc}\left[\frac{3h}{2\sqrt{2}}\right] - 2\mathrm{Erfc}\left[\sqrt{2}h\right].\end{aligned} \tag{7.40}$$

Note that we have neglected the complication that the distribution of chain starts is not uniform in the film; by definition the leftmost end of a random walk is more common close to the left wall and quite unlikely near the right wall. We simply assume a uniform distribution — a reasonable approximation for thick films, but potentially problematic for $h \ll 1$. Figure 7.3 compares the result of the two analytic models with simulation data from simulated binary thin film polymer blends [194]. The most noteworthy feature of the first correction to the Silberberg result is simply that it removes the unphysical upturn for films thinner than $h \approx 2$, but it also seems to almost quantitatively match the simulation data.

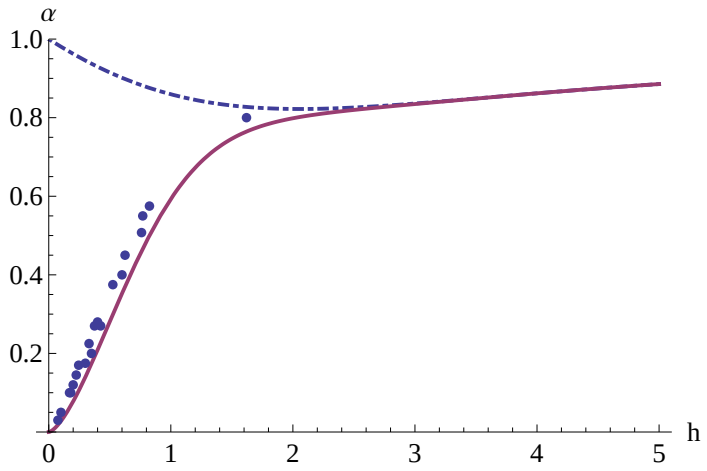

Figure 7.3: Film-thickness-averaged values of α for the Silberberg calculation (Dash-dotted curve) and the first correction to the Silberberg calculation (Thick curve). Points are data from [194]

We numerically calculate the modulus as function of α using Eq. 7.40 to convert α to film

thickness. An effective entanglement molecular weight (related to the inverse of the elastic modulus) is extracted from this prediction and compared with experiments on thin films of polystyrene [188] in Fig. 7.4. Qualitatively we predict the observed trend that the effective degree of entanglement decreases as the film thins (i.e. the system has a larger effective M_e, the molecular weight of a PP step or an entanglement strand). However, two discrepancies are noted. First, for all film thicknesses we overpredict the effect on the modulus; at $h = 1$ our effective entanglement molecular weight is roughly a factor of two too large. Second, we predict a modest effect of film thickness for films an order of magnitude larger than $R_{ee,z}$, whereas the experiments seem to approach the bulk value much more quickly. This might point to the inaccuracy of using a film-thickness-averaged value of α for the whole sample as we have done above instead of averaging the effective modulus itself over the film (i.e. the average of the inverse need not be the inverse of the average). On the other hand, the (complicated) experiments only very indirectly deduced M_e, and a simulation study of this problem should allow a more definitive assessment of the accuracy of the theoretical prediction.

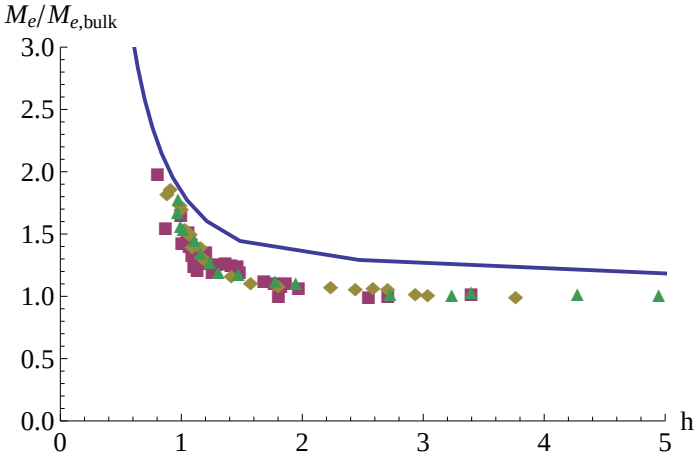

Figure 7.4: Effective normalized entanglement weight versus dimensionless film thickness using the corrected Silberberg calculation (Blue) and the simulation's interpolation formula (red) for connecting α and h. Data points are estimated from Ref. [188] from three different molecular-weight samples of polystyrene.

7.5 Summary

Our calculation for the entanglement plateau value of the shear modulus represents a potentially radical departure from the standard theoretical model of how stresses are stored in dense polymeric fluids. However, both the quantitative agreement with experiment and the scaling agreement with the classic phenomenological theories is very encouraging. In linear response the natural next step is to use the deformation-tensor approach outlined above to study different types of orientational order, particularly as induced under shear and extensional deformations. Perhaps the greatest impact of this advance, though, would be on the understanding of nonlinear deformations. As mentioned above, the standard tube-model approach requires extensive modification to describe nonlinear rheology [16, 169], and a key issue may be that the theoretical developments and approximations needed to understand the intramolecular part of the modulus may be formally correct but nevertheless addressing the wrong part of the problem.

Chapter 8

CONCLUSION AND OUTLOOK

This dissertation has explored the key role of non-Gaussian fluctuations in a variety of soft condensed matter systems, and attempted to do so at a microscopic, predictive, force-based level. Although the study of critical phenomena and the renormalization group have been the source of a vast amount of progress in condensed matter systems [36], unfortunately not all systems of interest find themselves close enough to a critical point to be well-described by such analyses. For instance, in the glass transition problem an apparently diverging relaxation time is accompanied by a static correlation length not more than an order of magnitude greater than a particle diameter [2, 3, 8] — hardly a system-spanning correlation. As such, we have approached these problems by combining self-consistent dynamical mean-field descriptions with the powerful nonlinear Langevin equation theory to capture some of the non-Gaussianity inherent in the problems.

In the realm of glassy colloidal dynamics — the first part of this thesis — we have extended the single-particle NLE theory [31] of activated dynamics to treat the correlated dynamics of two tagged particles in the a dense suspension [105, 195]. Such multi-particle correlations are at the heart of the wide variety of experimental phenomena that are collectively referred to as "dynamic heterogeneity" and are key indicators of the glassy regime of fluid behavior. We were able to qualitatively and quantitatively describe many such dynamically heterogeneous features, such as diffusion-relaxation decoupling, stretched-exponential behavior of correlation functions, and a modestly growing dynamical correlation length that matches well with experimental observations on hard-sphere suspensions.

We then extended the two-particle NLE theory to treat multiple space-time correlated

hopping, caging, and re-hopping events. This allowed the construction of simple models for the dynamics of neighbor loss and recovery that underlie the structural relaxation process. Comparisons with available simulations and colloid experiments reveal at least qualitative agreement. Our ability to define an "irreversible" event allows contact to be made with concepts that are at the heart of phenomenological, coarse-grained kinetically constrained models. In particular, we found persistence times that are well-described by the KCM-inspired parabolic law [113], decoupling that is reasonably well accounted for based on differences between mean persistence and exchange times, and some more general features of the persistence and exchange time distributions which are in qualitative accord with simulations of KCMs and coarse-grainings of atomistic glass-formers [111]. A general point is that by combining our microscopic theory for space-time correlated hopping with an intuitive picture of tracking the dynamics of two particles separating through multiple correlated hopping and re-caging processes starting from some initial configuration, we have suggested concrete, *structure*-based connections with diverse ways of thinking about the glass problem.

Our perspective in extending the single-particle NLE to the two-particle level is that cooperative rearrangements seem to involve many small motions combined with a few larger, particle-radius-scale attendant displacements, which in sum are related to unrecoverable thermal strains [107, 196]. The hope is that in the context of a dynamic mean-field theory one can capture information about the whole rearrangement event with a coarse-grained description of these larger motions. It is in this sense we expect the present two-particle approach to be more representative of structural relaxation events in real glass-forming liquids that the earlier single-particle activated dynamics NLE approach. Better still would be a microscopic activated-event theory which includes a collective mode(s) involving a cluster of particles that undergo a diversity of correlated displacements- a daunting challenge for a force-based theory. In addition to the topics addressed in Sec. 2.11, attempting to construct such a theory is a natural step to take next.

The second half of the dissertation studied a wide variety of macromolecular systems

where it is not equilibrium structure but rather topological constraints that completely determine system dynamics. Microscopic descriptions of entangled polymers have been exceptionally challenging to formulate, largely because exactly including these topological constraints (a singular interaction acting transverse to the statistically random backbone of a polymer chain) is so difficult. Early attempts at doing so relied on the mathematical discipline of knot theory and its description of topological invariants [197–199], but this program is beset with problems and is now viewed as intractable. For flexible linear chains the "knots" are at best transient objects that can unravel and disentwine over time. But even in the case of concatenated ring polymers, in which the knots that form are permanent, topological invariants are insufficiently unique to properly describe the problem. As such, for the past forty years the field has largely abandoned attempts at a microscopic description of entangled polymers, relying instead on the phenomenological single-chain mean-field theory.

The core of our theoretical advances combined the NLE theory with various extensions of a Gaussian dynamical mean-field theory that exactly expresses two-body uncrossability within a framework of self-consistent renormalization to approximately compute three- and higher-body effects [17, 24]. This allowed us to construct one of the only microscopic derivations of the ansatz at the heart of tube theories: the existence of a transverse confinement potential that hinders polymer motion and thus enforces the one-dimensional curvilinear diffusion process called reptation. However, whereas the phenomenological theory is forced to simply posit either a step [15] or harmonic [12] potential, our microscopic theory allows for a prediction of the anharmonic form of the tube [139]. A simple mapping between rigid rods and semiflexible biopolymers revealed excellent agreement with the specific anharmonic form we predict [25], and our theory of flexible chains as random walks of primitive path steps similarly seemed to accurately capture the effective confinement experienced by chain monomers relative to their closest primitive path step [30].

The anharmonic softening we predict is crucially important for rheological deformations, in which the distinction between a tube that can supply an effectively infinite restoring force

and one with a maximum restoring force becomes all-important. We thoroughly explored the rheology of rigid rods under nonlinear shear deformations, and found phenomena analogous to microscopic yielding in colloidal glasses and gels [168] that are utterly unanticipated by the tube model. Unfortunately, the deformation response of isotropic suspensions of rods has received much less attention experimentally or via simulations than flexible chains, and so there is precious little data for us to compare with.

With the advance of our theory to describe flexible chains this limitation may soon disappear, as such polymer systems have been extensively studied and the potential shortcomings of the tube model are well-documented [12, 16]. As a first step we needed to consider the very nature of stress in entangled polymer fluids, and we concluded that in the context of our model it is actually intermolecular interactions that store stress. This is in agreement with recent simulations [165–167] but diametrically opposed to the standard tube-model perspective [12]. We plan to combine this advance with appropriate constitutive equations to describe the shear rheology of flexible chains from our microscopic perspective, although some issues remain to be dealt with. In particular, the way chains retract after deformation-induced stretching is a key question, and while standard theories have assumed the chain retraction process occurs on a Rouse-like timescale it is not clear how topological constraints may affect the chain as it retracts back in its tube. This and other details are currently under study, and will hopefully be reported soon.

As one of the vanishingly few microscopic theories that respects topological constraints, there is also a great number of potential extensions of this work, particularly by generalizing the theory to simultaneously include the effects of both singular topological interactions and finite-range forces, such as those arising from excluded volume effects or coulombic repulsion. This is an unexplored frontier of research, and a unified theory capable of treating both types of interactions would open up a host of problems to microscopic study: polyelectrolyte solutions; entangled nematic liquid crystals; and an array of biopolymers where rigidity, charge, entanglements, and nonlinear mechanical response (rheology) is of high importance

in cell function, to name just a few.

Another more straightforward extension of the theory is the careful fleshing out of the "tracer" problem — one tagged polymer in a melt, solution, or cross-linked network of other macromolecules — which is key to understanding, e.g., the motion of biomolecules in F-actin/microtubule networks. Aspects of the tracer problem have been phenomenologically treated in the literature [20], but a full microscopic and predictive treatment is yet to be achieved. Although this would represent a highly non-trivial advance, much of the theoretical groundwork has already been laid for the simplest version of the microscopic tracer problem [17, 139]. The tracer problem treating a tagged particle in a polymer melt is also a first step in considering the (zero-concentration) limit of polymer nano-composites, an extremely important and burgeoning class of systems for the engineering of new materials.

As a concrete example, combining results of such a tracer calculation with the more foundational advance outlined above for also including finite-range forces could allow for a first microscopic treatment of DNA gel electrophoresis. This is a crucial technique in modern biological studies (e.g., genome mapping, where DNA must be separated by size), and different motions and relaxation mechanisms must be described depending on the architecture of the biopolymers and the level of applied field. Models based on the phenomenological tube theory are able to describe some of these, particularly in the low-field limit, but at higher fields ever more involved approximations must be brought to bear on the problem, just as in the case of applied deformations. As an example, because of the insistence on infinitely strong confinement constraints in the model, "herniation" events in which a section of DNA is pulled out of the tube must be introduced by hand [200], whereas in our microscopic theory the tube already has only a finite strength and such entropic-barrier-hopping events might be described very naturally, without the need for additional assumptions [140].

References

[1] J. C. Dyre. *Rev. Mod. Phys.*, 78:953, 2006.

[2] L. Berthier and G. Biroli. *Rev. Mod. Phys.*, 83:587, 2011.

[3] M. D. Ediger. *Annu. Rev. Phys. Chem.*, 51:99, 2000.

[4] G. L. Hunter and E. R. Weeks. *Rep. Prog. Phys.*, 75:066501, 2012.

[5] E. R. Weeks, J. C. Crocker, A. C. Levitt, A. Schofield, and D. A. Weitz. *Science*, 287:627, 2000.

[6] J. P. Hansen and I. R. McDonald. *Theory of Simple Liquids*. Academic Press, London, 2006.

[7] G. Tarjus and D. Kivelson. *J. Chem. Phys.*, 103:3071, 1995.

[8] G. Tarjus. An overview of theories of the glass transition. In L. Berthier, G. Biroli, J.-P. Bouchaud, L. Cipelletti, and W. Van Saarloos, editors, *Dynamical Heterogeneities in Glasses, Colloids, and Granular Media*. Oxford University Press, Oxford, 2011.

[9] W. Gotze and L. Sjogren. *Rep. Prog. Phys.*, 55:241, 1998.

[10] W. Gotze. *J. Phys. Condens. Matter*, 11:A1, 1999.

[11] S. P. Das. *Rev. Mod. Phys.*, 76:785, 2004.

[12] M. Doi and S. F. Edwards. *The Theory of Polymer Dynamics*. Oxford University Press, Oxford, 1986.

[13] J. R. C. van der Maarel. *Introduction to Biopolymer Physics*. World Scientific Publishing Co., Singapore, 2007.

[14] S. P. Obukhov and M. Rubinstein. *Phys. Rev. Lett.*, 65:1279, 1990.

[15] P.-E. de Gennes. *J. Chem. Phys.*, 55:572, 1971.

[16] T. C. B. McLeish. *Adv. Phys.*, 51:1379, 2002.

[17] G. Szamel and K. S. Schweizer. *J. Chem. Phys*, 100:3127, 1994.

[18] S. Prager. *J.Chem. Phys.*, 23:2404, 1955.

[19] Y. Han, A. M. Alsayed, M. Nobili, J. Zhang, T. C. Lubensky, and A. G. Yodh. *Scince*, 314:626, 2006.

[20] M. Doi, I. Yamamoto, and F. Kano. *J. Phys. Soc. Jpn.*, 53:3000, 1984.

[21] I. Bitsanis, H. T. Davis, , and M. Tirrell. *Macromolecules*, 23:1157, 1990.

[22] R. G. Larson. *J. Polym. Sci., Part B: Polym. Phys.*, 45:3240, 2003.

[23] A. E. Likhtman. *J. Non-Newtonian Fluid Mech.*, 157:158, 2009.

[24] G. Szamel. *Phys. Rev. Lett*, 70:3744, 1993.

[25] B. Wang, J. Guan, S. M. Anthony, S. C. Bae, K. S. Schweizer, and S. Granick. *Phys. Rev. Lett.*, 104:118301, 2010.

[26] J. Glaser, D. Chakraborty, K. Kroy, I. Lauter, M. Degawa, N. Kirchgeßner, B. Hoffmann, R. Merkel, and M. Giesen. *Phys. Rev. Lett.*, 105:037801, 2010.

[27] S. Ramanathan and D. C. Morse. *Phys. Rev. E*, 76:010501(R), 2007.

[28] R. M. Robertson and D. E. Smith. *Phys. Rev. Lett.*, 99:126001, 2007.

[29] Q. Zhou and R. G. Larson. *Macromolecules*, 39:6737, 2006.

[30] C. Tzoumanekas and D.N. Theodorou. *Macromolecules*, 39:4592, 2006.

[31] K. S. Schweizer and E. J. Saltzman. *J. Chem. Phys.*, 119:1181, 2003.

[32] K. S. Schweizer. *J. Chem. Phys.*, 123:244501, 2005.

[33] T. R. Kirkpatrick and P. G. Wolynes. *Phys. Rev. A*, 35:3072, 1987.

[34] R. Zwanzig. *Nonequilibrium Statistical Mechanics*. Oxford University Press, Oxford, 2001.

[35] P. C. Hohenberg and B. I. Halperin. *Rev. Mod. Phys.*, 49:435, 1977.

[36] N. Goldenfeld. *Lectures on phase transitions and the renormalization group*. Addison-Wesley, Advanced Book Program, Reading, Reading, 1992.

[37] K. Ngai. *J. Non-Cryst. Solids*, 275:7, 2000.

[38] K. S. Schweizer. *Curr. Opin. Colloid Interface Sci.*, 12:297, 2007.

[39] B. Dolliwa and A. Heuer. *Phys. Rev. E*, 61:6898, 2000.

[40] R. Yamamoto and A. Onuki. *Phys. Rev. Lett.*, 81:4915, 1998.

[41] S. K. Kumar, G. Szamel, and J. F. Douglas. *J. Chem. Phys.*, 134:214501, 2006.

[42] Y. Brumer and D. R. Reichman. *Phys. Rev. E*, 69:041202, 2004.

[43] G. Brambilla, D. El Masri, M. Pierno, L Berthier, L. Cipelletti, G. Petekidis, and Schofield A. B. *Phys. Rev. Lett.*, 102:085703, 2009.

[44] E. R. Weeks and D. A. Weitz. *Chem. Phys.*, 284:361, 2002.

[45] G. Szamel. *Europhys. Lett.*, 65:498, 2004.

[46] W. K. Kegel and A. van Blaaderen. *Science*, 287:290, 2000.

[47] E. Flener and G. Szamel. *Phys. Rev. E*, 72:011205, 2005.

[48] E. Flener and G. Szamel. *Phys. Rev. E*, 72:031508, 2005.

[49] D. R. Reichman, E. Rabani, and P. L. Geissler. *J. Phys. Chem. B*, 109:14654, 2005.

[50] E. Zaccarelli and W. C. K. Poon. *Proc. Nat. Acad. Sci. USA*, 106:15203, 2009.

[51] E. Bianchi, J. Largo, P. Tartaglia, E. Zaccarelli, and F. Sciortino. *Phys. Rev. Lett.*, 97:168301, 2006.

[52] F. Sciortino, E. Bianchi, J. F. Douglas, and P. Tartaglia. *J. Chem. Phy.*, 126:194903, 2007.

[53] E. J. Saltzman and K. S. Schweizer. *Phys. Rev. E*, 74:061501, 2006.

[54] Y.-L. Chen and K. S. Schweizer. *J. Chem. Phys.*, 120:7212, 2004.

[55] R. Zhang and K. S. Schweizer. *Phys. Rev. E*, 80:011502, 2009.

[56] G. Yatsenko and K. S. Schweizer. *Langmuir*, 24:7474, 2008.

[57] R. Zhang and K. S. SChweizer. *J. Chem. Phys.*, 133:104902, 2010.

[58] G. Yatsenko and K. S. Schweizer. *Phys. Rev. E*, 76:041506, 2007.

[59] J. Yang and K. S. Schweizer. *Europhys. Lett.*, 90:66001, 2010.

[60] D. C. Viehman and K. S. Schweizer. *Phys. Rev. E*, 78:051404, 2008.

[61] D. C. Viehman and K. S. Schweizer. *J. Chem. Phys.*, 128:084509, 2008.

[62] K. Chen and K. S. Schweizer. *Phys. Rev. Lett.*, 98:167802, 2007.

[63] K. S. Schweizer and E. J. Saltzman. *J. Chem. Phys.*, 121:1984, 2004.

[64] K. Chen, E. J. Saltman, and K. S. Schweizer. *J. Phys.: Condens. Matter*, 21:503101, 2009.

[65] K. Chen, E. J. Saltman, and K. S. Schweizer. *Annu. Rev. Condens. Matter Phys.*, 1:277, 2010.

[66] E. J. Saltzman, G. Yatsenko, and K. S. Schweizer. *J. Phys.: Condens. Matter*, 20:244123, 2008.

[67] K. Chen and K. S. Schweizer. *Europhys. Lett.*, 79:26006, 2007.

[68] V. Kobelev and K. S. Schweizer. *J. Chem. Phys.*, 123:164903, 2005.

[69] V. Kobelev and K. S. Schweizer. *Phys. Rev. E*, 71:021401, 2005.

[70] L. Berthier, D. Chandler, and J. P. Garrahan. *Europhys. Lett.*, 69:320, 2005.

[71] L. Berthier, G. Biroli, J.-P. Bouchaud, W. Kob, K. Miyazaki, and D. R. Reichman. *J. Chem. Phys.*, 126:184504, 2007.

[72] N. Lacevic, W. F. Starr, T. B. Schoeder, V. N. Novikov, and S. C. Glotzer. *Phys. Rev. E*, 66:030101, 2002.

[73] G. Szamel and E. Flenner. *Phys. Rev. E*, 73:011504, 2006.

[74] L. Berthier. *Phys. Rev. E*, 69:020201, 2004.

[75] F. Ritort and P. Sollich. *Adv. Phys.*, 52:219, 2003.

[76] E. Rabani, J. D. Gezelter, and B. J. Berne. *J. Chem. Phys.*, 107:6867, 1997.

[77] A. Widmer-Cooper, H. Perry, P. Harrowell, and D. R. Reichman. *J. Chem. Phys.*, 131:194508, 2009.

[78] K. Vollmayr-Lee. *J. Chem. Phys.*, 121:4781, 2004.

[79] E. Rabani, J. D. Gezelter, and B. J. Berne. *Phys. Rev. Lett.*, 82:3649, 1999.

[80] J. P. Garrahan and D. Chandler. *Proc. Natl. Sci. Acad. USA*, 100:9710, 2003.

[81] D. Chandler and J. P. Garrahan. *J. Chem. Phys.*, 123:044511, 2005.

[82] A. S. Keys, L. O. Hedges, J. P. Garrahan, S. C. Glotzer, and D. Chandler. *Phys. Rev. X*, 1:021013, 2011.

[83] J. M. Deutch and I. Oppenheim. *Faraday Discuss. Chem. Soc.*, 83:1, 1987.

[84] M. Guenza. *J. Chem. Phys.*, 110:7574, 1999.

[85] K. S. Schweizer. *J. Chem. Phys.*, 91:5802, 1989.

[86] C. Donati, J. F. Douglas, W. Kob, S. J. PLimpton, P. H. Poole, and S. C. Glotzer. *Phys. Rev. Lett.*, 80:2338, 1998.

[87] E. R. Weeks, J. C. Crocker, and D. A. Weitz. *J. Phys.: Condens. Matter*, 19:205131, 2007.

[88] K. S. Schweizer and G. Yatsenko. *J. Chem. Phys.*, 127:164505, 2007.

[89] H. Kramers. *Physica*, 7:284, 1940.

[90] P. Hanggi, P. Talkner, and M. Borkovec. *Rev. Mod. Phys.*, 62:251, 1990.

[91] J. Mattson, H. M. Wyss, A. Fernando-Nieves, K. Miyazaki, Z. Hu, D. R. Reichman, and D. A. Weitz. *Nature*, 462:83, 2009.

[92] E. J. Saltzman and K. S. Schweizer. *J. Chem. Phys.*, 125:044509, 2006.

[93] K. S. Schweizer and E. J. Saltzman. *J. Phys. Chem. B*, 108:17929, 2004.

[94] S. Swallen, K. Traynor, R. J. McMahon, and M. D. Ediger. *J. Phys. Chem. B*, 113:4600, 2009.

[95] W. van Megen, T. C. Mortensen, and S. R. Williams. *Phys. Rev. E*, 58:6073, 1998.

[96] M. Fuchs, I. Hofacker, and A. Latz. *Phys. Rev. A*, 45:898, 1992.

[97] R. Richert, K. Duwuri, and L.-T. Duong. *J. Chem. Phys.*, 118:1828, 2003.

[98] V. Lubchenko and P. G. Wolynes. *Annu. Rev. Phys. Chem.*, 58:235, 2007.

[99] M. D. Ediger. *J. Non-Cryst. Solids*, 235:10, 1998.

[100] R. Murarka and B. Bagchi. *Phys. Rev. E*, 67:041501, 2003.

[101] K. N. Pham, S. U. Egelhaaf, P. Pusey, and W. C. K. Poon. *Phys. Rev. E*, 69:011503, 2004.

[102] K. N. Pham, G. Petekidis, D. Vlassopoulos, S. U. Egelhaaf, P. Pusey, and W. C. K. Poon. *Europhys. Lett.*, 75:624, 2006.

[103] C. Monthus and J.-P. Bouchaud. *J. Phys. A*, 29:3847, 1996.

[104] A. Ghosh, V. Chikkadi, P. Schall, and D. Bonn. *Phys. Rev. Lett.*, 107:188303, 2011.

[105] D. M. Sussman and K. S. Schweizer. *J. Chem. Phys.*, 134:064516, 2011.

[106] R. Yamamoto and A. Onuki. *Phys. Rev. E*, 58:3515, 1998.

[107] P. Schall, D. A. Weitz, and F. Spaepen. *Science*, 318:1895, 2007.

[108] G. A. Appignanesi, J. A. Rodriguez-Fris, R. A. Montani, and W. Kob. *Phys. Rev. Lett.*, 96:057801, 2006.

[109] J. A. Rodriguez-Fris, G. A. Appignanesi, and E. R. Weeks. *Phys. Rev. Lett.*, 107:065704, 2011.

[110] L. O. Hedges and J. P. Garrahan. *J. Phys. Condens. Matter*, 19:205124, 2007.

[111] L. O. Hedges, L. Maibaum, D. Chandler, and J. P. Garrahan. *J. Chem. Phys.*, 127:211101, 2007.

[112] D. Jeong, M. Y. Choi, H. J. Kim, and Y. J. Jung. *Phys. Chem. Chem. Phys.*, 12:2001, 2010.

[113] Y. S. Elmatad, D. Chandler, and J. P. Garrahan. *J. Phys. Chem. B*, 113:5563, 2009.

[114] Y. J. Jung, J. P. Garrahan, and D. Chandler. *J. Chem. Phys.*, 123:084509, 2005.

[115] E. W. Montroll and G. H. Weiss. *J. Math. Phys.*, 6:167, 1965.

[116] H. Scher and E. W. Montroll. *Phys. Rev. B*, 12:2455, 1975.

[117] C. Monthus and J.-P. Bouchaud. *J. Phys. A: Math. Gen.*, 29:3847, 1995.

[118] J. K. E. Tunaley. *Phys. Rev. Lett.*, 33:1037, 1974.

[119] E. J. Saltzman and K. S. Schweizer. *Phys. Rev. E*, 77:051504, 2008.

[120] G. H. Vineyard. *Phys. Rev.*, 110:999, 1958.

[121] M. Tripathy and K. S. Schweizer. *Phys. Rev. E*, 83:041406, 2011.

[122] W. van Ketel, C. Das, and D. Frenkel. *Phys. Rev. Lett.*, 94:135703, 2005.

[123] P. Charbonneau, C. Das, and D. Frenkel. *Phys. Rev. E*, 78:011505, 2008.

[124] R. Everaers, S. K. Sukumaran, G. S. Grest, C. Svaneborg, and K. Kremer. *Science*, 303:823, 2004.

[125] W. Gotze. *Complex Dynamics of Glass-Forming Liquids: A Mode Coupling Theory*. Oxford University Press, Oxford, 2009.

[126] K. S. Schweizer, M. Fuchs, G. Szamel, M. Guenza, and H. Tang. *Macromol. Theory Simul.*, 6:1037, 1997.

[127] J. S. Shaffer. *J. Chem. Phys.*, 101:4205, 1994.

[128] K. Miyazaki and A. Yethiraj. *J. Chem. Phys*, 117:10448, 2002.

[129] M. K. Petersen, J. M. D. Lane, and G. S. Grest. *Phys. Rev. E*, 82:010201(R), 2010.

[130] B. Cichocki. *Z. Phys. B: Condens. Matter*, 66:537, 1987.

[131] E. Zaccarelli, G. Foffi, F. Sciortino, P. Tartaglia, and K. A. Dawson. *Europhys. Lett.*, 55:157, 2001.

[132] H. Lamb. *Hydrodynamics*. Dover, New York, 1945.

[133] G. Szamel and H. Lowen. *Phys. Rev. A*, 44:8215, 1991.

[134] T. Gleim, W. Kob, and K. Binder. *Phys. Rev. Lett.*, 81:4404, 1998.

[135] D. Long and F. Lequeux. *Eur. Phys. J. E*, 4:371, 2001.

[136] K. Foteinopoulou, N. C. Karayiannis, MavrantzasV. G., and M. Kroger. *Macromolecules*, 39:4207, 2006.

[137] K. Foteinopoulou, N. C. Karayiannis, M. Laso, and M. Kroger. *J. Phys. Chem. B*, 113:442, 2009.

[138] W. Bisbee, J. Qin, and S. T. Milner. *Macromolecules*, 44:8972, 2011.

[139] D. M. Sussman and K. S. Schweizer. *Phys. Rev. Lett.*, 107:078102, 2011.

[140] D. M. Sussman and K. S. Schweizer. *J. Chem. Phys.*, 135:131104, 2011.

[141] D. M. Sussman and K. S. Schweizer. *Phys. Rev. E*, 83:061501, 2011.

[142] S. Ramanathan. *Study of dynamics and viscoelasticity in entangled solutions of semi-flexible polymers by Brownian dynamics simulations*. PhD thesis, University of Minnesota, 2006.

[143] A. E. Likhtman. *Macromolecules*, 38:6128, 2005.

[144] S. Q. Wang, S. Ravindranath, Y. Wang, and P. Boukany. *J. Chem. Phys*, 127:064903, 2007.

[145] W. Krauth. *Statistical Mechanics: Algorithms and Computations*. Oxford University Press, Oxford, 2006.

[146] Y. C. Lin, G. H. Koenderink, F. C. MacKintosh, and D. A. Weitz. *Macromolecules*, 40:7714, 2007.

[147] P. E. Boukany, S. Q. Wang, and X. Wang. *Macromolecules*, 42:6261, 2009.

[148] Y. Wang and S. Q. Wang. *J. Rheol.*, 53:1389, 2009.

[149] M. S. Green and A. V. Tobolsky. *J. Chem. Phys.*, 14:80, 1946.

[150] A. S. Lodge. *Ind. Eng. Chem. Res.*, 34:3355, 1995.

[151] A. S. Lodge. *J. Rheol. Acta*, 12:41, 1973.

[152] A. Kushwaha and E. S. G. Shaqfeh. *J. Rheol.*, 55:463, 2011.

[153] S. Ravindranath and S. Q. Wang. *J. Rheol.*, 52:957, 2008.

[154] J. T. Padding and W. J. Briels. *J. Phys. Condens. Matter*, 23:233101, 2011.

[155] L. J. Fetters, D. J. Lohse, D. Richter, T. A. Witten, and A. Zirkel. *Macromolecules*, 27:4639, 1994.

[156] Y.-H. Lin. *Macromolecules*, 20:3080, 1987.

[157] T. A. Kavassalis and J. Noolandi. *Phys. Rev. Lett.*, 59:2674, 1987.

[158] M. Murat and K. Kremer. *J. Chem. Phys.*, 108:4340, 1998.

[159] I.Y. Lyubimov, J. McCarty, A. Clark, and M. G. Guenza. *J. Chem. Phys.*, 132:224903, 2010.

[160] S. Shanbhag and R. G. Larson. *Macromolecules*, 39:2413, 2006.

[161] C. Tzoumanekas, F. Lahmar, B. Rousseau, and D. N. Theodorou. *Macromolecules*, 42:7474, 2009.

[162] T. D. Hahn, E. T. Ryan, and J. Kovac. *Macromolecules*, 24:1205, 1991.

[163] L. J. Fetters, A. D. Kiss, D. S. Pearson, G. F. Quack, and F. J. Vitus. *Macromolecules*, 26:647, 1993.

[164] C. Baig, V. G. Mavrantzes, and M. Kroger. *Macromolecules*, 43:6886, 2010.

[165] M. Fixman. *J. Chem. Phys.*, 95:1410, 1991.

[166] J. Gao and J. H. Weiner. *Science*, 266:748, 1994.

[167] J. Rameriz, S. K. Sukumaran, and A. E. Likhtman. *J. Chem. Phys.*, 126:244904, 2007.

[168] D. M. Sussman and K. S. Schweizer. *Macromolecules*, 45:3270, 2012.

[169] R. S. Graham, A. E. Likhtman, T. C. B. McLeish, and S. T. Milner. *J. Rheol.*, 47:1171, 2003.

[170] G. Marrucci. *J. Non-Newt. Fluid Mech.*, 62:279, 1996.

[171] A. Bach, H. K. Rasmussen, and O. Hassager. *J. Rheol.*, 47:429, 2003.

[172] J. M. Deutsch and T. L. Madden. *J. Chem. Phys.*, 91:3252, 1989.

[173] M. H. Wagner. *J. Rheol.*, 38:655, 1994.

[174] S. Q. Wang, S. Ravindranath, and P. E. Boukany. *Macromolecules*, 44:183, 2011.

[175] K. Chen and K. S. Schweizer. *Macromolecules*, 44:3988, 2011.

[176] A. Dambal, A. Kushwaha, and E. G. S. Shaqfeh. *Macromolecules*, 42:7168, 2009.

[177] F. Snijkers and D. Vlassopoulos. *J. Rheol.*, 55:1167, 2011.

[178] N. Kuzuu and M. Doi. *Polym. J.*, 12:883, 1980.

[179] K. Chen and K. S. Schweizer. *Phys. Rev. E*, 82:041804, 2010.

[180] M. Doi and S. F. Edwards. *J. Chem. Soc., Faraday Trans. 2*, 75:38, 1979.

[181] M. Sato, W. H. Schwartz, S. C. Selden, and T. D. Pollard. *J. Cell Bio.*, 106:1205, 1988.

[182] R. B. Bird, C. F. Curtiss, R. C. Armstrong, and O. Hassager. *Dynamics of Polymeric Liquids, Vol. 2: Kinetic Theory*. Wiley-Interscience, New York, 1987.

[183] S. F. Edwards. *Proc. Phys. Soc.*, 92:9, 1967.

[184] J. Gao and J. H. Weiner. *Macromolecules*, 22:979, 1989.

[185] N. Uchida, G. S. Grest, and R. Everaers. *J. Chem. Phys.*, 128:044902, 2008.

[186] M. Fixman. Polymer Melt Stress Relaxation I. Homogeneous Systems. Unpublished manuscript. May 31, 2004.

[187] M. Rubinstein and R. Colby. *Polymer Physics*. Oxford University Press, Oxford, 2003.

[188] L. Si, M. V. Massa, K. Dalnoki-Veress, H. R. Brown, and R. A. L. Jones. *Phys. Rev. Lett.*, 94:127801, 2005.

[189] A. Silberberg. *J. Colloid and Interface Sci.*, 90:86, 1981.

[190] F. T. Oyerokun and K. S. Schweizer. *J. Chem. Phys.*, 123:224901, 2005.

[191] R. L. Jones, S. K. Kumar, D. L. Ho, R. M. Briber, and T. P. Russell. *Nature*, 400:146, 1999.

[192] M. Muller. *J. Chem. Phys.*, 116:9930, 2002.

[193] R. Metzler and J. Klafter. *Physica A*, 278:107, 2000.

[194] A. Cavallo, M. Muller, and K. Binder. *J. Phys. Chem. B*, 109:6544, 2005.

[195] D. M. Sussman and K. S. Schweizer. *Phys. Rev. E*, 85:061504, 2012.

[196] A. Widmer-Cooper and P. Harrowell. *Phys. Rev. E*, 80:061501, 2009.

[197] S. F. Edwards. *Proc. Phys. Soc.*, 91:513, 1967.

[198] S. F. Edwards. *J. Phys. A*, 1:15, 1968.

[199] S. Prager and H. L. Frisch. *J. Chem. Phys.*, 46:1475, 1967.

[200] B. Ackerman. *Phys. Rev. E*, 54:6685, 1996.